

AD-A144 840

CUMULATIVE DAMAGE MODEL FOR ADVANCED COMPOSITE
MATERIALS(U) DYNA EAST CORP PHILADELPHIA PA
P C CHOU ET AL. 09 MAR 84 AFWAL-TR-84-4004

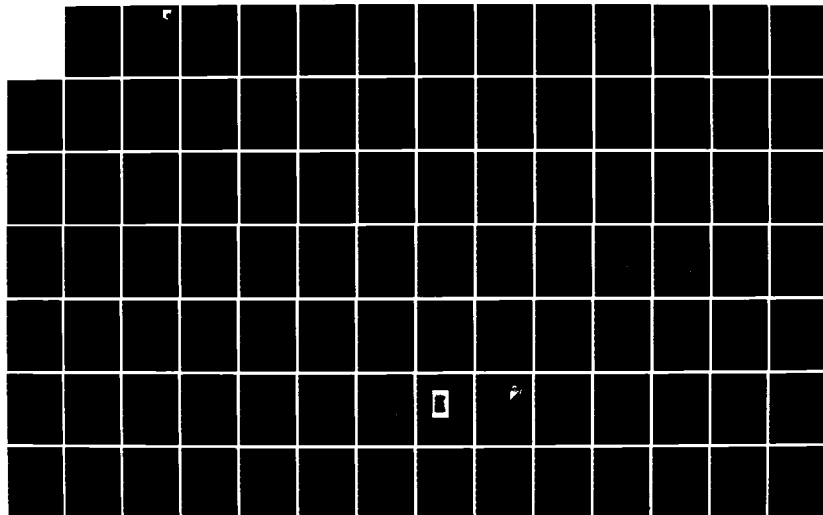
1/2

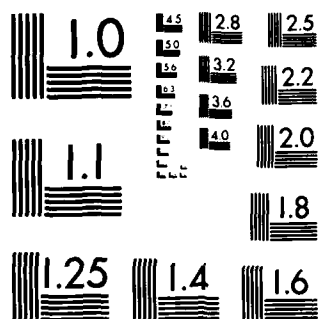
UNCLASSIFIED

F33615-80-C-5039

F/G 11/4

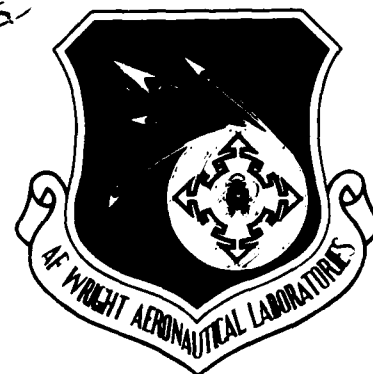
NL





MICROCOPY RESOLUTION TEST CHART
NATIONAL BUREAU OF STANDARDS-1963-A

AFWAL-TR-84-4004



CUMULATIVE DAMAGE MODEL FOR ADVANCED COMPOSITE MATERIALS PHASE II

Pei Chi Chou

Dyna East Corporation
227 Hemlock Road
Wynnewood, PA 19096

A.S.D. Wang
Charles S. Lei
Ronald B. Bucinell

Drexel University
Dept. of Mechanical Engineering
and Mechanics
Philadelphia, PA 19104

9 March 1984

Final Report for the period April 1982 - August 1983

Approved for public release; distribution unlimited.

MATERIALS LABORATORY
AIR FORCE WRIGHT AERONAUTICAL LABORATORIES
AIR FORCE SYSTEMS COMMAND
WRIGHT-PATTERSON AIR FORCE BASE, OHIO 45433

84 08 22 102

AD-A144 840

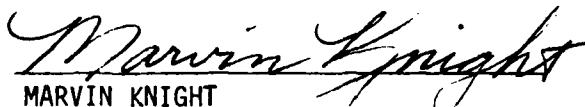
DTIC FILE COPY

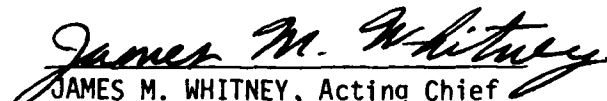
NOTICE

When Government drawings, specifications, or other data are used for any purpose other than in connection with a definitely related Government procurement operation, the United States Government thereby incurs no responsibility nor any obligation whatsoever; and the fact that the government may have formulated, furnished, or in any way supplied the said drawings, specifications, or other data, is not to be regarded by implication or otherwise as in any manner licensing the holder or any other person or corporation, or conveying any rights or permission to manufacture use, or sell any patented invention that may in any way be related thereto.

This report has been reviewed by the Office of Public Affairs (ASD/PA) and is releasable to the National Technical Information Service (NTIS). At NTIS, it will be available to the general public, including foreign nationals.

This technical report has been reviewed and is approved for publication.


MARVIN KNIGHT
Mechanics & Surface Interactions Br
Nonmetallic Materials Division


JAMES M. WHITNEY, Acting Chief
Mechanics & Surface Interactions Br
Nonmetallic Materials Division

FOR THE COMMANDER


F. D. CHERRY, Chief
Nonmetallic Materials Division

"If your address has changed, if you wish to be removed from our mailing list, or if the addressee is no longer employed by your organization please notify AFWAL/MLBM W-PAFB, OH 45433 to help us maintain a current mailing list."

Copies of this report should not be returned unless return is required by security considerations, contractual obligations, or notice on a specific document.

UNCLASSIFIED

SECURITY CLASSIFICATION OF THIS PAGE (When Data Entered)

REPORT DOCUMENTATION PAGE		READ INSTRUCTIONS BEFORE COMPLETING FORM
1. REPORT NUMBER AFWAL-TR-84-4004	2. GOVT ACCESSION NO. A144 890	3. RECIPIENT'S CATALOG NUMBER
4. TITLE (and Subtitle) CUMULATIVE DAMAGE MODEL FOR ADVANCED COMPOSITE MATERIALS, PHASE II		5. TYPE OF REPORT & PERIOD COVERED FINAL REPORT APRIL 1982 - AUGUST 1983
		6. PERFORMING ORG. REPORT NUMBER
7. AUTHOR(s) A.S.D. Wang Ronald B. Bucinell Pei Chi Chou Charles S. Lei		8. CONTRACT OR GRANT NUMBER(s) F33615-80-C-5039
9. PERFORMING ORGANIZATION NAME AND ADDRESS DYNA EAST CORPORATION 227 HEMLOCK ROAD WYNNEWOOD, PA 19096		10. PROGRAM ELEMENT, PROJECT, TASK AREA & WORK UNIT NUMBERS P.E. 62102F 2419-03-20
11. CONTROLLING OFFICE NAME AND ADDRESS MATERIALS LABORATORY (AFWAL/MLBM) AIR FORCE WRIGHT AERONAUTICAL LABORATORIES (AFSC) WRIGHT-PATTERSON AFB, OH 45433		12. REPORT DATE 9 March 1984
14. MONITORING AGENCY NAME & ADDRESS (if different from Controlling Office)		13. NUMBER OF PAGES 182
		15. SECURITY CLASS. (of this report) UNCLASSIFIED
		15a. DECLASSIFICATION/DOWNGRADING SCHEDULE
16. DISTRIBUTION STATEMENT (of this Report) APPROVED FOR PUBLIC RELEASE; DISTRIBUTION UNLIMITED		
17. DISTRIBUTION STATEMENT (of the abstract entered in Block 20, if different from Report)		
18. SUPPLEMENTARY NOTES		
19. KEY WORDS (Continue on reverse side if necessary and identify by block number) COMPOSITE MATERIALS; GRAPHITE-EPOXY LAMINATES; MATRIX CRACKS; EDGE DELAMINATION; FRACTURE MECHANICS; STRAIN ENERGY RELEASE RATE; RANDOM FLAW DISTRIBUTION; STOCHASTIC PROCESSES; FINITE ELEMENT SIMULATION; EXPERIMENTAL CORRELATION; FATIGUE GROWTH MODEL; CUMULATIVE DAMAGE MODEL		
20. ABSTRACT (Continue on reverse side if necessary and identify by block number) THIS REPORT PRESENTS THE DETAILS OF A METHODOLOGY DEVELOPED STUDY IN WHICH CUMULATIVE DAMAGE IN COMPOSITE LAMINATES IS MATHEMATICALLY MODELED. THE BASIC CONCEPT ADOPTED IN THE THEORETICAL DEVELOPMENT IS TO REGARD THE ACCUMULATION OF DAMAGE IN LAMINATES AS A LOAD AND/OR TIME DEPENDENT PROCESS. THE PROCESS BEGINS WITH THE INITIATION OF SUBLAMINATE CRACKS AT LOCATIONS WHERE DOMINATING MATERIAL FLAWS EXIST; UNDER SUSTAINING LOAD, THEN, THESE CRACKS MAY GROW AND COALESCE TO FORM A LARGE LAMINATE CRACK, OR CRACKED REGIONS. THUS, THE		

DD FORM 1 JAN 73 1473

EDITION OF 1 NOV 65 IS OBSOLETE

UNCLASSIFIED

SECURITY CLASSIFICATION OF THIS PAGE (When Data Entered)

UNCLASSIFIED

SECURITY CLASSIFICATION OF THIS PAGE(When Data Entered)

REQUIREMENT OF THE MODEL IS TO BE ABLE TO DESCRIBE THE PROCESS AND THEREBY RELATE THE LAMINATE STRENGTH, STIFFNESS, AND SERVICE LIFE PROPERTIES AS A FUNCTION OF LOADING HISTORY. ↖

IN THIS RESEARCH PROGRAM, THE CUMULATIVE DAMAGE MODEL DEVELOPMENT IS DEVELOPED FROM FIVE STAGES OF EFFORT: NUMERICAL, EXPERIMENTAL, THEORIZATION, SIMULATION, AND PREDICTION/CORRELATION. DETAILS IN EACH OF THE STAGES ARE HEREIN REPORTED.

UNCLASSIFIED

SECURITY CLASSIFICATION OF THIS PAGE(When Data Entered)

FOREWORD

This is the final technical report for Phase II of the research program sponsored by Air Force Materials Laboratory, Wright-Patterson Air Force Base, Ohio, under Contract No. F33615-80-C-5039 to Dyna East Corporation and sub-contract to Drexel University.

Dr. Pei Chi Chou of Dyna East Corporation is the project director; Dr. A.S.D. Wang of Drexel University is the principal investigator. Dr. Wang is assisted by Mr. Charles Lei and Mr. Ronald Bucinell, Drexel graduate students.

Mr. Marvin Knight of Air Force Materials Laboratory is the project monitor.

This report covers the technical work performed during the period April 23, 1982 to August 23, 1983.



A-1

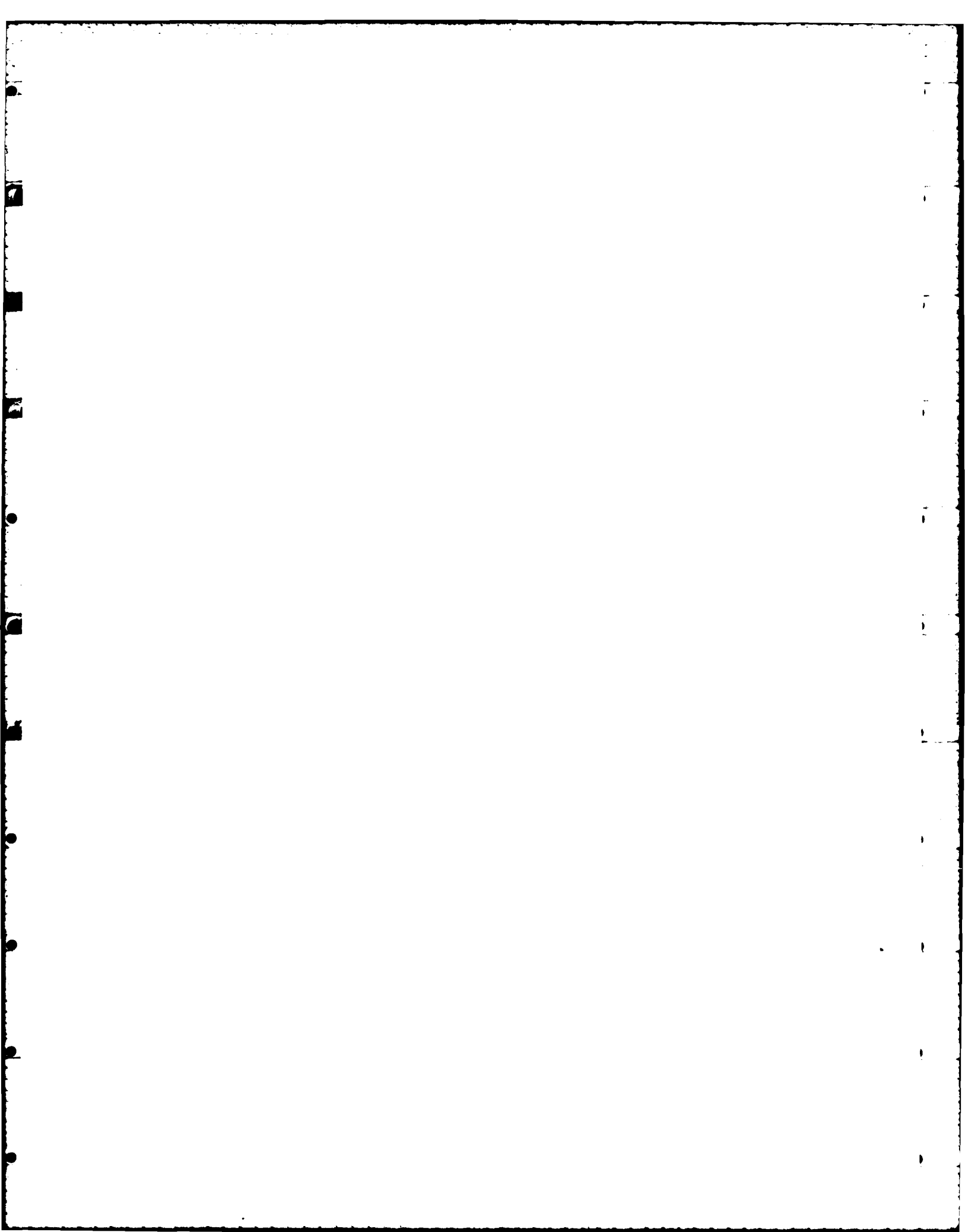


TABLE OF CONTENTS

	<u>PAGE</u>
INTRODUCTION.	1
II. ANALYTICAL DEVELOPMENT.	7
2.1. Major Modes of Sub-laminate Cracking.	7
2.2. Application of Fracture Mechanics	8
2.3. Mechanics of Multiple Transverse Cracks - Static Loading.	21
2.4. Mechanics of Multiple Transverse Cracks - Fatigue Loading	43
2.5. A Cumulative Damage Model for Transverse Cracks . . .	51
2.6. Mechanics of Free Edge Delamination	59
2.7. A Fatigue Model for Free Edge Delamination.	71
2.8. A Cumulative Damage Model for Free Edge Delamination.	76
2.9. Edge Delamination and Transverse Cracking Interactions.	80
III. EXPERIMENTAL PROGRAM AND RESULTS.	82
3.1. Scope of Experiment of Phase-I.	82
3.2. Scope of Experiment of Phase-II	84
IV. CURRENT STATUS OF RESEARCH AND METHODOLOGY SUMMARY.	86
4.1. Current Status.	86
4.2. Methodology Summary	88
REFERENCES.	91
APPENDICES.	95
A. Computation of Energy Release Rate Retention Factor .	96
B. Transverse Cracking - Static Loading.	100
C. Transverse Cracking - Fatigue Loading	110
D. Transverse Cracking - Cumulative Damage	130
E. Free Edge Delamination - Static Loading	142
F. Free Edge Delamination - Fatigue Loading.	146
G. Free Edge Delamination - Cumulative Damage.	153
H. Basic Material Characterization	165

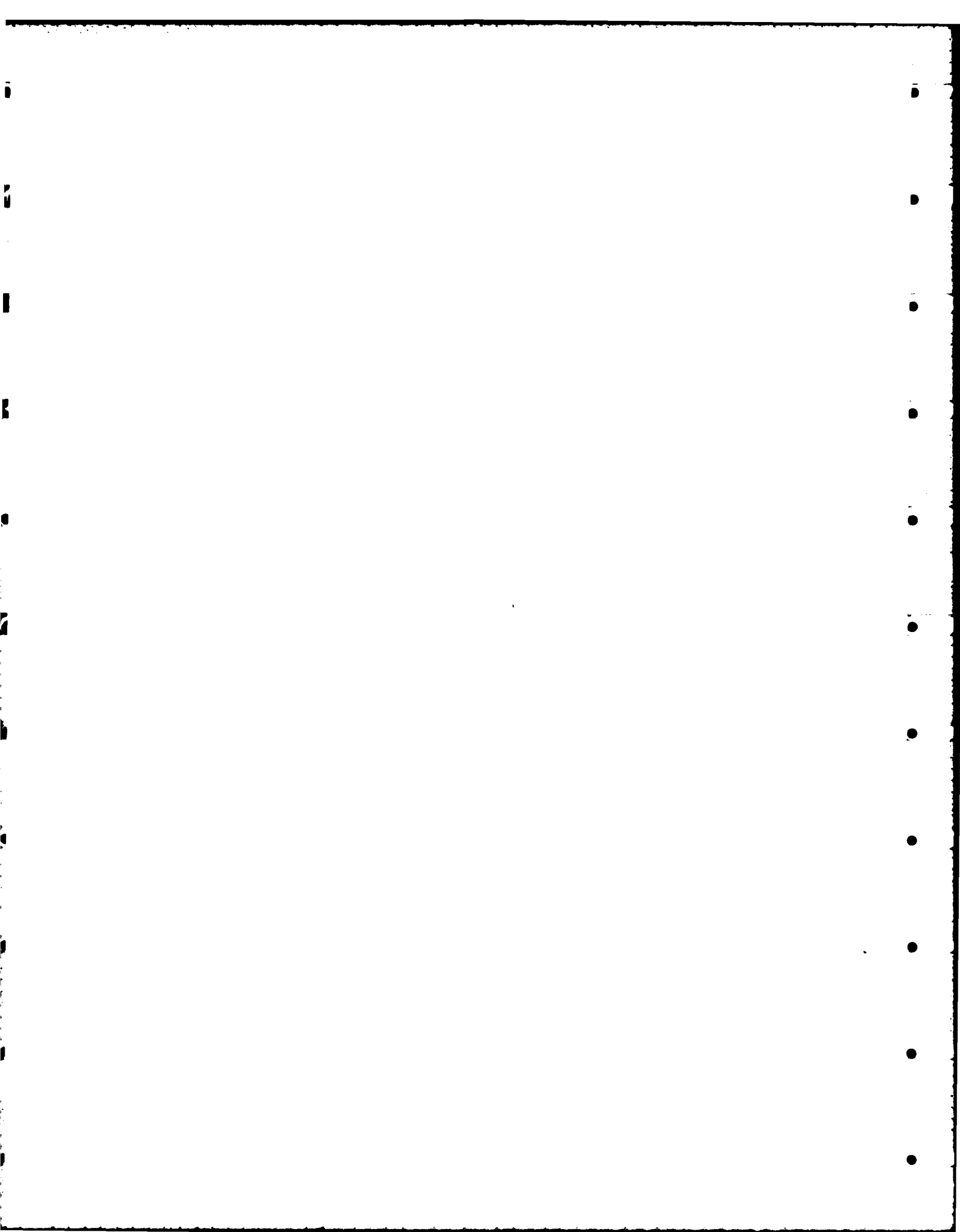
LIST OF FIGURES

<u>NUMBER</u>	<u>TITLE</u>	<u>PAGE</u>
1.1	Flow Chart for Cumulative Damage Model Construction.	6
2.1	0°/0°(a) Mode-I Delamination; (b) 90°/90° Delamination	19
2.2	Mixed-Mode $G_c (= G_{Ic} + G_{IIc})$ vs. G_{II}/G_I Ratio	20
2.3	Schematic of Multiple Transverse Cracks in $[0/90]_s$ Type Laminates.	31
2.4	Experimental Transverse Crack Density Versus Applied Laminate Stress σ_x . $[0_2/90_2]_s$	32
2.5	Experimental Transverse Crack Density Versus Applied Laminate Stress σ_x . $[0_2/90_3]_s$	33
2.6	Effective Flaws in 90°-Layer (top); Size a and Spacing S Distribution (below)	34
2.7	The Energy Release Rate as a Function of Flaw Size 2a.	35
2.8	Energy Release Rate Retention Factor as a Function of S, the Distance Between the Flaw and the Crack.	36
2.9	Flow-Chart for Monte-Carlo Simulation.	37
2.10	Energy Release Rate Coefficients for Mechanical Load $[0_2/90_2]_s$ and $[0_2/90_3]_s$	38
2.11	Energy Release Rate Coefficients for Thermal Load $[0_2/90_2]_s$ and $[0_2/90_3]_s$	39
2.12	Energy Release Rate Retention Factor $R(S)$ as a Function of Normalized Distance S/nt	40
2.13	Simulated Transverse Crack Density Versus Applied Laminate Stress $\bar{\sigma}_x$. $[0_2/90_2]_s$	41
2.14	Simulated Transverse Crack Density Versus Applied Laminate Stress $\bar{\sigma}_x$. $[0_2/90_3]_s$	42
2.15	Experimental Transverse Crack Density Versus Fatigue Cycle N. $[0_2/90_2]_s$	46
2.16	Experimental Transverse Crack Density Versus Fatigue Cycle N. $[0_2/90_3]_s$	47
2.17	Schematic Representation of the Fatigue Damage Function F_{TC} for Transverse Cracking.	48
2.18	Simulated Transverse Crack Density Versus Fatigue Cycle N. $[0_2/90_2]_s$	49

LIST OF FIGURES - Continued

<u>NUMBER</u>	<u>TITLE</u>	<u>PAGE</u>
2.19	Simulated Transverse Crack Density Versus Fatigue Cycle N. [0 ₂ /90 ₃] _s	50
2.20	Schematics for the Concept of Constant Damage States	55
2.21	Schematics for the Concept of a Cumulative Damage Model.	56
2.22	Constant Damage Lines for [0 ₂ /90 ₂] _s Laminates.	57
2.23	Constant Damage Lines for [0 ₂ /90 ₃] _s Laminates.	58
2.24	Typical Shape of Energy Release Rate G(a) for Delamination	65
2.25	Free Edge Delamination Induced by Compression. AS-3501-06 [90 ₂ /0 ₂ /±45 ₂] _s	66
2.26	Interlaminar Normal Stress Distribution and Energy Release Rate Coefficients for [90 ₂ /0 ₂ /±45 ₂] _s Under Compression	67
2.27	Delamination Growth (a/w) versus Applied Load for [±25/90] _n] _s	68
2.28	Energy Release Rate Coefficients for Delamination Under Mechanical Load.	69
2.29	Energy Release Rate Coefficients for Delamination Under Thermal Load	70
2.30	Percent Delamination vs. Fatigue Cycles for [±25/90] _s Laminates, σ = 29 ksi.	73
2.31	Percent Delamination vs. Fatigue Cycles for [±25/90] _s Laminates, σ = 33 ksi.	74
2.32	Percent Delamination vs. Fagigue Cycles for [±25/90] _s Laminates, σ = 40 ksi.	75
2.33	Cumulative Damage Tests: [±25/90] _s	78
2.34	Cumulative Damage Tests: [±25/90] _s	79
4.1	The Infrastructure of the Cumulative Damage Model.	90

* All Figures in the Appendices are not Listed Here.



I. INTRODUCTION

The objective of this research program is to develop a cumulative damage model which can be used to relate the strength, stiffness, and service life properties of epoxy-based structural composite laminates. The desired cumulative damage model would take into account the effect of load-history, characteristics of the applied stress (tension, compression, etc.), lamination stacking sequence, the effect of natural and man-made flaws and the inherent mechanical properties of the basic composite material system. In essence, a unified methodology for laminate failure analysis is to be developed in this research program.

The basic concept adapted in the model development is to regard the accumulation of damages in composite laminates as a load and/or time dependent "process." The process involves a certain type of sub-laminate cracks which initiate at locations where some dominating material flaws exist. Under sustained loading these sub-laminate cracks would grow and some would coalesce to form a large laminate crack. At this stage, failure of the laminate can be expected.

The term "sub-laminate cracks" pertains to small matrix cracks which generally occur internal to the laminate. The origin of sub-laminate cracks is thought to stem from sub-critical growth and coalescence of inherent material microflaws which exist throughout the laminate. These microflaws would act as local stress risers when external loading is applied or a temperature change is incurred. At a certain location where the stress condition reaches a critical value, some dominant flaws begin to coalesce and form a large plane-crack. The size of such a crack is orders of magnitude larger

than that of the microflaws. It is usually detectable at the macroscopic scale, e.g., by x-radiography, sonic scan and even visual inspection [1].

Because the matrix material and the matrix-fiber interface are weaker compared to the strength of the fibers, a sub-laminate crack is almost always propagated through the matrix phase of the material. Hence it is commonly labeled as a matrix crack.

Since laminates have a layered structure, an internal matrix crack cannot always undergo monotonic propagation; the crack may either be arrested or blunted at some layer interface boundaries. This crack-arresting mechanism permits an increase of the applied load without causing catastrophic failure of the laminate. Consequently, other flaws in the laminate may become critical and similar matrix cracks are formed as the applied load is increased.

Thus, after a certain loading process, be it monotonic or cyclic stressing, a distribution of matrix cracks within the laminate member is obtained.

Although the inherent material microflaws may exist randomly in the laminate, the general characteristics of the macroscopic matrix cracks are found to be highly dependent on the nature of loading as well as the lamination geometry, such as laminate stacking sequence, lamina thickness, laminate shape features, etc. [2]. Generally, for a given laminate under a given class of loading, the matrix cracking pattern is mechanically reproducible, though it may exhibit a certain statistical variation [3].

This fact suggests that the formation mechanisms of a certain mode of sub-laminate cracks is, at least partially, mechanically deterministic, while the precursors of the cracks (material microflaws) remain probabilistic.

This observation has led the development of the desired cumulative damage model to a methodology which combines both a probabilistic and a mechanistic approach.

The actual procedures followed for the model construction in this research program is illustrated by the schematic flow diagram shown in Figure 1.1. The various developmental stages in this flow diagram are displayed in a two-dimensional grid-work as shown. From the top to the bottom row there are three parallel tasks; namely:

- (a) Experimental investigation on laminates in which a certain sub-laminate cracking mode is developed under external loading. The entire load and/or time dependent crack growth process is monitored and documented. The physical parameters that influence the crack development mechanisms are identified and analyzed.
- (b) Analytical investigation in which the development of the specific sub-laminate cracking process is simulated by a stochastic procedure incorporating the mechanics of fracture and the concept of random material flaw distributions.
- (c) A correlation between the experiment and the analytical simulation whereby the desired damage cumulative model is constructed.

In each of the three tasks outlined above, there are four investigative stages shown in Figure 1.1; from left to right they are:

- (a) A study of the damage accumulation processes under static loading. In this stage, the major modes of sub-laminate cracking are identified. In each case, the predominant influencing physical parameters are taken into account in the simulation model and a load-damage growth relation is then established.
- (b) A study of the damage accumulation processes under constant amplitude cyclic loading. In this stage, a crack growth law is developed and a load-cycle-damage relation is established for each of the major failure modes.
- (c) From the results of stages (a) and (b) above a relationship between the load (σ) and the fatigue cycle (N) is established for a given laminate damage state.
- (d) Using the results of (c), a model for the cumulative damage process in laminates subjected to variable amplitude fatigue loading is then constructed based on the concept of the constant damage states.

In Chapter II of this report we shall present the details of the analytical developments as highlighted above. The predictive models are then applied to the specific cases for which experimental results have been generated.

Chapter III describes the scope of the experiment. Most of the relevant results are either tabulated and/or graphically displayed in the Appendices.

A brief discussion on the current status of the research program and a summary of the continued work in Phase III are highlighted in Chapter IV.

FLOW CHART FOR CUMULATIVE DAMAGE MODEL CONSTRUCTION

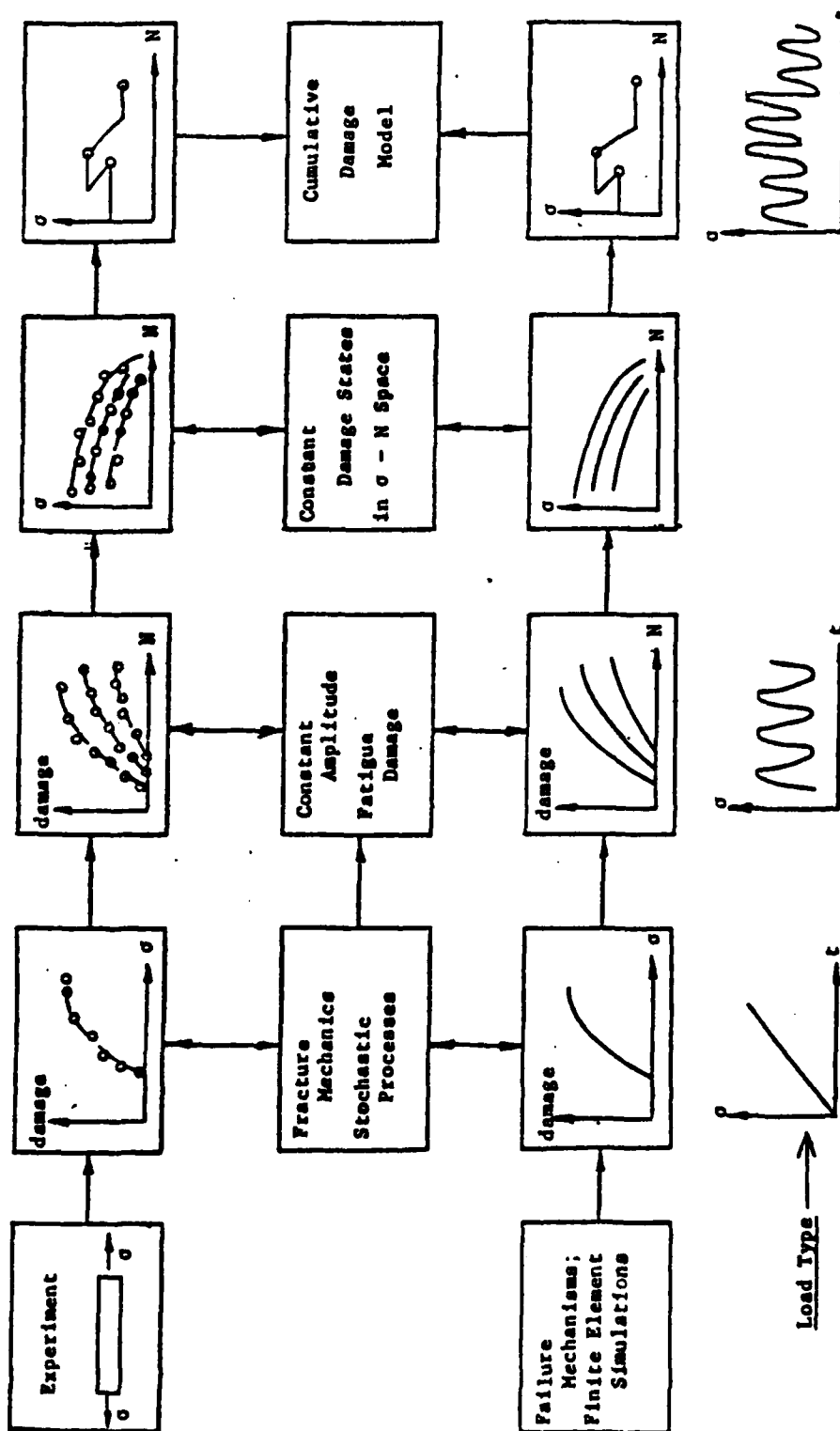


Figure 1.1 Flow Chart for Cumulative Damage Model Construction.

II. ANALYTICAL DEVELOPMENT

2.1. Major Modes of Sub-Laminate Cracking

Experiments using graphite-epoxy composite laminates have shown that transverse cracks, fiber splittings and free-edge induced delamination are among the most frequently encountered sub-laminate cracking modes. Furthermore, these cracking modes can occur independently or concurrently depending on the individual case conditions. Sometimes, one mode can interact with another resulting in a complicated damage state in the laminate.

For purpose of an analytical model construction, it is necessary to first understand the exact mechanisms of each individual cracking mode and then the mechanisms of two or more interacting modes. In this research program, it has been planned that the following cracking mechanisms be investigated:

- (a) Initiation and growth of multiple transverse cracks in laminates containing a 90° layer,
- (b) Initiation and growth mechanisms of a predominantly free-edge induced interlaminar cracking (delamination),
- (c) Interaction between multiple transverse cracking and free-edge delamination, and
- (d) Interaction between multiple transverse cracking and longitudinal (0° -layer) fiber splitting mechanisms.

In all cases both the static growth mechanisms and the fatigue growth mechanisms are to be studied. However, since Items (a) and (b) above

require a two-dimensional stress analysis, while items (c) and (d) require a three-dimensional stress analysis, the present research effort follows the same order as listed above.

In this chapter, a unified methodology is to be developed which is based on the fundamental concept of the classical fracture mechanics and the concept of effective material flaws.

2.2. Application of Fracture Mechanics

To facilitate our subsequent model development, let us first introduce briefly the basic concept of the classical fracture mechanics. Consider the well-known Griffith problem which pertained to an elastic homogeneous and isotropic plate uniformly stretched in one direction by σ . The plate has a through crack of size $2a$ orientated normal to the direction of σ . The length of the crack is assumed small but finite. Griffith postulated that: at the instance of crack extension, a loss of the stored elastic strain energy near the crack-tip region is incurred. This energy is assumed to be converted into the surface energy of the crack extension. Thus, a balance of energy at the instance of crack extension leads to the criterion

$$\frac{\partial U}{\partial a} = \frac{\partial S}{\partial a} \quad (1)$$

Equation (1) defines the general condition under which the existing crack begins to propagate in self-similar mode.

For the plate considered by Griffith, the critical stress at the instance of crack extension can be derived from (1), giving

$$\sigma_c = \left(\frac{2E\gamma}{\pi a} \right)^{1/2} \quad (2)$$

where γ is the free surface energy density (per unit area) of the material.

When applied to engineering problems, the Griffith theory is often modified for practical considerations. For instance, σ_c in Equation (2) becomes unbounded as $a \rightarrow 0$. Clearly, no real material can sustain an infinite stress. The limitation of Equation (2) can be conveniently circumvented by invoking the assumption of material flaws. That is to assume that the material possesses naturally some characteristic distribution of microflaws. It is then assumed that the worst flaw, having a finite empirical size of $2a_0$, acts like a real crack. This particular flaw determines a finite critical stress according to Equation (2).

Of course, flaws do exist in real materials, especially in fibrous composite systems. But, the real physical identity of the flaws cannot be practically included in the fracture analysis; only their aggregate effects could perhaps be considered. Thus, to apply the concept of the classical fracture mechanics to problems involving cracks in composites, a new concept of "effective material flaw distribution" will be introduced. Detailed discussion of this concept is presented in the next section.

Another practical consideration is related to the definition of γ , the free surface energy density of the material. For a crack in a brittle material such as glass, γ could be considered as defined above. For most other engineering materials, however, crack extension is found to associate a certain degree of inelastic deformation near the crack-tip region. For this reason a crack extension will consume more than just the elastic

strain energy released; it may also consume some amount of the inelastic deformation energy. Furthermore, the crack extension path or the crack surface, may show a certain degree of ruggedness depending on the heterogeneity of the material viewed at a microscale. Early studies on structural metals have regarded the quantity γ as the total irreversible work required to create a unit crack surface area. Or, it can be interpreted as the energy dissipated in the crack-tip region during crack extension. Then, γ will depend on the inelasticity and/or the microscopic heterogeneity of the material locally. It is regarded also as an intrinsic property of the material which can be defined only empirically.

These considerations are of fundamental importance when a crack-like failure in composite laminate is to be modeled using fracture mechanics method.

In common practice the right-hand side of Equation (1) is replaced by $G_c = (2\gamma)$, known as the critical energy release rate of the material. The left-hand side is a function of the applied load, the geometry of the body, and the size of the crack. Thus, for a crack undergoing self-similar extension, the Griffith criterion is expressed as

$$G(\sigma, a) = G_c. \quad (3)$$

Accordingly, the development of the fracture model for a known sub-laminate crack rests upon the calculation of $G(\sigma, a)$ and the physical measurement of G_c .

As has been mentioned earlier, the quantity a in $G(\sigma, a)$ represents the effective flaw size which is actually random in nature. Hence, a new concept must be developed which includes this important feature.

The Concept of Effective Material Flaw Distribution

In stress analysis of laminates, the basic approach has been the concept of ply-elasticity [4]. This concept pertains to laminates that are made of unidirectional composite plies and are stacked together with each ply orientated in a certain designed direction. For purpose of laminate analysis, the unidirectional ply is regarded as the building block of the laminate. The approach is to characterize the effective properties of the building block so as to predict the properties of the laminate. The fundamental assumption in ply-elasticity is that the unidirectional ply, which is microscopically heterogeneous, can be replaced by an "effective" homogeneous body without altering the global properties of the laminate. The assumption thus enables the representation of the unidirectional ply by two sets of homogeneous constants. The first is associated with the deformation properties, e.g., via the generalized Hookes Law:

$$\sigma_i = C_{ij} e_j \quad i, j = 1, 6 \quad (4)$$

where the stiffness constants, C_{ij} , are determined as averaged quantities over a solid volume of macroscopic dimension.

The second set of material constants is associated with the failure properties, e.g., via the strength criterion,

$$F_{ij} \sigma_i \sigma_j + F_i \sigma_i = 1 \quad i, j = 1, 6 \quad (5)$$

where F_{ij} and F_i are strength constants determined upon the first failure of the ply under the homogeneous stress condition σ_i .

However, it is generally accepted that failure of structural material is a local extremum property [5]. The tensile strength in the transverse

direction of the unidirectional ply, for instance, is determined by some local extrema. Local extrema, of course, included the inherent material microflaws which form a distribution both in size and in location. It is clear then, the ply strength constants F_{ij} and F_i are determined essentially by the "dominating" local flaw in the unidirectional ply. The presence of other (smaller) flaws cannot be reflected by the constants F_i and F_{ij} .

In order to model multiple failures in laminate such as described earlier, it is necessary to include the existence of the microflaw distribution in the ply. Hence, it will be postulated here that multiple failures in a lamina are governed by the initiation and propagation of a distribution of "effective" flaws. These hypothetical flaws act individually like cracks and are capable of propagating into matrix cracks during a certain course of loading. In this manner, failures in the lamina will be governed by a criterion of crack propagation rather than by a homogeneous failure law such as Equation (5).

Specifics of the effective flaw distribution will be covered when specific problems are discussed. At this point, let us just regard the quantity a in Equation (3) as a given random variable for the material system.

The Calculation of $G(\sigma, a)$

In the theory of the LEFM, the singular stress field near a crack tip in a homogeneous, isotropic elastic body has been represented by some analytical functions in the theory of complex variables [6]. These near-field stresses can result in three particular modes of the crack opening.

These are known as the opening mode (I), the sliding mode (II), and the anti-plane shearing mode (III). For each mode, the stresses are expressed in terms of the associated stress intensity factor K [7]; and consequently, the associated $G(\sigma, a)$ is computed in terms of K . Since the relation between K and G is one-to-one, Equation (3) reduces to the form

$$K(\sigma, a) = K_c \quad (6)$$

Similar relations between K and G for orthotropic media having a crack orientated along one of the major axes can also be obtained [8]. But the analytical solutions for the singular stress field often require tedious mathematical derivations.

Direct solution methods for $G(\sigma, a)$ have been available, among them are the well-known J-integral method [9, 10] and the virtual crack closure technique by Irwin [11].

Irwin [11] observed that the elastic strain energy released during a virtual crack extension, Δa , is equal to the work done in closing it again. But the inverse problem provides easily the solution for the surface transactions, $\bar{\sigma}$, over a . The crack-tip energy release rate is then represented by

$$G = \lim_{\Delta a \rightarrow 0} \frac{1}{2\Delta a} \int_0^{\Delta a} (\bar{\sigma} \cdot \Delta \bar{u}) da \quad (7)$$

where $\Delta \bar{u}$ is the crack opening displacement vector over Δa .

If the crack extension involves all three modes (I, II, III), the vector product in Equation (7) will give a sum of three scalars associated respectively with G_I , G_{II} , and G_{III} .

The virtual crack-closure representation is particularly adaptive to machine computations. Rybicki and Kanninen [12] suggested a two-dimensional finite element technique to evaluate G for a line crack in a plane. The crack-tip stress vector, $\bar{\sigma}$, and the displacement vector, $\Delta\bar{u}$, in Equation (7) are approximated by the nodal forces and displacements, respectively, in a finite element representation.

Wang and Crossman applied this technique and developed a generalized plane strain finite element routine [13, 14], which can simulate a line crack propagation in the two-dimensional cross-section of a laminate. Since a general laminate under load may suffer cross-sectional warping, the routine actually computes three-dimensional stresses and displacements and hence also the three modes of the energy release rate G_I , G_{II} , and G_{III} .

If a laminate is subjected to the far-field stress σ_o and a sub-laminate crack is to be simulated, the crack-tip energy release rate can be expressed in the general form

$$G_e = C_e(a/t) \cdot t \cdot (\sigma_o/E_o)^2 \quad (8)$$

where E_o is laminate stiffness in σ_o direction and t is the linear scale between the actual model and the finite element model. C_e is a function dependent only on the crack size a which is routinely generated for a known sub-laminate cracking mode in a given laminate, see [13].

Similarly, if the laminate is subjected to a uniform temperature drop ΔT and if a thermally induced crack opening is resulted then the associated energy release rate at the crack tip is expressed by

$$G_T = C_T(a/t) \cdot t \cdot (\Delta T)^2 \quad (9)$$

Generally, the laminate is prestressed by a ΔT due to curing, so a combined effect is resulted when σ_o is applied; the combined energy release rate is:

$$G = [(C_e)^{1/2} e_o + (C_T)^{1/2} \Delta T]^2 \cdot t \quad (10)$$

where e_o is the far-field strain ($= \sigma_o / E_o$).

It is seen that the finite element technique is extremely versatile, and can be efficiently executed for simulating complicated sub-laminate cracking growth such as delamination.

In this research program the finite element routine developed by Wang and Crossman [13, 14] was applied for the energy release rate calculations. Some details of this routine have also been discussed in the Phase I Final Report [15].

The Evaluation of G_c

When fracture occurs in the material, the energy released in the process is expected to depend in part on the microscopic morphology of the fracture surface. Fibrous composites are known to possess very complex fracture surface details [16]. The observed delamination surfaces in graphite-epoxy composites, for instance, reveal a considerable raggedness because the crack must pass around the reinforcing fibers. But, any such crack surface details will be "smoothed out" by the assumption used in ply-elasticity and their effects can be reflected only in the measured quantity of the fracture energy release rate G_c .

For this reason, G_c measured for some matrix-predominant fractures in epoxy-based composites has been found to depend on the direction of fracture propagation. Cullen [16] and Williams [17] considered two

different cases of delamination in a graphite-epoxy composite system as illustrated in Figure 2.1. The first case is a $0^\circ/0^\circ$ delamination in which the crack path is in the fiber direction; while the second is a $90^\circ/90^\circ$ delamination where the crack path is transverse to the fiber direction. Both were subjected to mode-I cracking condition. They found that the microscopic morphology of the $90^\circ/90^\circ$ delamination surface exhibited considerably more raggedness than the $0^\circ/0^\circ$ delamination surface. This resulted in a marked difference for the measured G_c . Note that these two fracture events occur essentially in the same interface when viewed macroscopically. Yet, the respective G_c values can differ greatly depending on the direction of the crack propagation.

Clearly, when the Griffith formula Equation (3) is applied for crack extension in composites, the term G_c requires a precise qualification. Similarly, when a test method is devised to measure G_c , the dimensional and directional characteristics of the measured data must also be considered.

Mode-I Interlaminar G_{Ic} . A commonly used test method to determine interlaminar G_{Ic} is the splitting cantiliver beam. Cullen [16] and Wilkins [18] have used this method to determine the interlaminar G_{Ic} when the crack is propagating in the direction of the fibers ($0^\circ/0^\circ$ delamination). For the graphite-epoxy systems used in their study, (AS-3501-02), they found that G_{Ic} at room temperature is about 0.85 lb/in, or 130 J/m^2 . This value is about twice the G_{Ic} measured for the pure epoxy resin. Williams [17] used a compact specimen which simulates roughly a $90^\circ/90^\circ$ delamination. He found, for the same material system, a G_{Ic} value of 1.3 lb/in, or about three times that of the pure resin. Williams explained that the fracture

surface in his specimens showed fiber breakage as well as fractured epoxy debris; this had resulted in a higher value for G_{Ic} .

In another paper by Wilkins, et al. [19], it is reported that G_{Ic} in delamination of $0^\circ/90^\circ$ interface is also found higher than that of $0^\circ/0^\circ$ delamination. These findings reaffirm the directional dependent nature of G_{Ic} .

Mixed-mode interlaminar $G_{(I, II)c}$. The splitting cantiliver beam method has also been used in mixed-mode crack growth experiments. In this case, it is necessary to apply different loads at the top and the bottom parts of the split so as to create both an opening (I) and a sliding (II) action. Vanderkley [20] and Wilkins [18] conducted tests on the same graphite-epoxy system (used for their mode-I tests) and found the total energy release rate $G_{(I, II)c} = G_{Ic} + G_{IIc}$ that exhibited a strong dependence on the G_{II}/G_I ratio.

This phenomenon (G_{II}/G_I ratio dependence) is not uncommon in a mixed-mode fracture. Similar observations were reported for brittle metals as well as pure epoxy resins [21]. It is, perhaps, more pronounced in fibrous composites. Generally, the increased fracture resistance in mixed-mode cracks is attributed to possible matrix yielding under shear as well as crack-closure friction due to the sliding action. In any event, this question requires further research.

In a test on a series of double-notched off-axis directional graphite-epoxy (AS-3501-06) laminates, Wang, et al. [22] measured the mixed-mode $G_{(I, II)c}$ as a continuous function of G_{II}/G_I ; their results are shown in Figure 2.2. It is seen that $G_{(I, II)c}$ is monotonically increasing with

G_{II}/G_I , possibly reaching an asymptotic value.

Having established a reasonable understanding about the quantities on both sides of the fracture equation, Equation (3), we are now ready to apply this equation to some specific types of sub-laminate cracking. The remainder of this chapter is devoted entirely for this purpose.

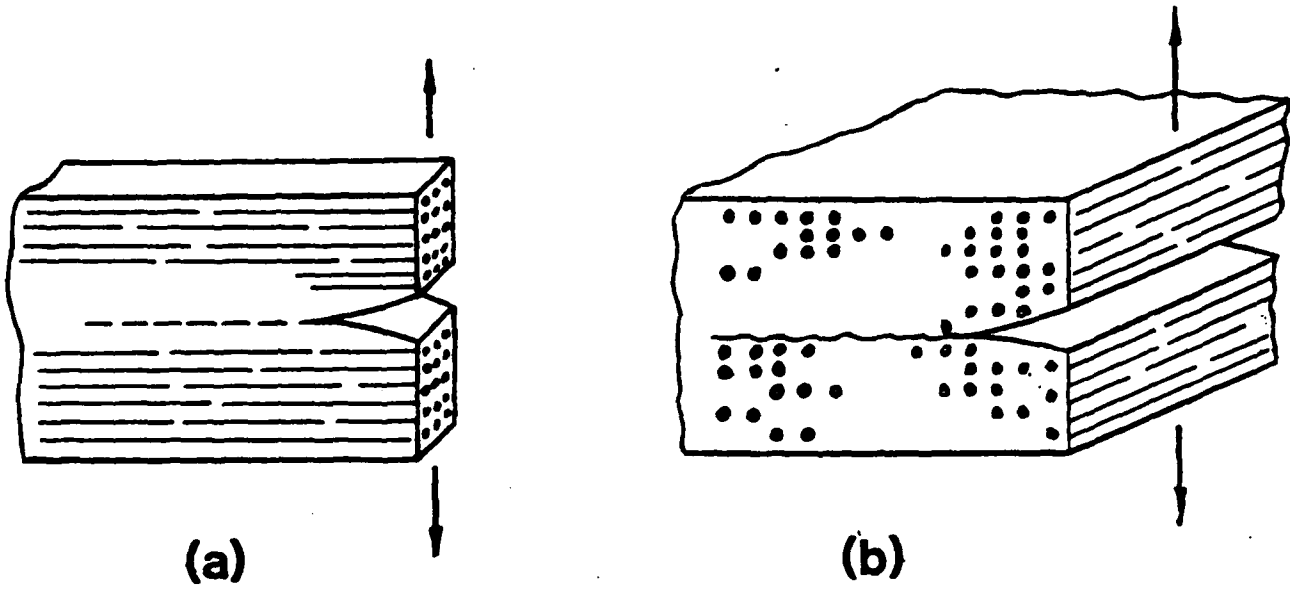


Figure 2.1 0°/0° Mode-I Delamination; (b) 90°/90° Delamination.

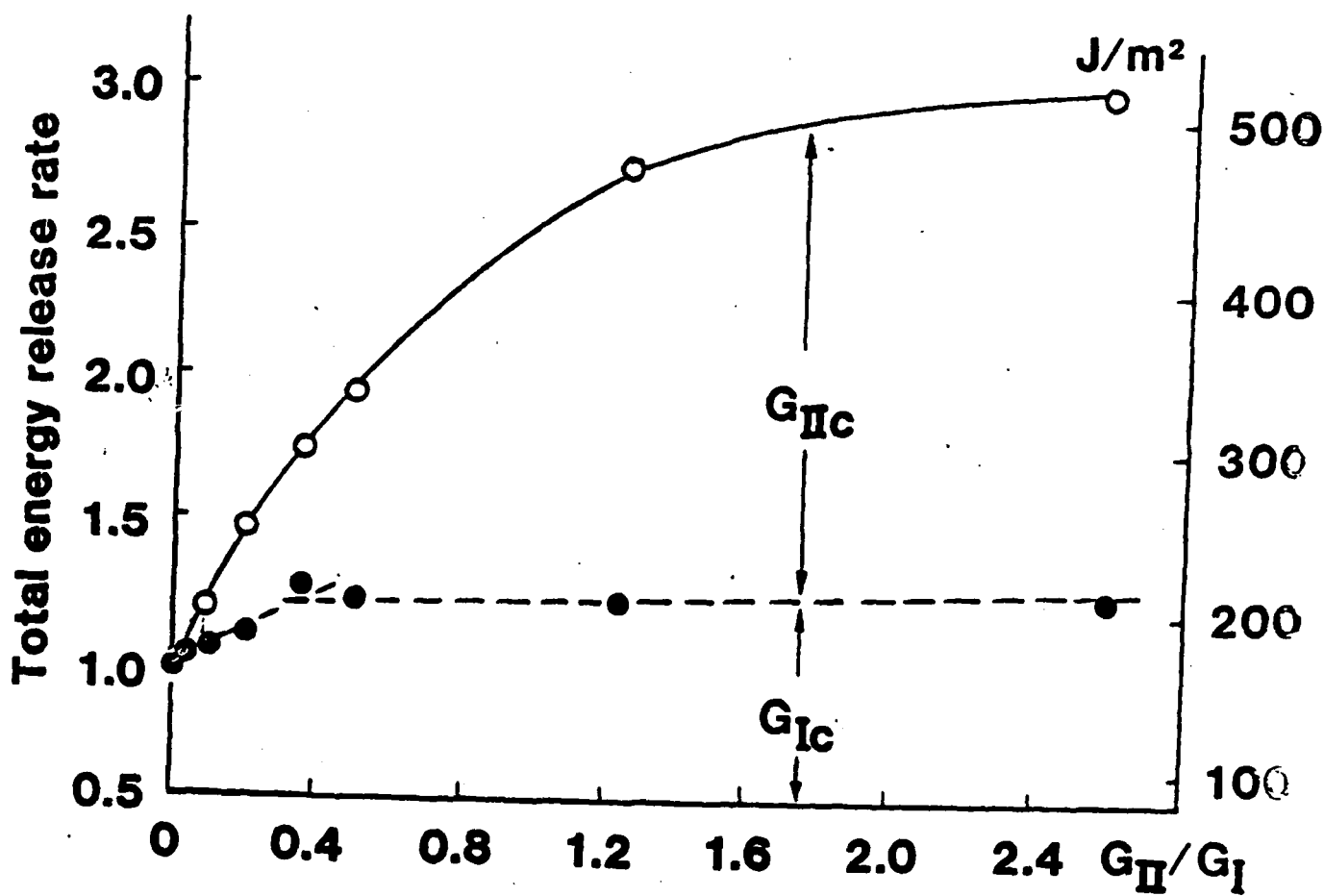


Figure 2.2 Mixed-Mode $G_c (=G_{Ic} + G_{IIc})$ vs. G_{II}/G_I Ratio.

2.3. Mechanics of Multiple Transverse Cracks - Static Loading.

Transverse cracks are found in epoxy-based laminates usually at a relatively low loading level. When viewed at the macroscopic scale, the cracking action is simply a sudden separation of fibers by breaking the epoxy bond. To illustrate, consider as an example a $[0/90]_s$ type laminate such as shown in Figure 2.3. Under the far-field tensile stress the 90° -layer may suffer multiple transverse cracks. Generally, the sequence of events is as follows: a single crack forms first when the applied load reaches a certain critical value, which defines the "onset" of the events; as the applied load increases, more similar cracks are formed. If there is no other failure mode setting in at high load, the number of transverse cracks will continue increasing, until it reaches a saturation density.

Figures 2.4 and 2.5 show the experimentally obtained crack density (number of transverse cracks per unit length of specimen) versus the applied far-field stress plots for, respectively, $[0_2/90_2]_s$ and $[0_2/90_3]_s$ laminates (these results were reported earlier in Reference [15]). It is seen that the thickness of the 90° -layer in these two laminates has a profound influence on the characteristics of the crack formation and growth behaviors. Specifically, the laminate with thinner 90° -layer requires a higher load for onset of transverse cracking; it is also capable of yielding a higher crack density than the laminate with the thicker 90° -layer.

The 90° -layer thickness effect on transverse cracking behavior in $[0/90]_s$ laminates was first documented experimentally by Baser, et al. [23]. The effect was attributed to the constraining actions of the

adjacent 0° -layers; they observed that a transverse crack can be no larger than the 90° -layer thickness and the energy release rate which drives the crack is also limited by the same factor.

The 90° -layer thickness effect on crack density has been explained by the existence of a "shear-lag" zone at the transverse crack root [23 - 25]. That is, an interlaminar shear stress zone is developed near the $0/90$ interface where a transverse crack terminates. This shear stress is singular at the crack root but decays exponentially a distance away. Inversely, the in-situ tensile stress in the 90° -layer is nil on the transverse crack surface but it regains its far-field value outside the shear-lag zone. Ideally, any two adjacent cracks should be spaced by the shear-lag distance and the shear-lag distance is proportional to the 90° -layer thickness, hence the observed 90° -layer thickness effect on crack density.

Although the shear-lag argument is ideally correct, an evenly spaced transverse cracks pattern does not occur in practice; and the transverse cracking behavior is influenced strongly also by the inherent flaw distribution in the 90° -layer.

The Energy Model for Transverse Cracks

For purpose of clarity, consider a $[0/90]_s$ type laminate such as shown in Figure 2.3. Assume that, in the 90° -layer, the material has a random distribution of microflaws. The gross effects of the microflaws at the macroscopic scale are represented by a hypothetical distribution of "effective" flaws which cannot be physically identified at the macro-scale. But, under stress, these effective flaws are capable

of propagating into transverse cracks, which are physically real. The individual size of the effective flaws is denoted by $2a$ and any two adjacent flaws are spaced by a distance S , see Figure 2.6. Let us then assume that for a given laminate specimen of a unit length, a characteristic effective flaw distribution can be found and it is represented by the probability density function $f(a)$ and the probability density function $f(S)$. For sake of simplicity and of no evidence to suggest otherwise, the two functions are assumed to take the form of a normal distribution,

$$f(a) = \frac{1}{a\sqrt{2\pi}} \exp \left[- (a - \mu_a)^2 / 2\sigma_a^2 \right] \quad (11)$$

$$f(S) = \frac{1}{S\sqrt{2\pi}} \exp \left[- (S - \mu_s)^2 / 2\sigma_s^2 \right] \quad (12)$$

where μ and σ are the mean and the standard deviation of the respective distribution functions.

Among all the "effective" flaws, let the size of the "worst" one be denoted by $2a_0$. Then, this flaw determines the first failure of the 90° -layer. The propagation of the first flaw under the applied laminate load thus forms the "onset" of the transverse cracking process. With increased applied load, flaws of lesser size continue to form transverse cracks allowing multiple failures of the 90° -layer.

In the representations (11) and (12), the parameters μ_a , σ_a , μ_s , and σ_s are not, strictly speaking, properties of a unidirectional ply. Rather, it is more appropriate to regard these as properties of the 90° -layer in the laminate under consideration. For example, the size of the "worst" flaw $2a_0$ must be smaller than the thickness of the 90° -layer, $2h$, see Figure 2.6. Thus, for a normal distribution such as expressed in (11),

let a_o be the 99 percentile of $f(a)$. Then, the following must be valid [26]:

$$a_o \sim \mu_a + 3\sigma_a < h \quad (13)$$

Note that h can be made arbitrarily small or large depending on the lamination design.

Within the framework of the foregoing discussions, the "effective" flaw concept becomes readily amenable to methods of classical fracture mechanics. To illustrate, consider the laminate shown in Figure 2.6. A distribution of "effective" flaws is assumed to exist along the length of the 90° -layer. Let the distribution be represented by the probability functions $f(a)$ and $f(S)$ as expressed in (11) and (12) and the parameters μ and σ in these functions are assumed known. Then, the "worst" flaw whose size is $2a_o$ will propagate and form the first transverse crack when the available energy release rate, $G(\bar{\sigma}_x, a_o)$, equals the material's critical energy release rate G_c :

$$G(\bar{\sigma}_x, a_o) = G_c. \quad (14)$$

The stability of the propagation is stable if

$$G(\bar{\sigma}_x, a_o + \Delta a) < G_c \quad (15)$$

unstable if

$$G(\bar{\sigma}_x, a_o + \Delta a) > G_c. \quad (16)$$

Under the laminate tensile stress, $\bar{\sigma}_x$, G is a function of the effective flaw size a . The general shape of this function is illustrated in Figure 2.7. Calculation of G for a specific laminate may be performed by a numerical procedure based on ply elasticity (see details in Ref. [13]).

The critical laminate load at the onset of the first crack is determined from the fracture criterion (14), given the value of a_0 .

The second crack will form from another flaw in the flaw distribution $f(a)$ when the same energy condition surrounding that flaw is reached. But, this flaw not only is smaller in size but also is located at a random distance from the first crack. Assuming the far-field laminate load $\bar{\sigma}_x$ remains unchanged, the stresses near any flaw which is located in the close vicinity of the crack will be reduced. The available energy release rate at the tip of the flaw depends on its relative distance S from the crack, see Figure 2.8. This quantity may be expressed in the following form:

$$G(\bar{\sigma}_x, a) = R(S) \cdot G_0(\bar{\sigma}_x, a) \quad (17)$$

where G_0 is the energy release rate of the flaw of size $2a$ without the presence of a neighboring crack, and $R(S)$ is the energy release rate retention factor when the presence of the neighboring crack is considered. Depending on the value of S , $R(S)$ may take a value between 0 and 1, Figure 2.8.

Hence, given the values of a and S , the laminate load corresponding to the formation of the second crack can be determined from the energy criterion:

$$R(S) \cdot G_0(\bar{\sigma}_x, a) = G_c \quad (18)$$

Generally, $\bar{\sigma}_x$, determined from (18), is slightly higher than that determined for the first crack.

For a flaw located between two cracks, the energy release rate is given by:

$$G(\bar{\sigma}_x, a) = R(S_l) \cdot G_0(\bar{\sigma}_x, a) \cdot R(S_r) \quad (19)$$

where S_l and S_r , are respectively, distances to the left and to the right

cracks from the considered flaw.

To determine the entire load-sequence of the multiple crack formation process, a stochastic simulation procedure will be followed. The procedure essentially simulates the cracking process as it would occur naturally. Each simulation represents a test case of a sample; and repeated simulations represent tests on a group of replicates.

A Stochastic Simulation Procedure.

The simulation is basically a numerical Monte-Carlo random search routine [27]. A flow diagram of the computer routine is illustrated in Figure 2.9. The routine combines both the fracture mechanics and the probabilistic representation of the material flaw distribution. Specifically, fracture mechanics provides a criterion for the flaws to become cracks; while the probabilistic flaw distribution yields a continuous load-sequence for the cracks formation process.

The flow diagram in Figure 2.9 shows that input information is generated for the specific laminate which is to undergo crack simulation. First, the energy release rate $G_o(\bar{\sigma}_x, a)$ is generated for a flaw of $2a$ without the presence of a neighboring crack. Both $\bar{\sigma}_x$ and a are treated as arbitrary parameters. This is done by expressing $G_o(\bar{\sigma}_x, a)$ in the form [2]:

$$G_o(\bar{\sigma}_x, a) = [\sqrt{C_e} \cdot e_o + \sqrt{C_T} \cdot \Delta T]^2 \cdot t \quad (20)$$

where e_o is the laminate strain ($= \bar{\sigma}_x / \bar{E}_x$), ΔT denotes the uniform temperature drop due to laminate curing, t is a characteristic length parameter, and C_e and C_T are coefficient functions that depend only on a . Thus, a separate calculation of C_e and C_T is performed before the simulation.

Secondly, the energy release rate retention factor, $R(S)$, is generated for the considered laminate by computing $G(\bar{\sigma}_x, a)$ for a flaw of size $2a$ under the influence of a transverse crack located at a distance, S , away, (see Figure 2.8).

Another input to the simulation routine is the knowledge of the laminate ultimate strength $\bar{\sigma}_u$. This is used to merely terminate the simulation once the applied load, $\bar{\sigma}_x$, reaches $\bar{\sigma}_u$.

With the above input information, the simulation starts with generating a set of n uniformly random values in the interval $(0,1)$. Then, by equating the cumulative function $F(a)$ of the assumed flaw size distribution function $f(a)$ to each of the random values, a set of n values for a is computed, say, $\{a_i\}$, $i = 1, n$. Here, one needs to assign a priori, appropriate values for μ_a and σ_a , in order to computer $\{a_i\}$. These parameters will be correlated later with experiments.

Similarly, a set of $(n-1)$ values for S is also computed, $\{S_i\}$, $i = 1, (n-1)$. S_i is then assigned as the spacing between the i th and the $(i+1)$ th flaws.

The computer search begins with the identification of the flaws most likely to become transverse cracks. The first to occur, clearly, is the largest flaw in the $\{a_i\}$ set. The corresponding applied load for the onset of the first crack in the process is determined by the fracture criterion (14).

After the first crack, the routine searches for the next flaw most likely to become a crack by comparing the $G(\bar{\sigma}_x, a)$ values of all the other flaws with the presence of the first transverse crack. Equation (18)

is used to determine the applied load associated with the next crack. Similarly, for the rest of the cracks, the corresponding loads are determined using (19). The simulation goes on until the applied load, $\bar{\sigma}_x$, reaches the laminate strength, $\bar{\sigma}_u$.

When one simulation is complete, another simulation may begin. The random number generator may be adjusted to reflect the natural scatter of a given group of test specimens, see flow diagram in Figure 2.9.

Simulation Examples* - Static Loading.

The experimental examples shown in Figures 2.4 and 2.5 (quasi-static loading case) will be simulated by the foregoing discussed stochastic search routine. The laminates considered were made from the AS-3501-06 graphite-epoxy system. The nominal single ply thickness of the material is 0.005 in. (0.125 mm). The unidirectional ply is experimentally characterized as one of monoclinic symmetry [4] and its elastic moduli were reported in Ref. [15].

In the calculation involving equations (14) - (20), the following laminate properties were also experimentally characterized [15]:

$$\Delta T = 225^\circ\text{F} (125^\circ\text{C})$$

$$t = 0.0052 \text{ in. (0.13 mm)} \quad (21)$$

$$G_c = 1.3 \text{ in-lb/in}^2 (227.5 \text{ J/m}^2) \text{ for transverse cracking.}$$

For the definition of the "effective" flaw distributions $f(a)$ and $f(S)$ in the 90° -layers of both the $[0_2/90_2]_s$ and $[0_2/90_3]_s$ laminates, the

* All examples in this chapter are from the test data reported in Ref. [15].

normal distributions as expressed in (11) and (12) were adapted. The parameters μ and σ were chosen as:

$$\begin{aligned}\mu_a &= 0.0032''; & \sigma_a &= 0.0008'' \\ & (0.08 \text{ mm}) & & (0.02 \text{ mm}) \\ \mu_s &= 0.0125''; & \sigma_s &= 0.0046'' \\ & (0.313 \text{ mm}) & & (0.115 \text{ mm})\end{aligned}\tag{22}$$

These parameters were chosen to reflect the fact that the largest flaw in the $\{a_1\}$ set, say the 99 percentile of $f(a)$, may take a value:

$$a_o \sim \mu_a + 3\sigma_a = 0.0056''\tag{23}$$

(0.14 mm)

and that for $\mu_s = 0.0125''$, it implies 80 effective flaws for each inch of the 90°-layer along the length of the specimen (32 flaws per cm). The choice of σ_a is based on actual test data from sample specimens.

Having defined the specific form of the effective flaw distribution, there remain three other inputs of information in order to start the simulation. Namely, the calculated energy release rate function, $G_o(\bar{\sigma}_x, a)$, the calculated strain energy retention factor, $R(S)$, and the ultimate laminate tensile strength, $\bar{\sigma}_u$.

For $G_o(\bar{\sigma}_x, a)$ it is necessary to calculate for each of the two laminates their respective coefficient functions $C_e(a)$ and $C_T(a)$, see Equation (20). Figures 2.10 and 2.11 show the calculated $C_e(a)$ and $C_T(a)$, respectively.

For the laminate family $[0_2/90_2]_s$ and $[0_2/90_3]_s$, a single $R(S)$ curve can be generated when S is normalized in terms of the 90°-layer thickness. This is shown in Figure 2.12. The $R(S)$ curve can be fitted by a simple

exponential equation as,

$$R(S/nt) = 1 - 1.0056 \exp (-0.7776 S/nt). \quad (24)$$

The detail of the $R(S)$ calculation is included in Appendix A.

Finally, input for $\bar{\sigma}_u$ for $[0_2/90_2]_s$ was set at $\bar{\sigma}_u = 140$ ksi (958 mpa) and for $[0_2/90_3]_s$ at $\bar{\sigma}_u = 120$ ksi (821 mpa). Both were suggested by experiment.

The actual simulation was carried out by a computer routine programmed on a VAX 11-750 computer.

Figures 2.13 and 2.14 depict the transverse cracking simulation results for the $[0_2/90_2]_s$ and the $[0_2/90_3]_s$ laminates, respectively, under quasi-static tension. In each case, five simulated specimens were used. The results in these two figures are to be compared to that shown respectively, in Figures 2.4 and 2.5. For all practical purposes, the comparison is extremely close.

More simulated transverse cracking results have been generated and compared to experiments in the present study. These are found in Appendix B. Generally, the simulation model describes well the transverse cracking process under static tension.

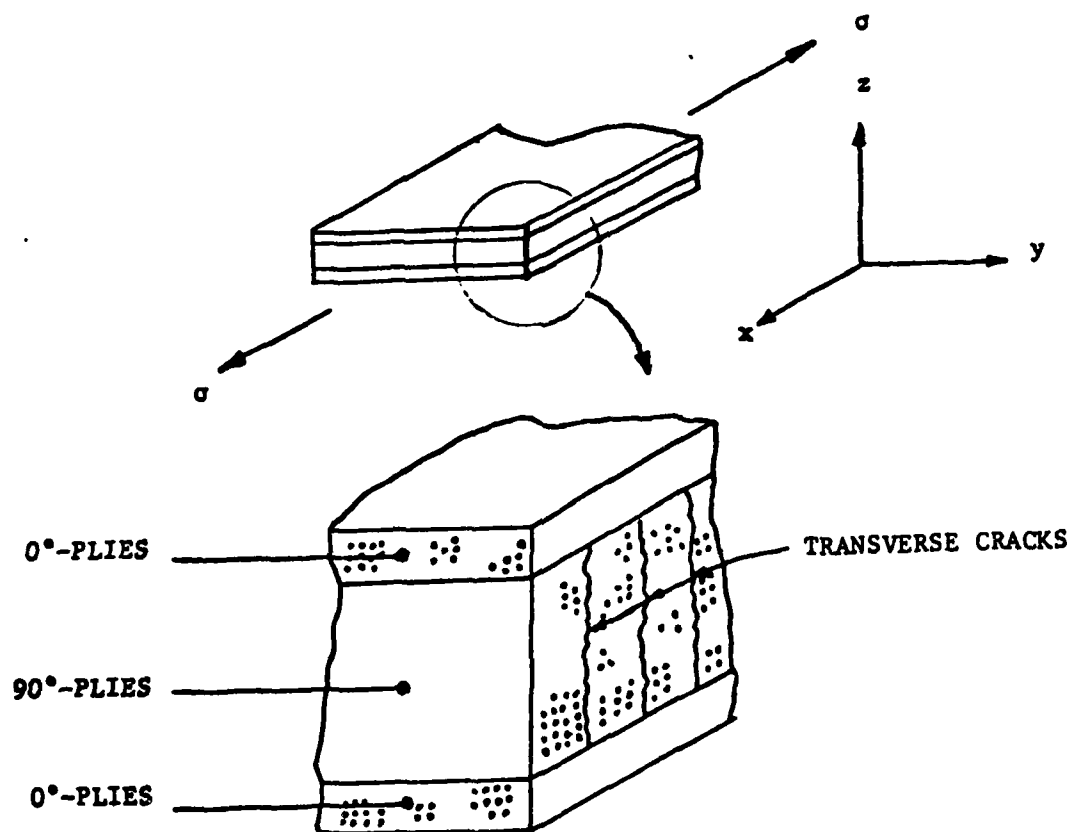


Figure 2.3 Schematics of Multiple Transverse Cracks in $[0/90]_s$ Type Laminates.

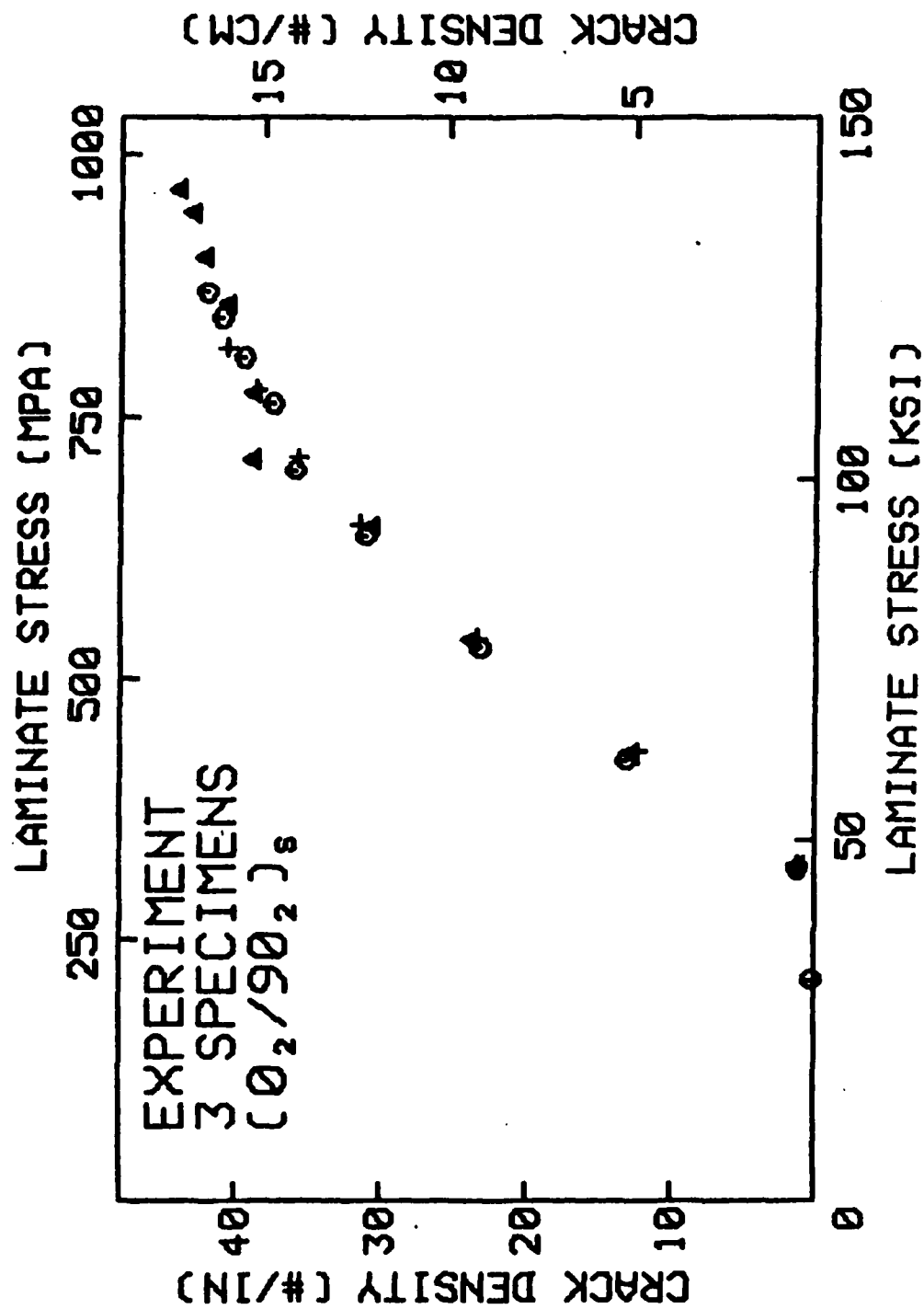


Figure 2.4 Experimental Transverse Crack Density Versus Applied Laminate Stress $\bar{\sigma}_x$. [0₂/90₂]_s

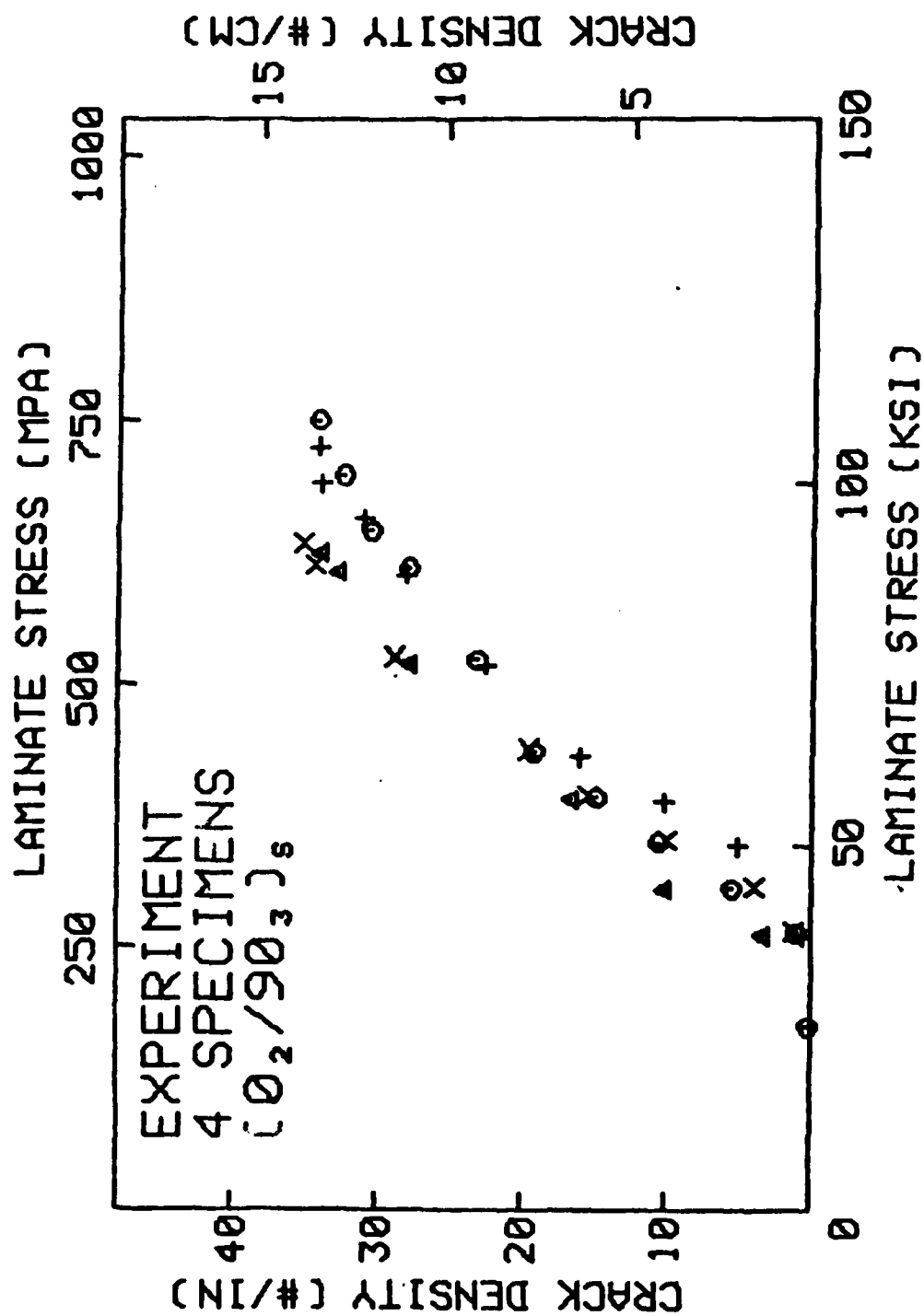


Figure 2.5 Experimental Transverse Crack Density Versus Applied Laminate Stress $\bar{\sigma}_x$. [0₂/90₃]_s

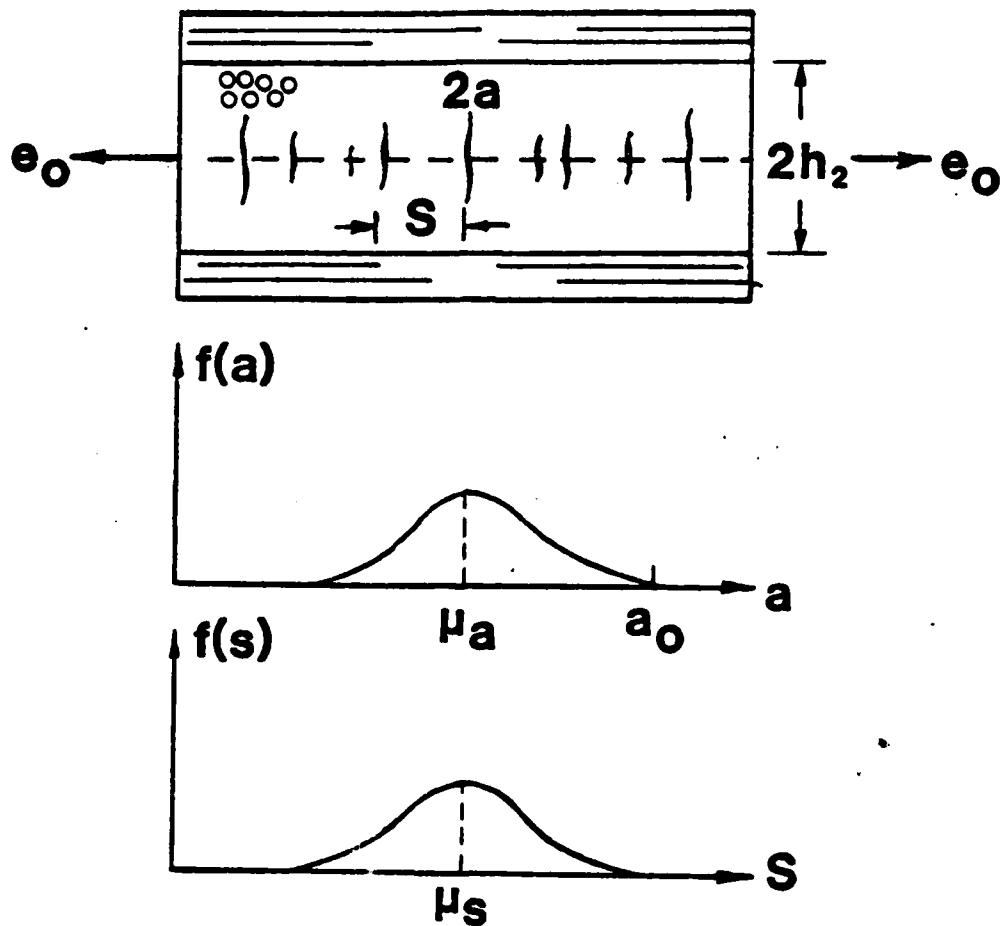


Figure 2.6 Effective Flaws in 90° Layer (top); Size a and Spacing S Distribution (below).

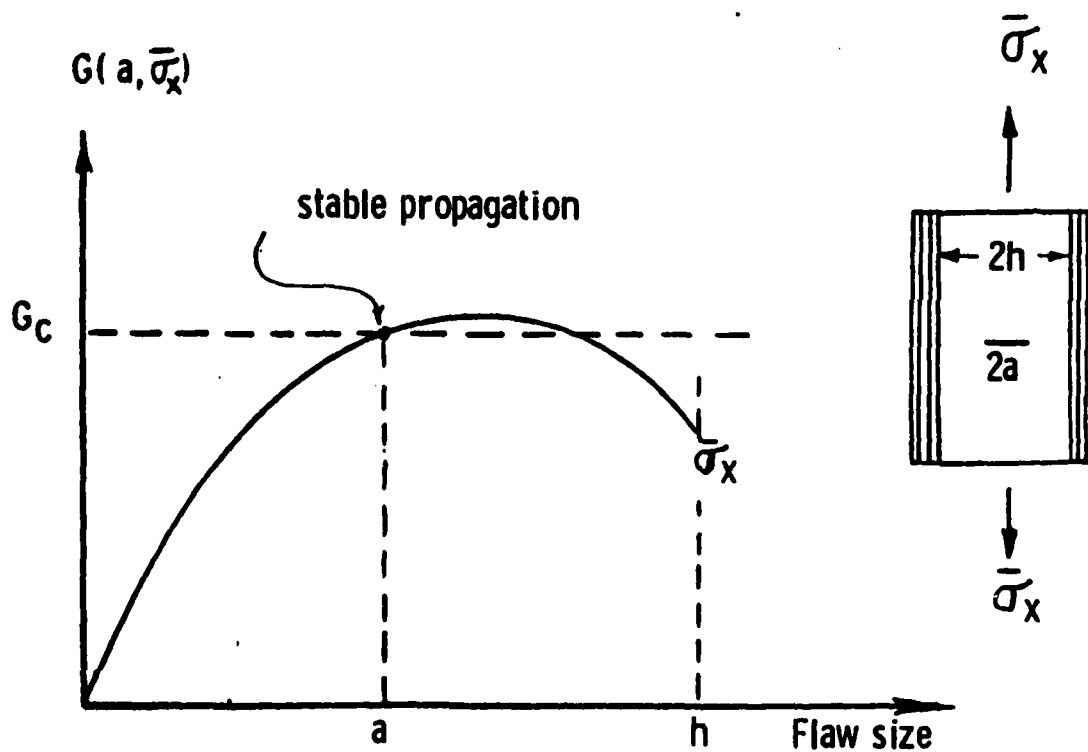


Figure 2.7 The Energy Release Rate As A Function of Flaw Size $2a$

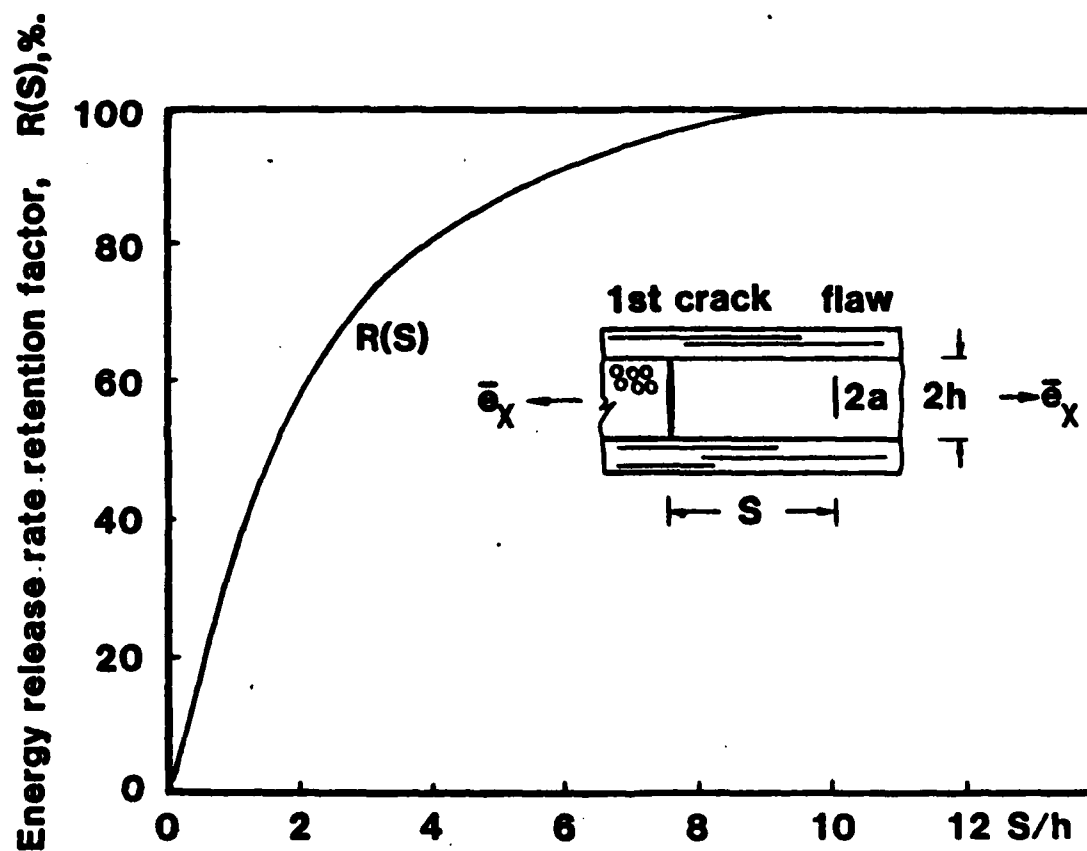


Figure 2.8 Energy release Rate Retention Factor As A Function of S ,
the Distance Between the Flaw and the Crack.

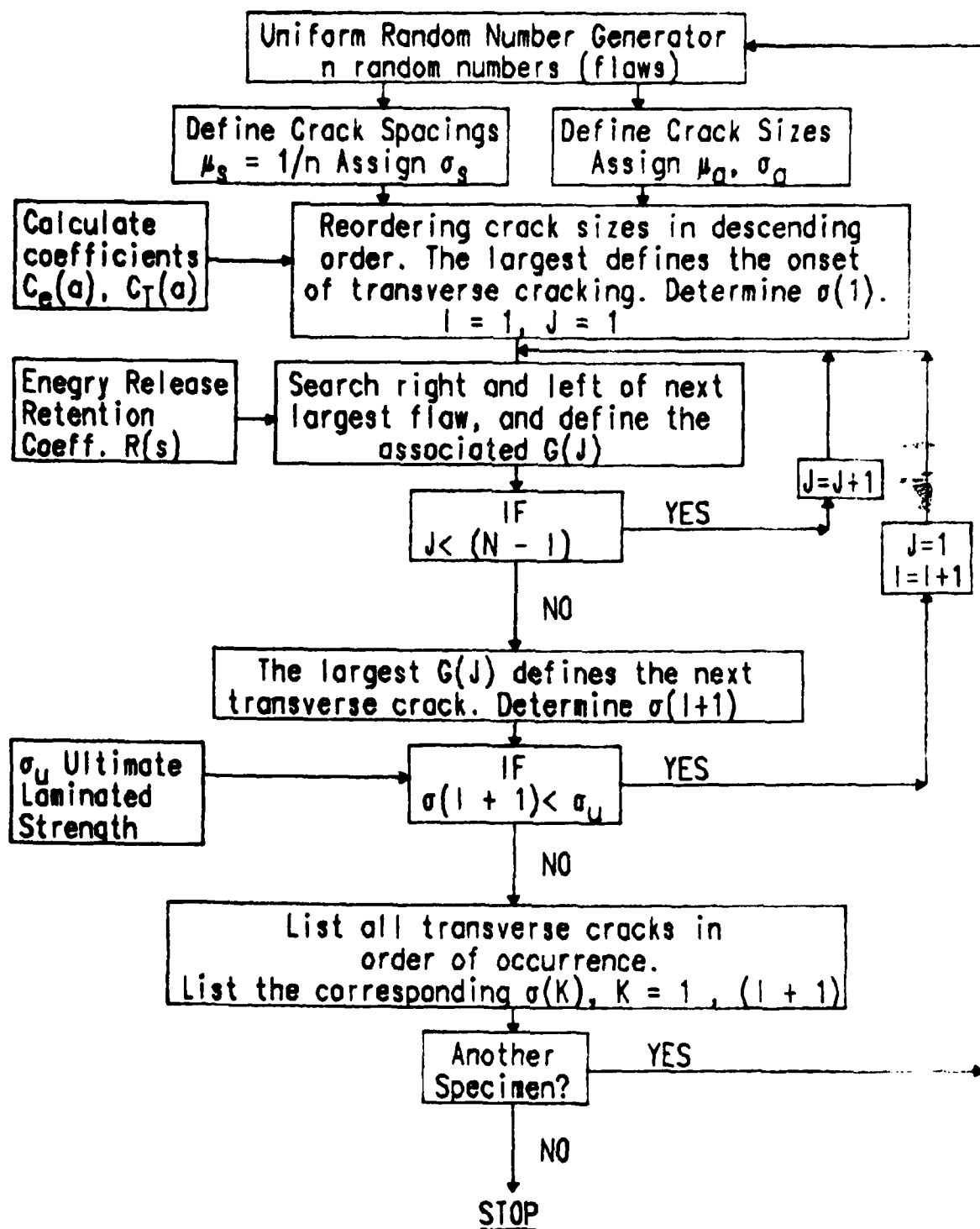


Figure 2.9 Flow-Chart For Monte-Carlo Simulation

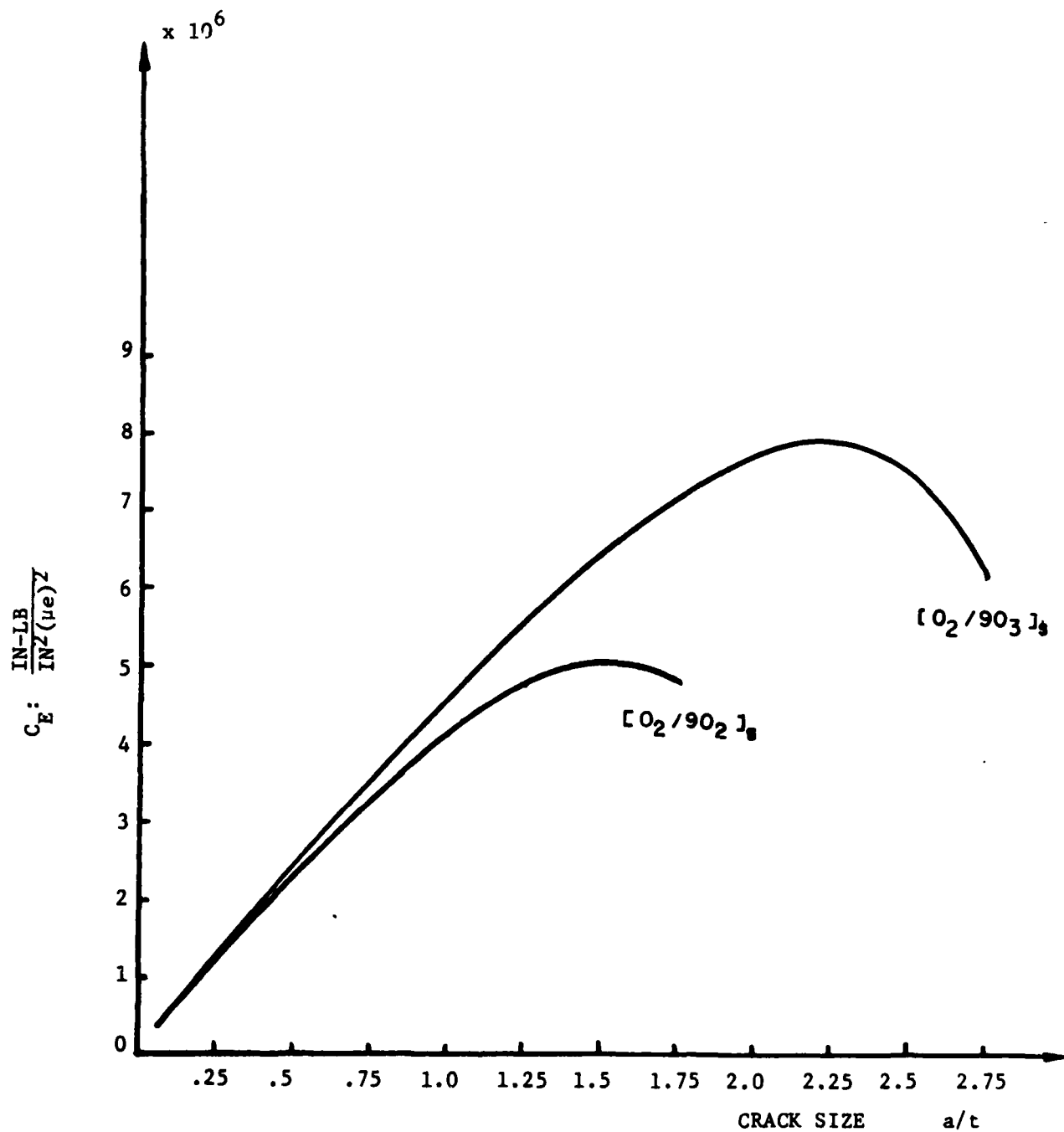


Figure 2.10 Energy Release Rate Coefficients For Mechanical Load $[0_2/90_2]_s$ and $[0_2/90_3]_s$.

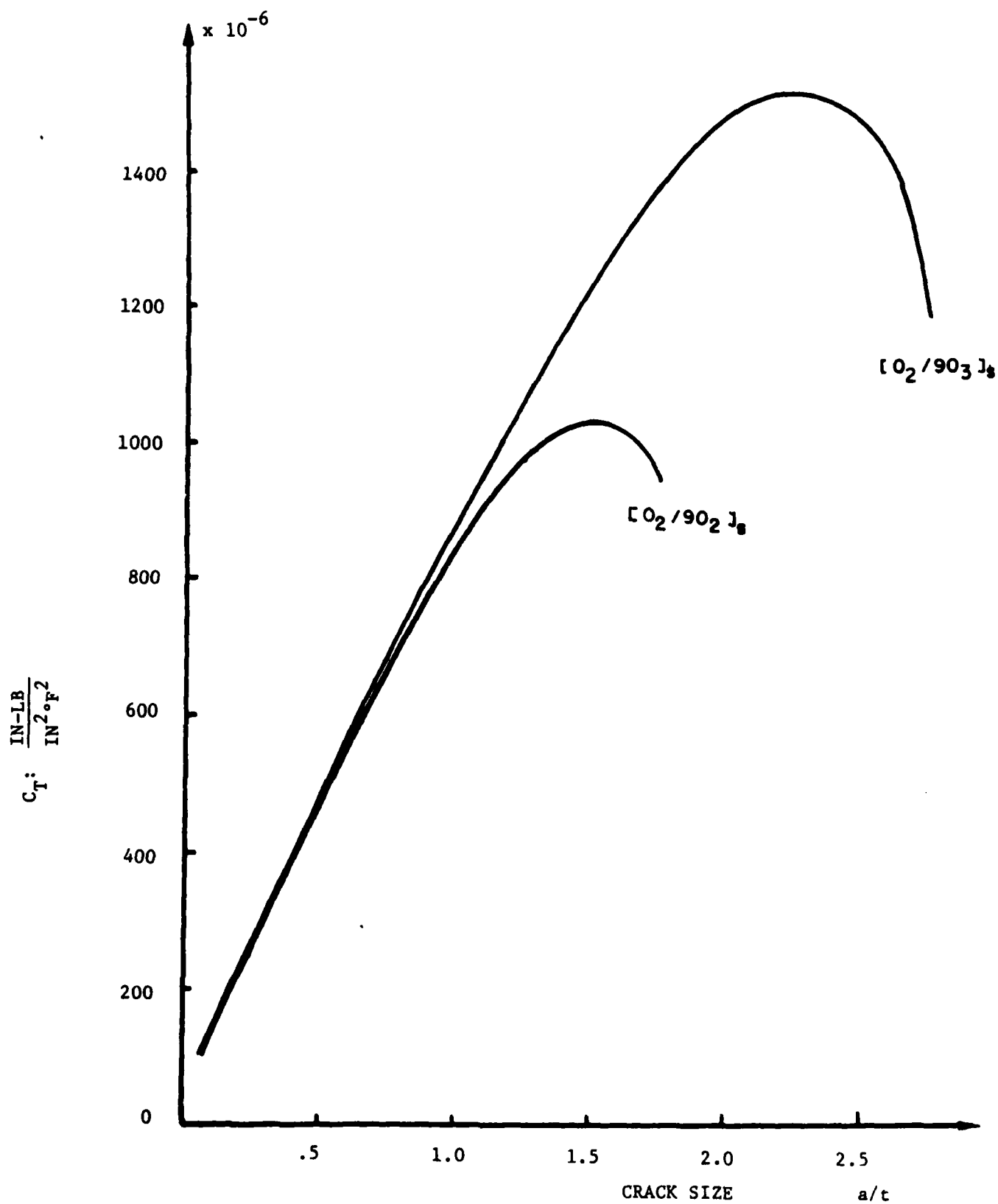


Figure 2.11 Energy Release Rate Coefficients for Thermal Load $[O_2/90_2]_s$ and $[O_2/90_3]_s$.

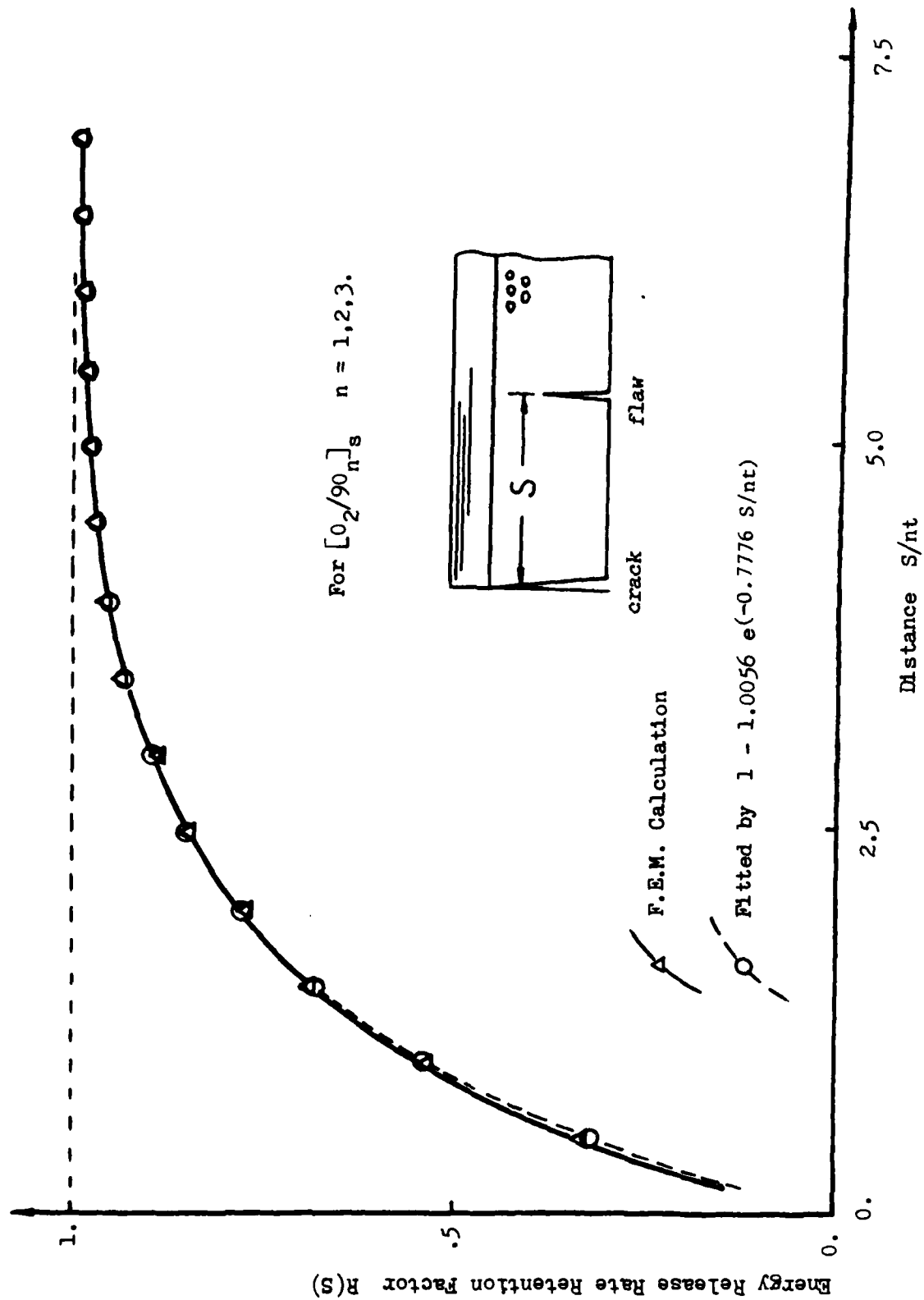


Figure 2.12 Energy Release Rate Retention Factor $R(S)$ As A fu nction of Normalized Distance S/nt .

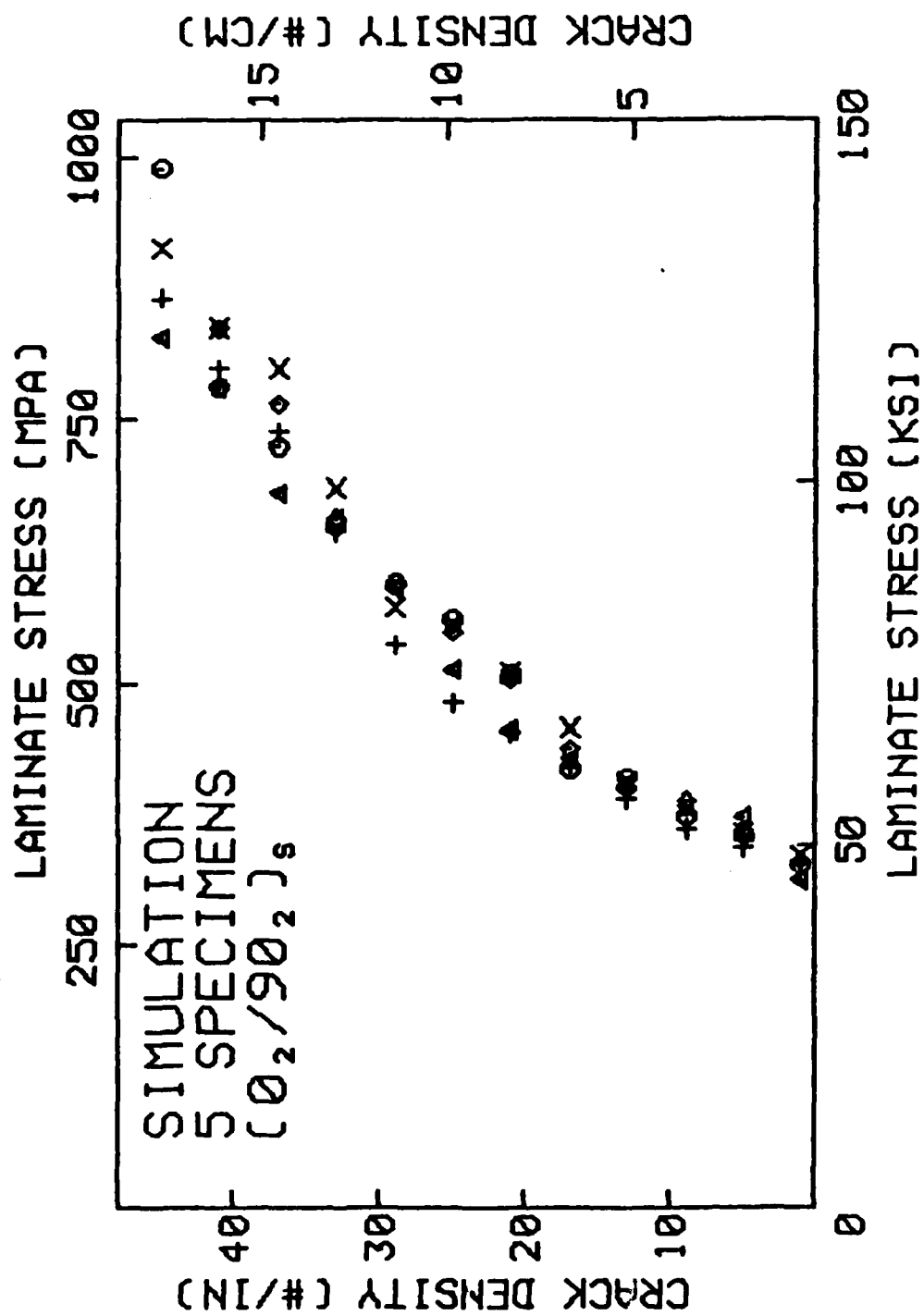


Figure 2.13 Simulated Transverse Crack Density Versus Applied Laminate Stress $\bar{\sigma}_x \cdot [0_2/90_2]_s$

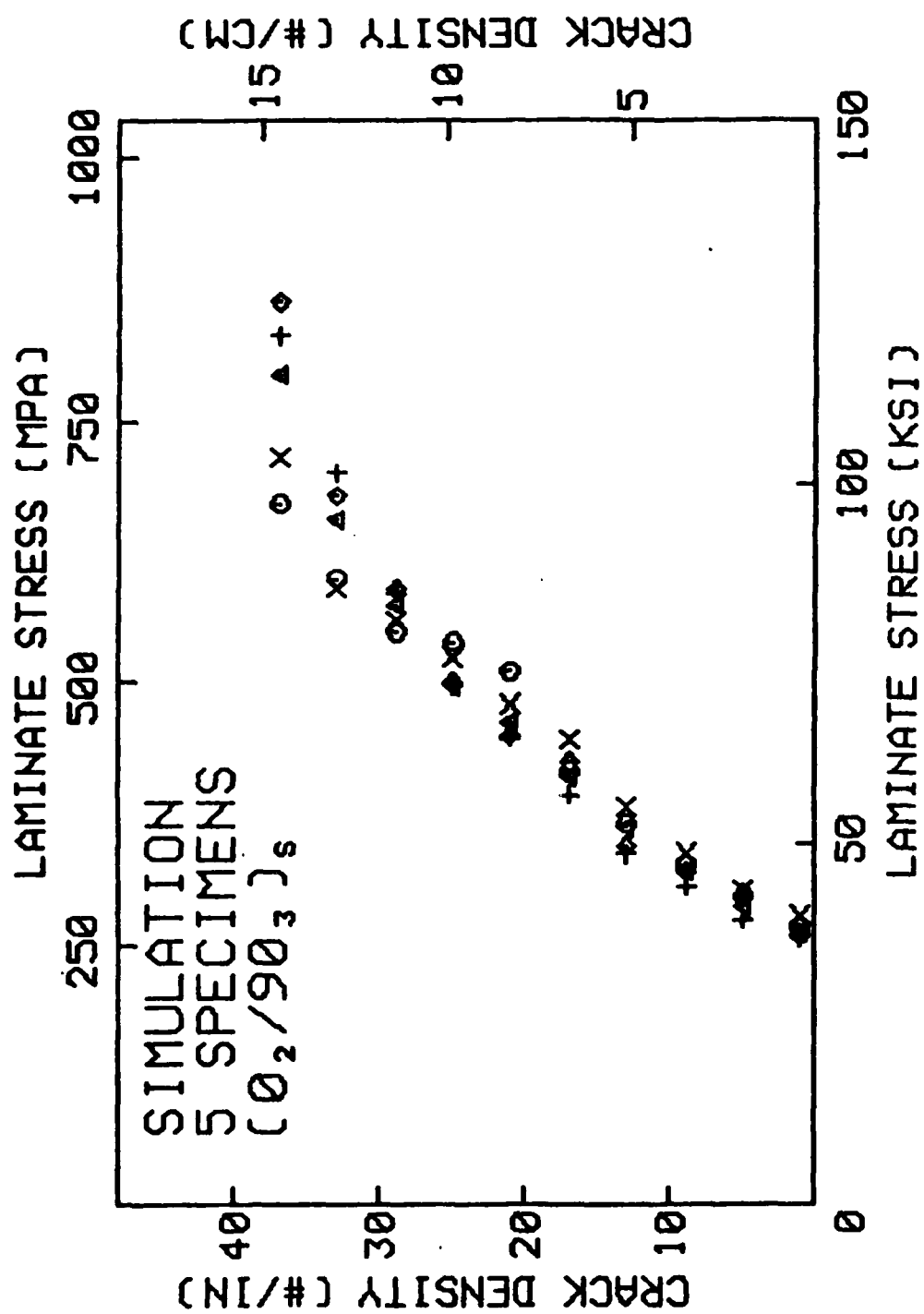


Figure 2.14 Simulated Transverse Crack Density Versus Applied Laminated Stress σ_x . $[0_2/90_3]_s$

2.4 Mechanics of Multiple Transverse Cracks - Fatigue Loading.

In this section, the energy release rate concept for crack growth will be extended to model the transverse cracking process found in laminates when they are subjected to constant amplitude fatigue loads.

For most laminates, fatigue experiments have shown that the developmental process of transverse cracks is similar to that found under statically applied load. The effect of the fatigue loading is essentially a shift of the damage event with time (or fatigue cycles). Figures 2.15 and 2.16 show the experimental crack density versus cycle plots for, respectively, $[0_2/90_2]_s$ and $[0_2/90_3]_s$ laminate under different levels of fatigue amplitudes. Figure 2.17 illustrates the similarity between the crack development processes under static and fatigue loads. The similarity between them suggests the existence of a "damage" function which maps the damage growth curve in $n - \sigma$ space onto $n - N$ space. This mapping function relates the parameters n , σ , N in a certain form.

Recall in the previous quasi-static loading case that the effective flaws are regarded as the aggregate representation of the inherent material microflaws. This same concept may be equally valid in the case of fatigue loading. Accordingly, assume here that the sizes $\{a_i\}$ of the effective flaws increase continuously with time during fatigue loading. When the individual size reaches a characteristic size a^* , a transverse crack is formed. This assumption provides the necessary criterion for a flaw to become a crack; and it also defined the time under load when the crack is formed with the aid of a flaw growth equation.

The previous crack simulation routine can thus be applied to fatigue induced transverse cracking such as shown in Figures 2.15 and 2.16,

provided a flaw growth law is formulated for the "effective" flaws under cyclic loads.

Let the growth of the effective flaw follow the conventional power law for some brittle metals [26]:

$$\frac{da}{dN} = \bar{\alpha} \left[\frac{G(\bar{\sigma}_f, a)}{G_c} \right]^{\bar{p}} \quad (25)$$

where $\bar{\alpha}$ and \bar{p} remain as disposable constants and $\bar{\sigma}_f$ is the amplitude of the applied laminate fatigue load.

Equation (25) contains implicitly $\bar{\sigma}_x$, a , and the effects of the laminate's layering structure through the quantity $G(\bar{\sigma}_f, a)$. Furthermore, by defining $G(\bar{\sigma}_f, a)$ in the form (19), the influence of existing transverse cracks on a flaw is also included. The material resistance against flaw growth is expressed by G_c . The parameters $\bar{\alpha}$ and \bar{p} are expected to be material related only.

The choice of the parameters $\bar{\alpha}$ and \bar{p} in (25) will clearly involve some degree of empiricisms. However, justification for the choice can come only from a careful and exhaustive experimental correlation. It seems that a verification by direct physical measurement at the macroscopic dimensional level is impractical if not impossible.

An integration of (25) gives:

$$N^* = \int_a^{a^*} \frac{1}{\bar{\alpha}} \left[\frac{G(\bar{\sigma}_f, a)}{G_c} \right]^{-\bar{p}} da \quad (26)$$

where N^* is the number of cycles at which the flaw of size $2a$ becomes a transverse crack.

The simulation routine outlined in Figure 2.9 is slightly modified to model the transverse cracking process under fatigue loads. The simulation provides the desired time-sequence crack formation curve under the applied cyclic load.

Simulation Examples - Fatigue Loading.

In the simulation of fatigue induced cracks, the same laminates $[0_2/90_2]_s$ and $[0_2/90_3]_s$ will be considered. The criterion for the formation of a crack from a flaw of size $2a$ is defined when $a = a^*$, a^* is set equal to h (half the thickness of the 90° -layer). The law which governs the growth of a under the constant amplitude cyclic load $\bar{\sigma}_x$ takes the form of (25), with:

$$\bar{\alpha} = 0.004t; \bar{p} = 20 \quad (27)$$

And, of course, the effective flaw distributions $f(a)$ and $f(S)$ in the 90° -layer remain the same as before (see Equations (11) and (12)); their parameters have the same value as expressed in Equation (22). In addition, the calculated $G_o(\bar{\sigma}_f, a)$ and $R(S)$ functions also remain the same (see Figures 2.10, 2.11, and 2.12). All simulations are terminated once N^* reaches 10^6 cycles.

Figures 2.18 and 2.19 depict the transverse cracking simulation results for the two types of laminates under a family of tensile fatigue loads. For each fatigue load amplitude, three simulated specimens were used. These results are to be compared to their experimental counterparts shown in Figures 2.15 and 2.16. Again, the comparison appears quite good. More comparative study cases between the simulations and experiments for fatigue induced transverse cracking are found in Appendix C.

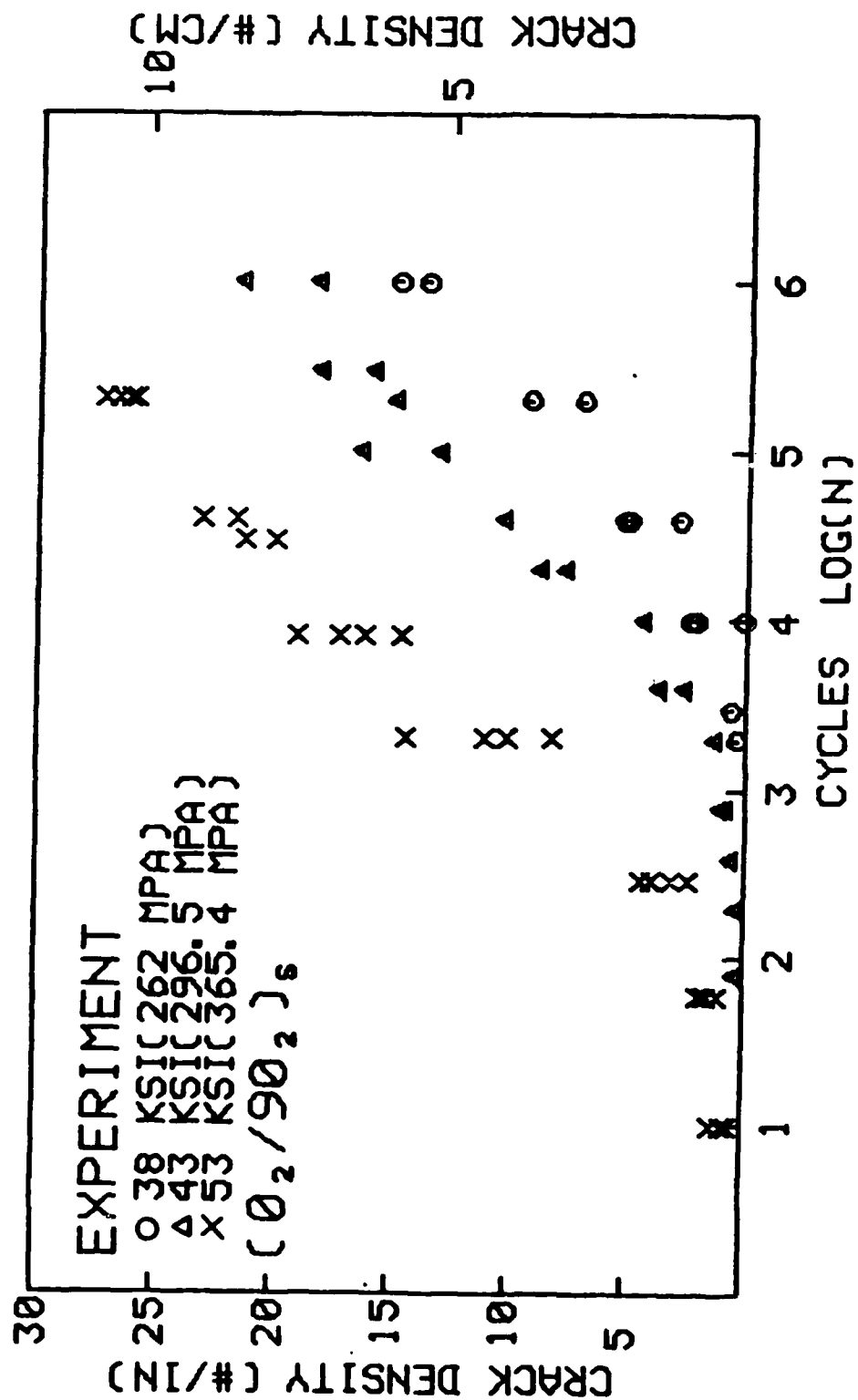


Figure 2.15 Experimental Transverse Crack Density Versus Fatigue Cycle N. $[O_2/90_2]_s$

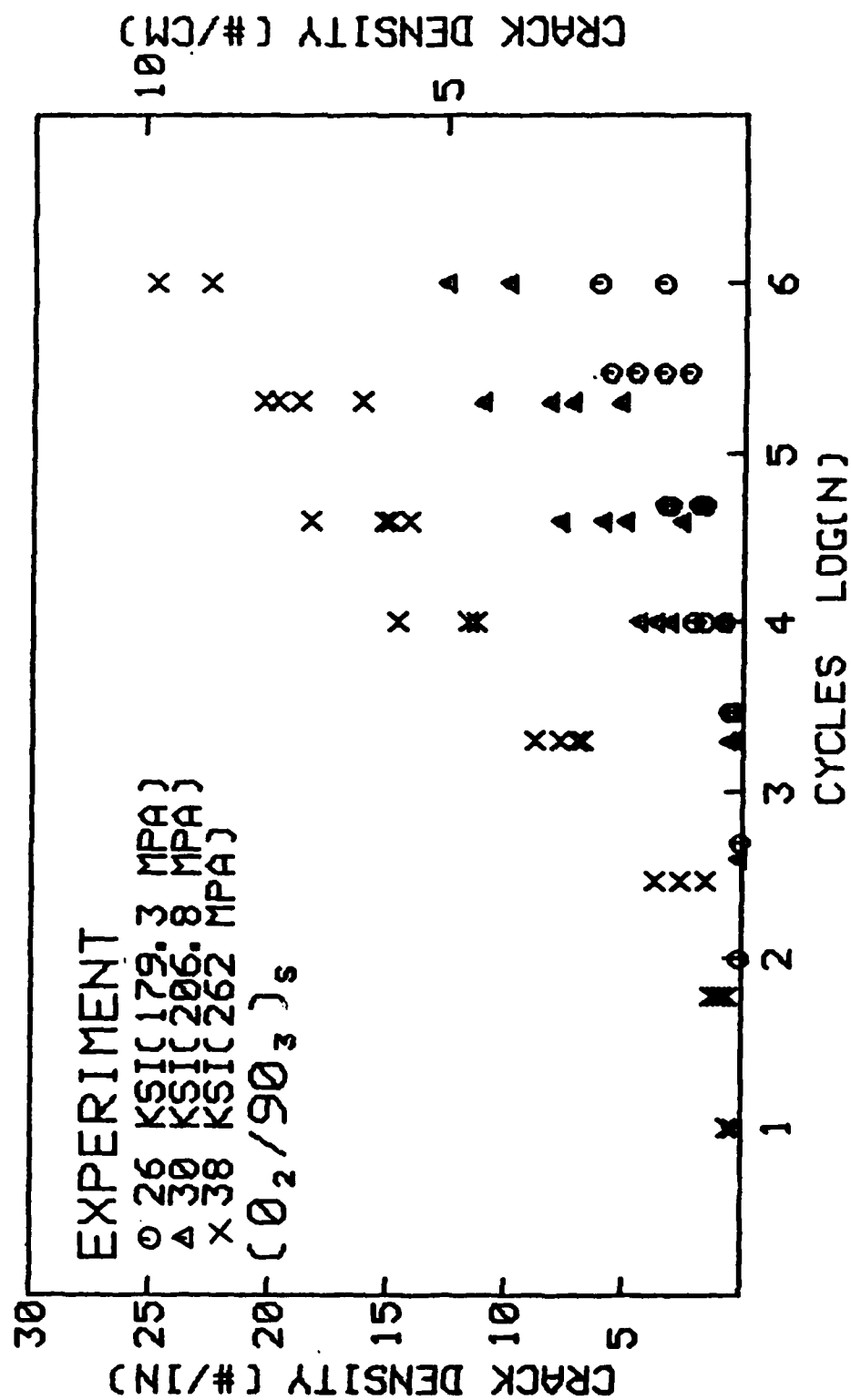


Figure 2.16 Experimental Transverse Crack Density Versus Fatigue Cycle N. [0₂/90₃]_s

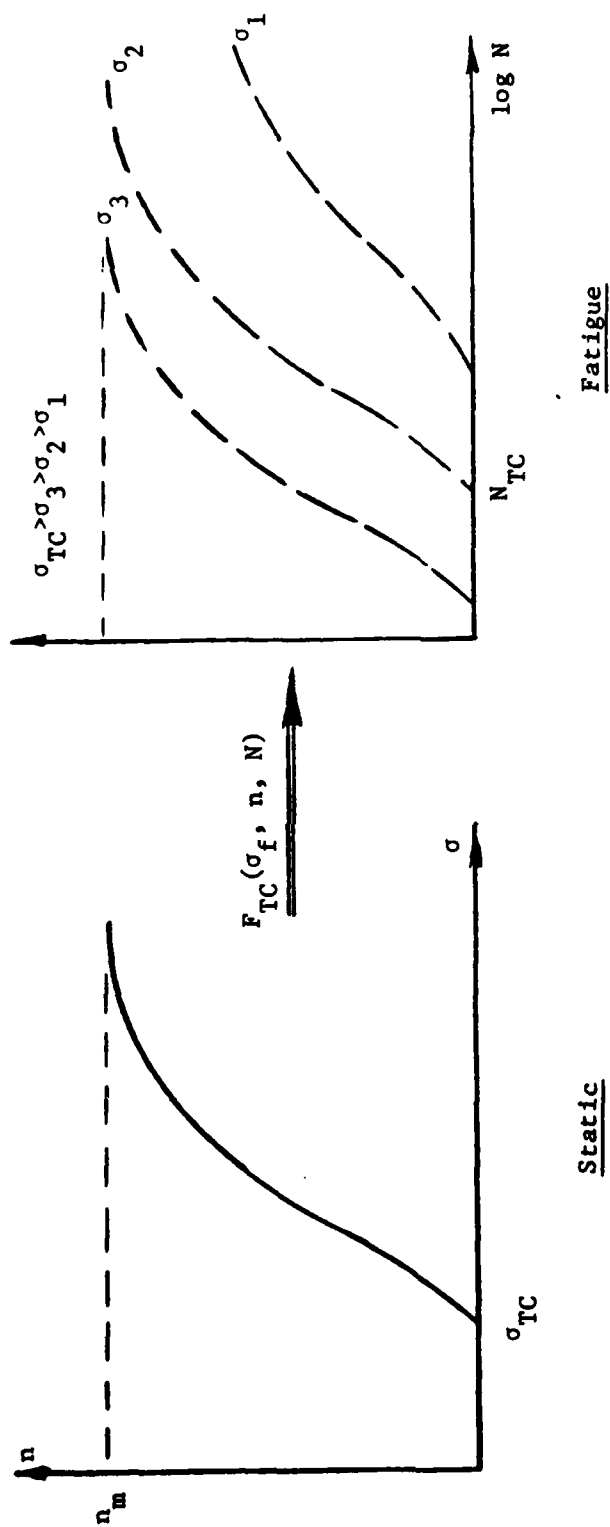


Figure 2.17 Schematic Representation Of The Fatigue Damage Function F_{TC} For Transverse Cracking

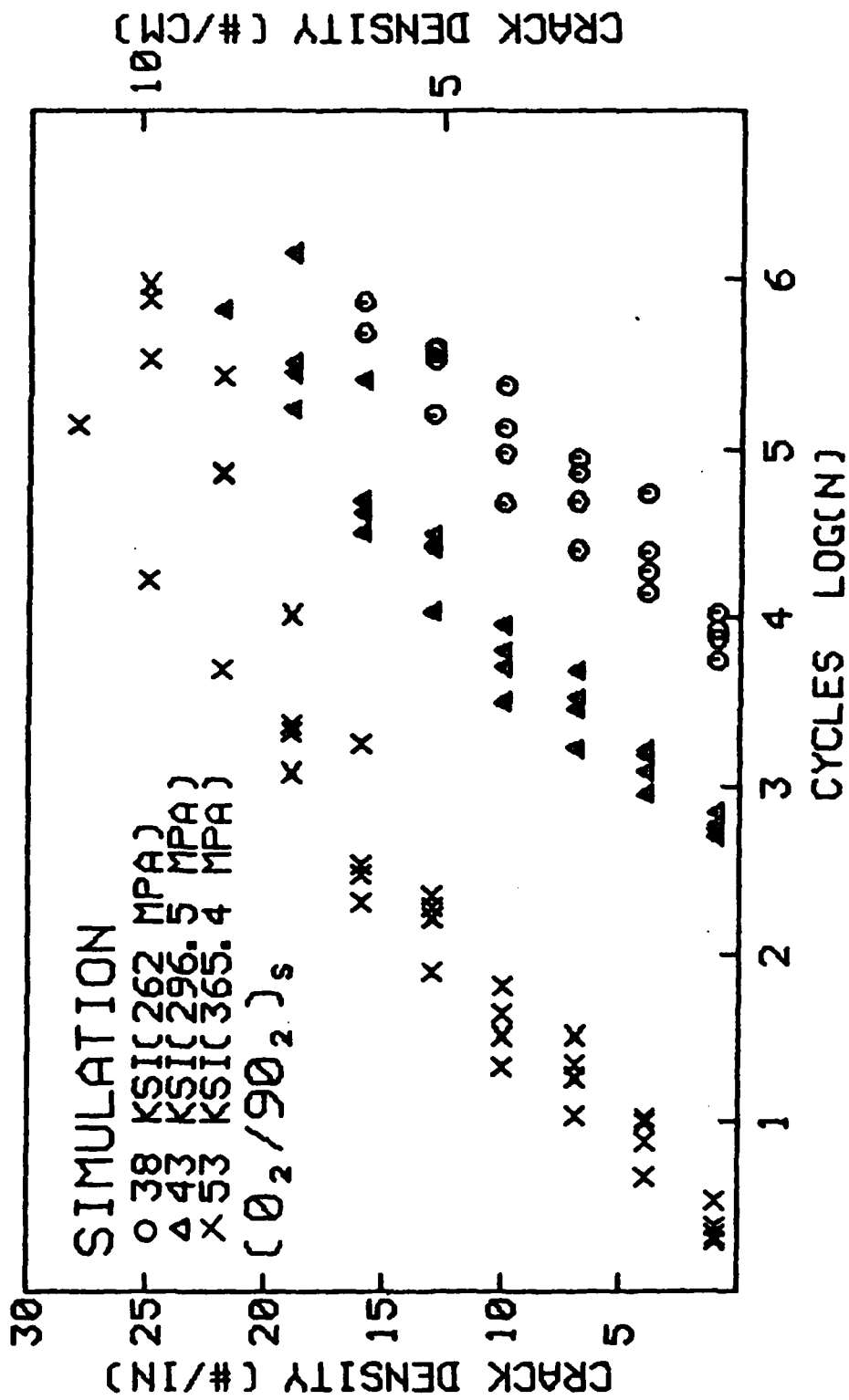


Figure 2.18 Simulated Transverse Crack Density Versus Fatigue Cycle N. $[O_2/90_2]_s$

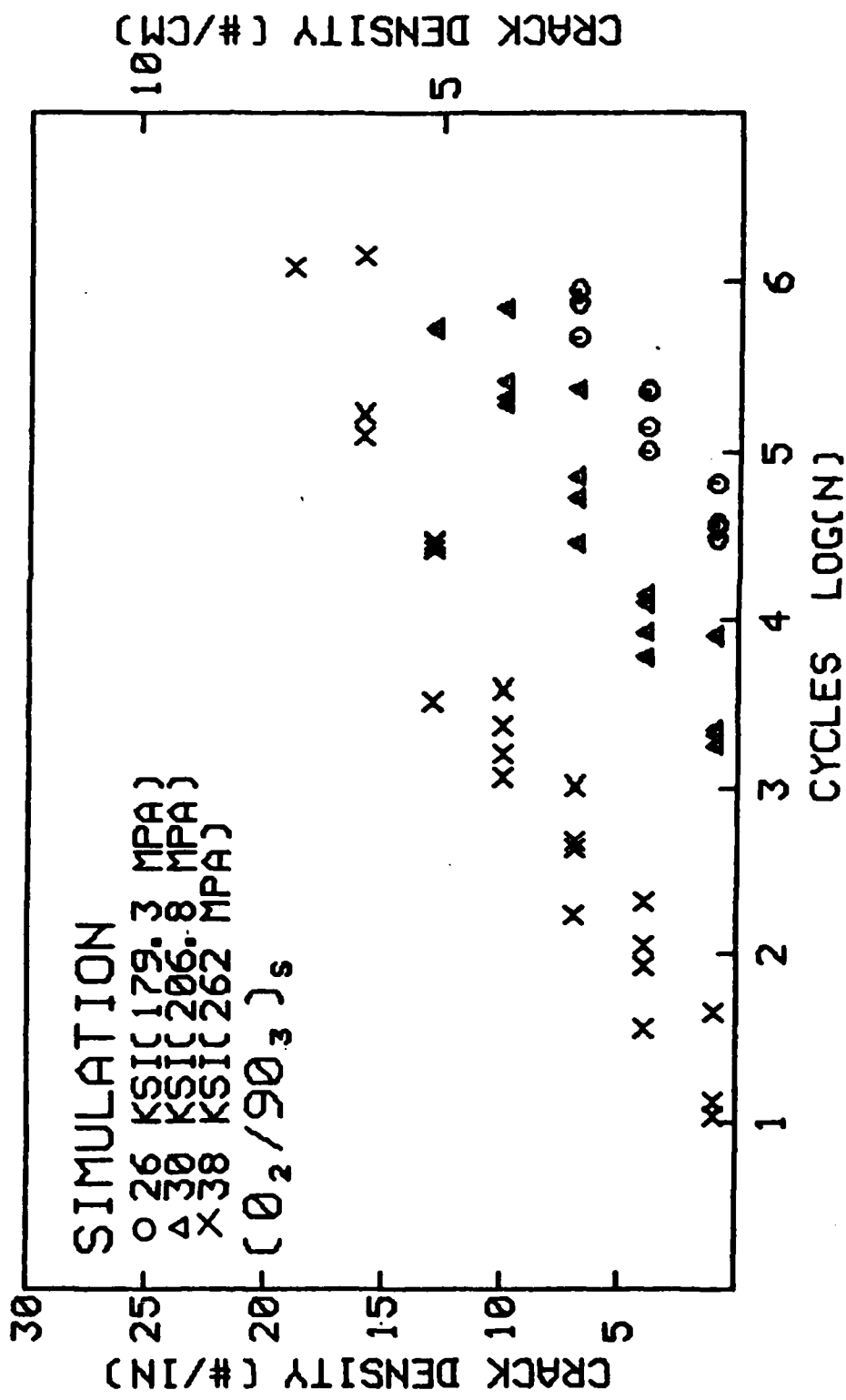


Figure 2.19 Simulated Transverse Crack Density Versus Fatigue Cycle N. $[0_2/90_3]_s$

2.5. A Cumulative Damage Model for Multiple Transverse Cracks.

From the previously developed model for multiple transverse crack growth under constant amplitude fatigue load, a state of "constant damage" can be quantitatively defined. For instance, the transverse crack density n as a measure of the "damage state." The damage state n can be induced either by the constant amplitude fatigue load σ_f in N cycles or by the static load $\bar{\sigma}_x$. It is assumed that a unique $\sigma - N$ relationship could be determined for a given damage state n . This relationship can be found by means of the previously developed fatigue crack growth model.

Figure 2.20 illustrates schematically a family of constant damage lines in the $\sigma - N$ space. These curves are calculated numerically from the fatigue crack growth simulation routine by setting n at some given constant value. Note that these constant damage curves can also be generated from the experimental crack density growth curves.

From the constant damage curves in the $\sigma - N$ plane, a cumulative damage model for the crack growth process under spectrum load is constructed as follows.

Consider the spectrum load history such as shown in Figure 2.21(a). The laminate is subjected first to a constant amplitude fatigue load σ_1 for a period of N_1 cycles. The damage at the end of N_1 cycles is found at point A in the $\sigma - N$ domain, Figure 2.21(b). The constant damage curve passing point A is denoted by N_1 . Then, the amplitude of the fatigue load is increased to σ_2 for a period of $(N_2 - N_1)$ cycles, see Figure 2.21(a). Since the damage in the laminate at the onset of σ_2 is

still N_1 , the location of this damage state is at the intersect of σ_2 and the curve N_1 , point B. For a period of $(N_2 - N_1)$ fatigue cycles, the damage state in the laminate advances to C, which is located on the constant damage line N_2 . At the end of N_2 cycles, the fatigue amplitude is lowered to σ_1 again for a period of $(N_3 - N_2)$ cycles. During this period, the damage state advances from point D on curve N_2 to point E on curve N_3 .

At each level of the fatigue load, the initial damage state is determined if the number of cycles is specified. Actually, the damage state at the end of the spectrum loading is found from integrating the damage growth equation:

$$N_3 = \sum_{i=1}^3 \int_{N_{i-1}}^{N_i} \bar{\alpha}(G_i/G_c) \bar{P}_i dN \quad (28)$$

This method can easily be extended, on a cycle by cycle basis, to random spectrum loadings.

Simulation Examples - Spectrum Loading.

Let us consider again the laminates $[0_2/90_2]_s$ and $[0_2/90_3]_s$. The transverse crack growth processes in these laminates under constant amplitude fatigue loading have been simulated by the proposed stochastic procedure. Families of crack density (n) versus fatigue cycles (N) were generated and shown in Figures 2.18 and 2.19. From these crack density growth curves in the $n - N$ space, a family of constant damage lines may be obtained by a graphical method. This is done by drawing a constant n line in, say, Figure 2.18. The intersecting points with the $n(N)$ family curves yield the desired constant n curve in the $\sigma - N$ space. Figure 2.22 shows

the constant damage family lines for $[0_2/90_2]_s$ and Figure 2.23 shows the same for $[0_2/90_3]_s$.

The constant damage lines will be used to construct the desired cumulative damage model which predicts the transverse cracking state in the laminates under a given variable amplitude (spectrum) fatigue load. The procedure has already been explained earlier in this section.

To illustrate the accuracy of the cumulative model, a number of variable loading cases have been considered. Four typical test cases between the predicted results and the experimental results are displayed in the following table. In each case, the prediction is based on the graphical determination such as illustrated in Figure 2.21. The graphs used in the four test cases are shown in Figures 2.23 and 2.24. More theoretical/experimental comparison may be found in Appendix D of this report.

Generally, the comparison is very close.

PREDICTED AND TESTED CUMULATIVE DAMAGE STATES

<u>Laminate</u>	<u>Load Amplitude Ksi</u>	<u>Cycle @ Load</u>	<u>Experiment, n (2 Samples)</u>	<u>Predicted, n (Average)</u>
[0 ₂ /90 ₂] _s	60	100	16, 18	16
		1,000	21, 23	20
		10,000	28, 30	24
		100,000	33, 34	28
	80	100	34, 34	30
		1,000	34, 35	33
		10,000	36, 36	35
		100,000	36, 36	36
[0 ₂ /90 ₂] _s	80	10	26, 25	26
		100	30, 29	30
	60	1,000	31, 30	30
		10,000	33, 31	31
		100,000	36, 34	33
[0 ₂ /90 ₃] _s	50	1,000	11, 14	13
	70	1,000	28, 28	27
	50	100,000	30, 30	29
[0 ₂ /90 ₃] _s	26	10,000	1, 1	0
	30	100	1, 1	0
		1,000	1, 1	0
		10,000	5, 2	3
		30,000	7, 6	6
	26	100,000	8, 7	8

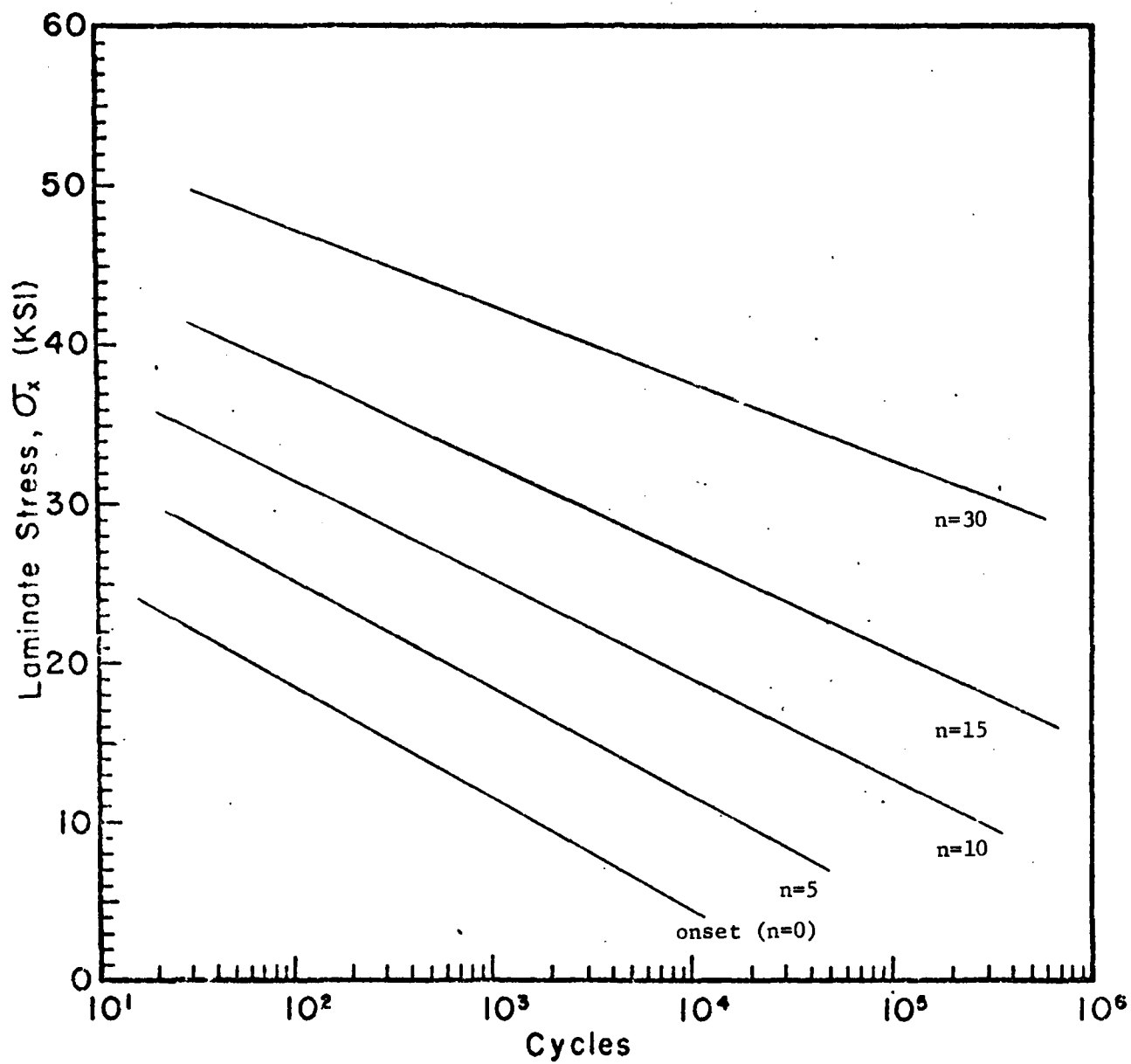
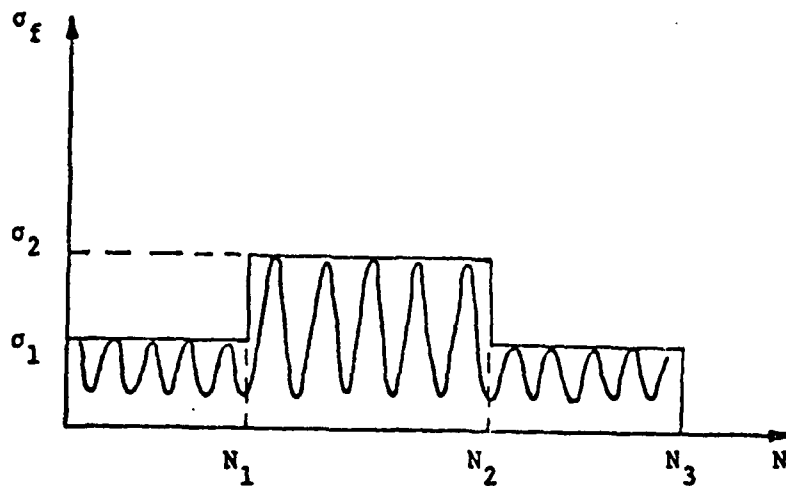
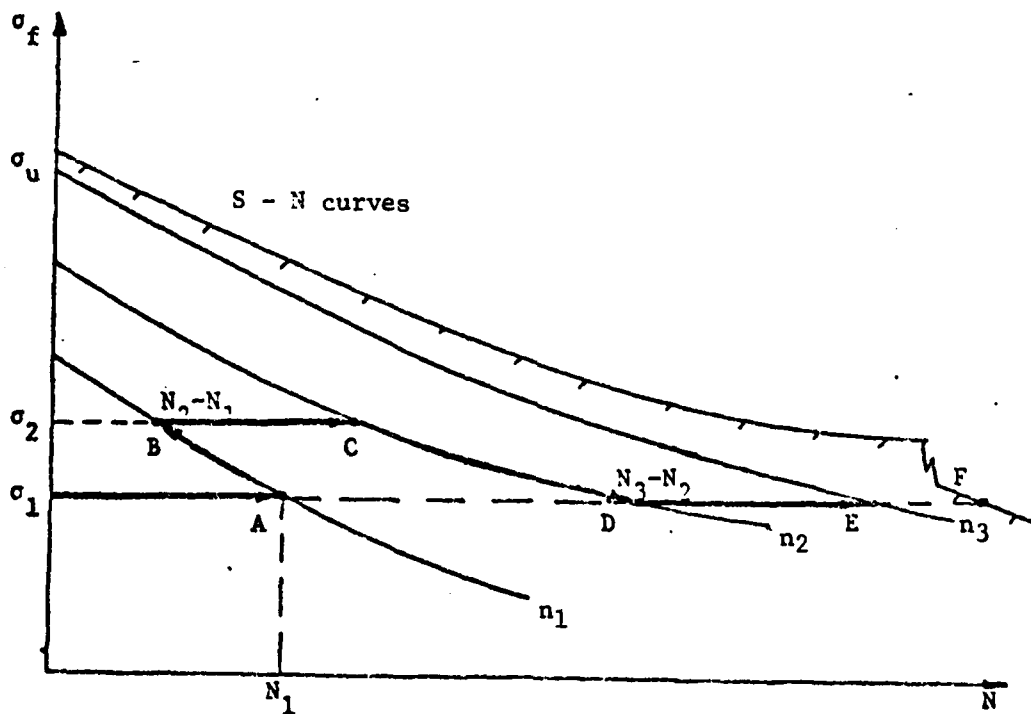


Figure 2.20 Schematics for the Concept of Constant Damage States.



(a) Schematic of a Spectrum Loading History



(b) Damage Growth Path in the Load-Life Plane

Figure 2.21 Schematics for the Concept of a Cumulative Damage Model.

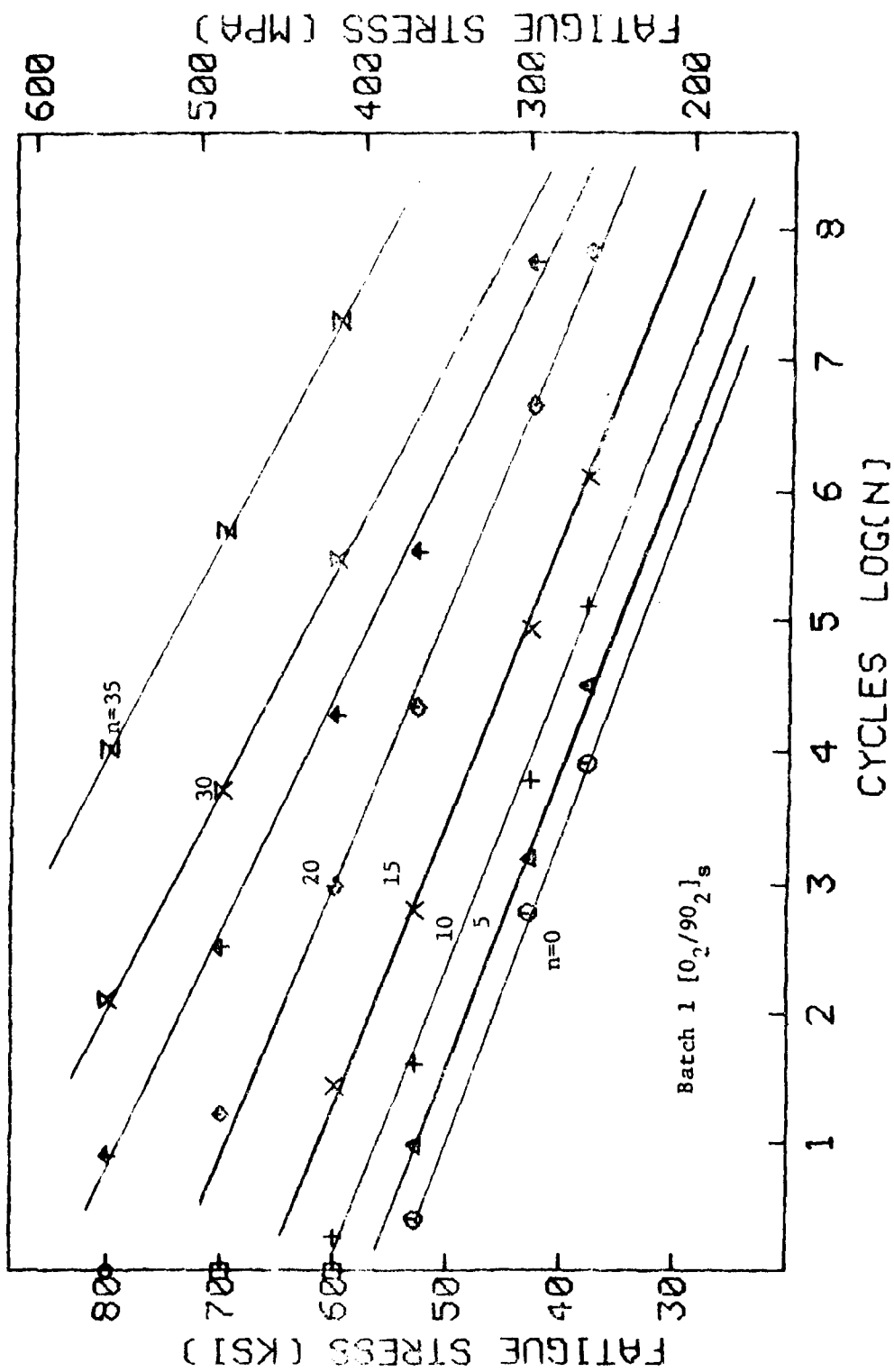


Figure 2.22 Constant Damage Lines for $[0_2/90_2]_s$ Laminates.

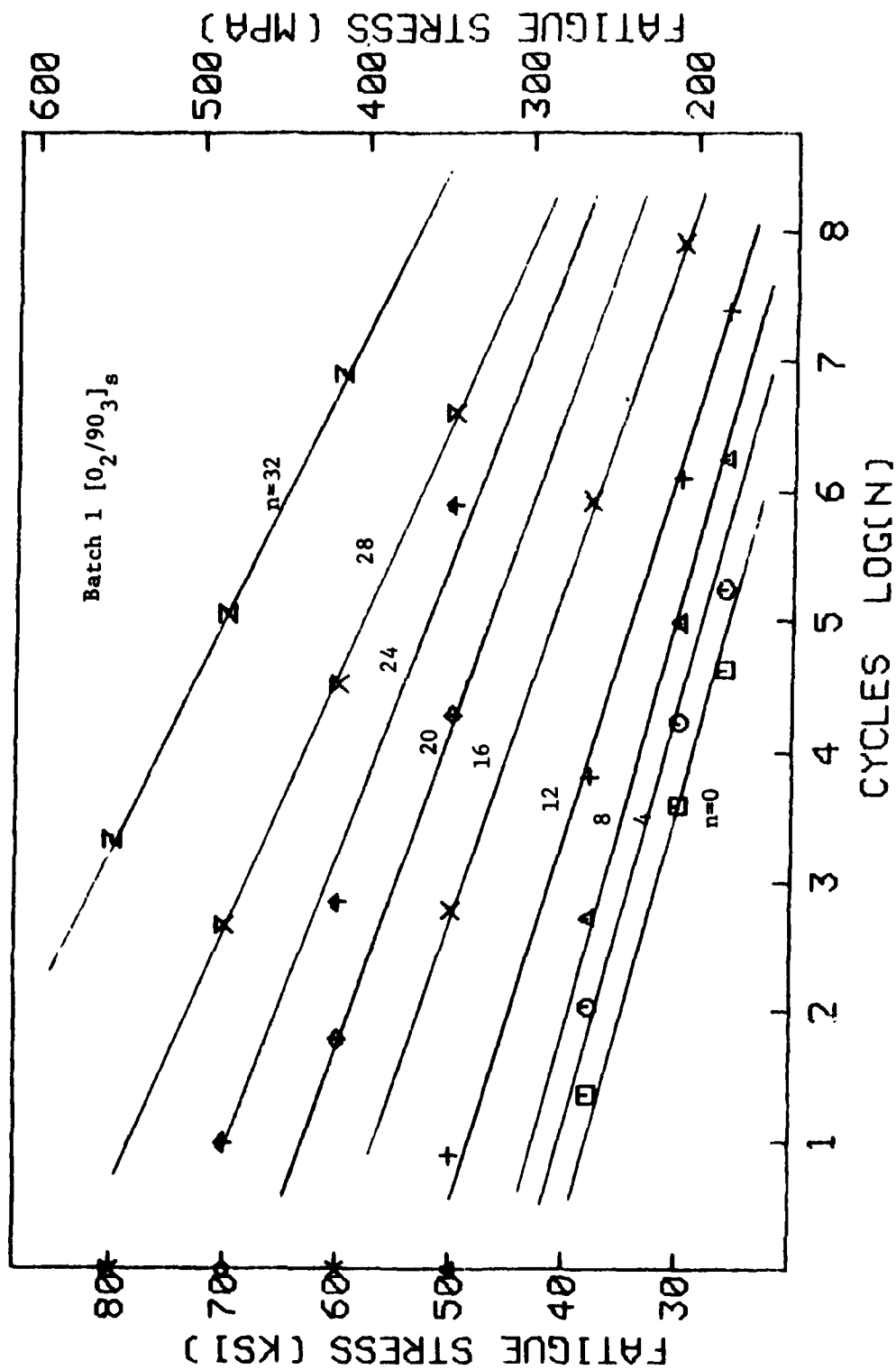


Figure 2.23 Constant Damage Lines for $[0_2/90_3]_s$ Laminates

2.6. Mechanics of Free Edge Delamination - Static Loading.

Free edge induced delamination crack growth has been frequently observed as the most damaging sub-laminate failure mode. The crack development process is generally idealized as a plane crack which is formed along the laminate free edge, propagating inward along an interface of two adjacent layers. But, post-failure examination of free edge delamination often showed a complicated crack growth path; the path is usually not contained in one given layer interface. For example, consider a laminate in the form, say, $[\pm 25/90]_s$ under uniaxial tension. Because the laminate contains a 90° -layer, transverse cracking in this layer could be induced by the applied tensile load. However, the thickness of the 90° -layer is not large; a relatively high load is required to produce the transverse crack, according to the energy theory presented earlier. In this case, then, a free edge delamination may be induced before transverse cracking. Once edge delamination is started, multiple transverse cracks in the 90° -layer could still be formed inside the delamination area. Frequently, the delamination growth process is complicated by the presence of transverse cracks, e.g., the delamination plane can be shifted to the 25/90 interface because of the transverse cracks in the 90° -layer.

As a counterexample, consider the laminate of $[\pm 25/90_2]_s$, also under uniaxial tension. In this case, transverse cracking will be the first to occur because of the larger 90° -layer thickness. The presence of the transverse cracks, in turn, causes delamination in the 25/90 interface. It seems that the actual thickness of the 90° -layer in the laminate can alter the competing damage modes and their occurrence sequences. In this section, we shall confine our discussion to the mechanisms of delamination

alone, not complicated by other interacting failure modes. The latter subject, though extremely important, will be studied separately.

Analytical studies of the free edge delamination problem have originated from the much celebrated work of Pipes and Pagano [28], who formulated and computed the boundary-layer interlaminar stress solutions for a long symmetric laminate under tension. The formulation is based on the macroscopic ply-elasticity theory, which regards the material layers as individually homogeneous media; material and geometrical discontinuities exist only across the layer interfaces.

Generally, the free edge stress field is three-dimensional and is singular at the intersection of the free-edge with the layer interface [29]. Clearly, interface delamination is caused by the highly concentrated edge stresses, especially the interlaminar normal stress σ_z .

In a series of tensile strength tests, Bjeletich, et al. [30] examined the failure modes of six families of quasi-isotropic laminates by alternating the stacking sequence of the 0° , 90° and $\pm 45^\circ$ layers. Edge stress analysis indicated a compressive σ_z along the free edge of the $[0/90/\pm 45]_s$ laminate, while a tensile σ_z for the $[\pm 45/0/90]_s$ laminate. The latter developed premature delamination and the growth of it had led to a much lowered tensile strength. Though the knowledge of the free-edge stresses can provide an explanation why delamination occurs, a quantitative prediction for its occurrence requires an independently defined criterion.

In a study on delamination for similar graphite-epoxy laminates, Rodini et al., [31] determined experimentally the critical tensile loads at the onset of free edge delamination in a $[\pm 45_n/0_n/90_n]_s$, $n = 1, 2, 3$ family. They found that the critical laminate tensile stress, $\bar{\sigma}_x$, varied

greatly with the value of n . Specifically, the critical $\bar{\sigma}_x$ decreases at the rate of about \sqrt{n} , even though an edge stress analysis yields identical $\bar{\sigma}_z$ for the same $\bar{\sigma}_x$ for all values of n .

As we now know more about the failure sequence in laminates such as $[\pm 45/0/90]_s$, the results of Rodini et al., [31] evidently also involved transverse cracking in the 90° -layers. It is possible that all three laminates ($n = 1, 2, 3$), or at least those of $n = 2$ and 3 , had transverse cracks before delamination. Hence, in order to analytically describe the delamination process generally, one must take into account the interacting effects of the transverse cracks.

The Energy Criterion

Wang and Crossman [13] assumed that material flaws also exist randomly on any one of the interfaces between the material layers. Those flaws which are located within the free-edge stress zone from an "effective" flaw having a size a_0 at the instant of onset delamination, see inset in Figure 2.24. Note that a_0 is still an unknown quantity. And, it can also be random in nature.

Following the finite element crack-closure procedure by allowing virtual extension of a along the layer interface, energy release rate curves for externally applied load are generated (for detail, see [13]).

Figure 2.24 shows a typical G curve. The energy release rate G increases sharply with a , but reaches an asymptote at $a = a_m$. Generally, the value of a_m is about one-half the layer-thickness which contains the delamination [13]. Thus, the layer thickness may in some cases affect the value of a_m , and also the value of G .

Expressing the computed energy release rate in the form

$$G(e_o, a) = [\sqrt{C_e(a)} \cdot e_o + \sqrt{C_T(a)} \cdot \Delta T]^2 \cdot t \quad (29)$$

and applying the Griffith criterion (14) for the onset of the delamination crack, one obtains the critical far-field strain:

$$e_o = \frac{\sqrt{G_c/t} - \sqrt{C_T(a)} \cdot \Delta T}{\sqrt{C_e(a)}} ; a = a_o. \quad (30)$$

The problem comes down to two important questions; namely, what value is a_o and in which interface is it located?

To answer the first question, recall our earlier discussions about the effective flaw distribution $f(a)$ in the 90° -layers. The worst flaw may have a size equal to one ply thickness for commercial graphite-epoxy systems. It is believed that the worst flaw a_o which is responsible for delamination is at least of this magnitude if not larger, because of possible additional cutting flaws along the free edge. In any event, if a_m in Figure 2.24 is less than 2 times the ply thickness, one simply uses $a = a_m$ and predicts from Equation (30) the minimum possible load for the onset of delamination. Thus

$$(e_o)_{cr} = \frac{\sqrt{G_c/t} - \sqrt{C_T(a)} \cdot \Delta T}{\sqrt{C_e(a)}} ; a = a_m. \quad (31)$$

The answer to the second question, however, requires additional analysis. Consider as an example a $[90_2/0_2/+45_2]_s$ under uniform compression. Interlaminar tensile σ_z is developed in this laminate and edge delamination is induced before global buckling, see Figure 2.25. A three-dimensional through-thickness display of σ_z is shown in Figure 2.26. The largest σ_z is located on the $45/-45$ interface (in fact, this σ_z is

singular at the free edge). On the other hand, σ_z along the mid-plane ($z = 0$) is finite at the free edge. In addition, there is also a singular interlaminar shear stress τ_{xz} along the 45/-45 interface. Thus, the analysis suggests the 0/45 interface as the most probable delamination site.

However, according to the energy release rate argument as well as the "effective" flaw hypothesis, one must rely upon the calculated energy release rate curve in order to define which one of the interfaces is likely to delaminate.

The finite element crack-closure results of the $G(a)$ curves for this example problem is shown in Figure 2.26. Indeed, the interface that yields the highest possible energy release rate is the mid-plane ($z = 0$), not the 45/-45 interface (though the reverse is true when a is smaller than one ply thickness). Besides, a delamination in the mid-plane is in mode-I, while it is mixed-mode (I, III) in the 45/-45 interface. Mixed-mode G_c is usually higher than G_{Ic} . Thus, the mid-plane is the most probable delamination site, not the 0/45 interface.

Numerical Examples - Static Loading.

In order to assess the accuracy of the energy model presented above, experiments have been conducted using AS-3501-06 graphite-epoxy $[+25/90_n]_s$, $n = 1, 2, 3$ (see Reference [15], for experimental details). Onset and growth of free edge delamination were recorded in all cases. Figure 2.27 displays the delamination versus the applied load plots. From these plots, the average onset load for each laminate case can be extrapolated. The growth of delamination is essentially stable, but the growth pace is

rather rapid. In all cases, delamination growth led to final failure.

Delamination in $[+25/90_2]_s$ and $[+25/90_3]_s$ started after the occurrence of transverse cracks in the 90° -layer. Hence, we shall defer the discussion on these two laminates to later in this section. Here, we shall consider only $[+25/90]_s$.

A free edge stress analysis and an energy release rate calculation indicate that for the $[+25/90]_s$ laminate, mid-plane delamination is most probable. The energy-release rate curves C_e and C_T as a function of delamination size a in the mid-plane are displayed in Figures 2.28 and 2.29, respectively.

Using the energy curves and the value of $G_c = 1.0 \text{ in-lb/in}^2$ for mode-I delamination growth (see discussion on G_c in Section 2.2), the minimum load at the onset of edge delamination is calculated via Equation (31). The following gives a comparison between the predicted and the experimental results for the delamination onset load:

<u>Experimental, Ksi</u>	<u>Predicted, Ksi</u>
48 - 50 (3 samples)	48 (Average)

The prediction is based on a mid-plane delamination while the experimental observation of the delaminated specimens indicated a delamination path which zig-zags between the $90/90$ and the $25/90$ interfaces. Even with these practical differences between the theory and the experiment, the energy model has yielded exceedingly satisfactory results. More results from this study are found in Appendix E.

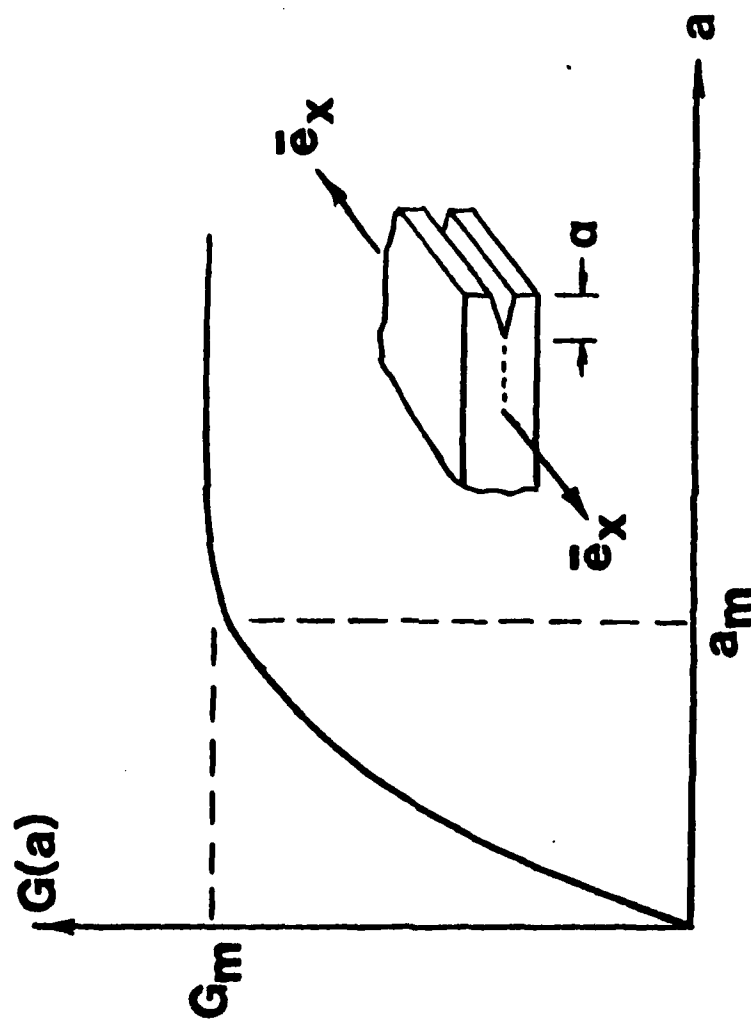
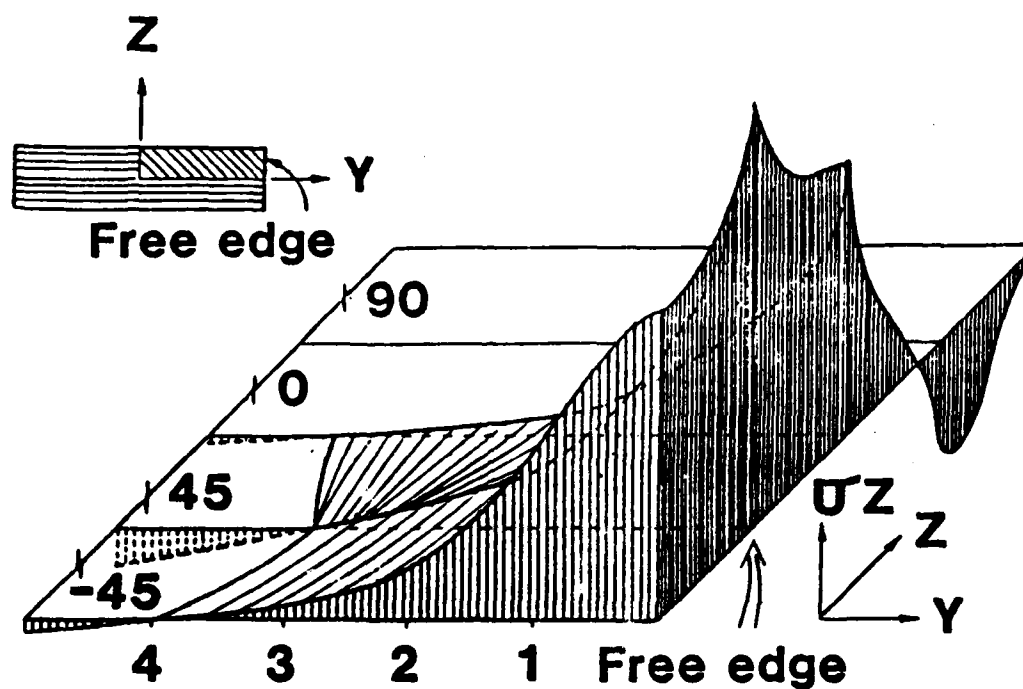


Figure 2.24 Typical Shape of Energy Release Rate $G(a)$ for Delamination.



Figure 2.25 Free Edge Delamination Induced by
Compression. AS-3501-06 $[90_2/0_2/+45_2]_s$.



Interlaminar normal stress distribution

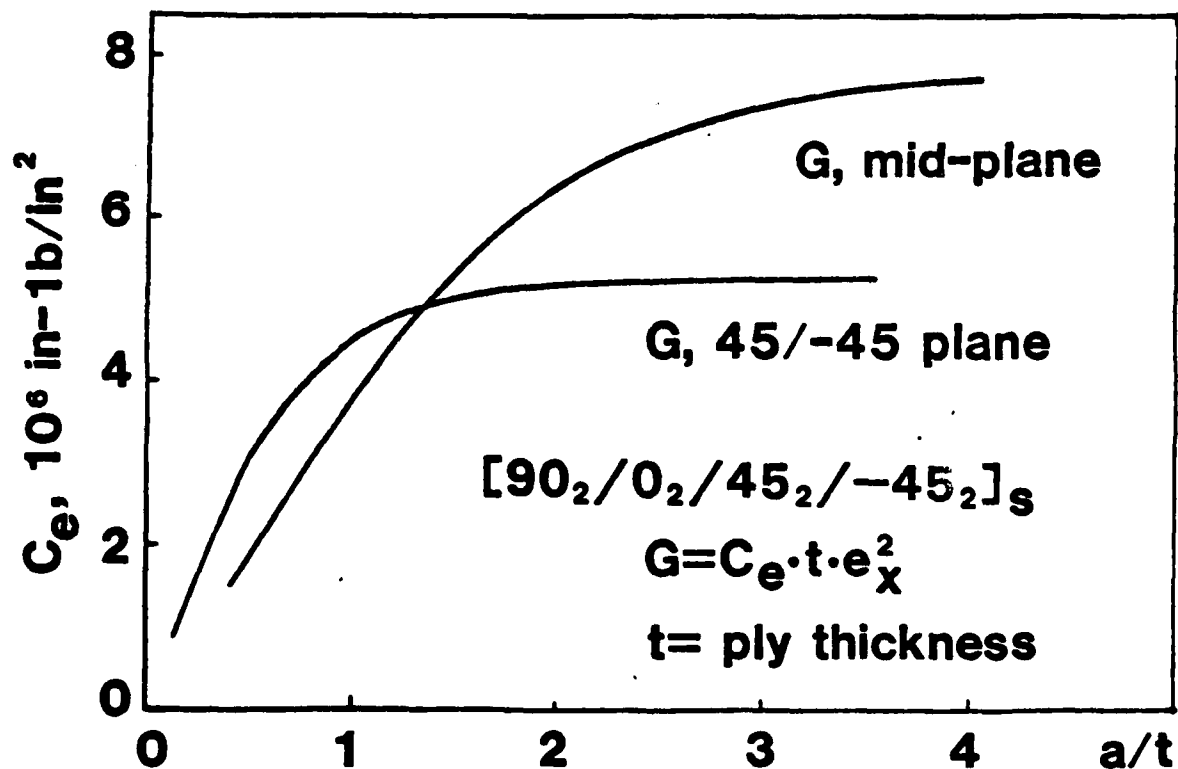


Figure 2.26 Interlaminar Normal Stress Distribution and Energy Release Rate Coefficients for $(90_2/0_2/\pm 45_2)_s$ Under Compression.

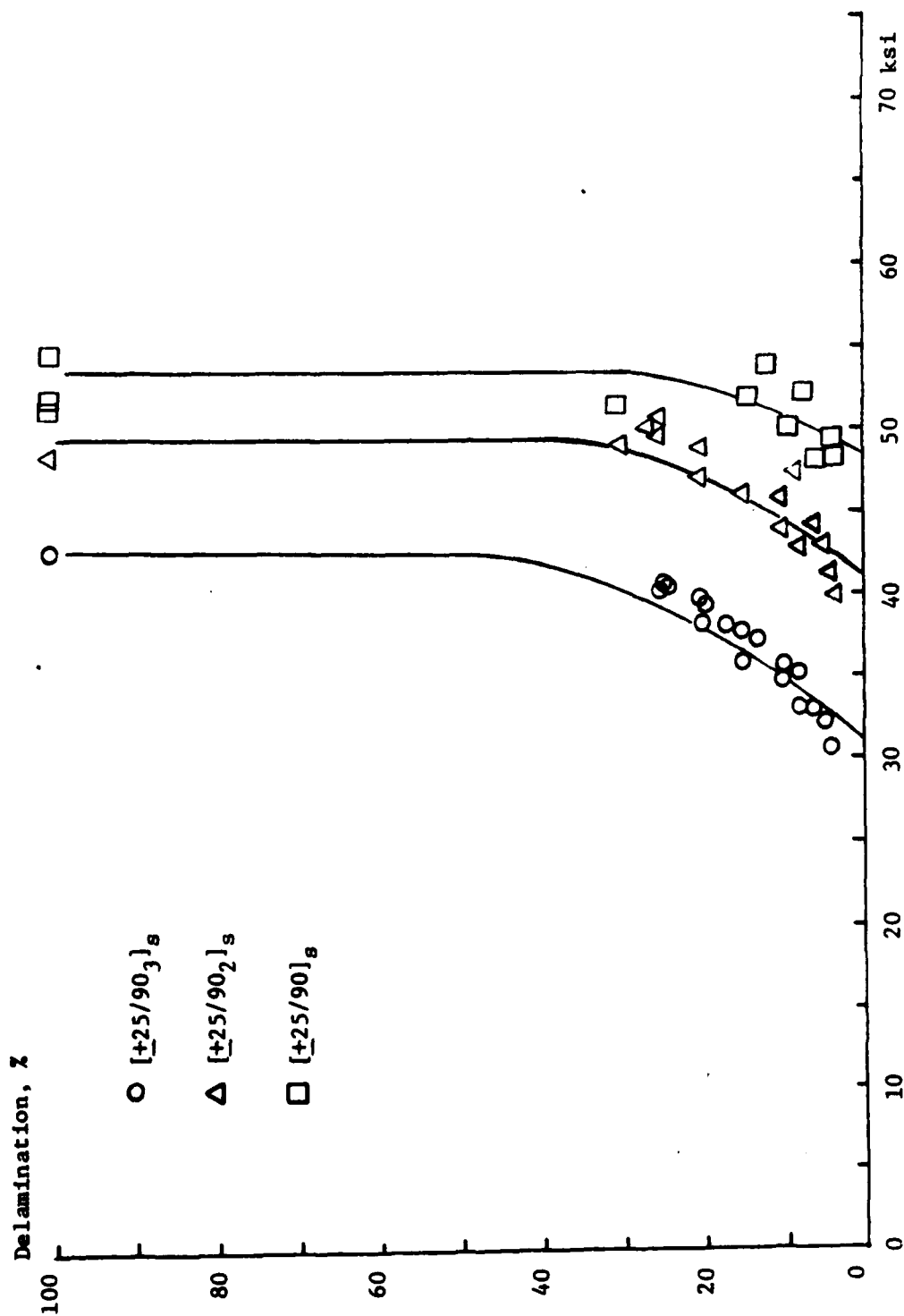


Figure 2.27 Delamination Growth (a/w) versus Applied Load for $[+25/90_n]_s$.

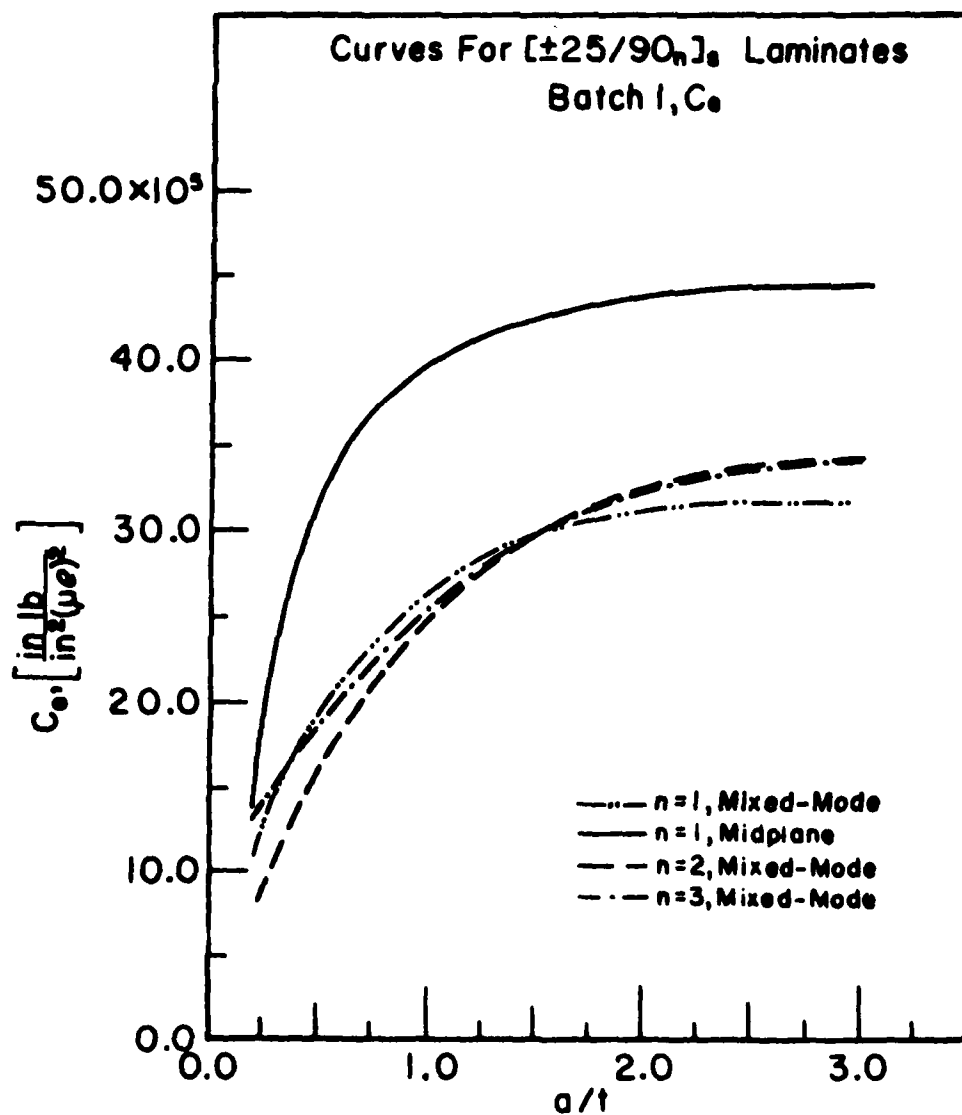


Figure 2.28 Energy Release Rate Coefficients For Delamination Under Mechanical Load.

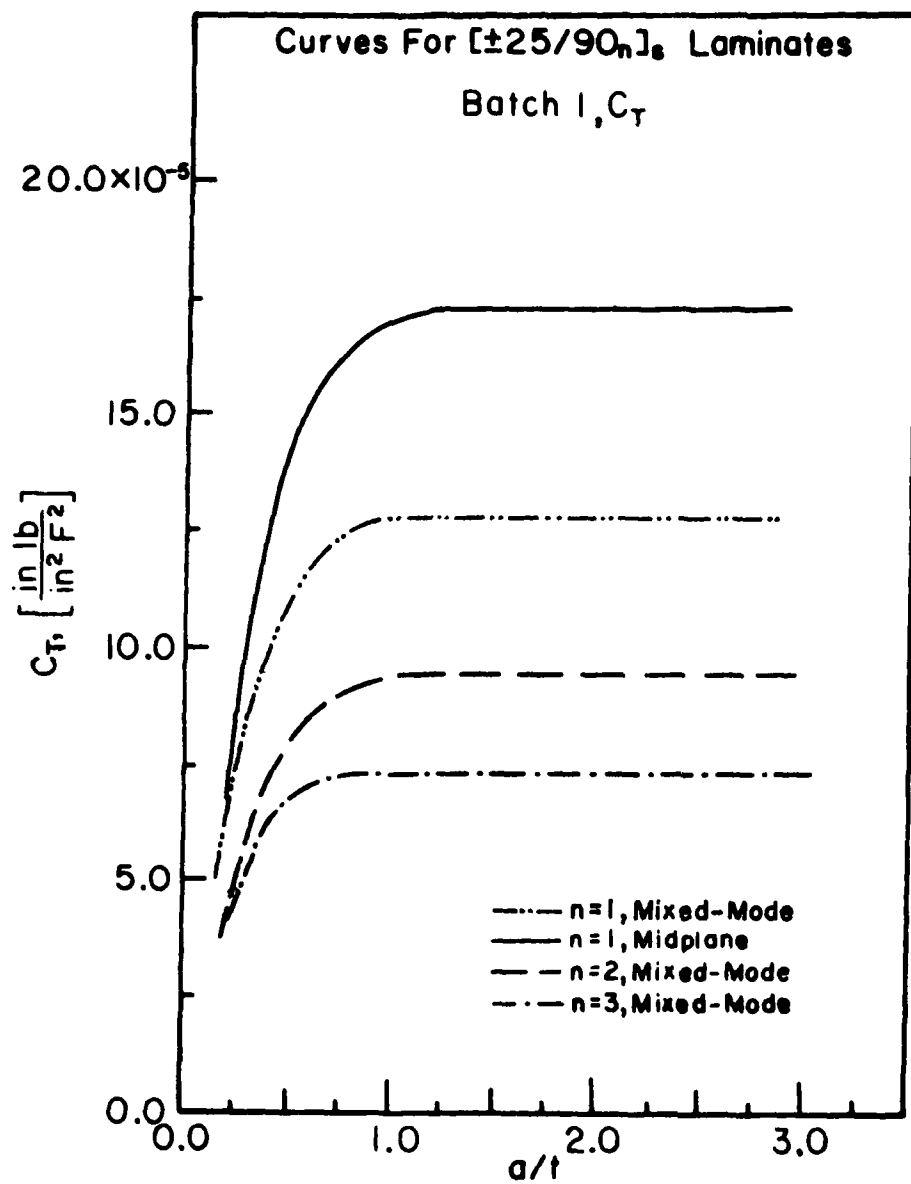


Figure 2.29 Energy Release Rate Coefficients For Delamination Under Thermal Load.

2.7. Mechanics of Free Edge Delamination - Fatigue Loading

It is well known that cyclic fatigue loads also induce sublaminar matrix cracks, including many forms of delamination growth. In fact, such cracks can be propagated at fatigue stress levels much below the threshold stress determined statically. Laboratory tests tend to indicate that fatigue load induced damage process is generally similar to that induced by static load; and the effects of cyclic loading/unloading are manifested by a shift-of-time.

Figures 2.30, 2.31, and 2.32 show the experimental delamination (in terms of percent specimen width) versus the number of cycle plots for the $[+25/90]_S$ laminate under the fatigue stress of 29, 33, and 40 ksi, respectively.

The crack growth rate law which is used widely for fine-grain metallic material is

$$\frac{da}{dN} = \bar{\alpha} [G(\sigma_f, \Delta T, a)/G_c]^{\bar{p}} \quad (32)$$

where σ_f is the fatigue stress amplitude, N is fatigue cycle and α and p are two undetermined empirical constants.

Since in Equation (32) the quantity $G(\sigma_f, \Delta T, a)$ includes already the laminate stacking sequence, lamina thicknesses, laminate shape features, the crack geometry, and the nature of loading and since the quantity G/G_c represents the relative magnitude of the crack driving force, then α and p are expected to be pure material constants. And, in particular, the exponent p is the most important measure of the crack growth rate.

Recall that the same crack growth rate law (32) was used in the stochastic simulation of multiple transverse cracks in $[0/90]_S$ type of laminates

subjected to tension/tension fatigue loading ($R = 0.1$). There, the constant $\bar{\alpha} = 2 \times 10^{-5}$ inch and $\bar{p} = 20.0$ were used for mode-I growth.

At this point, it is perhaps appropriate to review some other related works. Wilkins [19] conducted fatigue growth experiments on mode-I and mixed-mode delamination. The test results suggest that a power law such as Equation (32) would govern the delamination growth. For, if taking logarithm on both sides of (32), a linear relationship between da/dN and $G(\sigma_f, a)$ is obtained; the constant ratio between them yields the exponent p . Wilkins' results confirmed the adequacy of the crack growth law in the form of (32), for both mode-I and mixed-mode growth.

But, Wilkins also pointed out that the exponent p for mode-I growth is much larger than that for mixed-mode growth. For the material used in his study (AS-3501-06), he found $p \sim 20$ for mode-I and $p \sim 8$ for mixed-mode delamination growth. Since the value of G/G_c in (32) is normally smaller than unity, a larger p (positive) implies slower growth rate. It has been suggested that mode-I delamination is, generally, a static issue; and mixed-mode delamination is a fatigue issue, so far as epoxy-based composite laminates are concerned.

To fit the experimental data shown in Figures 2.30, 2.31 and 2.32, the corresponding mixed-mode energy release rate curves are used, see Figures 2.28 and 2.29. And for mixed-mode cracking $G_c = 1.3 \text{ in-lb/in}^2$. The value of $\bar{\alpha}$ and \bar{p} are set at

$$\bar{\alpha} = 0.04 \text{ inch; } \bar{p} = 8.3 \quad (33)$$

Thus, the predicted delamination growth curves as a function of fatigue amplitude and fatigue cycles are shown in solid lines in Figures 2.30, 2.31

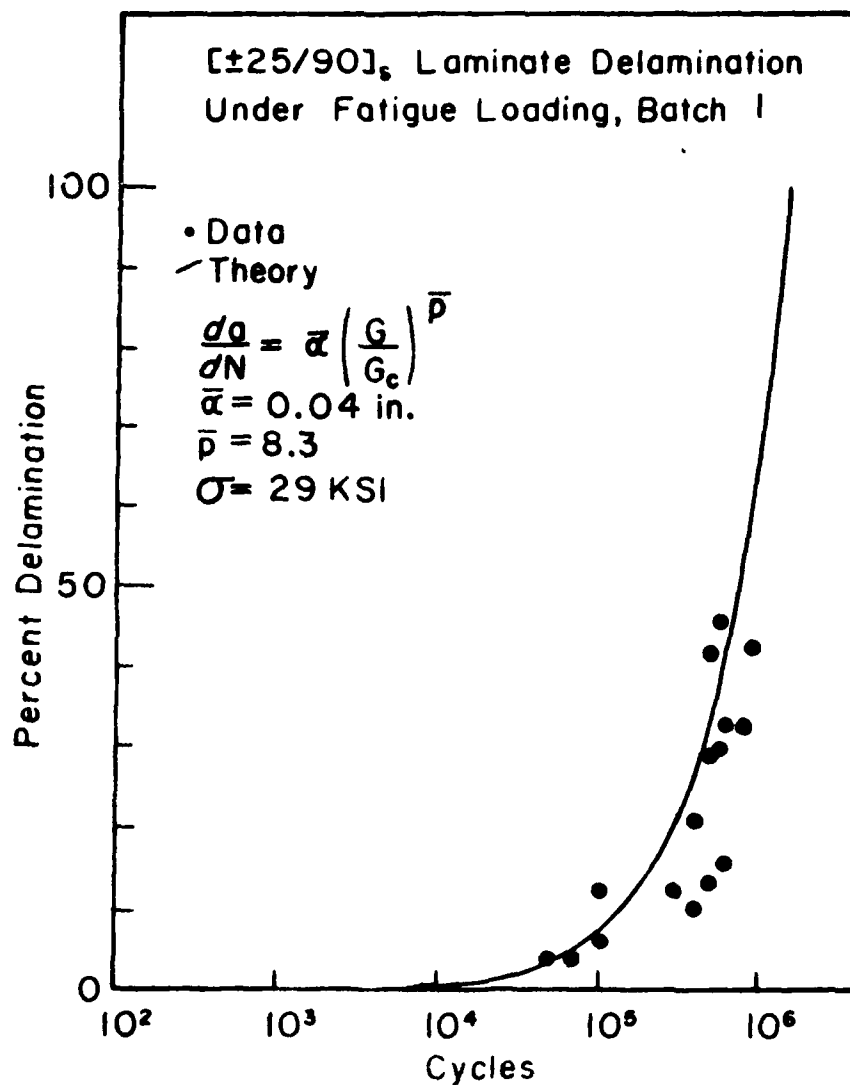


Figure 2.30 Percent Delamination vs. Fatigue Cycles for [±25/90]_s Laminates, $\sigma=29$ KSI.

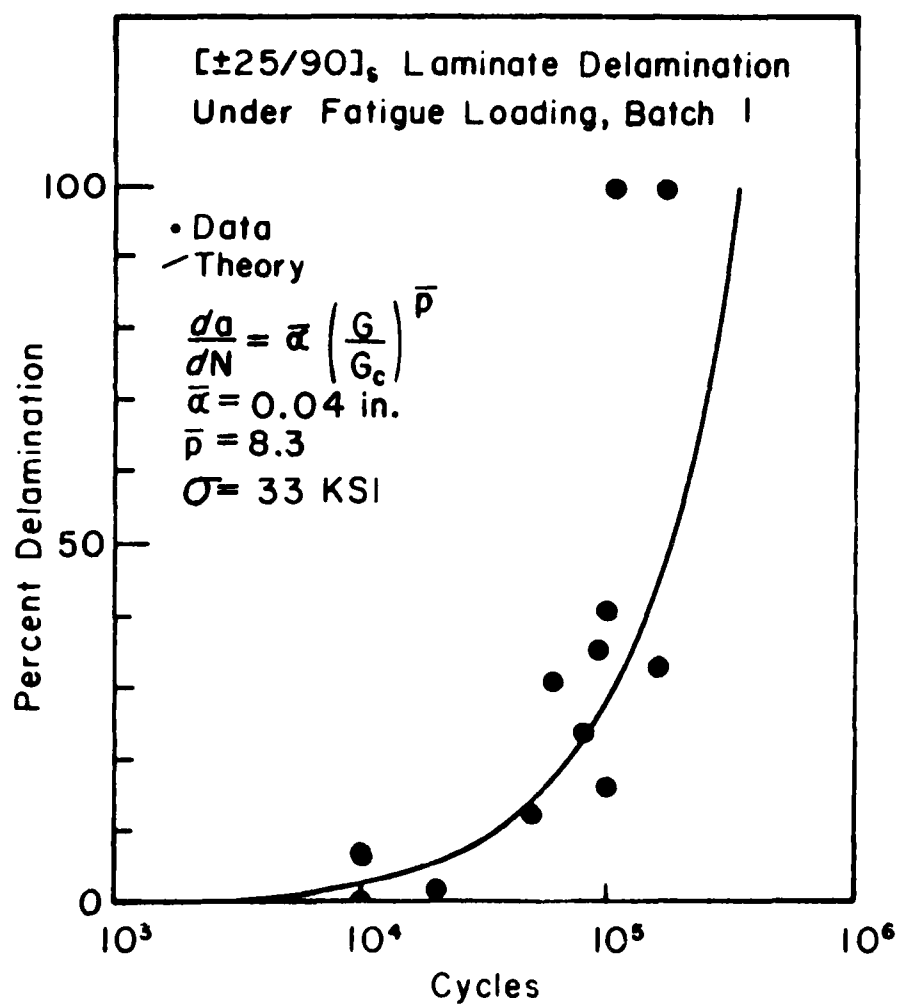


Figure 2.31 Percent Delamination vs. Fatigue Cycles for
[±25/90]_s Laminates, $\sigma=33$ KSI.

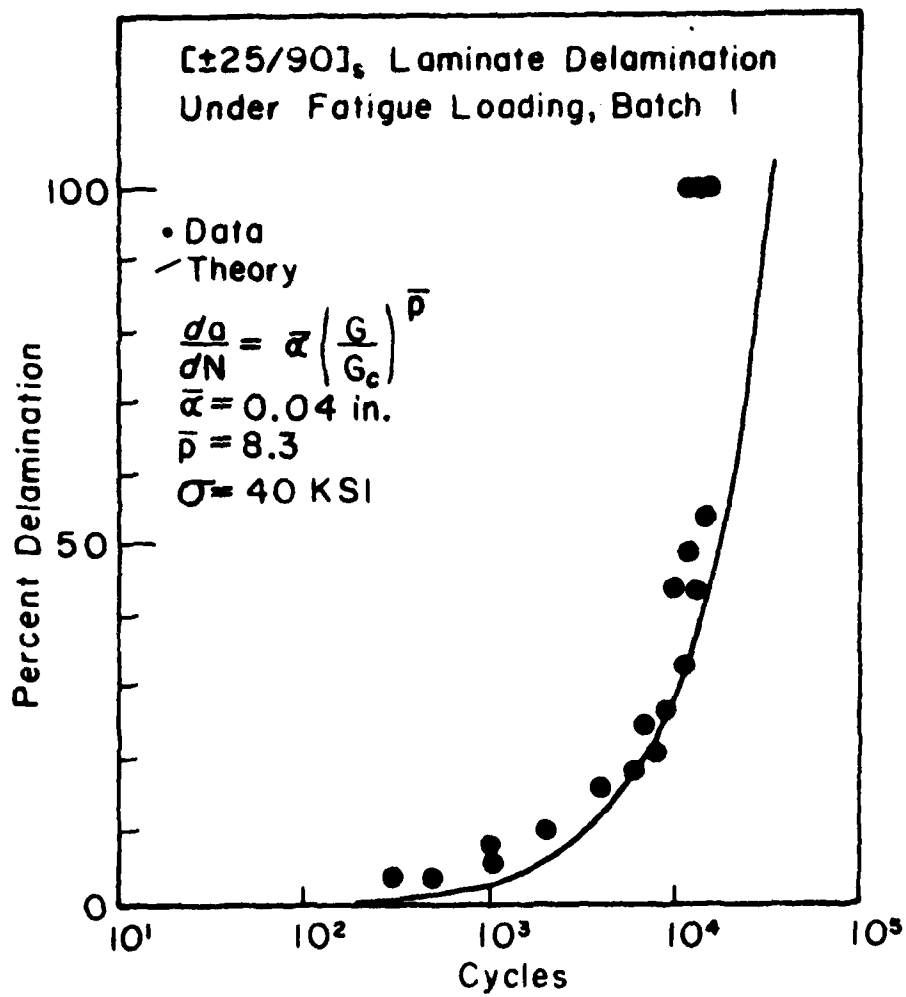


Figure 2.32 Percent Delamination vs. Fatigue Cycles for [±25/90]_s Laminates, $\sigma=40$ KSI.

and 2.32. More comparative results on this particular laminate under other load amplitudes are included in Appendix F.

2.8. A Cumulative Damage Model for Free Edge Delamination

As shown in the previous section, the growth of edge delamination can be satisfactorily simulated by a suitable crack growth law. Specifically, Equation (32) is written in a form which contains the loading factor, lamination geometry, the basic material moduli, etc., through the computed quantity $G(\sigma_f, a)$. The previously developed constant damage concept describes the delamination growth accumulation process for the same laminate under variable amplitude fatigue loads. The procedure is similar to that used for the transverse cracking problems discussed in Section 2.5. Upon integrating Equation (32), a family of constant damage lines can be generated numerically or graphically in the $\sigma - N$ space. Take, as an example the $[\pm 25/90]_s$ laminate's results shown in Figures 2.30, 2.31, and 2.32; a set of constant damage lines can be obtained using these curves. The latter is shown in Figure 2.33 where the state of damage is expressed in terms of the normalized size of delamination, a/w (w is the half-width of the specimen). The constant damage curves can predict the amount of cumulative damage (delamination size) in the laminate under spectrum loads.

As examples, consider first a case where the $[\pm 25/90]_s$ laminate is under $\sigma_c = 20$ ksi (138 mpa) for 10^5 cycles and is then loaded by $\sigma_f = 30$ ksi (207 mpa) for 3×10^5 cycles. To predict the cumulative damage, we used the curves in Figure 2.33. Under $\sigma_f = 20$ ksi for 10^5 cycles, there will be no delamination according to the constant damage lines. When the

load σ_f is increased to 30 ksi, $a/w = 25\%$ is predicted. The experimental results for this case show a 21% delamination at the end of loading, see Figure 2.33.

Another case concerns the same laminate loaded under $\sigma_f = 20$ ksi for 3×10^5 cycles, followed by $\sigma_f = 40$ ksi (276 mpa) for 500 cycles, followed by $\sigma_f = 30$ ksi for 2×10^5 cycles. At the end of each loading step, the predicted damage state is, $a/w = 0, 3\%$ and 25% , respectively, while the experiment indicated $a/w = 0, 4\%$ and 33% , see Figure 2.34.

The experimental results for the above two cases have been reported in Ref. [15]. A more detailed comparison between the prediction and the experiment for these two cases is given below:

Fatigue Amplitude Ksi (mpa)	Cycles @ Load	Delamination, %w	
		Experiment	Prediction
20 (173)	10^5	0	0
30 (259)	10^5	10	12
	3×10^5	21	25
<hr/>			
20 (173)	3×10^5	0	0
40 (346)	10^2	1	1
	5×10^2	4	3
30 (259)	10^5	25	20
	2×10^5	33	25
<hr/>			

The above shows that the prediction based on the constant damage lines also appears satisfactory. Many more comparative cases have been conducted in this research. All the results are found in Appendix G.

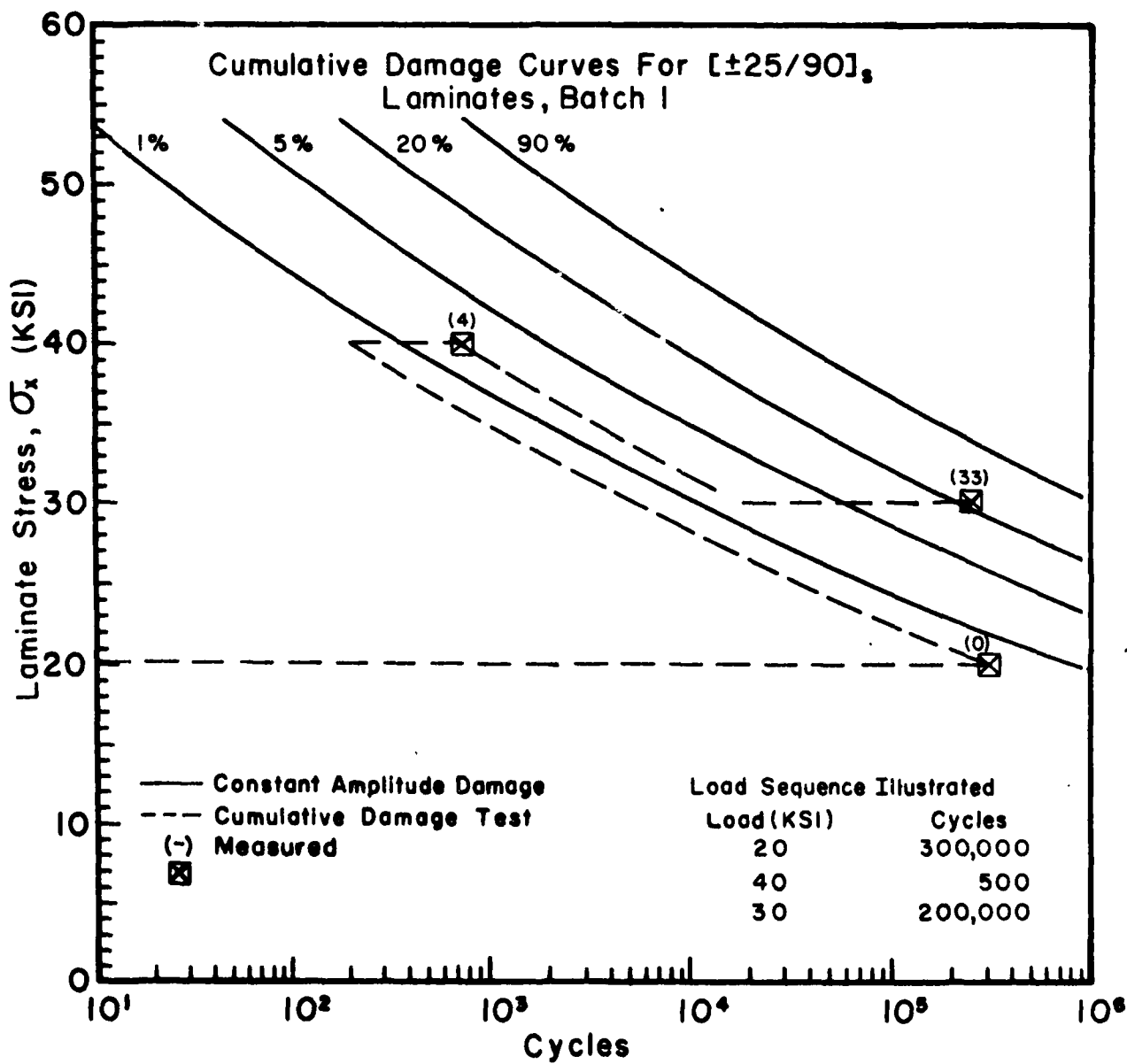


Figure 2.33 Cumulative Damage Tests: $[\pm 25/90]_s$.

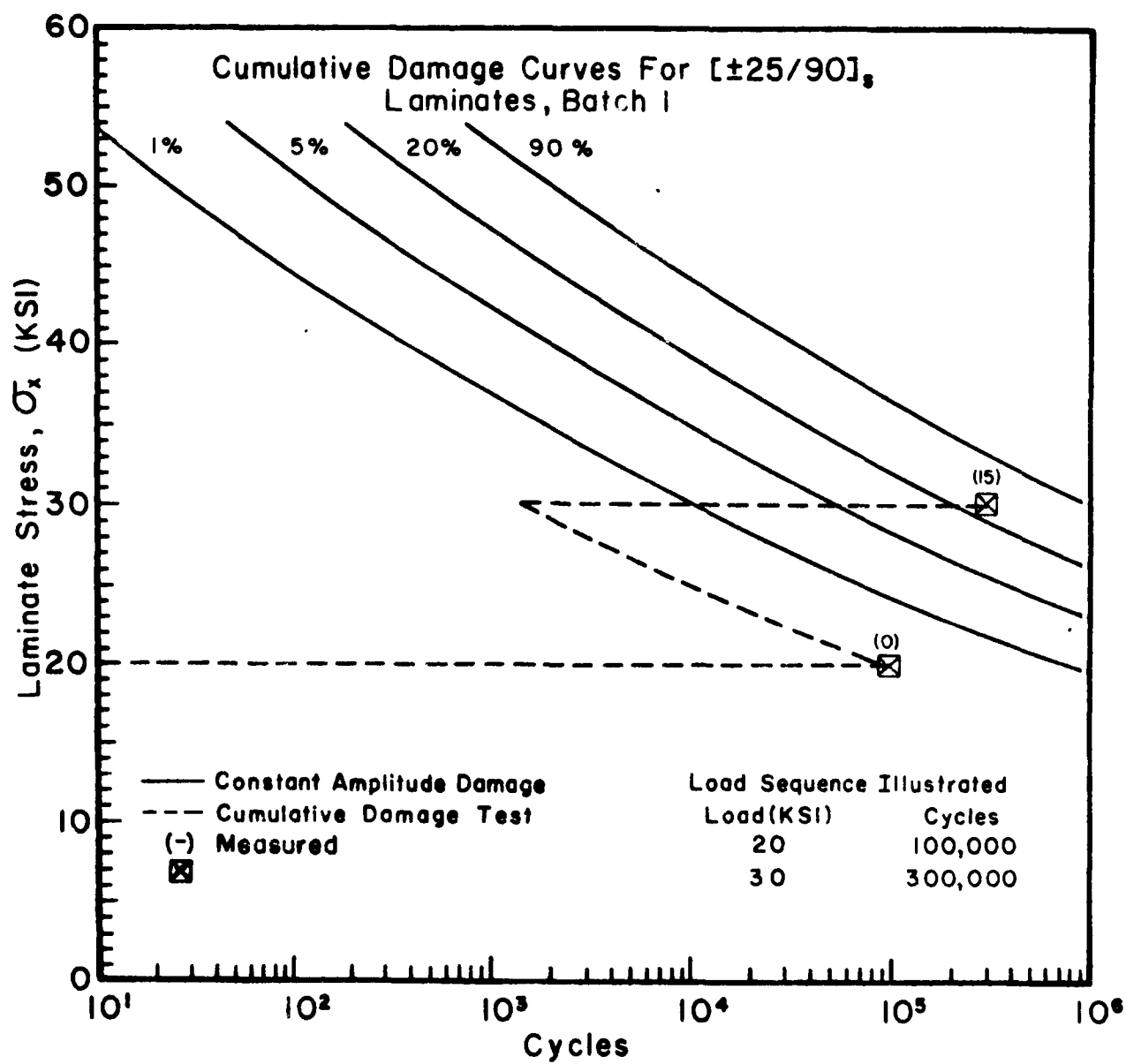


Figure 2.34 Cumulative Damage Tests: $[\pm 25/90]_8$.

2.9. Edge Delamination and Transverse Cracking Interactions

In the previous examples, the laminates considered are such that edge delamination is the first and only sub-laminate failure mode; the onset load for delamination could be determined accurately using the energy model. In most other cases, however, edge delamination and transverse cracking are competing failure modes which interact with each other through a complicated mechanism.

Recall the laminate $[\pm 25/90]_s$ which was discussed earlier. The thickness of the 90° -layer is made small so that transverse cracking is not possible before edge delamination. Nonetheless, the stress field in the 90° -layer, which contains the delamination, is actually very complex, so much so that high density transverse cracks could be observed during the entire delamination process.

On the other hand, in the tests of the $[\pm 25/90_2]_s$ laminate, the laminate suffered first transverse cracks in the 90° -layer; subsequently, edge delamination in the 25/90 interface was developed at a slightly higher load. And, the delamination, in turn, caused many more transverse cracks. Similar failure sequence was also observed in the $[\pm 25/90_3]_s$ laminates. These examples clearly demonstrate the profound interacting effects among competing failure modes, which exist in most practical laminates.

In an attempt to simulate the problem approximately, Law [32] assumed that when transverse cracks occurred in the 90° -layer, the tensile modulus, E_T , and the Poisson ratio, ν_{TL} , of the 90° -layer will both reduce to nearly zero. With this reduced moduli in the 90° -layer, the overall laminate becomes energetically delamination prone in the 25/90 interface, resulting

in a mixed-mode cracking (I, II). Then, by simulating a mixed-mode delamination in the 25/90 interface (for details see [32]), the total energy release rate $G = G_I + G_{II}$ can be calculated using the same two-dimensional crack-closure routine. For instance, the computed G_e and G_T curves for $[\underline{+25/90}_2]_s$ and $[\underline{+25/90}_3]_s$ are shown in Figures 2.28 and 2.29. Using these curves and setting $G_c = 1.0 \text{ in-lb/in}^2$ for mixed-mode delamination, the minimum onset load for edge delamination can be predicted. A comparison between the prediction and the experiment is given as follows:

<u>Laminate</u>	<u>Onset Laminate Stress, Ksi (mpa)</u>	
	<u>Experiment</u>	<u>Prediction</u>
$[\underline{+25/90}_2]_s$	40 - 43	41 (283)
$[\underline{+25/90}_3]_s$	32 - 33	38 (262)

This shows that the prediction for $[\underline{+25/90}_3]_s$ was not satisfactory. The short-fall in this case may stem from the fact that the interaction effect could not be adequately addressed by the assumption made by Law [33]. Further refinement of the simulation model, which includes failure modes interaction, remains to be developed.

In fact, such a model development has been planned in the Phase-III study of this research program. At this reporting time, however, no simulation results have been available for a comparison with the experimental results obtained for $[\underline{+25/90}_2]_s$ and $[\underline{+25/90}_3]_s$ laminates.

III. EXPERIMENTAL PROGRAM AND RESULTS

3.1. Scope of Experiment of Phase-I.

In Phase-I of the present research project, the experimental program consisted of four major tests:

- (a) material and laminate characterization tests;
- (b) static load-damage growth tests;
- (c) constant amplitude fatigue-damage growth tests; and
- (d) cumulative damage growth under variable amplitude fatigue load tests.

The scope of test (a) was to characterize the basic material and laminate properties in order to qualify the material system used as well as to obtain the basic material constants needed for stress and fracture analyses.

The scope of test (b) was to identify the various failure modes in laminates under static loading conditions. The tests were designed to yield information about the onset, growth, and final failure mechanisms of transverse cracking and free edge delamination. Essentially, the laminates $[0_2/90_2]_s$, $[0_2^{90}/3]_s$, and $[\pm 25/90_n]_s$, $n = 1, 2, 3$ were tested.

These laminates were also tested in (c) and (d); data from these tests were used to correlate the fatigue crack growth equations and the cumulative damage model.

All test results obtained in Phase-I were collectively reported in the Phase-I final report [15]. Some of these results were also used in Chapter II of this report in the presentation of the various failure modes.

A complete presentation of the test data along with the analytical results can also be found in Appendices A through H.

The details of the test methods and other related information are contained in Ref. [15].

3.2. Scope of Experiment of Phase-II

In Phase-II of this research, new specimens had to be made. Though using the same AS-3501-06 material system as in Phase-I, the new batch of specimens, however, were fabricated at the University of Delaware (while specimens used in Phase-I were fabricated at NADC). For this reason, key material and laminate characterization tests had to be performed again in Phase-II.

The test details were maintained the same as those reported in Ref. [15]. A complete account of the test program is given below:

<u>Laminate</u>	<u>Purpose of Test</u>	<u>Load Type</u>	<u>Specimens Used</u>
$[0_8]$	Basic Data	Static to Fail	18
$[90_{12}]$	Basic Data	Static to Fail	2
$[0_2/90_2]_s$	Basic Data	Static to Fail	2
	T.C. Growth	Step Load	8
	T.C. Growth	Fatigue Load (5 Fatigue Loads)	20
	T.C. Growth	Variable Fatigue (3 cases)	6
$[0_2/90_3]_s$	Basic Data	Static to Fail	2
	T.C. Growth	Step Load	6
	T.C. Growth	Fatigue Load (5 Fatigue Loads)	17
	T.C. Growth	Variable Fatigue (3 cases)	6
$[+25/90]_s$	Basic Data	Static to Fail	2
	Edge Delamination	Static to Fail	5
	Edge Delamination	Fatigue Load (6 Fatigue Loads)	20
	Edge Delamination	Variable Fatigue (5 cases)	11

<u>Laminate</u>	<u>Purpose of Test</u>	<u>Load Type</u>	<u>Specimens Used</u>
[+25/90 ₂] _s	Basic Data	Static to Fail	2
	Interaction	Step Load	5
	Interaction	Fatigue Load (2 Fatigue Loads)	6
<hr/>			
[+25/90 ₃] _s	Basic Data	Static to Fail	2
	Interaction	Step Load	5
	Interaction	Fatigue Load (2 Fatigue Loads)	6
<hr/>			
TOTAL SPECIMENS			151

All data obtained in Phase-II are presented in Appendices A through H. Except for the [+25/90₂]_s and [+25/90₃]_s laminates, all the data has been used in correlation with the analytical model. Results from the model are listed in these Appendices, along with their experimental counterparts.

IV. CURRENT STATUS OF RESEARCH AND METHODOLOGY SUMMARY

4.1. Current Status

The principal objective of this research has been illustrated and discussed in Chapter I. The details of the model development are presented in Chapter II. At this reporting time, the status of the research project may be summarized as follows:

- (a) A concept of "effective flaw distribution" has been introduced. This concept postulates that natural flaws in the basic material ply (unidirectional) and/or between ply interface (interlaminar flaws) could be effectively represented by a suitable distribution function. This concept is then used in conjunction with energy method of the classical fracture mechanics. Together they provide a methodology for multiple failure sequences in the laminate.
- (b) A simple crack growth law, based on the energy argument, has been introduced and describes the individual effective flaw growth behavior under constant amplitude fatigue loading. This crack growth law implicitly or explicitly contains the material factor (fracture toughness), the load factor (nature of load, amplitude, etc.) and the geometrical factor (ply thickness, stacking sequence, free edges, etc.) of the considered laminate.
- (c) The concept of constant damage state has been introduced. It describes, in quantitative terms, the state of damage in load-cycle ($\sigma - N$) space. This concept is used to form a simple cumulative damage model when the laminate is subjected to

AD-A144 848

CUMULATIVE DAMAGE MODEL FOR ADVANCED COMPOSITE
MATERIALS(U) DYNA EAST CORP PHILADELPHIA PA
P C CHOU ET AL. 89 MAR 84 AFWAL-TR-84-4084

2/2

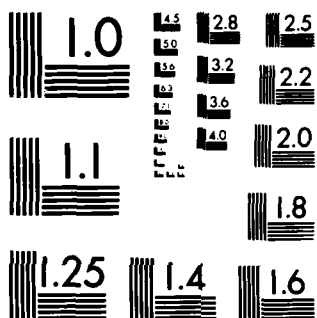
UNCLASSIFIED

F33615-80-C-5039

F/G 11/4

NL

END



MICROCOPY RESOLUTION TEST CHART
NATIONAL BUREAU OF STANDARDS-1963-A

variable amplitude fatigue load.

- (d) All the above have been applied to the failure modes of transverse cracking and free edge delamination. The modelling of these two failure modes has been successfully correlated with the experimental test results.
- (e) The presently developed methodology has been applied to simple laminates, where only one single failure mode is induced by the load. It remains to demonstrate that the modelling method can be applied equally well to laminates having complicated lamination geometry. Complication may arise, however, when two or more failure modes occur simultaneously and/or sequentially. In these cases, modes' interaction will be encountered. We feel that the methodology should serve well for these cases. The necessary numerical tool must be developed to handle the expected three-dimensional stress fields when two or more interacting singularities are present.
- (f) For laminates which suffer extensive delamination before final failure, it seems practical to use the "delamination state" as a criterion for final failure. However, this criterion is not expected to be a general rule, as in many laminates, delamination may not govern. This is especially true for laminates which contain a high percentage of 0° -plies. Clearly, it is still a long way before we understand the complexity of the damage processes when the laminate is approaching final failure. Until then, the development of a general laminate strength criterion (including the S - N curve in the σ - N space) can only be ad-hoc in nature.

4.2. Methodology Summary

This summary is intended to illustrate more clearly the various elements which comprise the cumulative damage model. Figure 4.1 is a block diagram showing the infrastructure of the methodology. It shows that there are five levels of development in the model construction. Namely, these are (1) numerical, (2) experimental, (3) theorization, (4) simulation, and (5) prediction/correlation.

Numerical Development. The major objectives in the numerical development are (1) to accurately and efficiently compute the three-dimensional stress field in a given laminate with or without a prescribed macrocrack in it, and (2) to compute the crack front (or crack-tip in one-dimensional crack propagation) energy release rate if the laminate does contain a prescribed macrocrack.

Depending on the nature of the prescribed problem, a two-dimensional and/or three-dimensional solution method must be used. In the present research, the finite-element method is adapted because of its versatility in handling complicated laminate geometry, as well as loading combinations.

When multiple failures are to be simulated, random material flaws must be represented by using a random number generator, which can be easily incorporated in the crack simulation model.

Experimental Development. Experiments are necessary to determine the pertinent material properties required as input data for the analytical model. Four types of properties are required which must be obtained from independent tests using the basic UD material. These are (1) ply deformation

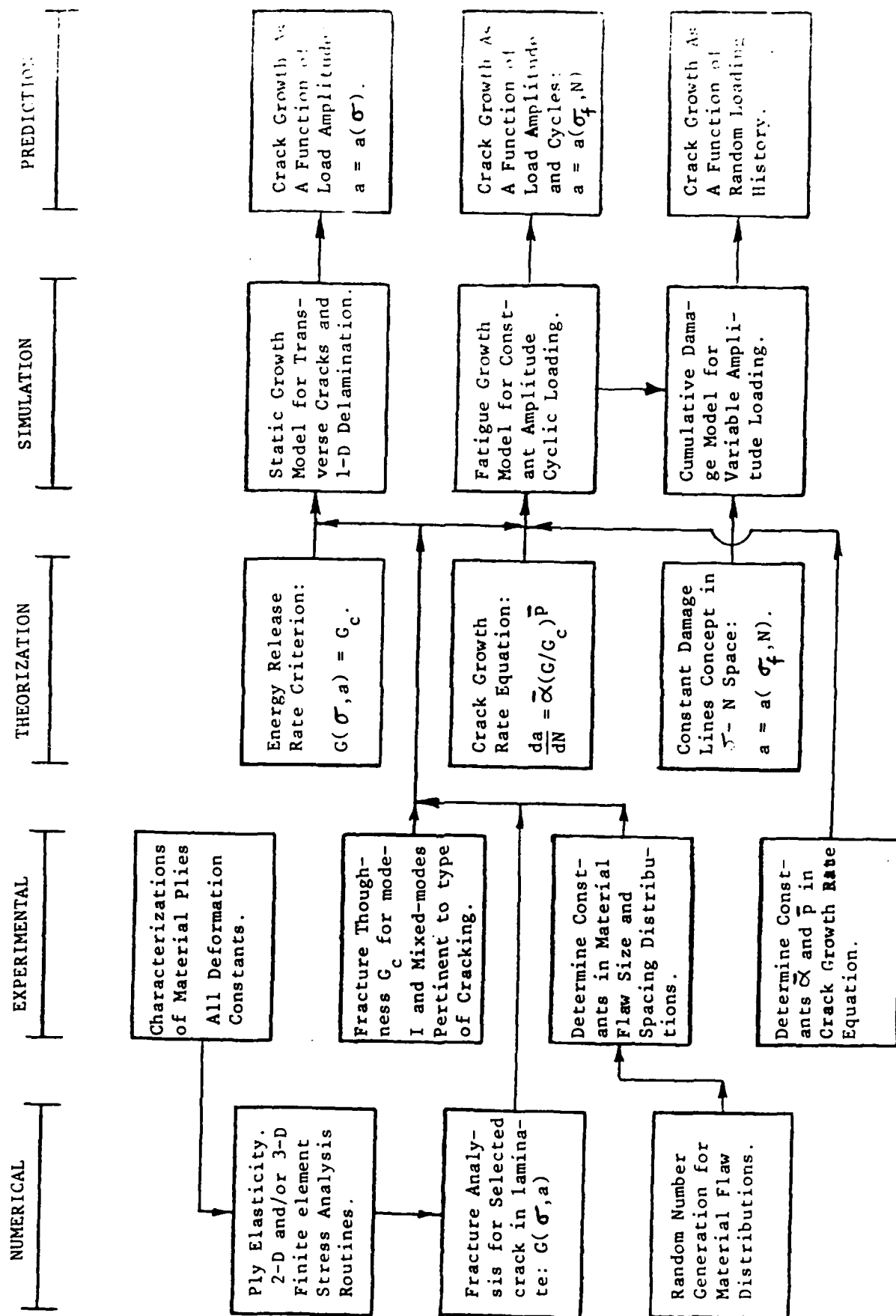
moduli (C_{ij}), (2) fracture toughness for matrix-dominant crack propagation (G_c), (3) effective flaw distribution parameters for multiple failures in laminates, and (4) fatigue growth parameters for matrix-dominant crack growth rate under fatigue load. All, except (1), are still in their early stage of development. But, increased information is becoming available.

Theorization Development. For static crack growth, the energy release rate criterion is used; for fatigue growth, the power law based on energy release rate for the crack growth rate is used; and for growth under random loading, the concept of constant damage lines is used. Again, all are in their early stage of development; more research is needed in order to settle some of the basic questions in their use.

Simulation Development. This is the actual modeling of the crack growth process, which puts together the use of the computational tool, the experimental input data for material properties, and the basic theory for crack growth. The model(s) thus produce the desired output information for which the reliability of the laminate is to be assessed.

Prediction/Correlation. The predicted outcome is compared by experiment. The comparison serves two purposes (1) to re-adjust the simulation and/or theorization developments and (2) to verify the applicability of the model(s) and establish the bounds in which it is applicable.

Figure 4.1 The Infrastructure of the Cumulative Damage Model.



REFERENCES

- [1] Harrison, R.P. and Bader, M.G., "Damage Development in CFRP Laminates Under Monotonic and Cyclic Stressing," Fiber Science and Technology, Vol. 18, 1983, pp. 163-180.
- [2] Wang, A.S.D., "Fracture Mechanics of Sublaminar Cracks in Composite Laminates," Proceedings AGARD Structures and Materials Specialist Meeting, London, 1983.
- [3] Reifsnider, K.L. and Highsmith, A., "Characteristic Damage States: A New Approach to Representing Fatigue Damage in Composite Laminates," Proceedings Materials Experimentation and Design in Fatigue, London, 1981.
- [4] Tsai, S.W. and Hahn, H.T., "Introduction to Composite Materials," Technomic, 1980.
- [5] Griffith, A.S., "The Phenomena of Rupture and Flow in Solids," Phil. Trans. Roy. Soc., Vol. A221, 1920, p. 163.
- [6] Muskhelishvili, N.I., "Some Basic Problems from the Mathematical Theory of Elasticity," Noordhoff, Holland, 1953.
- [7] Sneddon, I.N., "Integral Transform Methods," in Methods of Analysis and Solutions of Crack Problems, Noordhoff, Holland, 1973, p. 315.
- [8] Lekhnitsky, S.G., "Theory of Elasticity of an Anisotropic Elastic Body," Holden-Day, San Francisco, 1963.
- [9] Rice, J.R., "A Path Independent Integral and Approximate Analysis of Strain Concentration by Notches and Cracks," J. Appl. Mech. Trans. ASME, 1968, p. 379.
- [10] Bucci, R.J.; Paris, P.C.; Landis, J.D.; and Rice, J.R., "J-Integral Estimation Procedures," in Fracture Toughness, ASTM STP 514, 1972, p. 40.
- [11] Irwin, G.R., "Fracture," Handbuch der Physik, Vol. 5, Springer-Verlag, 1958, p. 551.
- [12] Rybicki, E.F. and Kanninen, M.F., "A Finite Element Calculation of Stress Intensity Factors by a Modified Crack-Closure Integral," Eng. Fract. Mech., Vol. 9, 1977, p. 931.
- [13] Wang, A.S.D. and Crossman, F.W., "Initiation and Growth of Transverse Cracks and Edge Delamination in Composite Laminates: Part 1. An Energy Method," J. Comp. Matls., Suppl. Vol., 1980, p. 71.
- [14] Crossman, F.W.; Warren, W.T.; Wang, A.S.D.; and Law, G.E., "Initiation and Growth of Transverse Cracks and Edge Delamination in Composite Laminates: Part 2. Experimental Correlation," J. Comp. Matls., Suppl. Vol., 1980, p. 88.

- [15] Chou, P.C.; Wang, A.S.D.; and Miller, H., "Cumulative Damage Model for Advanced Composite Materials," Phase I, Final Report, AFWAL-TR-82-4083, 1982.
- [16] Cullen, J.S., "Mode-I Delamination of Unidirectional Graphite-Epoxy Composite Under Complex Load Histories," M.S. Thesis, Texas A & M University, 1981.
- [17] Williams, D., "Mode-I Transverse Cracking in an Epoxy and a Graphite Fiber Reinforced Epoxy," M.S. Thesis, Texas A & M University, 1981.
- [18] Wilkins, D.J., "A Comparison of the Delamination and Environmental Resistance of a Graphite-Epoxy and a Graphite-Dismaleimide," NAV-GD-0037, Naval Air System Comm., 1981.
- [19] Wilkins, D.J.; Eisenmann, J.R.; Camin, R.A.; Margolis, W.S.; and Benson, R.A., "Characterizing Delamination Growth in Graphite-Epoxy," ASTM STP 775, 1982, p. 168.
- [20] Vanderkley, P.S., "Mode-I and Mode-II Delamination Fracture Toughness of an Unidirectional Graphite-Epoxy Composite," M.S. Thesis, Texas A & M University, 1981.
- [21] Bascom, W.D.; Cottingham, R.L.; and Timmons, C.O., "Fracture Design Criteria for Structural Adhesive Bonding - Promise and Problems," Naval Eng. Jour., Aug. 1976, p. 73.
- [22] Wang, A.S.D.; Kishore, N.N.; and Feng, W.W., "On Mixed-Mode Fracture in Off-Axis Unidirectional Graphite-Epoxy Composites," Proc. ICCM-IV, Vol. 1, Tokyo, 1982, p. 599.
- [23] Bader, M.G.; Bailey, J.E.; Curtis, P.T.; and Parvizi, A., "The Mechanisms of Initiation of Development of Damage in Multi-Axial Fiber-Reinforced Plastics Laminates," in Mechanical Behavior of Materials, ICM-3, Vol. 3, 1979, p. 227.
- [24] Aveston, J. and Kelly, A., "Theory of Multiple Fracture of Fibrous Composites," J. Matls. Sciences, Vol. 8, 1973, p. 352.
- [25] Reifsnider, K.L. and Masters, J.L., "Investigation of Characteristic Damage States in Composites Laminates," ASME Paper No. 79-WA-AERO-4, 1978.
- [26] Jivinal, R.C., "Stress, Strain and Strength," McGraw-Hill, N.Y., 1967, p. 346.
- [27] Rubinstein, R.Y., "Simulation and the Monte-Carlo Method," J. Wiley & Sons, New York, 1981, p. 11.
- [28] Pipes, R.B. and Pagano, N.J., "Interlaminar Stresses in Composite Laminates Under Uniform Axial Tension," J. Comp. Matls., Vol. 4, 1970, p. 538.

- [29] Wang, S.S. and Choi, I., "Boundary Layer Effects in Composite Laminates," Part 1 and Part 2, J. Appl. Mech., Vol. 49, 1982, p. 541, p. 549.
- [30] Bjeletich, J.G.; Crossman, F.W.; and Warren, W.J., "The Influence of Stacking Sequence on Failure Modes in Quasi-Isotropic Graphite-Epoxy Laminates," Failure Modes in Composites - IV, AIME, 1979.
- [31] Rodini, B.T. and Eisenmann, J.R., "An Analytical and Experimental Investigation of Edge Delamination in Composite Laminates," in Fibrous Composites in Structural Design, Ed. E.M. Lenoe, et al., Plenum Press, NY, 1978, p. 441.
- [32] Law, G.E., "Fracture Analysis of $[+25/90]_{n_s}$ Graphite-Epoxy Composite Laminates," Ph.D. Thesis, Drexel University, 1981.

APPENDICES

	<u>PAGE</u>
A. COMPUTATION OF ENERGY RELEASE RATE RETENTION FACTOR R(S). . . .	96
B. TRANSVERSE CRACKING - STATIC LOADING	100
C. TRANSVERSE CRACKING - FATIGUE LOADING	110
D. TRANSVERSE CRACKING - CUMULATIVE DAMAGE	130
E. FREE EDGE DELAMINATION - STATIC LOADING	142
F. FREE EDGE DELAMINATION - FATIGUE LOADING	146
G. FREE EDGE DELAMINATION - CUMULATIVE DAMAGE	153
H. BASIC MATERIAL CHARACTERIZATION	165

APPENDIX A

COMPUTATION OF ENERGY RELEASE RATE RETENTION FACTOR $R(S)$

Consider the $[0_2/90_2]_s$ laminate, see inset in Figure A-1. Assume that there exists already a transverse crack which is to the right of a flaw having a size of $2a$. The effect of the crack on the energy release rate behavior of the flaw is a reduction of the energy release rate, depending on the distance S between the two.

Figure A-1 shows a family of curves for the energy release rate coefficient C_e (as a function of flaw size a/t) at different values of S . It is seen that a flaw located at $S \geq 15t$, nearly 100% of the energy release rate is retained. This implies that the existing crack no longer has any effect on the flaw, or that the flaw is outside the shear-lag zone of the existing crack.

In fact, for a flaw of any size, the influencing factor depends only on the value of S . Thus, from the family of curves such as shown in Figure A-1, an energy release rate retention factor $R(S)$ may be determined. For the $[0_2/90_2]_s$ and $[0_2/90_3]_s$ laminates, for instance, $R(S)$ curves are displayed in Figure A-2 as plotted against S/t (t being the thickness of one ply).

The $R(S)$ curves for $[0_2/90_n]_s$, $n = 1, 2, 3...$ can in fact be reduced to a single curve when S is normalized by nt , see Figure A-3. And, this single curve can be fitted by an exponential function

$$R(S/nt) = 1 - 1.0056e^{-0.7776S/nt}$$

for

$$1 < S/nt < 8$$

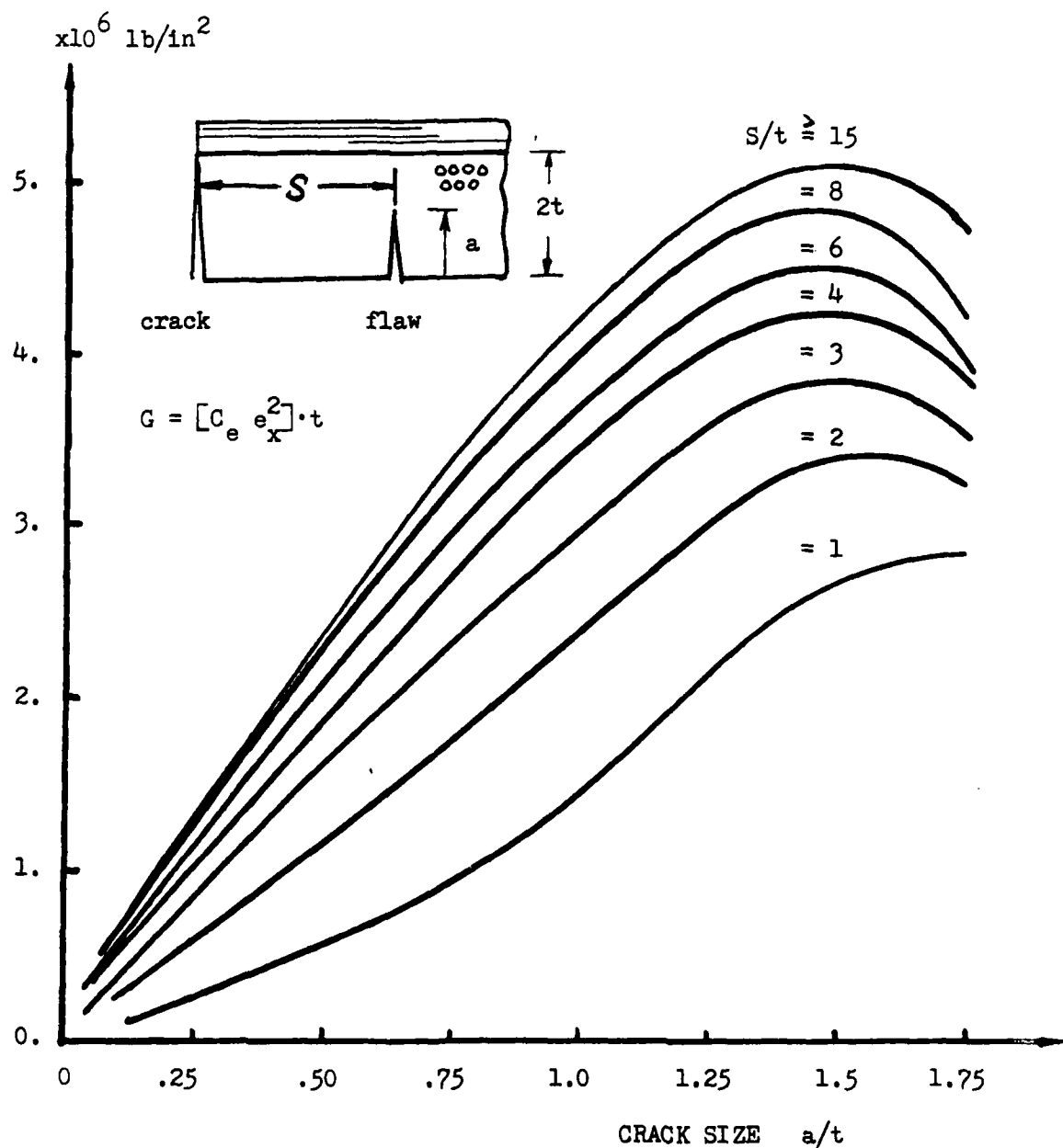


Figure A-1 Energy Release Rate Coefficient C_e As a Function of a/t for A Flaw Located At Variable Distance S from An Existing Transverse Crack. $[O_2/90_2]_S$

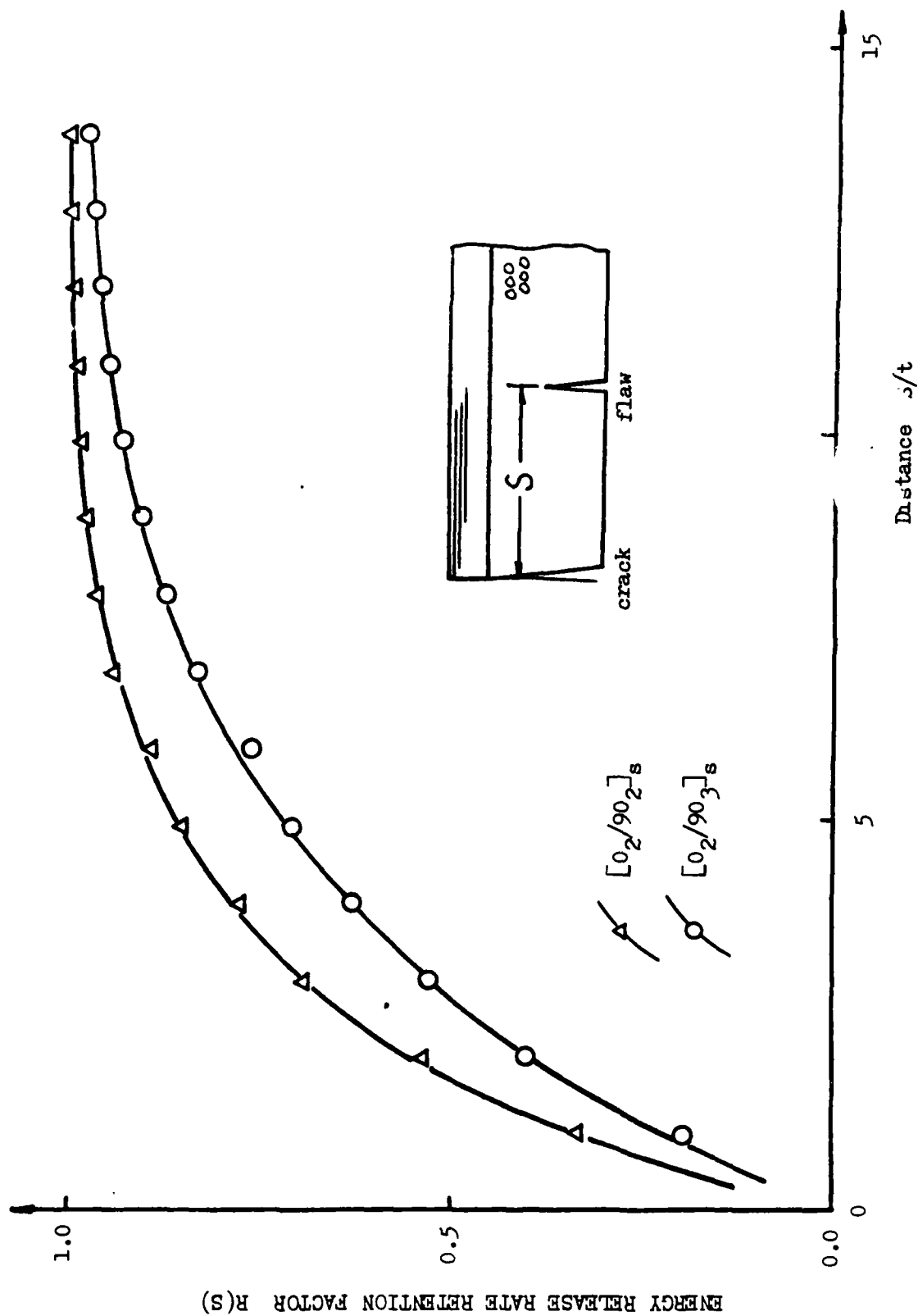


Figure A-2 Energy Release Rate Retention Factor $R(S)$ of A Flaw Located At S From An Existing Transverse Crack.

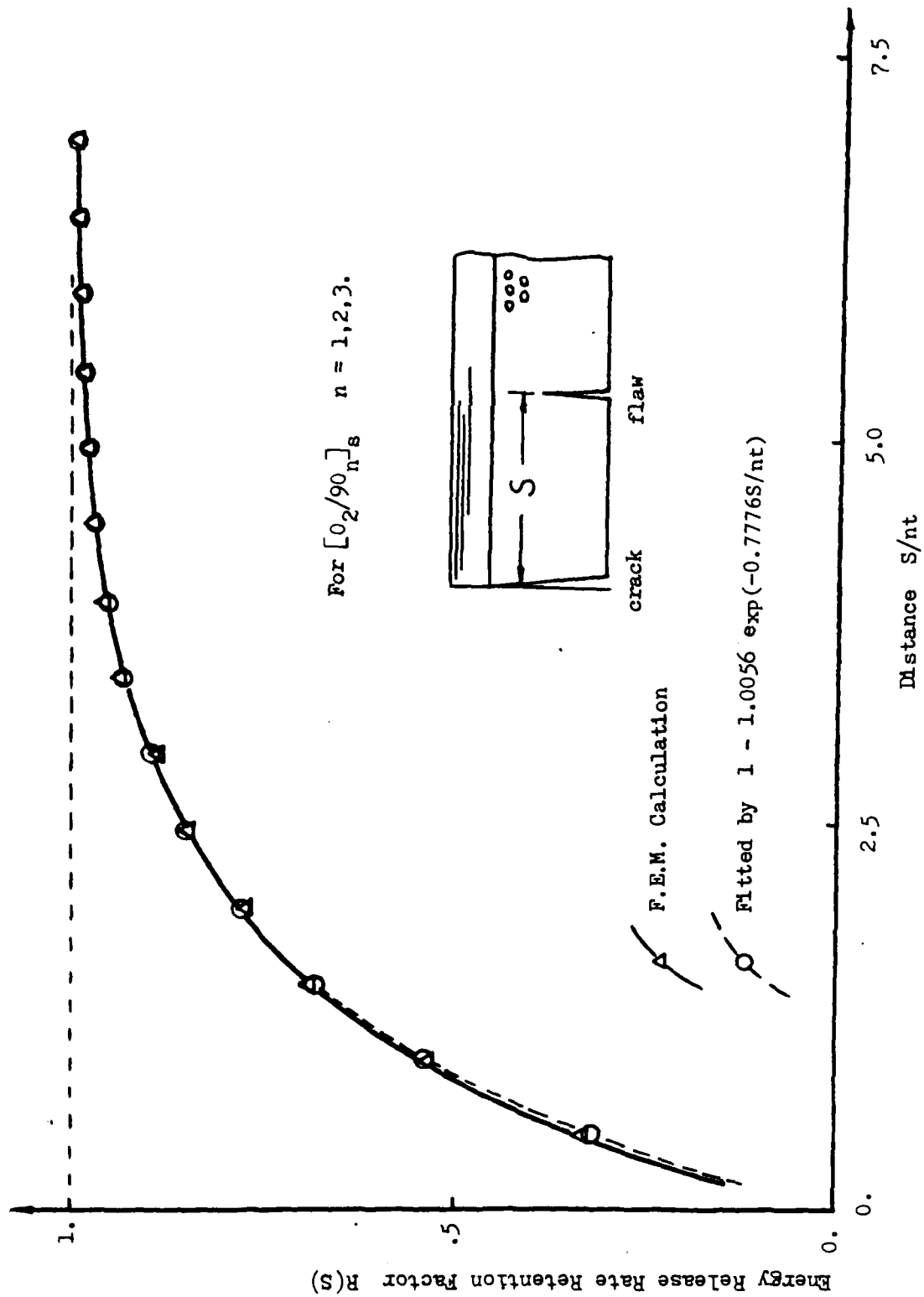


Figure A-3 Energy Release Rate Retention Factor $R(S)$ As A fu nction of Normalized Distance S/nt .

APPENDIX B. TRANSVERSE CRACKING - STATIC LOADING

The basic material used in the experiment was AS-3501-06. But, the test specimens used in Phase-I were fabricated (autoclave curing) at NADC (Warminster, PA); while the test specimens used in Phase-II were fabricated at the University of Delaware. The basic material data between the two batches of specimens exhibited a slight difference, but enough to indicate that they must be treated as two different material systems in our modelling correlation.

For the transverse cracking simulation, two sets of elastic moduli were used. These are summarized in a comparative table in Appendix H. For mode-I cracking, the critical energy release rate G_c was set at $G_c = 1.3 \text{ lb/in}$ (228 J/m^2) for both batches of specimens. The effective flaw size distribution $f(a)$ for batch 1 and batch 2 were both assumed in the form of normal distribution. But their individual mean and standard deviation were slightly different:

<u>Batch 1:</u>	$\mu_a = 0.0032''$ (0.08 mm)
	$\sigma_a = 0.0008''$ (0.02 mm)
<u>Batch 2:</u>	$\mu_a = 0.0026''$ (0.007 mm)
	$\sigma_a = 0.00042''$ (0.011 mm)

The experimental data for transverse crack growth under static loading of batch 1 specimens are shown in Figures B-1 and B-2 for, respectively, $[0_2/90_2]_s$ and $[0_2/90_3]_s$ laminates. The Monte-Carlo simulations for these two laminates are shown in Figures B-3 and B-4, respectively.

The experimental data for transverse crack growth under static loading of batch 2 specimens are shown in Figures B-5 and B-6 for, respectively, $[0_2/90_2]_s$ and $[0_2/90_3]_s$ laminates. The corresponding Monte-Carlo simulations are depicted in Figures B-7 and B-8.

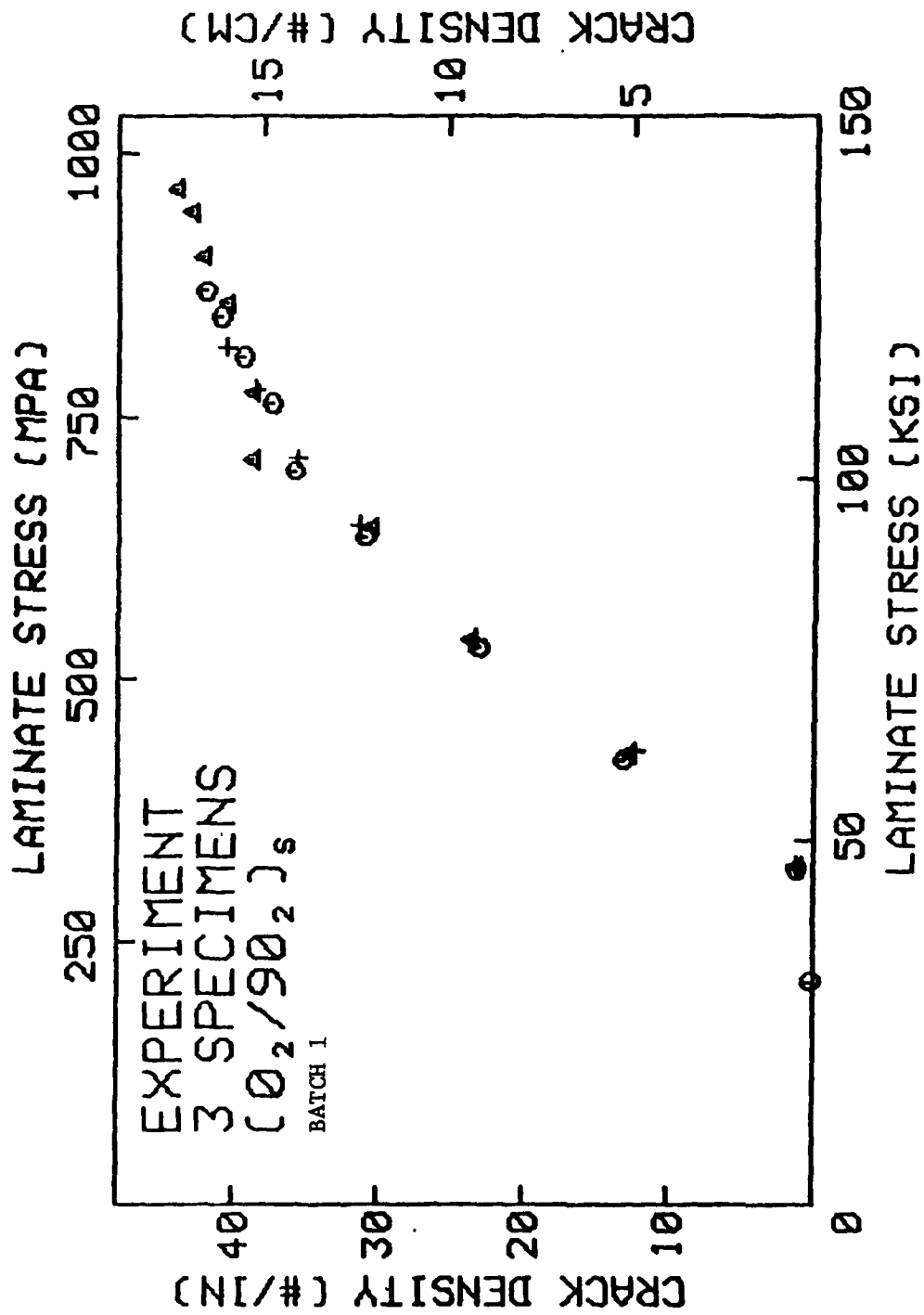


Figure B-1 Experimental Transverse Crack Density Versus Applied Laminated Stress σ_x , [0₂/90₂]_s

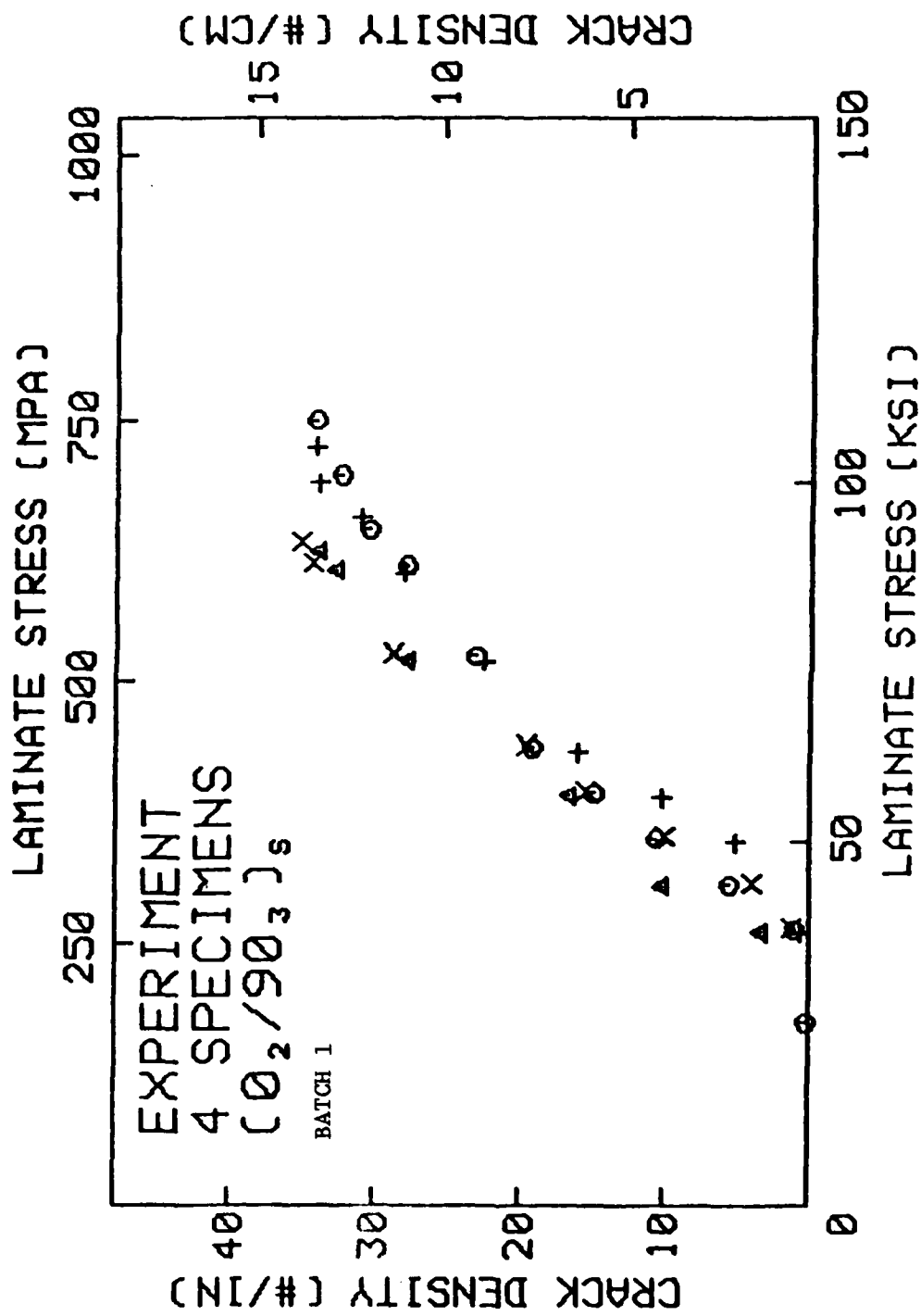


Figure B-2 Experimental Transverse Crack Density Versus Applied Laminate Stress $\bar{\sigma}_x$, [0₂/90₃]_s

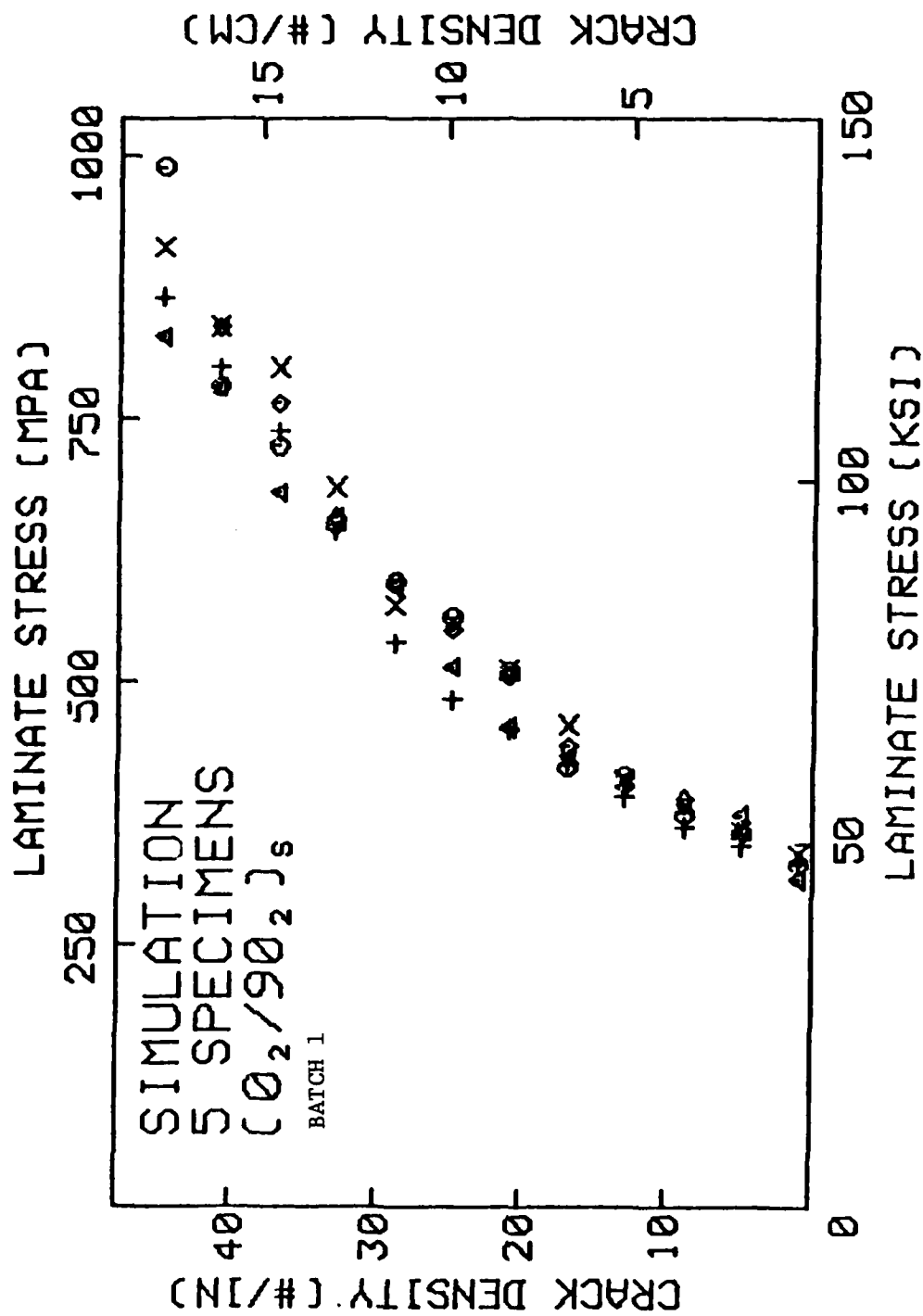


Figure B-3 Simulated Transverse Crack Density Versus Applied Laminate Stress $\bar{\sigma}_x$. [$0_2/90_2$]_s

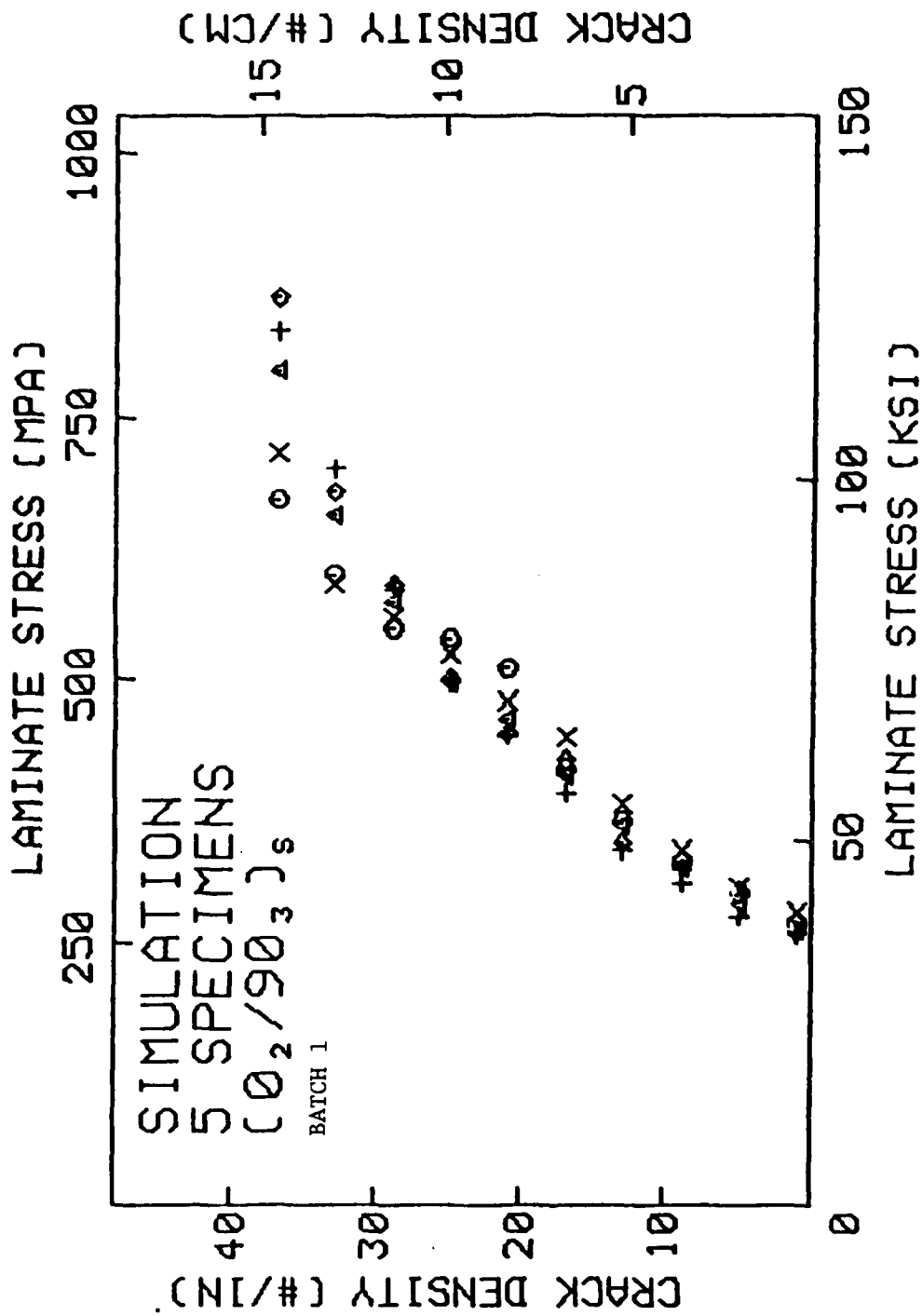


Figure B-4 Simulated Transverse Crack Density Versus Applied Laminate Stress σ_x . [0₂/90₃]_s

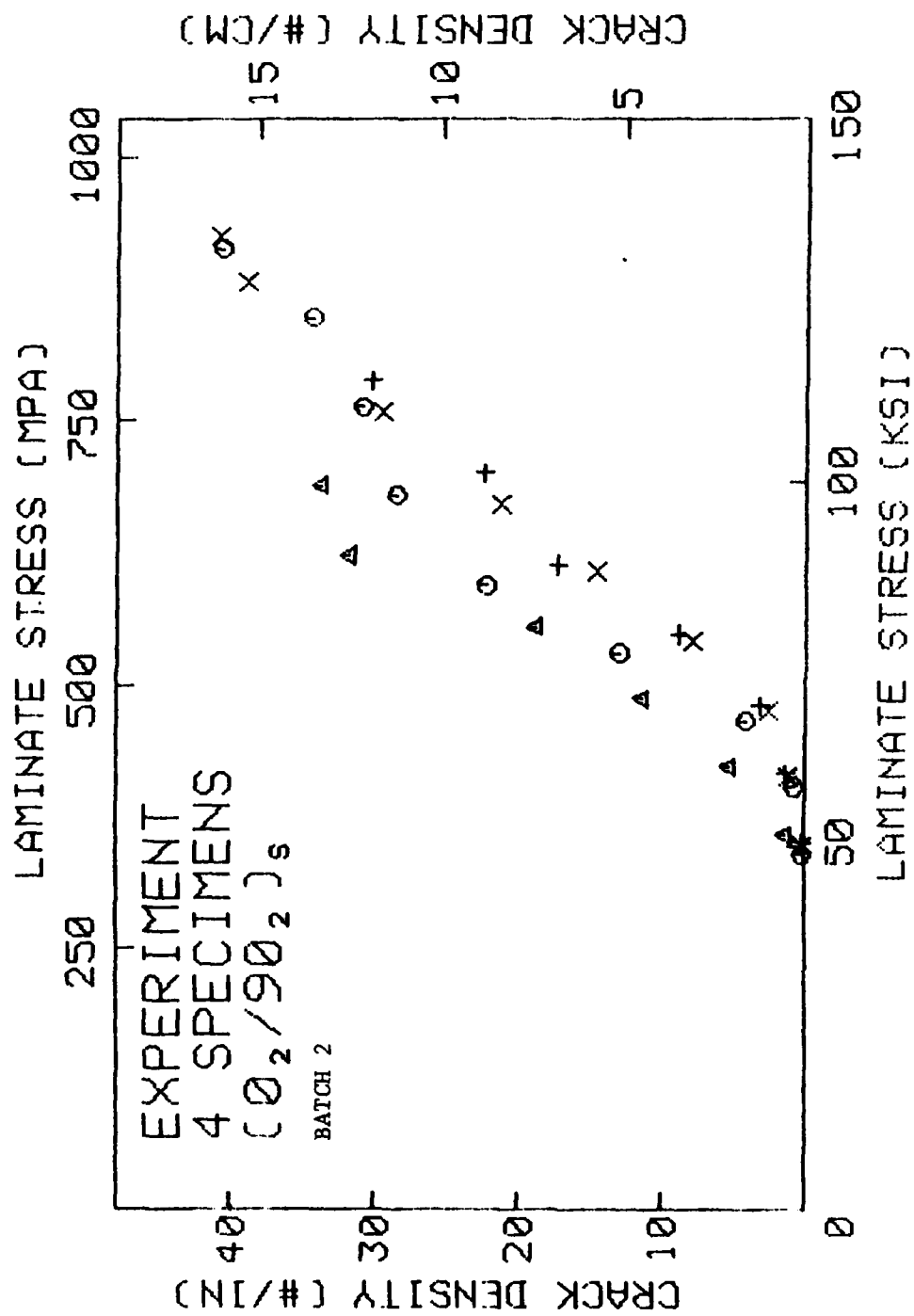


Figure 3-5 Experimental Transverse Crack Density Versus Applied Laminate Stress σ_x for [0₂/90₂]_s Laminates.

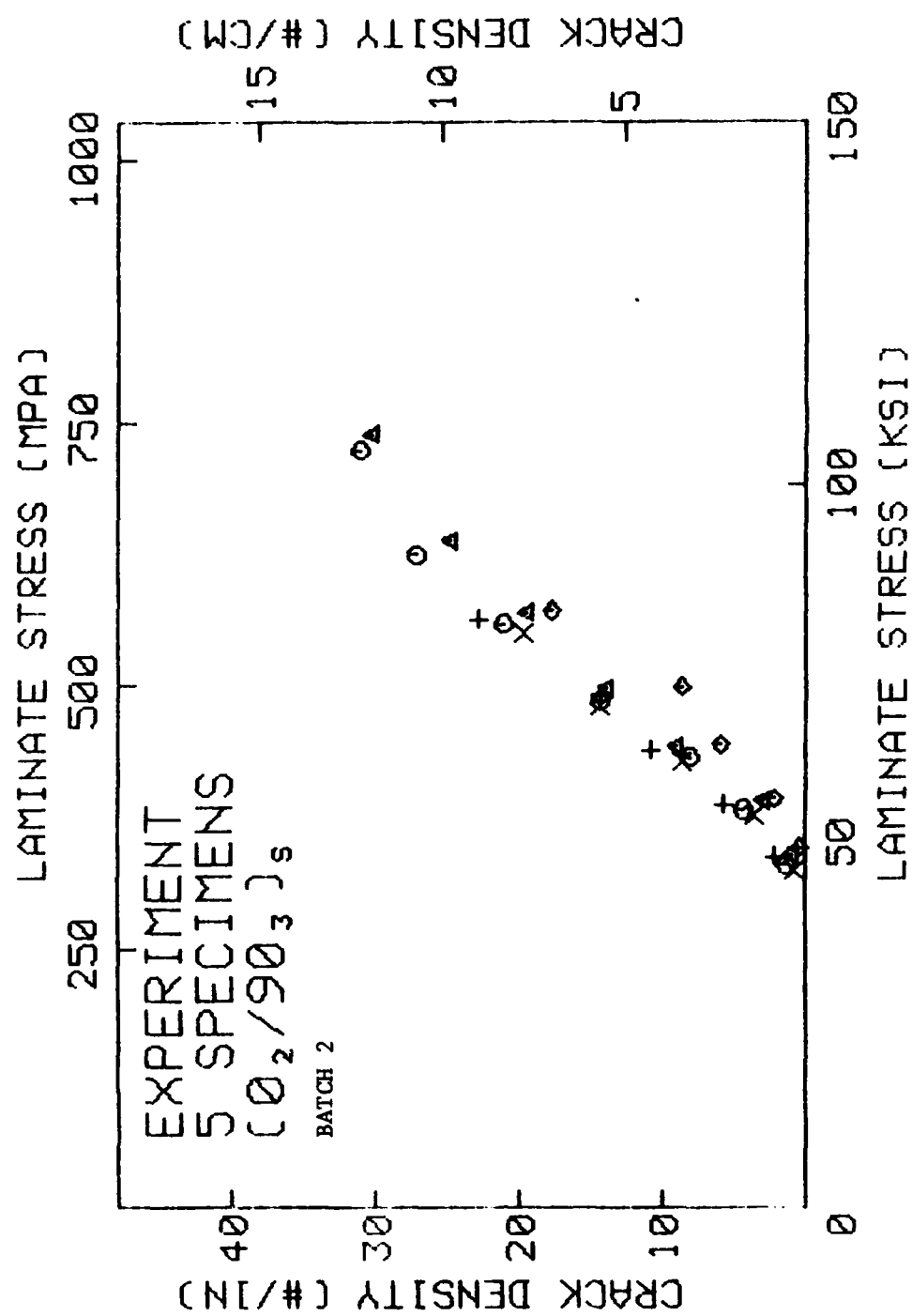


Figure B-6 Experimental Transverse Crack Density Versus Applied Laminate Stress σ_x for [0₂/90₃]_s Laminates.

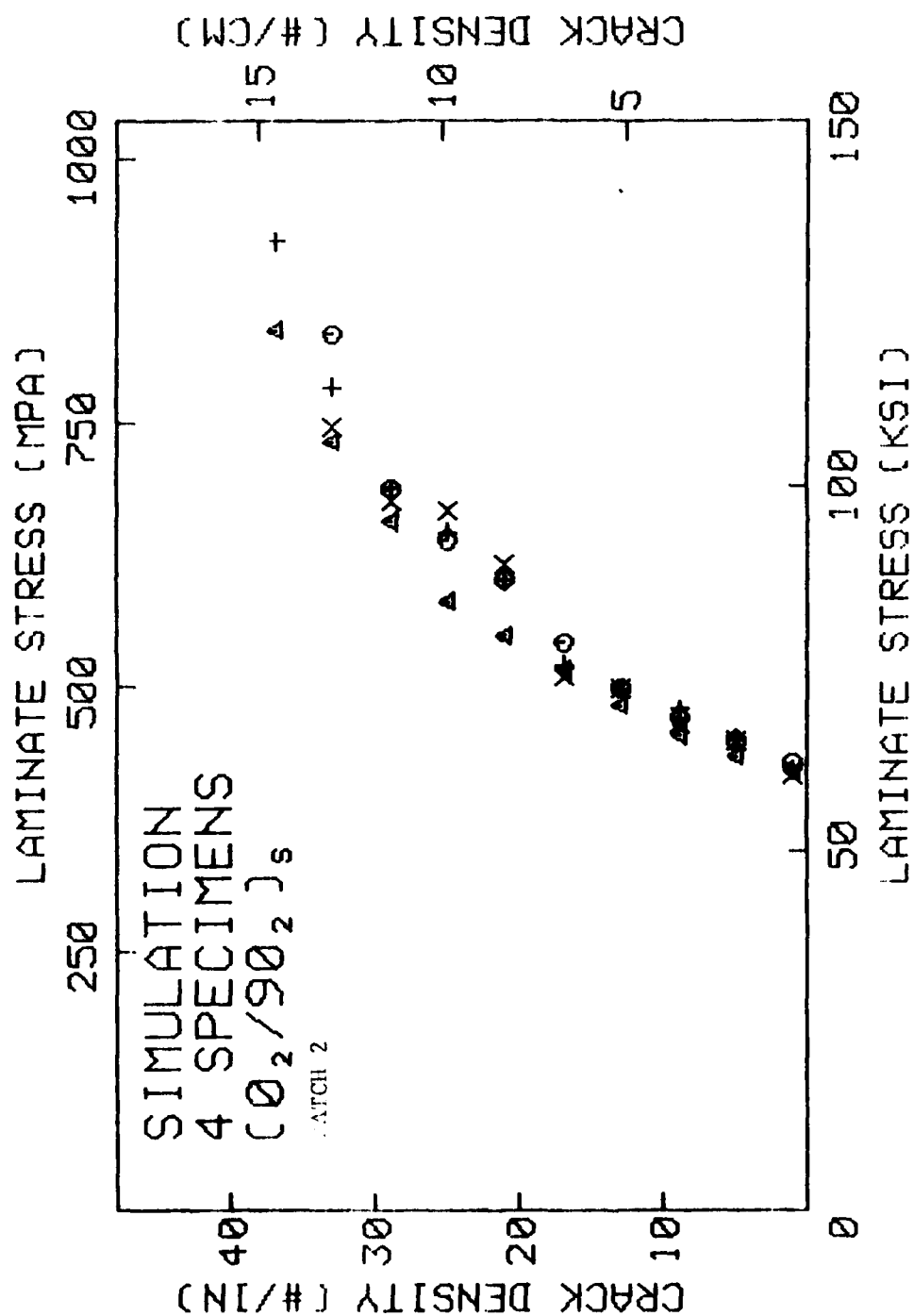


Figure B-7 Simulated Transverse Crack Density Versus Applied Laminate Stress σ_x for $[0_2/90_2]_s$ Laminates.

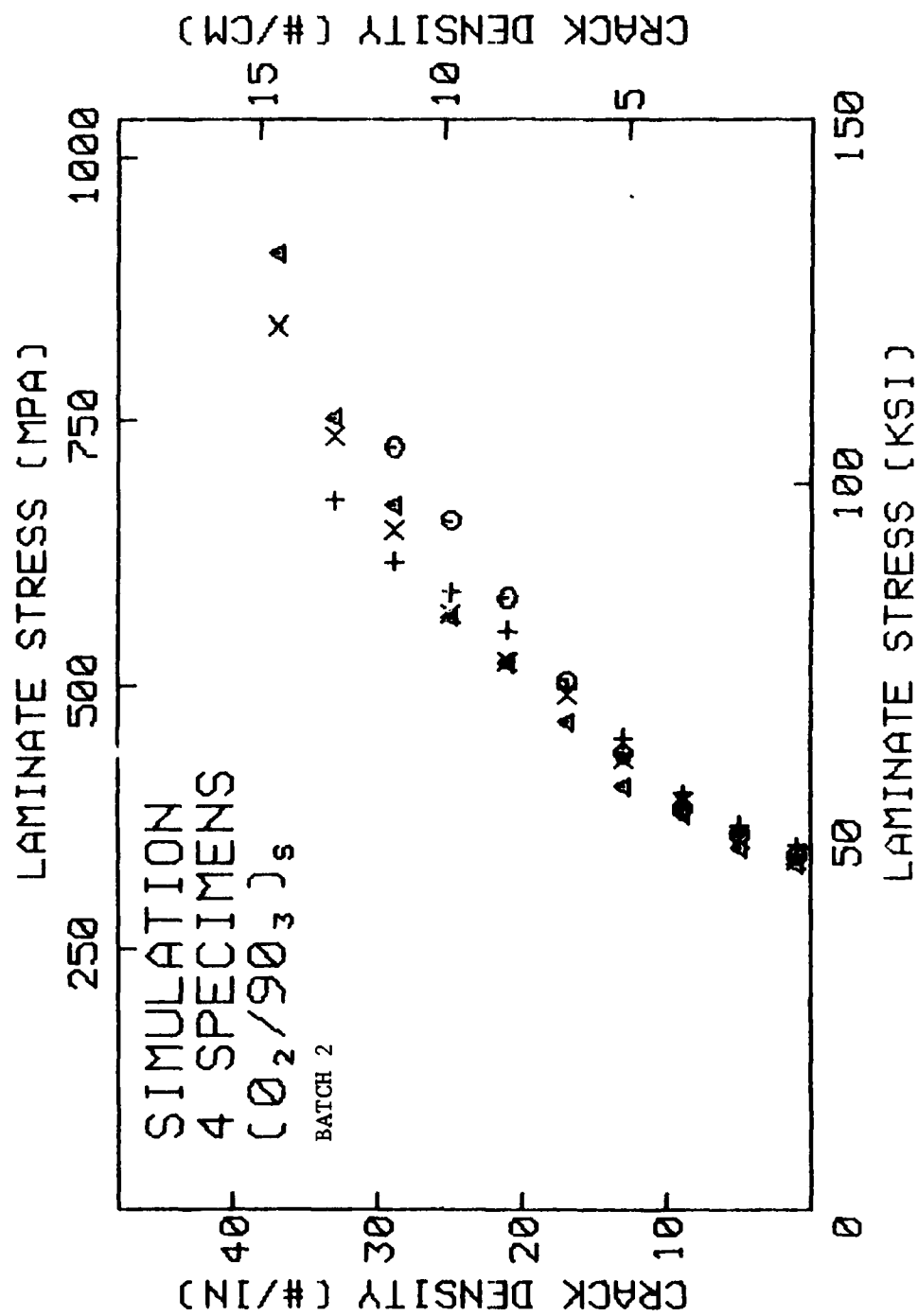


Figure B-8 Simulated Transverse Crack Density Versus Applied Laminate Stress σ_x for [0₂/90₃]_s Laminates.

APPENDIX C. TRANSVERSE CRACKING - FATIGUE LOADING

In Phase-I, transverse cracking under constant amplitude fatigue loading was studied for $[0_2/90_2]_s$ and $[0_2/90_3]_s$ laminates. Experiments were performed under amplitudes $\sigma_f = 26$ ksi (179 mpa), 30 ksi (207 mpa), and 38 ksi (262 mpa) for $[0_2/90_3]_s$; and under amplitudes $\sigma_f = 38$ ksi (262 mpa), 43 ksi (297 mpa), and 55 ksi (365 mpa) for $[0_2/90_2]_s$. The experimental data are shown graphically in Figure C-1 for $[0_2/90_2]_s$ and Figure C-2 for $[0_2/90_3]_s$.

Simulation results using the batch 1 material constants and the crack growth equation

$$\frac{da}{dN} = \bar{\alpha} \left[\frac{G(\sigma_f, a)}{G_c} \right] \bar{p} \quad (C-1)$$

with

$$\bar{\alpha} = 0.004t, \quad \bar{p} = 20 \quad (C-2)$$

are shown, respectively, in Figures C-3 and C-4.

In Phase-II, the same laminates were tested as in Phase-I, except that the batch 2 specimens were characterized with a set of different material properties as discussed earlier.

Experiments under constant amplitude fatigue loading were performed under $\sigma_f = 35$ ksi (241 mpa), 45 ksi (310 mpa), 60 ksi (413 mpa), 68 ksi (468 mpa), and 76 ksi (524 mpa) for $[0_2/90_2]_s$; and under 25 ksi (172 mpa), 35 ksi (241 mpa), 45 ksi (310 mpa), 50 ksi (345 mpa), and 55 ksi (379 mpa) for $[0_2/90_3]_s$.

Figures C-5 through C-8 show graphically the experimental data obtained for $[0_2/90_2]_s$. Note that data for $\sigma_f = 35$ ksi was not shown. The

reason is that no transverse cracks were found under this loading for up to one million cycles.

For the same reason, data for $\sigma_f = 25$ ksi and $\sigma_f = 35$ ksi in the $[0_2/90_3]_s$ tests were also not shown. Data obtained under the other three amplitudes are shown in Figures C-9 through C-11.

Fatigue simulations of the cases shown in Figures C-5 through C-11 were conducted using the material constants obtained for the batch 2 specimens. The fatigue crack growth equation remained as in Equation C-1; and the constants $\bar{\alpha}$, \bar{p} also remained as in Equation C-2.

The corresponding simulated results are shown in Figures C-12 through C-18.

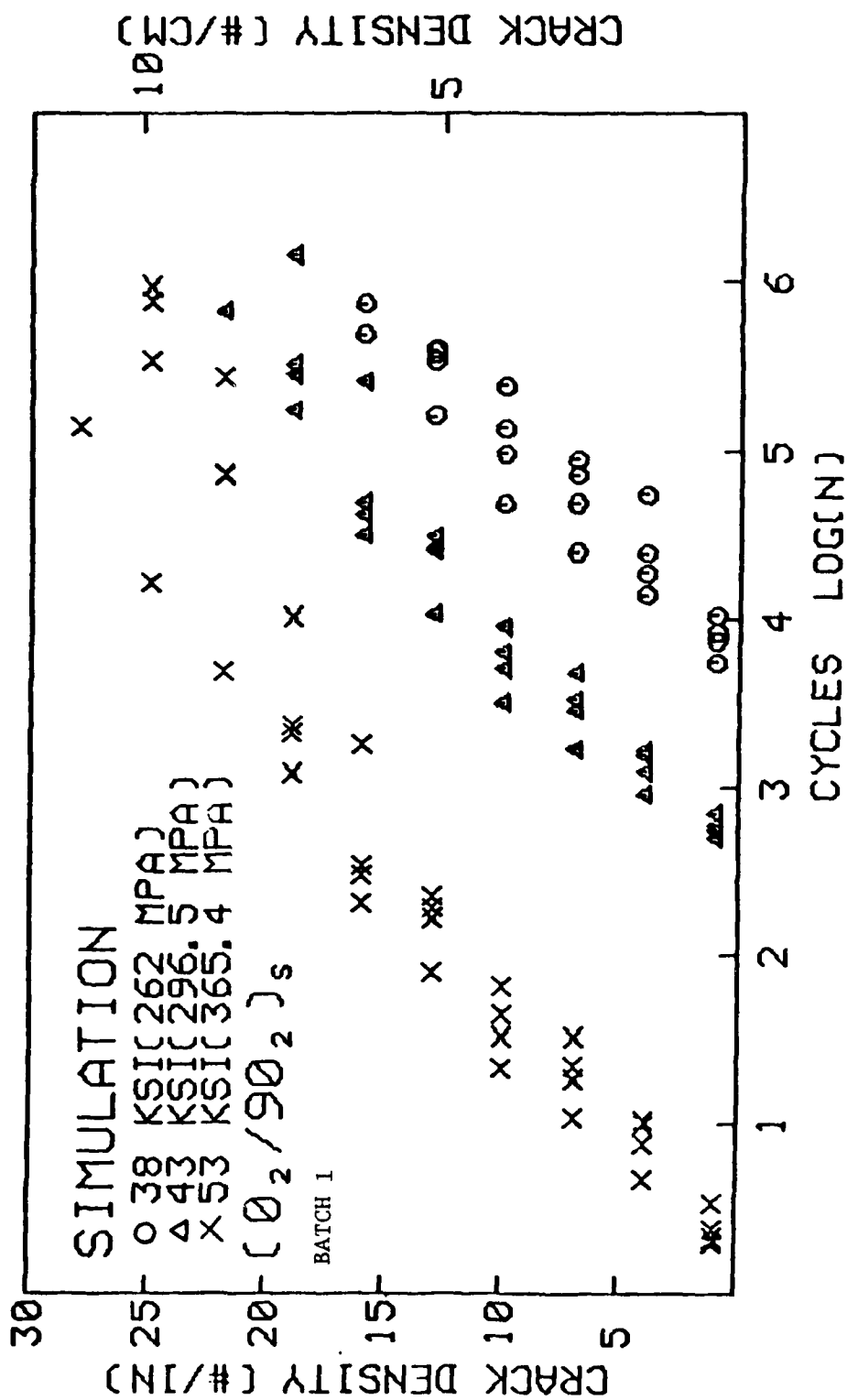


Figure C-1 Simulated Transverse Crack Density Versus Fatigue Cycle N. $[O_2/90_2]_s$

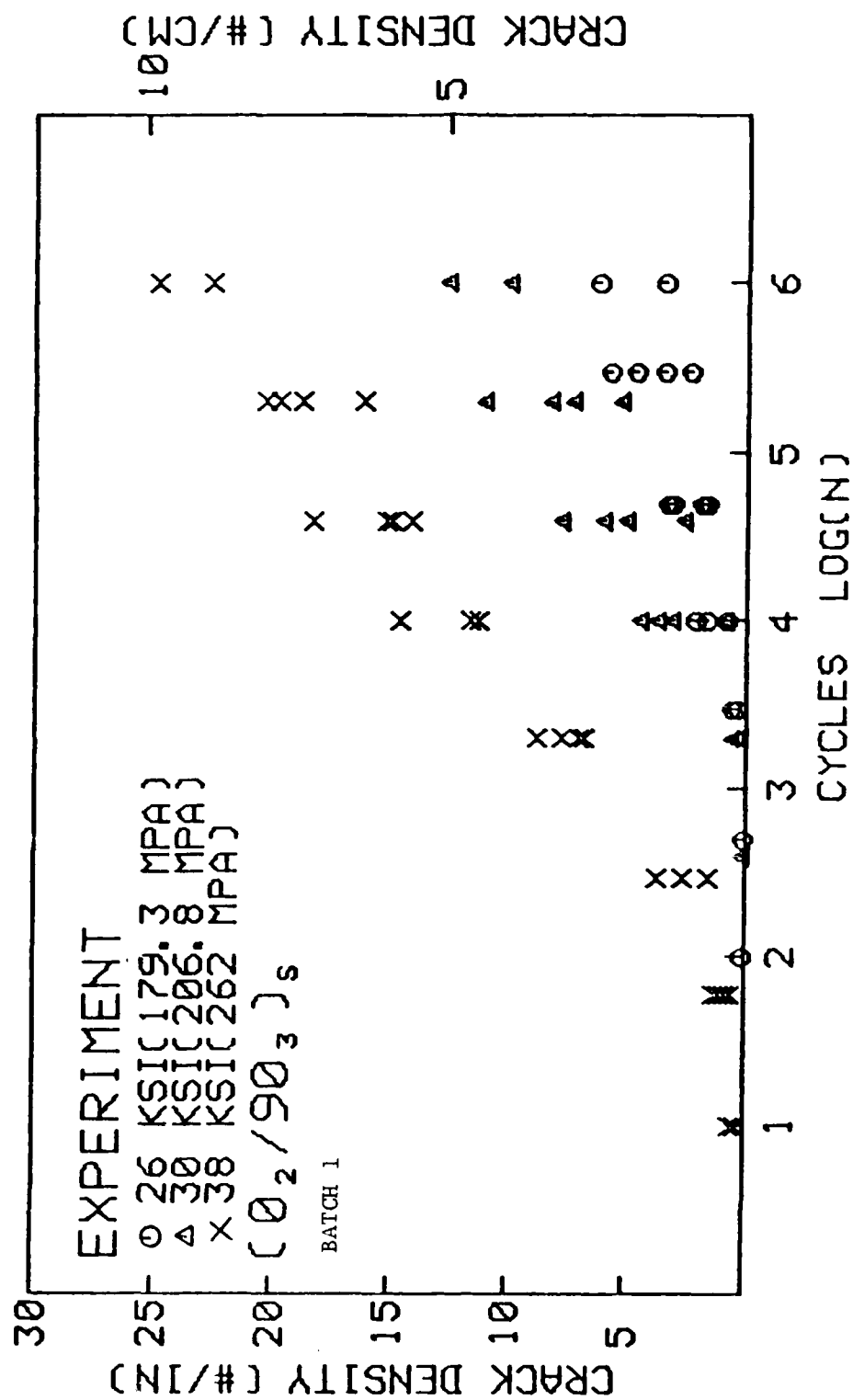


Figure C-2 Experimental Transverse Crack Density Versus Fatigue Cycle N. $[O_2/90_3]_s$

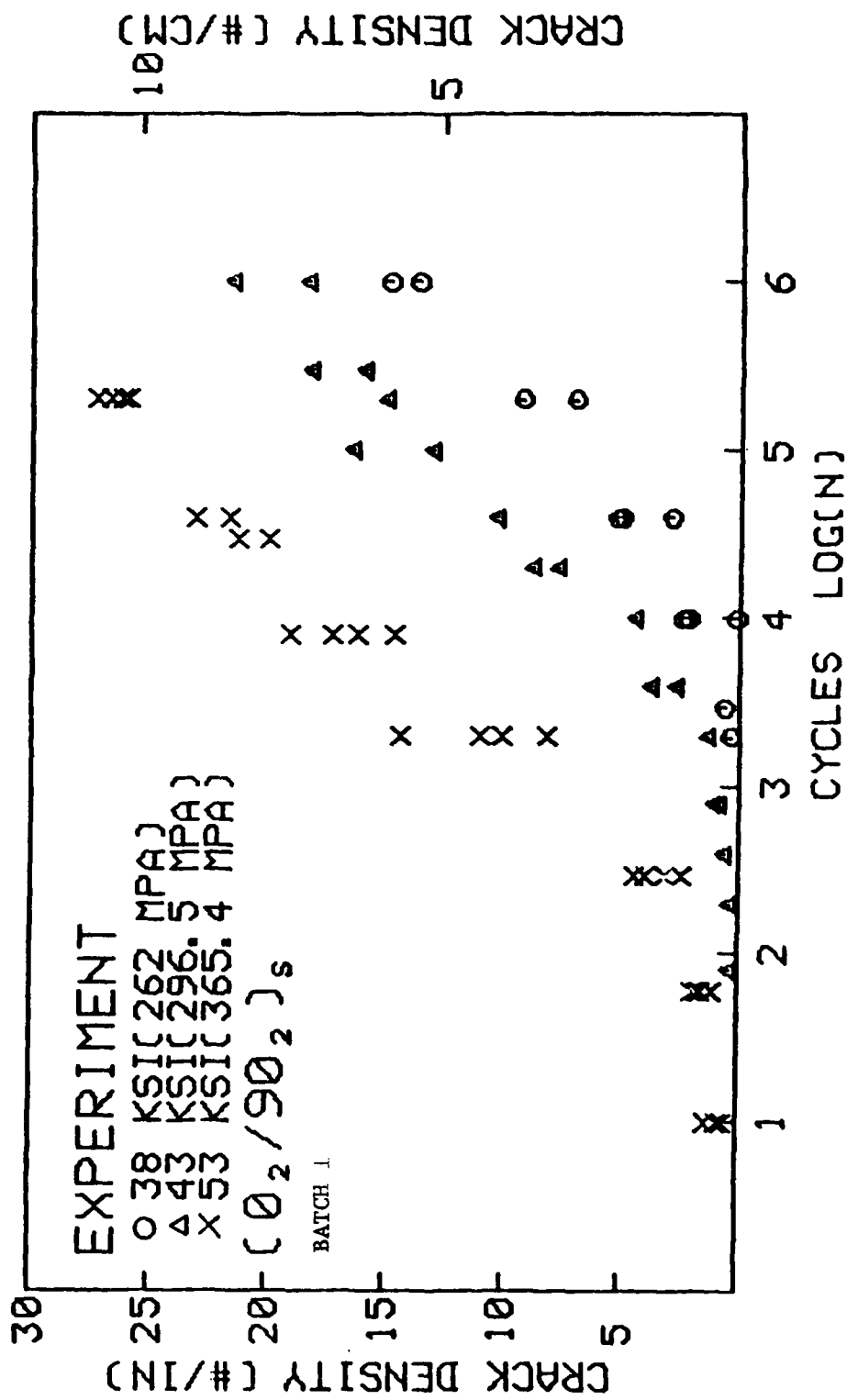


Figure C-3 Experimental Transverse Crack Density Versus Fatigue Cycle N. $[O_2/90_2]_s$

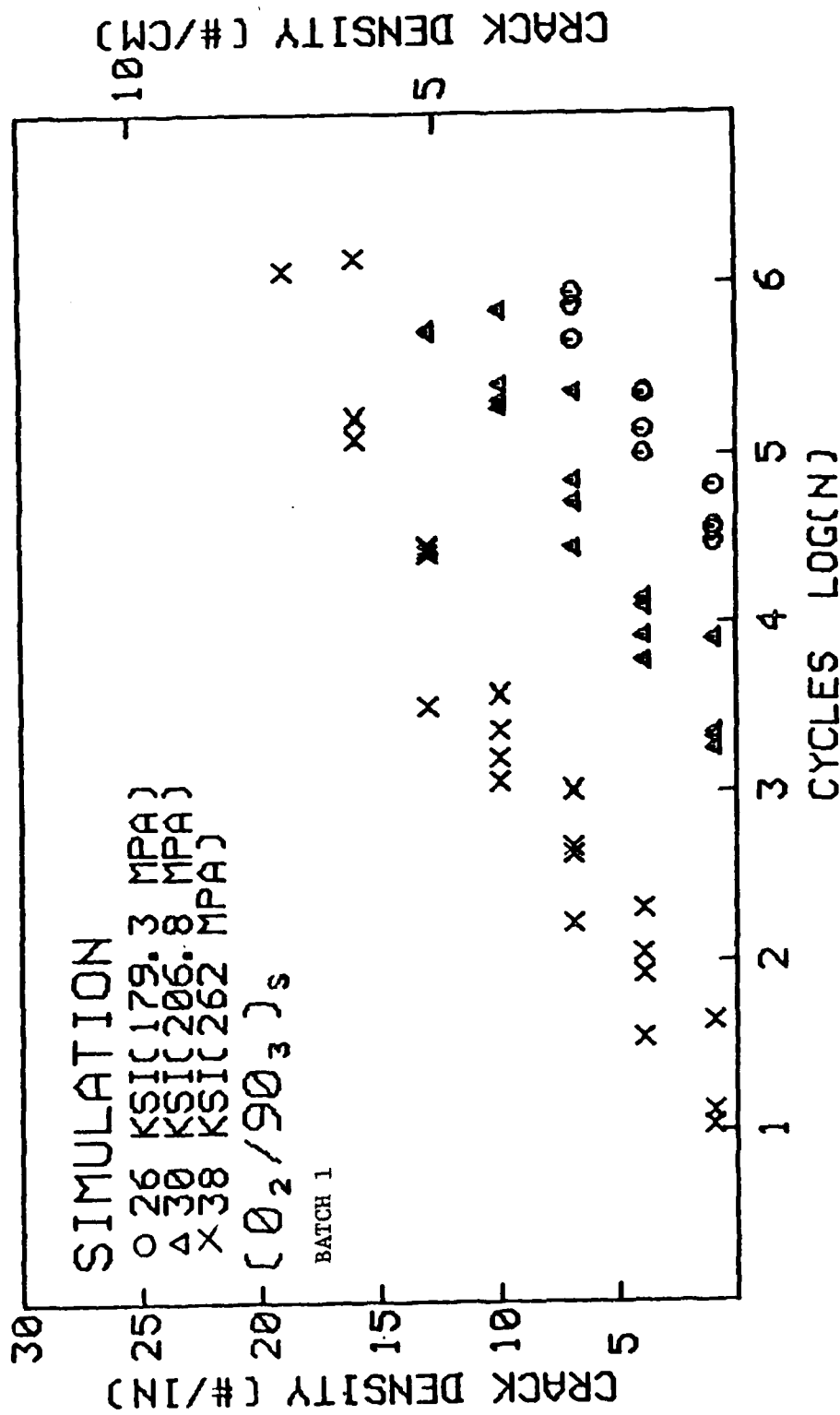


Figure C-4 Simulated Transverse Crack Density Versus Fatigue Cycle N. [0₂/90₃]_s

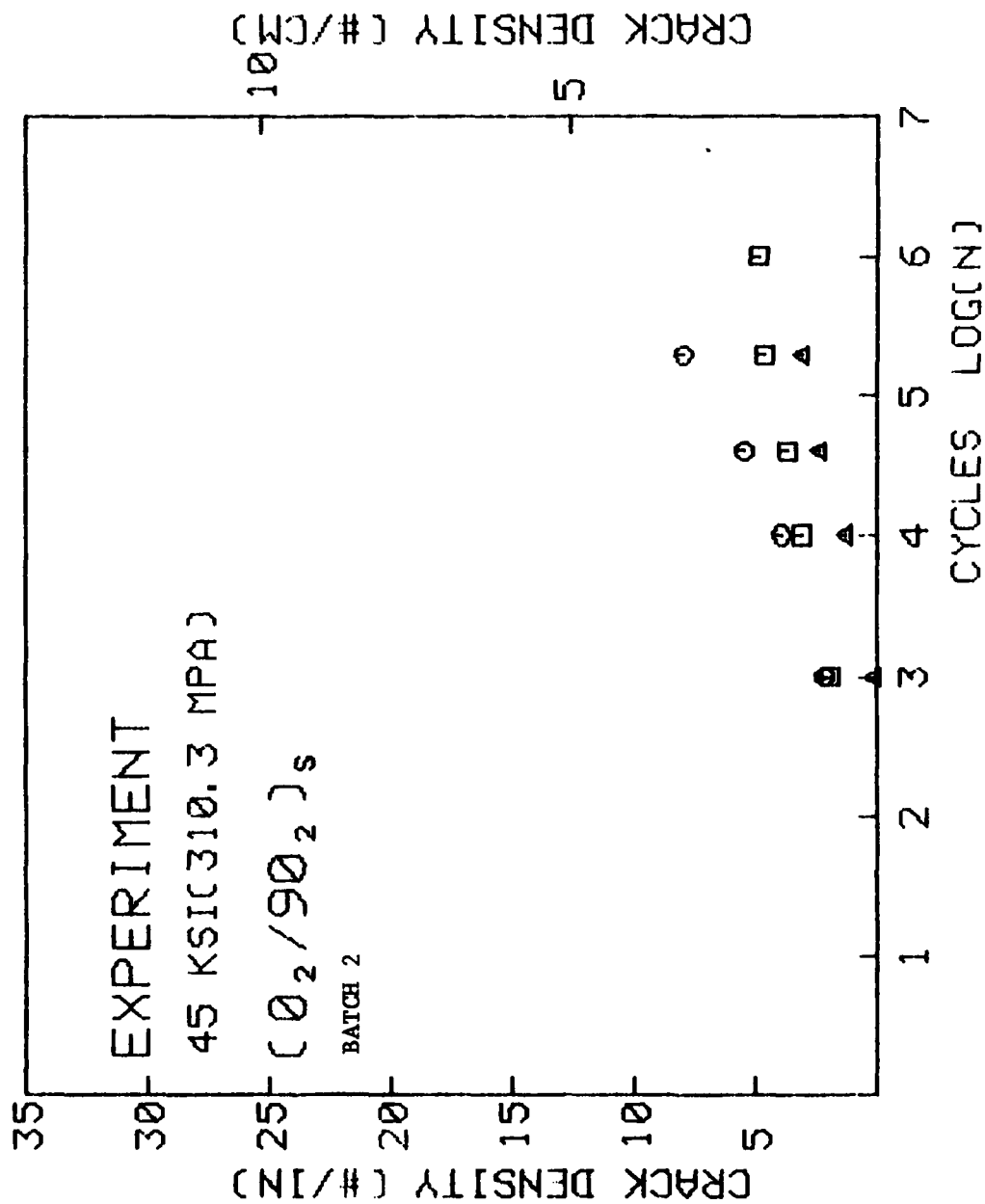


Figure C-5 Experimental Transverse Crack Density Versus Fatigue Cycles N for [0₂/90₂]_s Laminates. Maximum Stress of $\sigma_x = 45$ KSI.

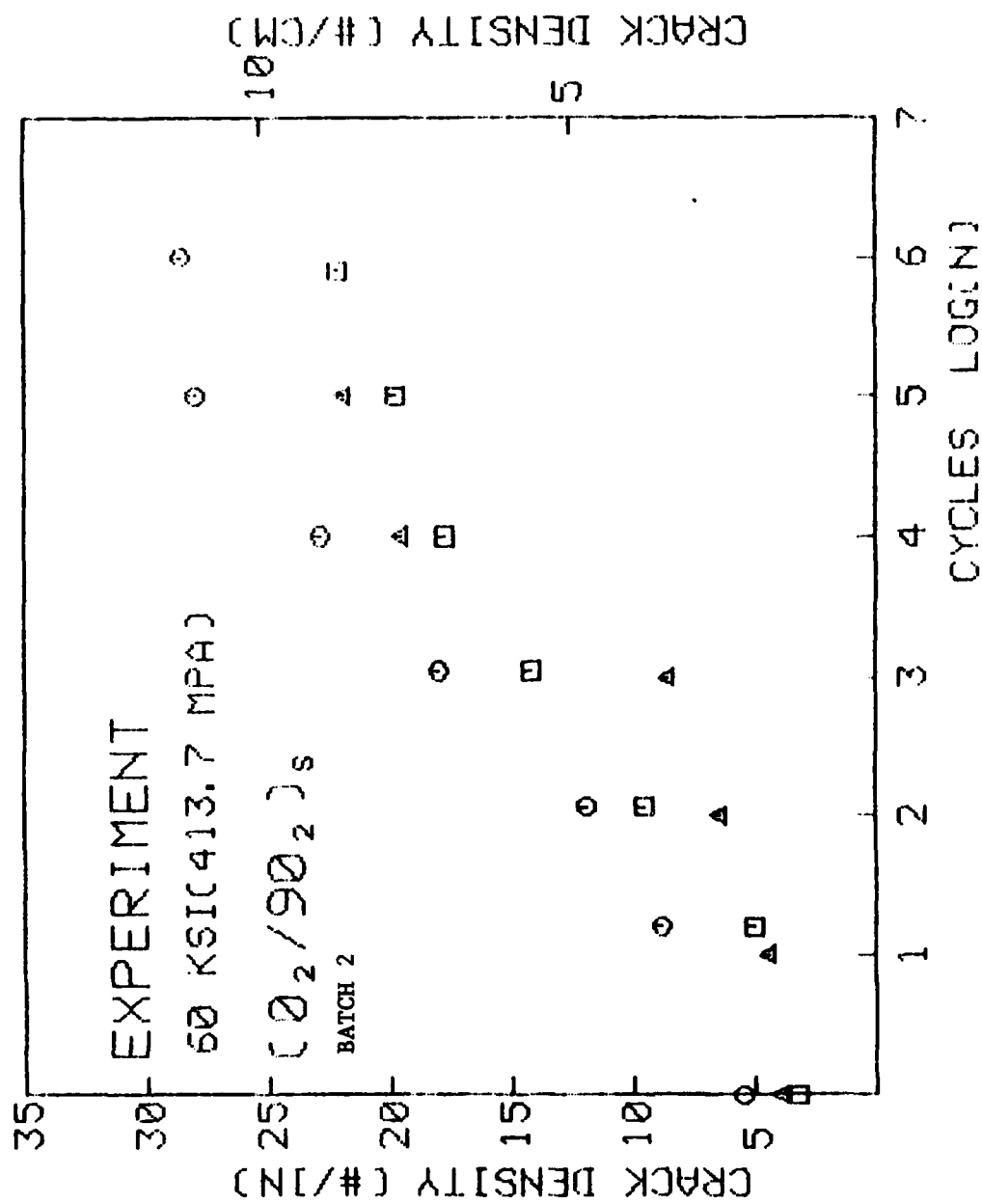


Figure C-6 Experimental Transverse Crack Density Versus Fatigue Cycles N for [0₂/90₂]_s Laminates. Maximum Stress of $\sigma_x = 60$ KSI.

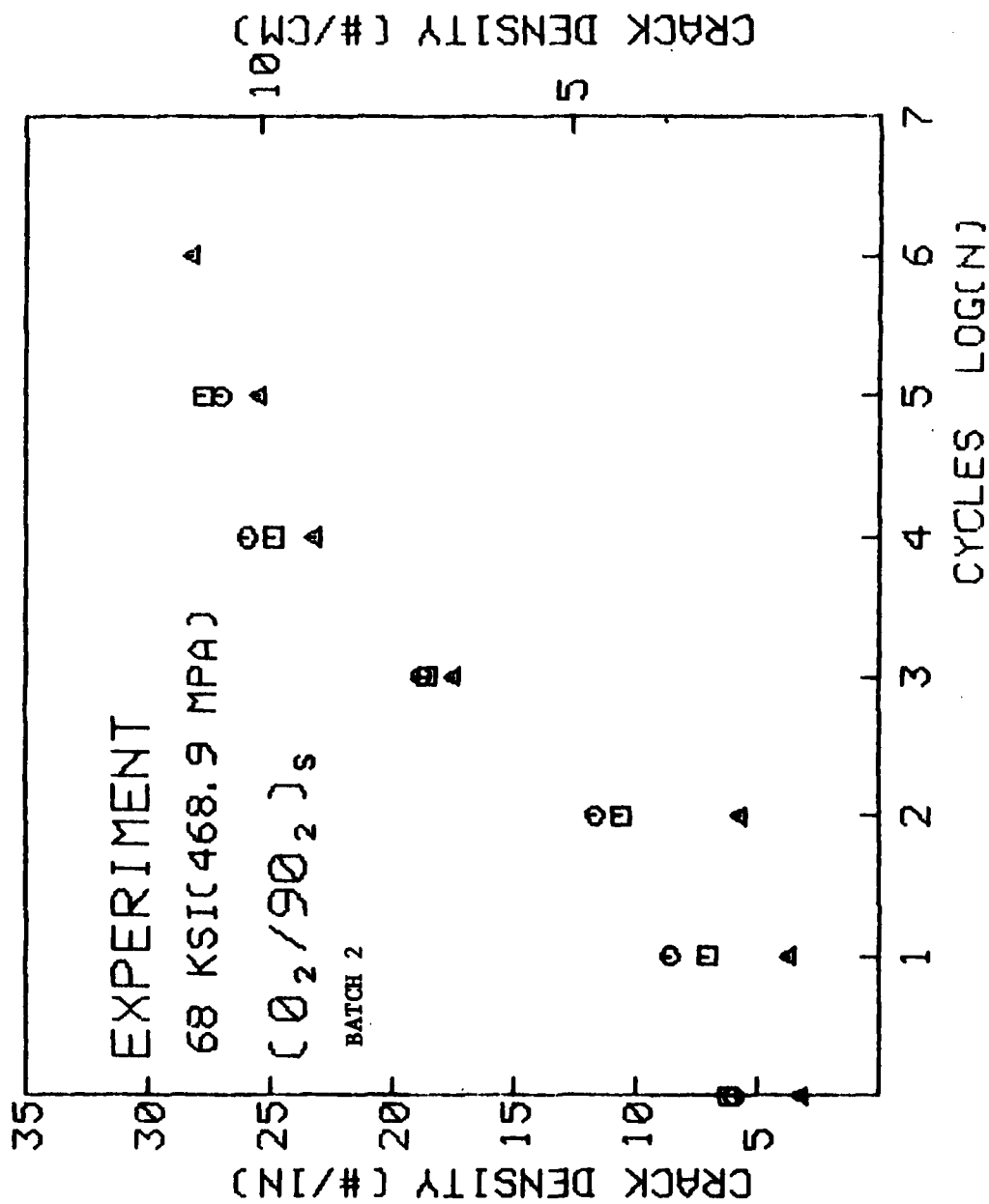


Figure C-7 Experimental Transverse Crack Density Versus Fatigue Cycles N for [0₂/90₂]_s Laminates. Maximum Stress of $\sigma_x = 68$ KSI.

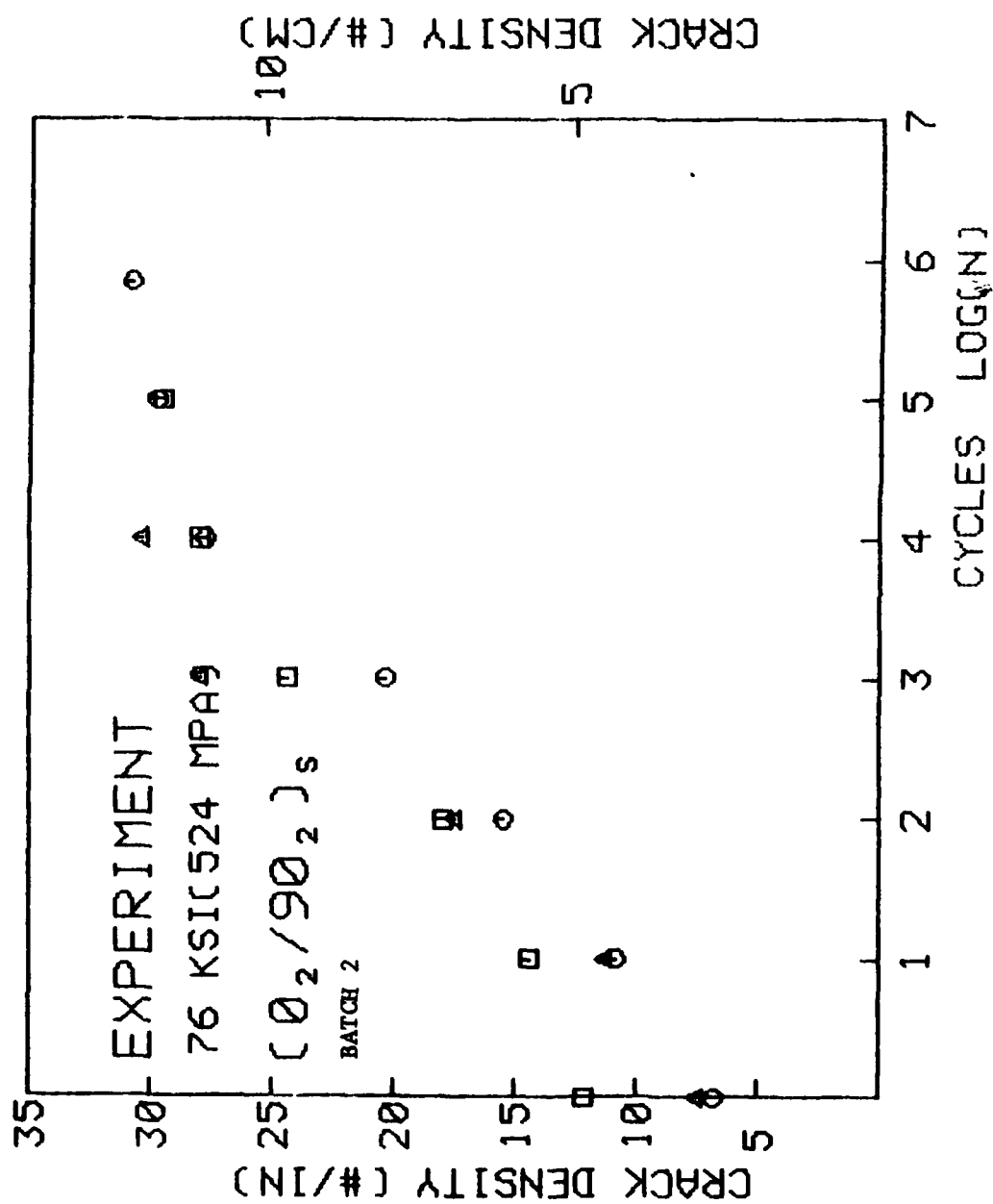


Figure C-8 Experimental Transverse Crack Density Versus Fatigue Cycles N for [0₂/90₂]_s Laminates. Maximum Stress of $\sigma_x = 76$ KSI.

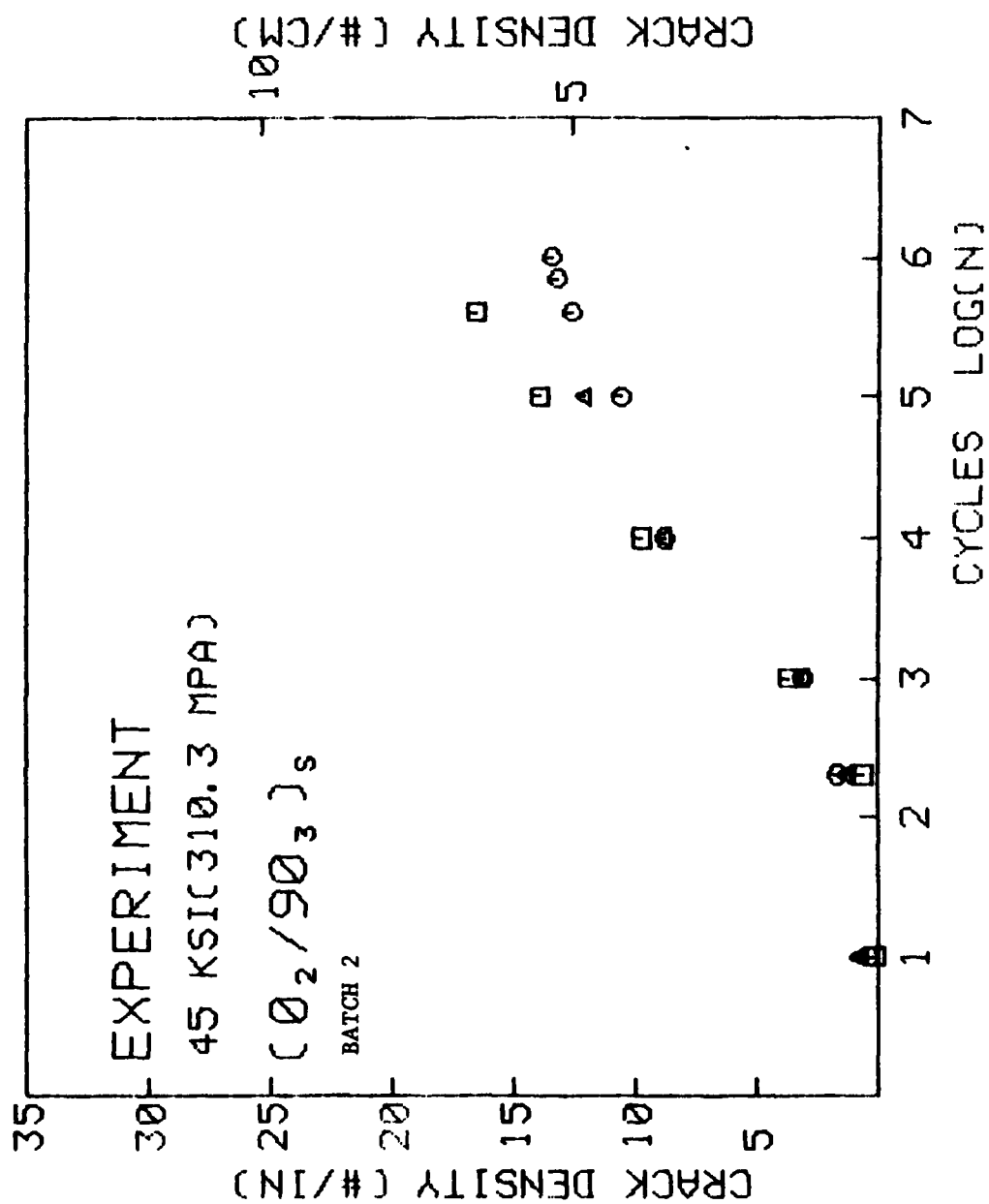


Figure C-9 Experimental Transverse Crack Density Versus Fatigue Cycles N for [0₂/90₃]_s Laminates. Maximum Stress of $\sigma_x = 45$ KSI.

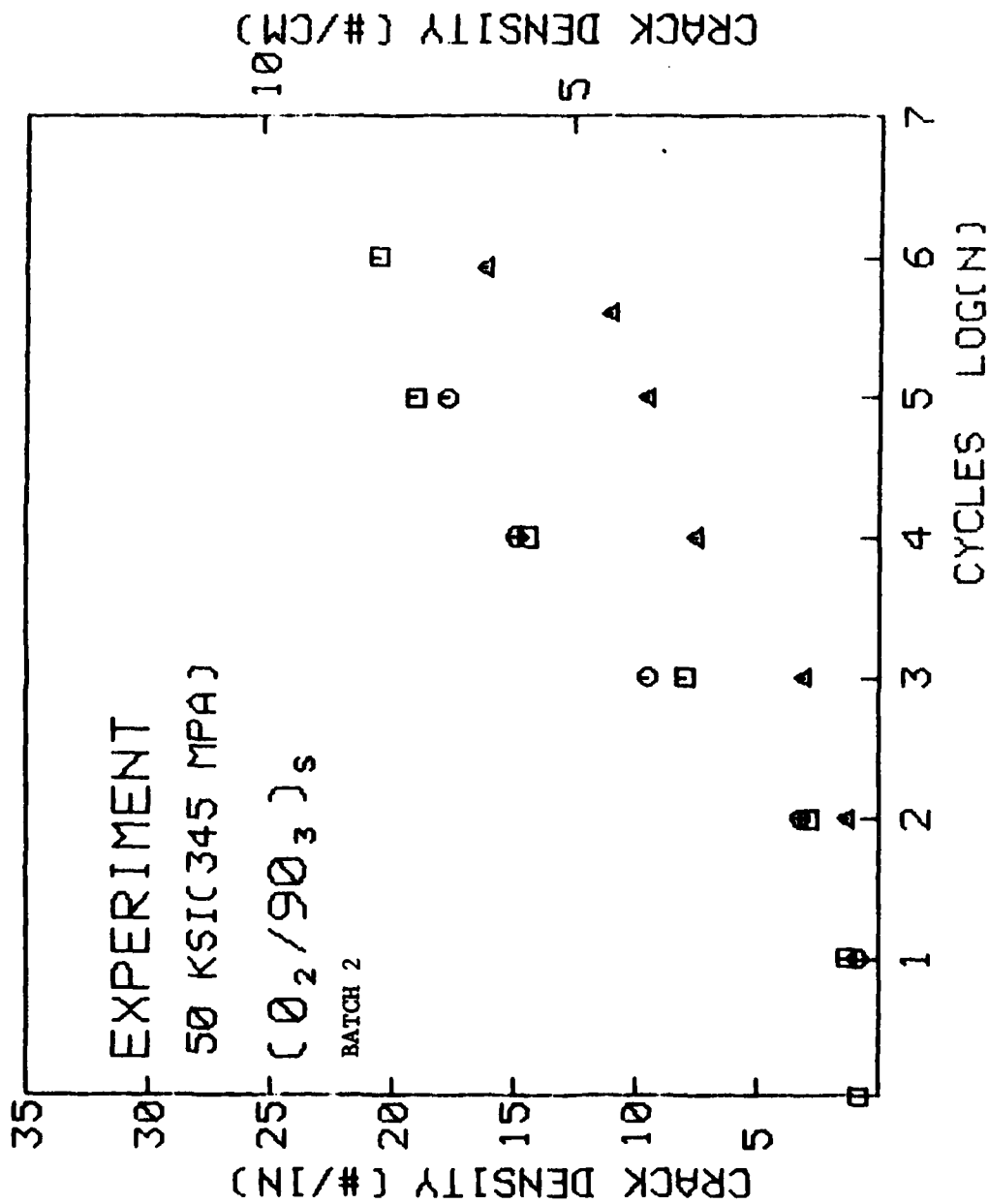


Figure C-10 Experimental Transverse Crack Density Versus Fatigue Cycles N for [0₂/90₃]_s Laminates. Maximum Stress of $\sigma_x = 50$ KSI.

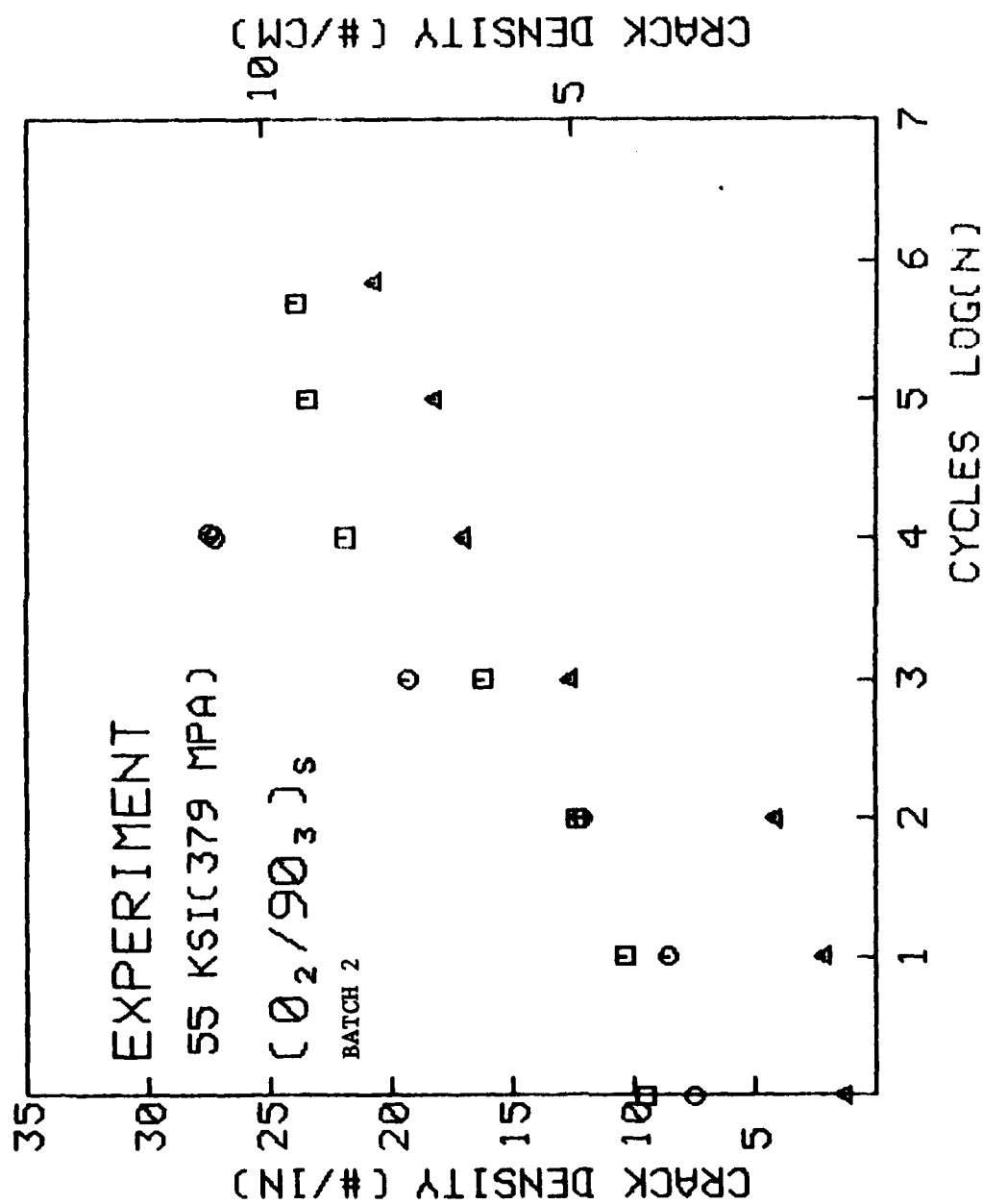


Figure C-11 Experimental Transverse Crack Density Versus Fatigue Cycles N for [0₂/90₃]_s Laminates. Maximum Stress of $\sigma_x = 55$ KSI.

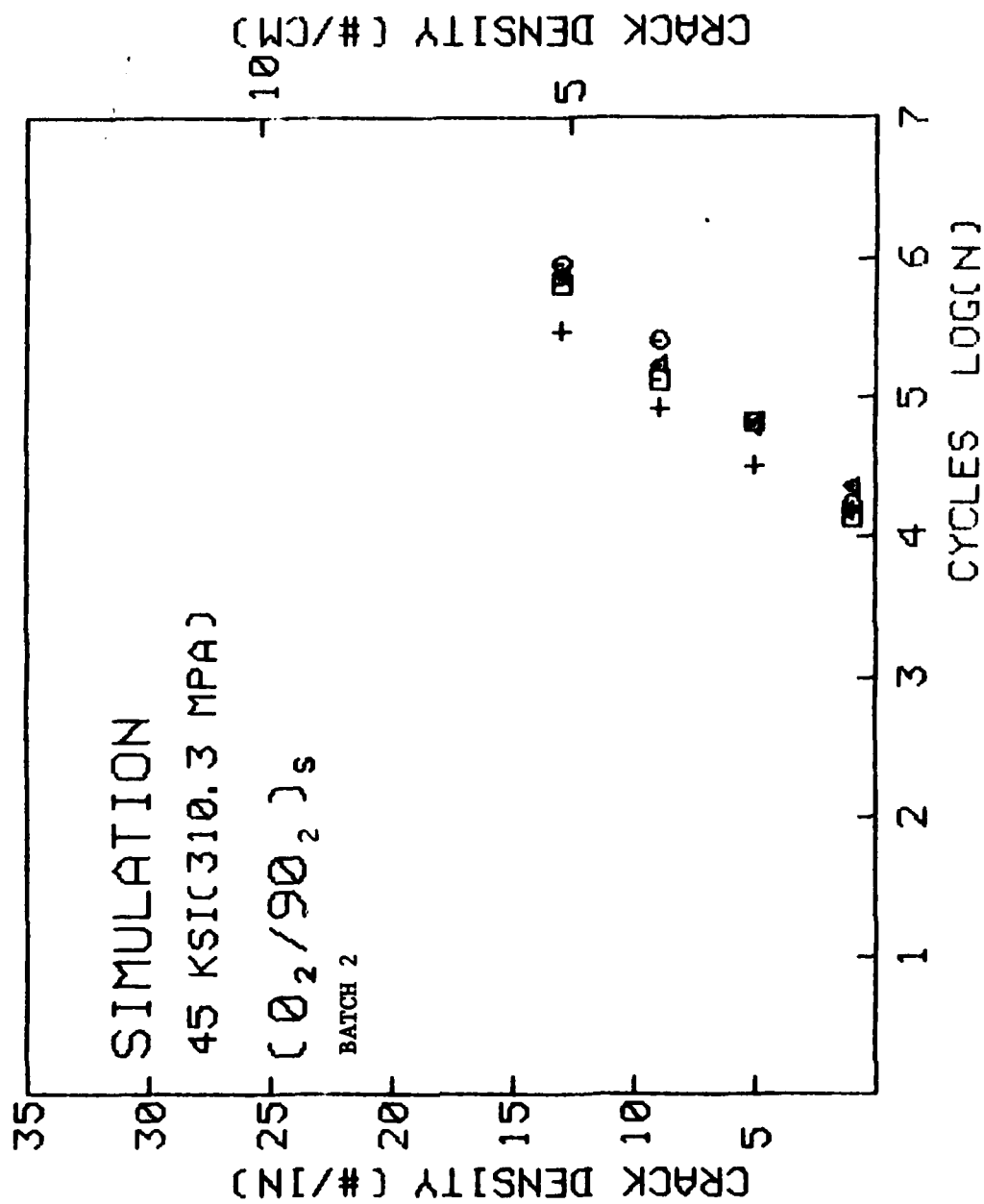


Figure C-12 Simulated Transverse Crack Density Versus Fatigue Cycles N for [0₂/90₂]_s Laminates. Maximum Stress of $\sigma_x = 45$ KSI.

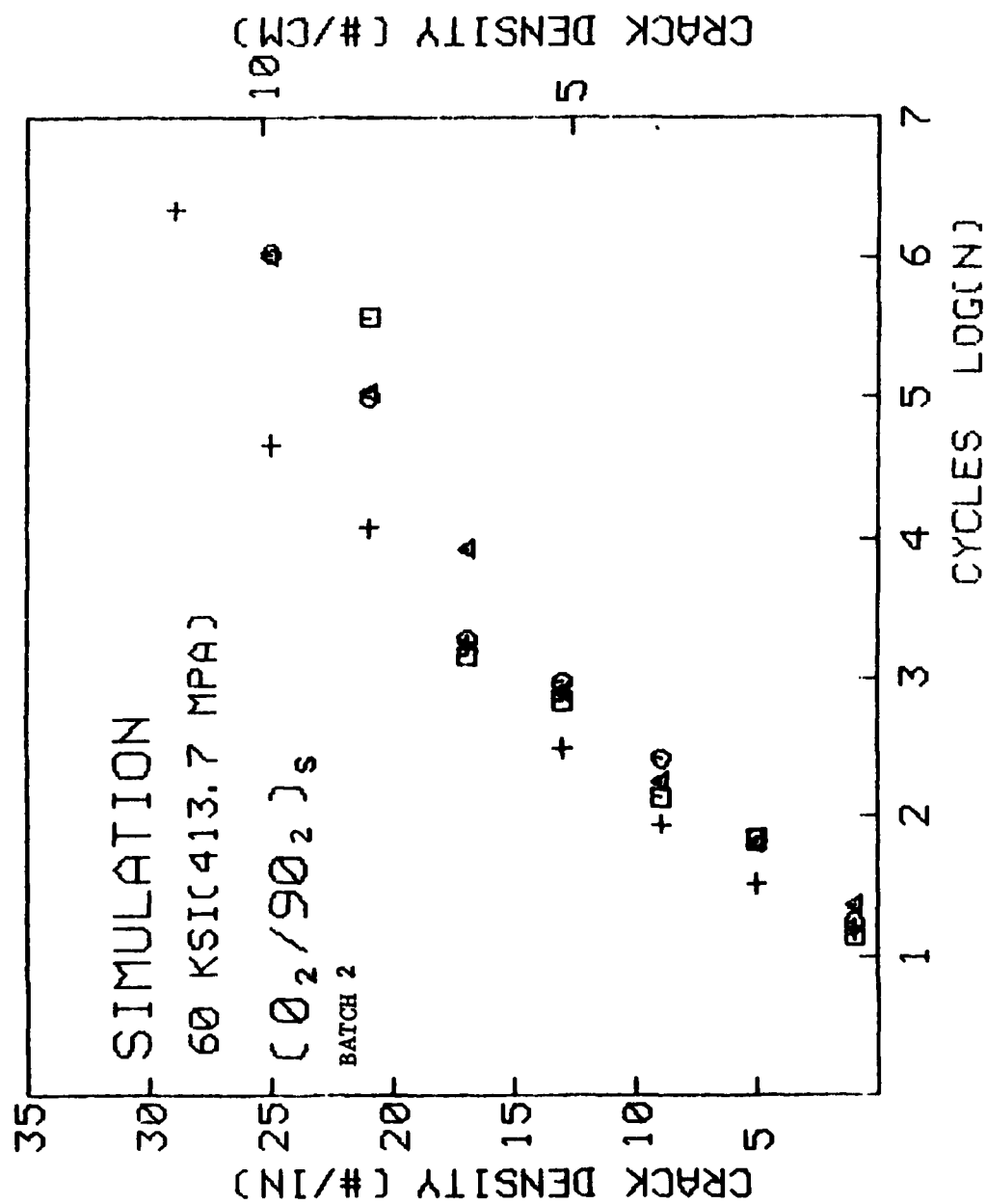


Figure C-13 Simulated Transverse Crack Density versus Fatigue Cycles N for $[0_2/90_2]_s$ Laminates. Maximum Stress of $\sigma_x = 60$ KSI.

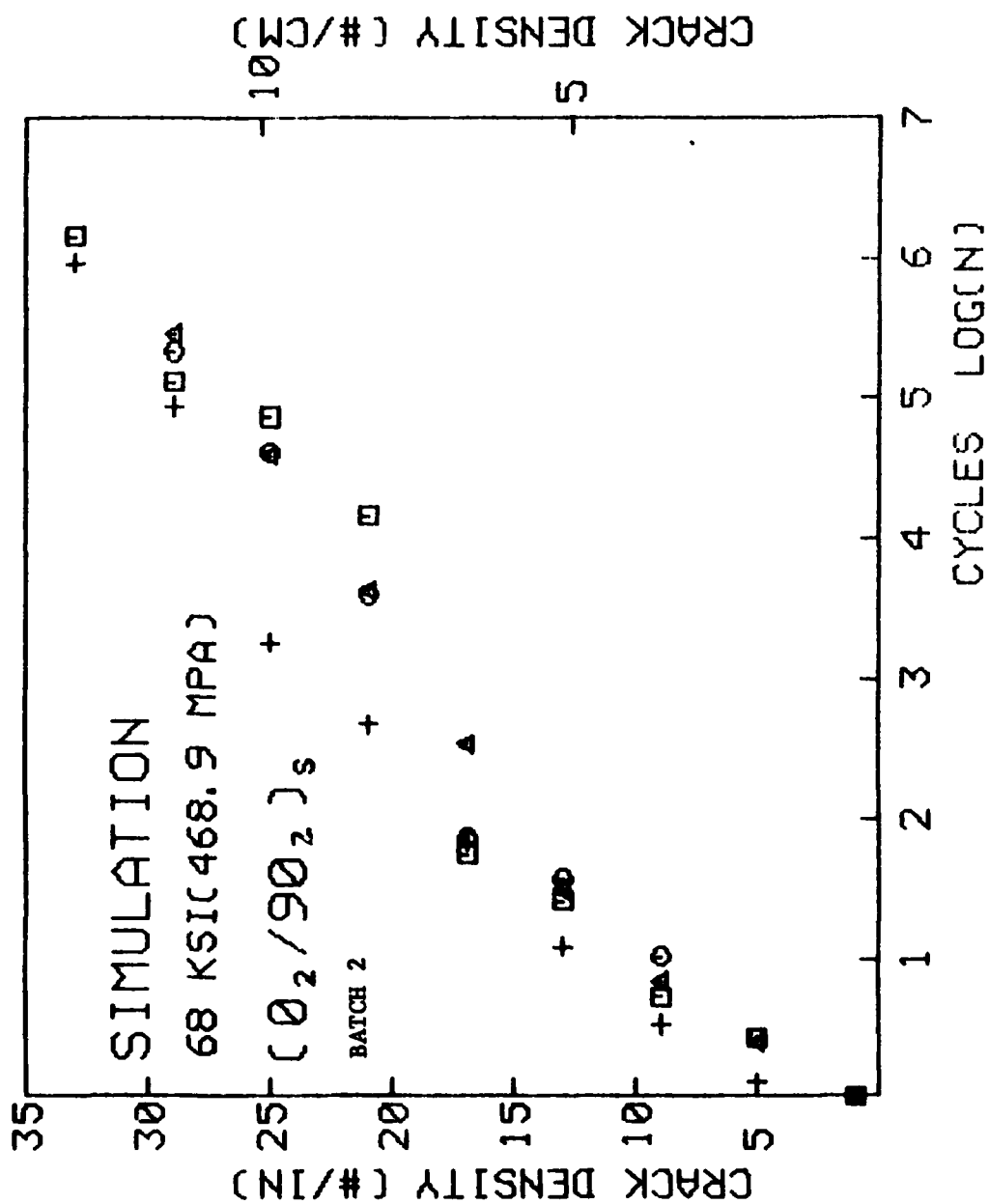


Figure C-14 Simulated Transverse Crack Density Versus Fatigue Cycles N for $[0_2/90_2]_s$ Laminates. Maximum Stress of $\sigma_x = 68$ KSI.

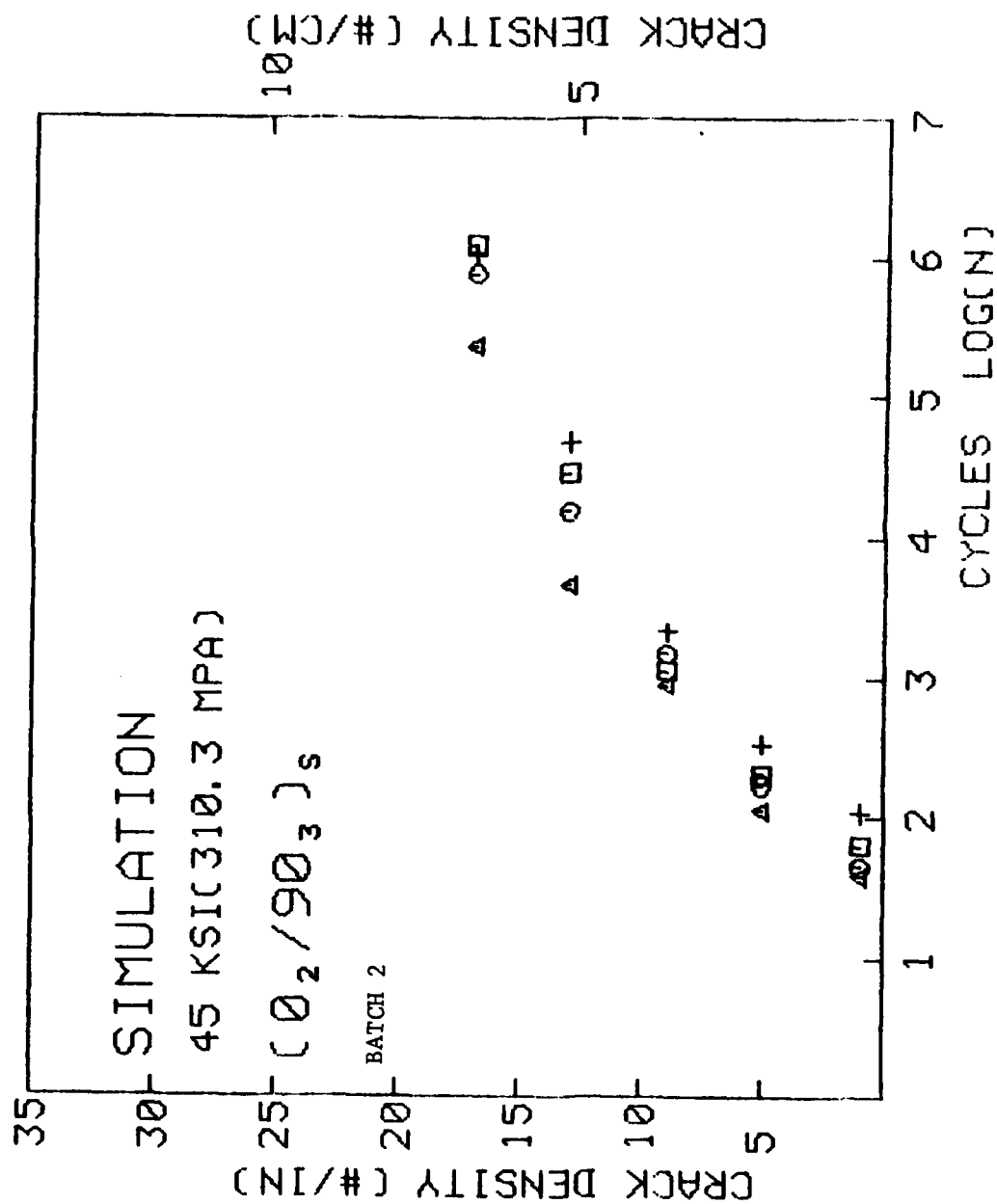


Figure C-16 Simulated Transverse Crack Density Versus Fatigue Cycles N for [0₂/90₃]_s Laminates. Maximum Stress of $\sigma_x = 45$ KSI.

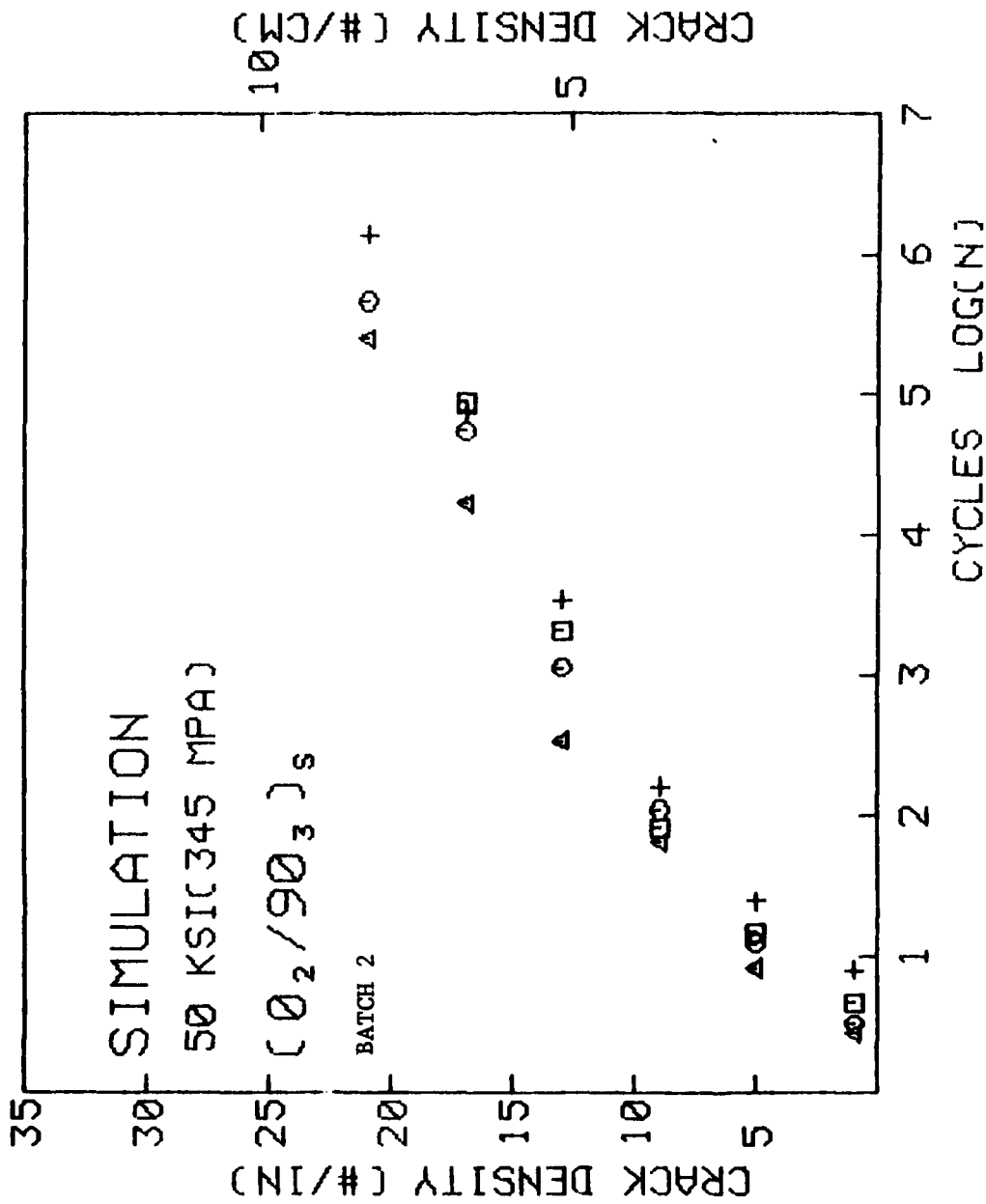


Figure C-17 Simulated Transverse Crack Density Versus Fatigue Cycles N for [0₂/90₃]_s Laminates. Maximum Stress of $\sigma_x = 50$ KSI.

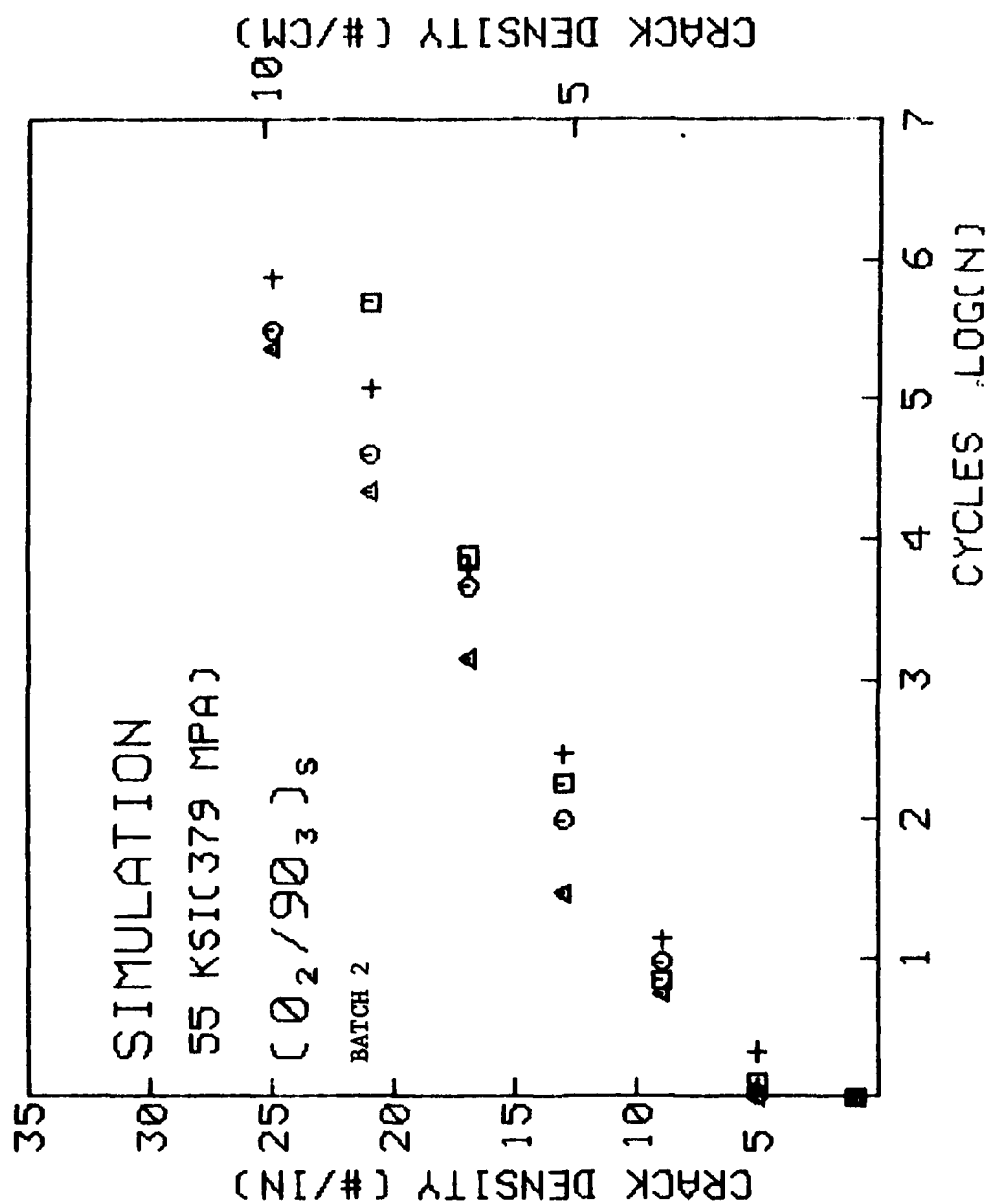


Figure C-18 Simulated Transverse Crack Density Versus Fatigue Cycles N for [0₂/90₃]_s Laminates. Maximum Stress of $\sigma_x = 55$ KSI.

APPENDIX D. TRANSVERSE CRACKING - CUMULATIVE DAMAGE

D1. Phase-I Data

The simulation results of transverse crack growth under static and constant amplitude fatigue loading were presented in Appendices B and C. There, the material effective flaw size distribution in the 90°-layer was assumed in the form of a normal distribution, with the parameters (mean and standard deviation):

$$\mu_a = 0.0032" \text{ (0.08 mm)}$$

$$\sigma_a = 0.0008" \text{ (0.02 mm)}$$

For fatigue growth, the parameters $\bar{\alpha}$ and \bar{p} in the growth rate equation were chosen as

$$\bar{\alpha} = 0.004t, \quad \bar{p} = 20.$$

Using these parameter values in the simulation routines for fatigue growth, a set of "constant damage" lines was generated in the $\sigma - N$ space for each of the $[0_2/90_2]_s$ and the $[0_2/90_3]_s$ laminates. These two sets of "constant damage" lines are shown in Figures D-1 and D-2.

For cumulative damage growth under variable amplitude fatigue, both the $[0_2/90_2]_s$ and $[0_2/90_3]_s$ laminates were tested in the experiment. The following test cases were carried out:

$$\begin{aligned} [0_2/90_2]_s: \quad \sigma_f &= 60 \text{ ksi (414 mpa) for } 10^5 \text{ cycles} \\ &= 80 \text{ ksi (552 mpa) for } 10^5 \text{ cycles} \\ \sigma_f &= 80 \text{ ksi (552 mpa) for } 10^2 \text{ cycles} \\ &60 \text{ ksi (414 mpa) for } 4 \times 10^5 \text{ cycles} \end{aligned}$$

$[0_2/90_2]_s$: σ_f = 50 ksi (345 mpa) for 10^3 cycles
 70 ksi (483 mpa) for 10^3 cycles
 50 ksi (345 mpa) for 10^5 cycles

$[0_2/90_3]_s$: σ_f = 26 ksi (179 mpa) for 10^4 cycles
 30 ksi (207 mpa) for 3×10^4 cycles
 26 ksi (179 mpa) for 10^5 cycles

σ_f = 15 ksi (104 mpa) for 10^5 cycles
 50 ksi (345 mpa) for 10^6 cycles

σ_f = 80 ksi (552 mpa) for 10 cycles
 40 ksi (276 mpa) for 10^6 cycles

Transverse cracks per unit length specimen were determined after each load-step. These are then compared to the same, which are predicted by the cumulative damage model using the constant damage lines shown in Figures D-1 and D-2. The comparison is illustrated in Tables D-1 and D-2.

TABLE D-1. CUMULATIVE DAMAGE DATA FOR PHASE-I

<u>Laminate</u>	<u>Fatigue Loads</u>	<u>Cycles at Load</u>	<u>Damage, Ck/in</u>	
			<u>Experiment</u>	<u>Prediction</u>
[0 ₂ /90 ₂] _s	60 ksi	10 ⁵	33	27
	80 ksi	10 ⁵	36	37
	60 ksi	10 ⁵	34	27
	80 ksi	10 ⁵	36	37
	60 ksi	10 ⁵	34	27
	80 ksi	10 ⁵	37	37

	80 ksi	10 ²	29	29
	60 ksi	10 ⁵	36	31
	80 ksi	10 ²	29	29
	60 ksi	10 ⁵	34	31
	80 ksi	10 ²	31	29
	60 ksi	10 ⁵	37	31

	50 ksi	10 ³	19	13
	70 ksi	10 ³	31	28
	50 ksi	10 ⁵	32	29
	50 ksi	10 ³	11	13
	70 ksi	10 ³	28	28
	50 ksi	10 ⁵	30	29
	50 ksi	10 ³	16	13
	70 ksi	10 ³	28	28
	50 ksi	10 ⁵	30	29

TABLE D-2. CUMULATIVE DAMAGE DATA FOR PHASE-I

<u>Laminate</u>	<u>Fatigue Loads</u>	<u>Cycles at Load</u>	<u>Damage, Ck/in</u>	
			<u>Experiment</u>	<u>Prediction</u>
$[0_2/90_3]_s$	26 ksi	10^4	1	0
	30 ksi	3×10^4	9	5
	26 ksi	10^5	10	5
	26 ksi	10^4	1	0
	30 ksi	3×10^4	8	5
	26 ksi	10^5	9	5
	26 ksi	10^4	1	0
	30 ksi	3×10^4	8	5
	26 ksi	10^5	8	5
	26 ksi	10^4	2	0
	30 ksi	3×10^4	6	5
	26 ksi	10^5	7	5
	15 ksi	10^5	0	0
	50 ksi	10^6	28	26
	15 ksi	10^5	0	0
	50 ksi	10^6	28	26
	80 ksi	10	30	28.5
	40 ksi	10^6	31	29
	80 ksi	10	28	28.5
	40 ksi	10^6	30	29

D2. Phase-II Data.

The material effective flaw size distribution in the 90°-layer for the Phase-II study was also assumed in the form of a normal distribution. But, the parameters were chosen as follows:

$$\begin{aligned}\mu_a &= 0.0026'' (0.07 \text{ mm}) \\ \sigma_a &= 0.00042'' (0.011 \text{ mm})\end{aligned}$$

All other values used in the simulation were the same as in Phase-I. The constant damage lines for $[0_2/90_2]_s$ and $[0_2/90_3]_s$ laminates were also generated by the same simulation routine. These are shown in Figures D-3 and D-4, respectively.

Cumulative damage tests on these two laminates were carried out for the following cases:

$$\begin{aligned}[0_2/90_2]_s: \quad \sigma_f &= 60 \text{ ksi (345 mpa) for } 10^5 \text{ cycles} \\ &80 \text{ ksi (552 mpa) for } 10^5 \text{ cycles} \\ \sigma_f &= 80 \text{ ksi (552 mpa) for } 10^2 \text{ cycles} \\ &60 \text{ ksi (414 mpa) for } 10^2 \text{ cycles} \\ \sigma_f &= 50 \text{ ksi (345 mpa) for } 10^3 \text{ cycles} \\ &70 \text{ ksi (483 mpa) for } 10^3 \text{ cycles} \\ &50 \text{ ksi (345 mpa) for } 10^5 \text{ cycles} \\ [0_2/90_3]_s: \quad \sigma_f &= 26 \text{ ksi (179 mpa) for } 10^4 \text{ cycles} \\ &30 \text{ ksi (207 mpa) for } 2 \times 10^4 \text{ cycles} \\ &26 \text{ ksi (179 mpa) for } 10^5 \text{ cycles} \\ \sigma_f &= 15 \text{ ksi (104 mpa) for } 10^5 \text{ cycles} \\ &50 \text{ ksi (345 mpa) for } 10^5 \text{ cycles}\end{aligned}$$

$[0_2/90_3]_s$: $\sigma_f = 80 \text{ ksi (552 mpa)}$ for 10 cycles
40 ksi (276 mpa) for 10^6 cycles

Cumulative damage in terms of transverse crack growth (cracks per inch) are determined both from experiment and from the cumulative damage model (using the constant damage lines).

The comparison between them is tabulated in Table D-3 for $[0_2/90_2]_s$ and in Table D-4 for $[0_2/90_3]_s$.

TABLE D-3. CUMULATIVE DAMAGE DATA FOR PHASE-II

<u>Laminate</u>	<u>Fatigue Loads</u>	<u>Cycles at Load</u>	<u>Damage, Ck/in</u>	
			<u>Experiment</u>	<u>Prediction</u>
[0 ₂ /90 ₂] _s	60 ksi	10 ⁵	22	21
	80 ksi	10 ⁵	33	33
	60 ksi	10 ⁵	13	21
	80 ksi	10 ³	34	30
	(Failed before 10 ⁵ cycles)			
	80 ksi	10 ²	15	21
	60 ksi	10 ⁵	20	22
	80 ksi	10 ²	17	21
	60 ksi	10 ⁵	27	22
	50 ksi	10 ³	1	0
	70 ksi	10 ³	16	20
	50 ksi	10 ⁵	23	21
	50 ksi	10 ³	2	0
	70 ksi	10 ³	20	20
	50 ksi	10 ⁵	25	21

TABLE D-4. CUMULATIVE DAMAGE DATA FOR PHASE-II

<u>Laminate</u>	<u>Fatigue Loads</u>	<u>Cycles at Load</u>	<u>Damage, Ck/in</u>	
			<u>Experiment</u>	<u>Prediction</u>
[0 ₂ /90 ₃] _s	26 ksi	10 ⁴	0	0
	30 ksi	3 x 10 ⁴	0	0
	26 ksi	10 ⁵	0	0
	26 ksi	10 ⁴	0	0
	30 ksi	3 x 10 ⁴	1	0
	26 ksi	10 ⁵	2	0

	15 ksi	10 ⁵	0	0
	50 ksi	10 ⁵	16	17
	15 ksi	10 ⁵	0	0
	50 ksi	10 ⁵	21	17

	80 ksi	10	19	24
	40 ksi	10 ⁶	20	24
	80 ksi	10	16	24
	40 ksi	10 ⁶	20	24

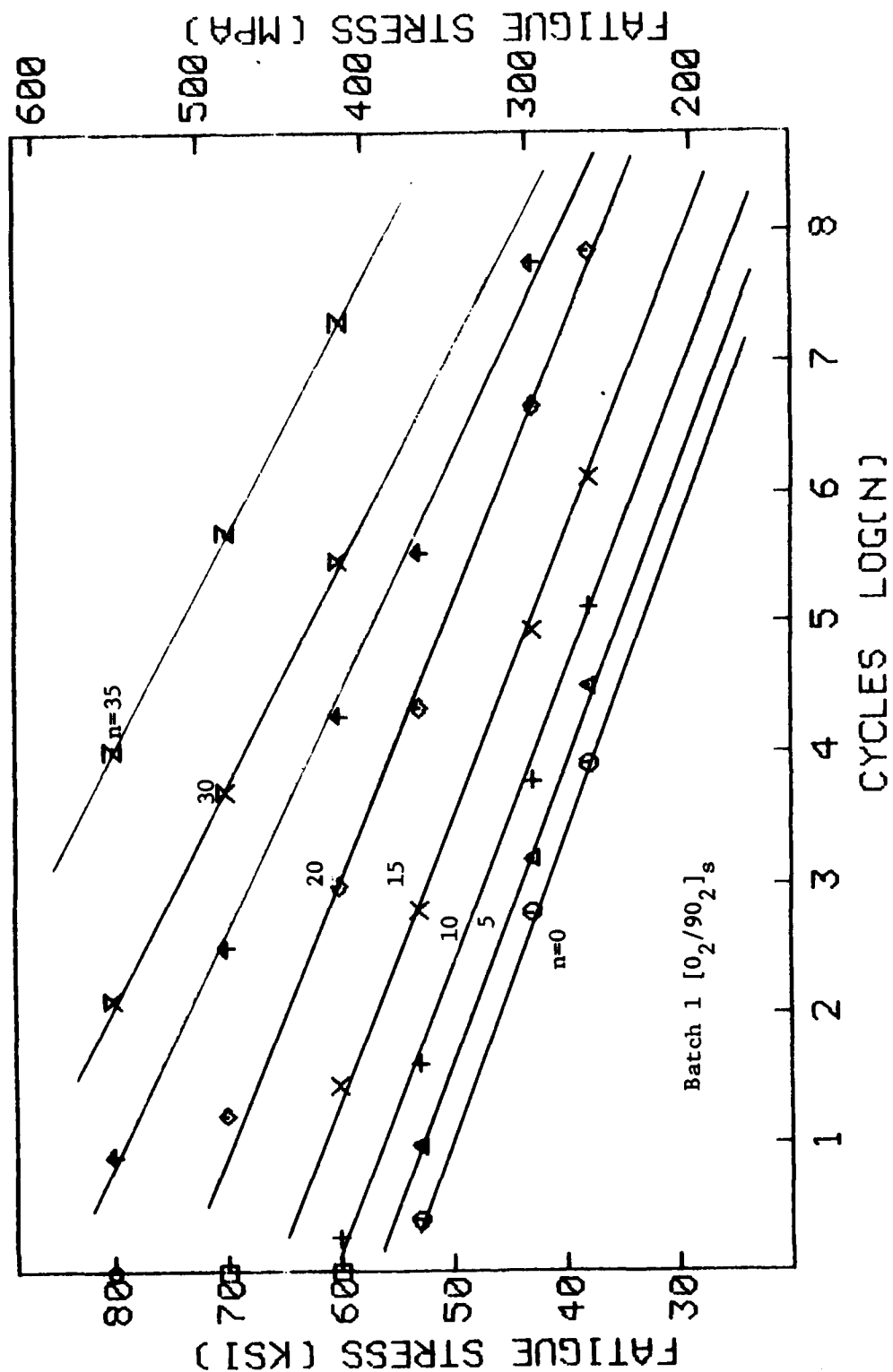


Figure D-1 Constant Damage Lines for Batch 1 $[0_2/90_2]_s$ Laminates.

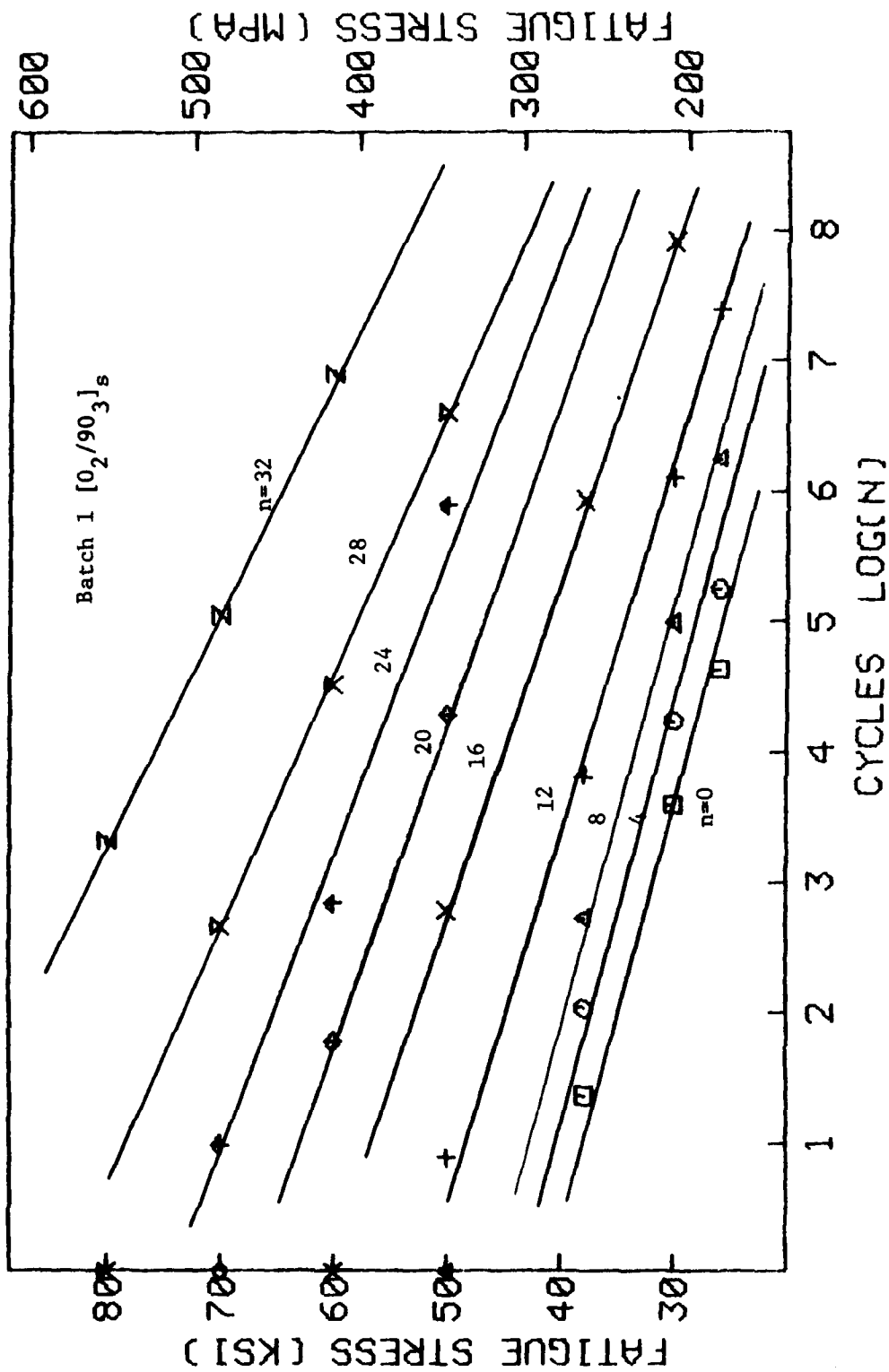


Figure D-2 Constant Damage Lines for Batch 1 $[0_2/90_3]_s$ Laminates.

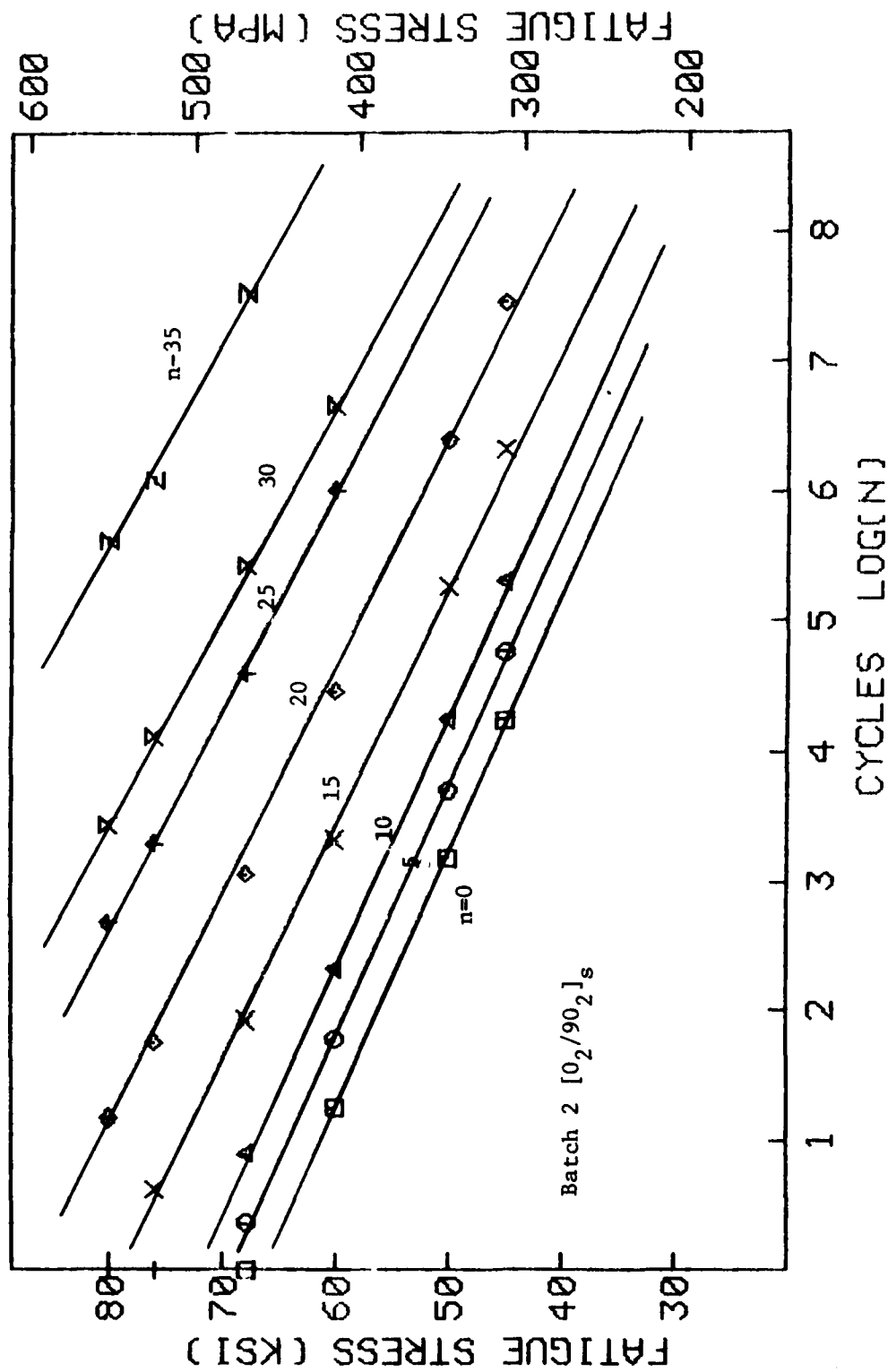


Figure D-3 Constant Damage Lines for Batch 2 $[0_2/90_2]_s$ Laminates.

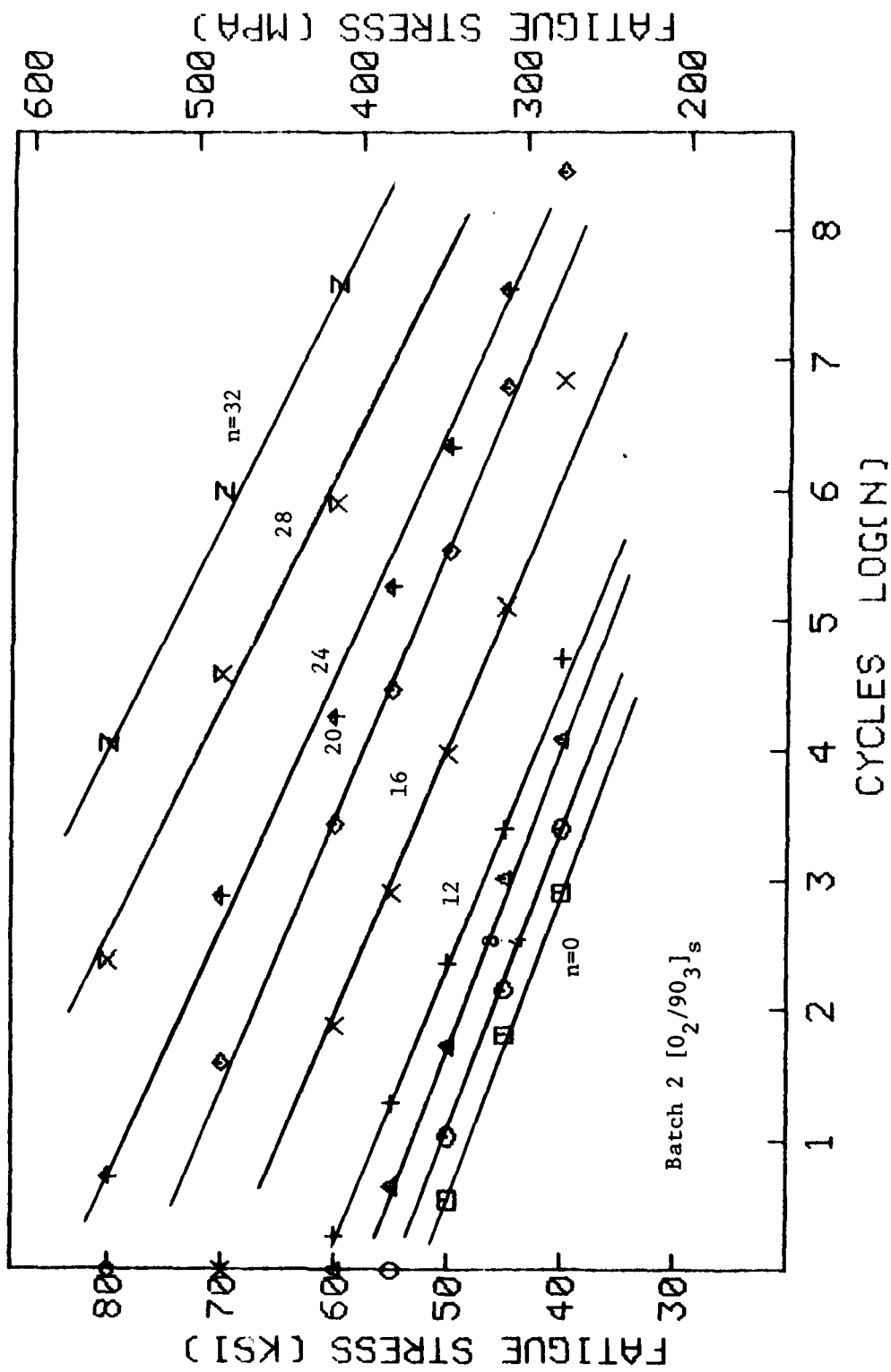


Figure D-4 Constant Damage Lines for Batch 2 $[0_2/90_3]_s$ Laminates.

APPENDIX E. FREE EDGE DELAMINATION - STATIC LOADING

E1. Phase-I Data.

Free edge delamination data obtained under static loading in Phase-I study has already been presented in Section 2.6. There, the laminates $[\pm 25/90_n]_s$, $n = 1, 2, 3$, were tested and simulated. It was noted that the cases of $n = 2$ and 3 involved transverse crack/delamination interactions. Consequently, a vigorous delamination simulation for these two cases was not available. However, the onset of delamination loads for the latter, were determined approximately (see discussions in Section 2.6 and Section 2.9). In order to avoid duplication, these results will not be included here.

E2. Phase-II Data.

In Phase-II, free edge delamination study was conducted also using the laminates $[\pm 25/90_n]_s$, $n = 1, 2, 3$. For the cases of $n = 2$ and 3 , similar transverse crack/delamination interaction was also encountered. In the simulation, a new set of energy release rate curves was generated, using the new material moduli for the batch 2 material. These curves are shown in Figures E-1 and E-2.

By means of the energy release rate curves and the Griffith crack growth criterion, the predicted onset loads for free edge delamination are compared to experiment as listed in the following, ($G_c = 1.0 \text{ in-lb/in}^2$):

<u>Laminate</u>	<u>Onset Laminate Strain, $\bar{\epsilon}_x$</u>	
	<u>Experiment</u>	<u>Prediction</u>
$[\pm 25/90]_s$	5.78×10^{-3}	5.68×10^{-3}
$[\pm 25/90_2]_s$	5.52×10^{-3}	5.68×10^{-3}
$[\pm 25/90_3]_s$	5.07×10^{-3}	5.22×10^{-3}

For details on the calculated results, refer to Section 2.6 for $[\underline{+25/90}]_s$, and Section 2.9 for $[\underline{+25/90}]_2$ and $[\underline{+25/90}]_3$.

Some graphical data pertaining to the above may be found in Appendix H.

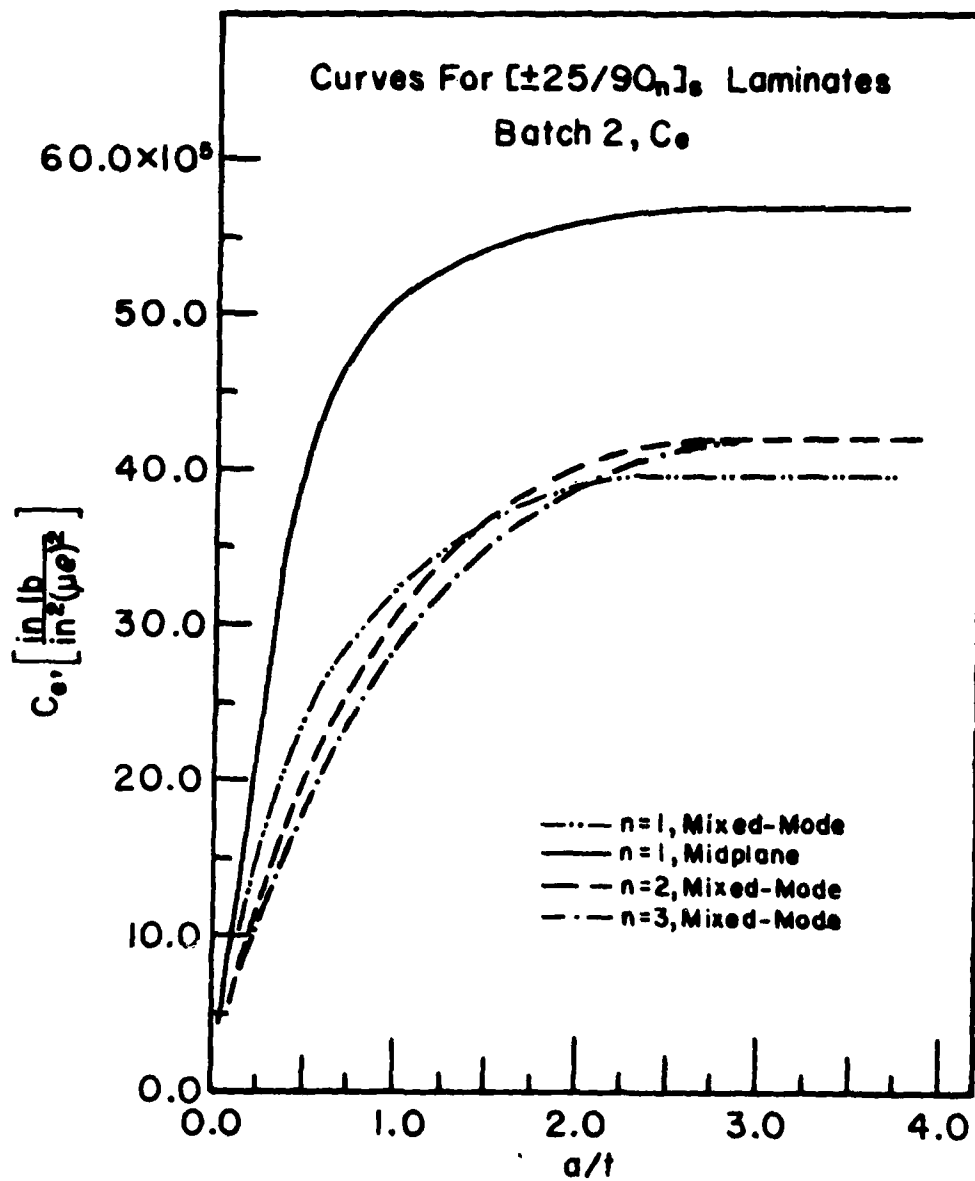


Figure E-1 Energy Release Rate Coefficients for Delamination Under Mechanical Load.

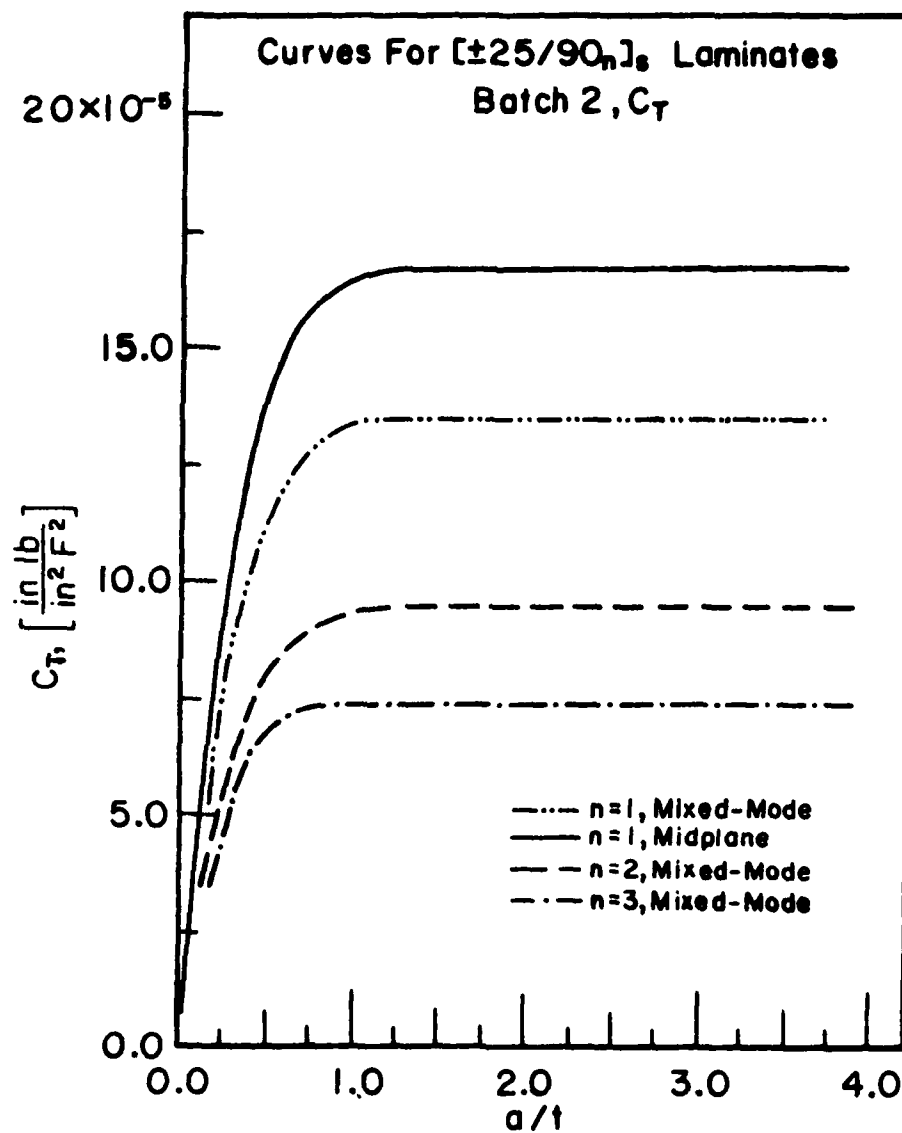


Figure E-2 Energy Release Rate Coefficients for Delamination Under Thermal Load.

APPENDIX F. FREE EDGE DELAMINATION - FATIGUE LOADING

F1. Phase-I Data.

Again, the delamination growth data under constant amplitude fatigue loading obtained in Phase-I has already been presented in Section 2.7. Recall that only the laminate $[\pm 25/90]_s$ was tested and simulated. The simulated results were based on the crack growth in the 25/90 interface and by means of the equation

$$\frac{da}{dN} = \bar{\alpha} [G(\sigma_f, a)/G_c]^{\bar{p}} \quad (F-1)$$

where the parameters were selected as

$$\bar{\alpha} = 0.04 \text{ inch}; \quad \bar{p} = 8.3. \quad (F-2)$$

Given the $G(\sigma_f, a)$ curve, and setting $G_c = 1.3 \text{ in-lb/in}^2$, the crack growth equation can be integrated numerically to obtain the quantity a (size of delamination) in terms of σ_f and N . All relevant results are found in Section 2.7.

F2. Phase-II Data.

The $[\pm 25/90]_s$ laminates made of batch 2 material were tested and simulated for free edge delamination under the following fatigue loads:

$$\begin{aligned} \sigma_f = & 29 \text{ ksi (200 mpa); } 33 \text{ ksi (278 mpa); } \\ & 40 \text{ ksi (276 mpa); } 45 \text{ ksi (310 mpa); } \\ & 50 \text{ ksi (345 mpa); } 55 \text{ ksi (379 mpa). } \end{aligned}$$

The tested and simulated results for the above are shown in Figures F-1 to F-6. All simulations were based on the growth equation (F-1), with the same parameter values in (F-2).

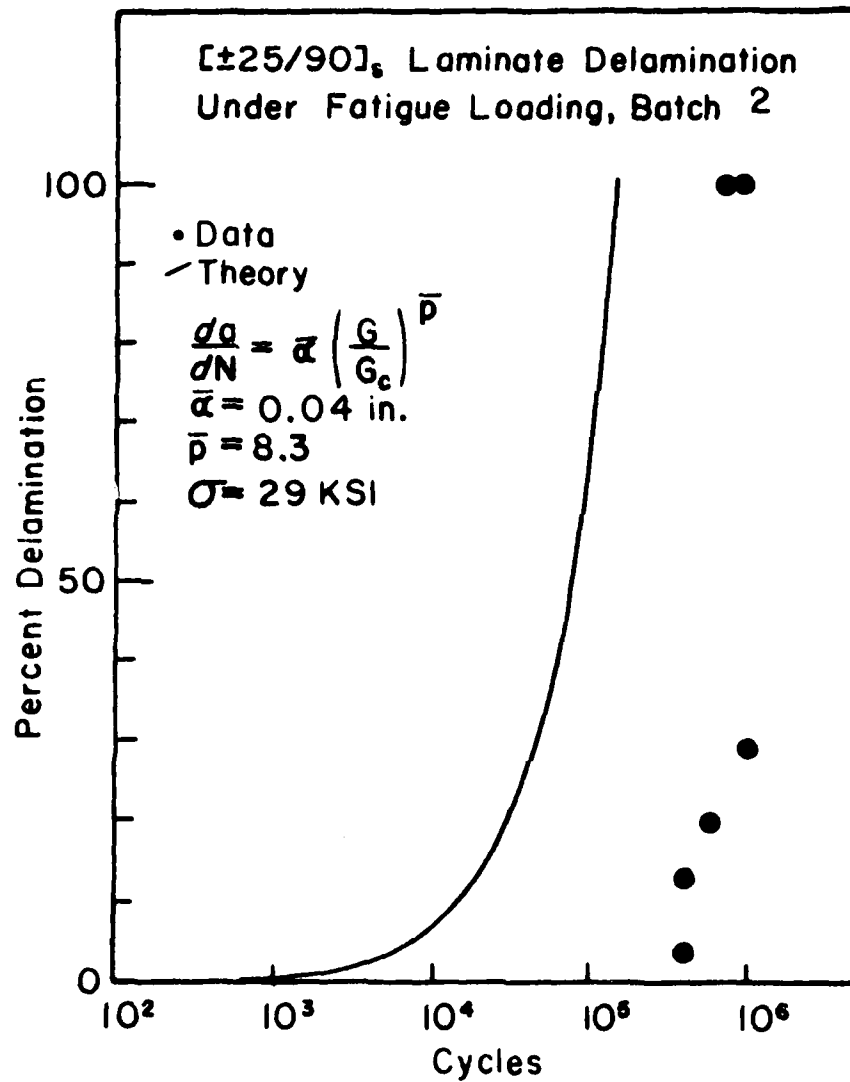


Figure F-1 Percent Delamination, vs. Fatigue Cycles for
[±25/90]_s Laminates, $\sigma = 29 \text{ KSI}$.

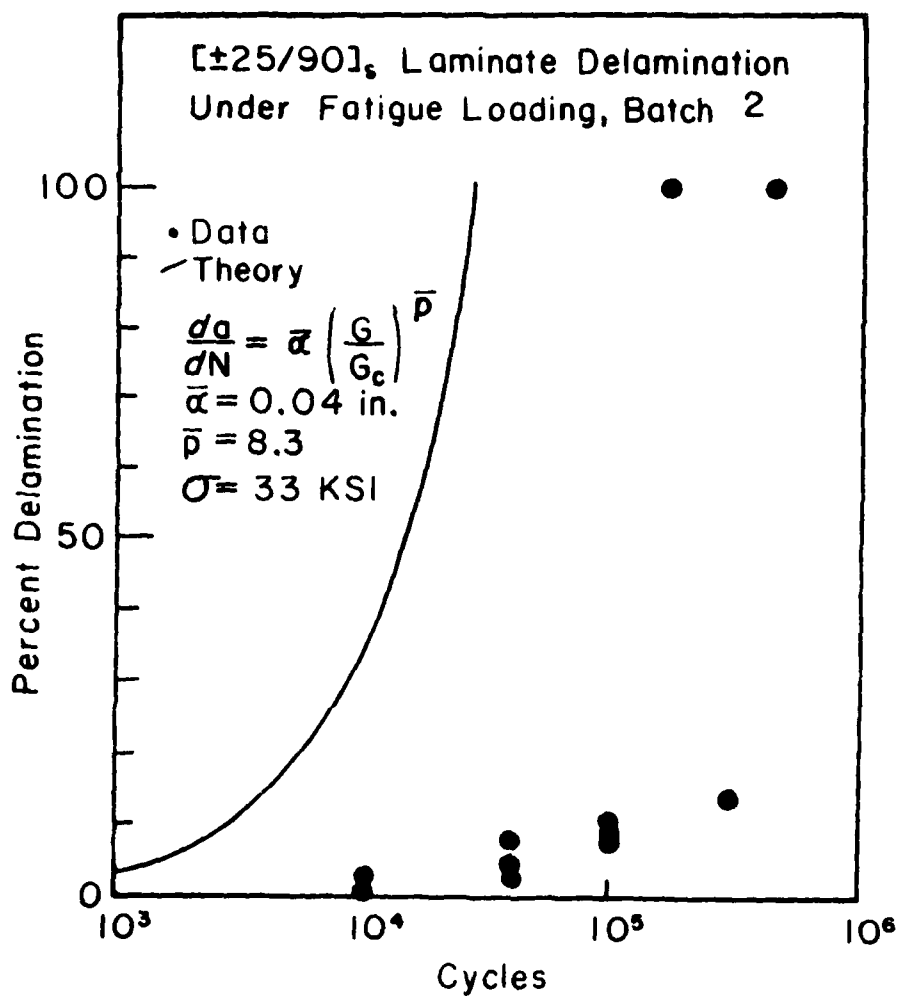


Figure F-2 Percent Delamination vs. Fatigue Cycles for
[±25/90]_s Laminates, $\sigma = 33 \text{ KSI}$.

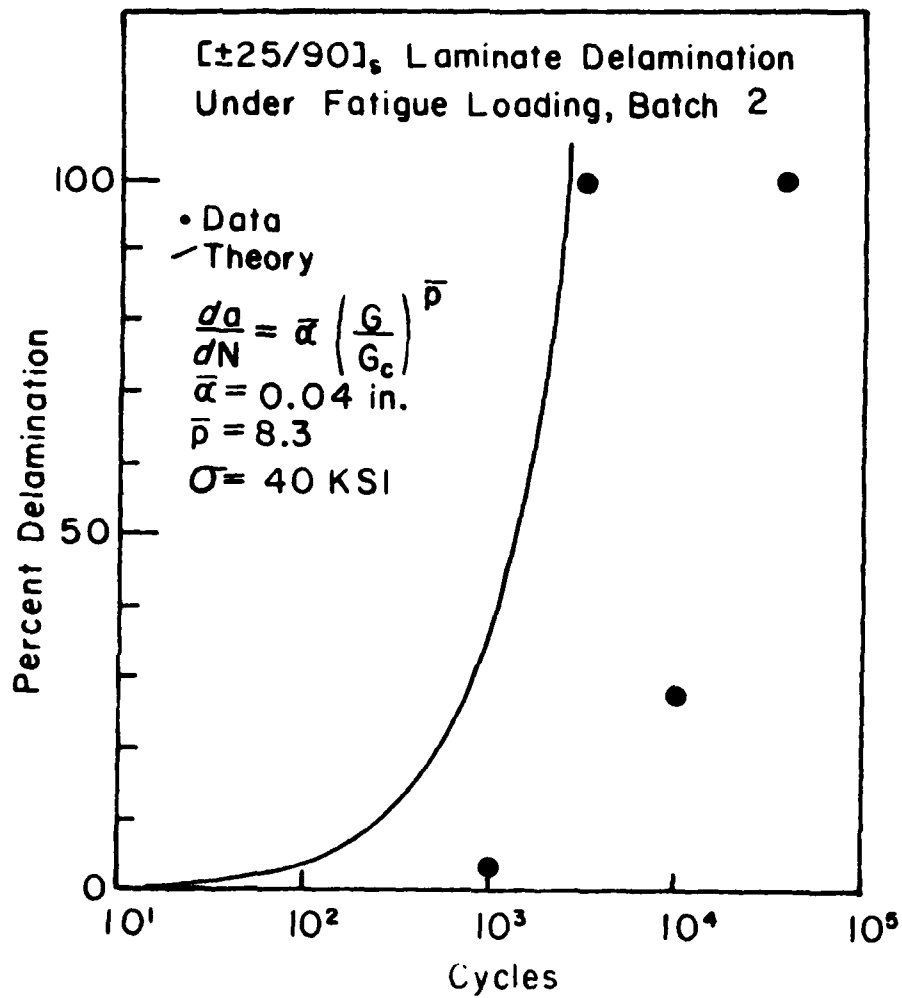


Figure F-3 Percent Delamination vs. Fatigue Cycles for Laminates,
 $\sigma = 40 \text{ KSI}$.

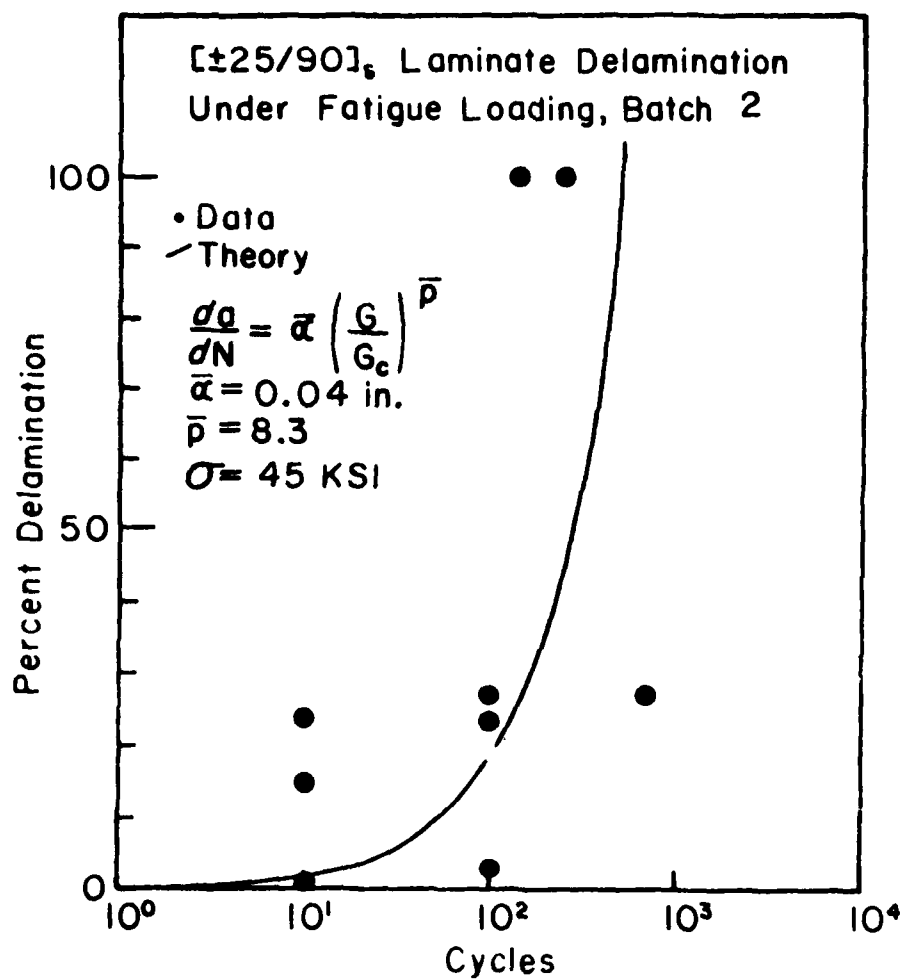


Figure F-4 Percent Delamination vs. Fatigue Cycles for
[±25/90]_s Laminates, $\sigma = 45 \text{ KSI}$.

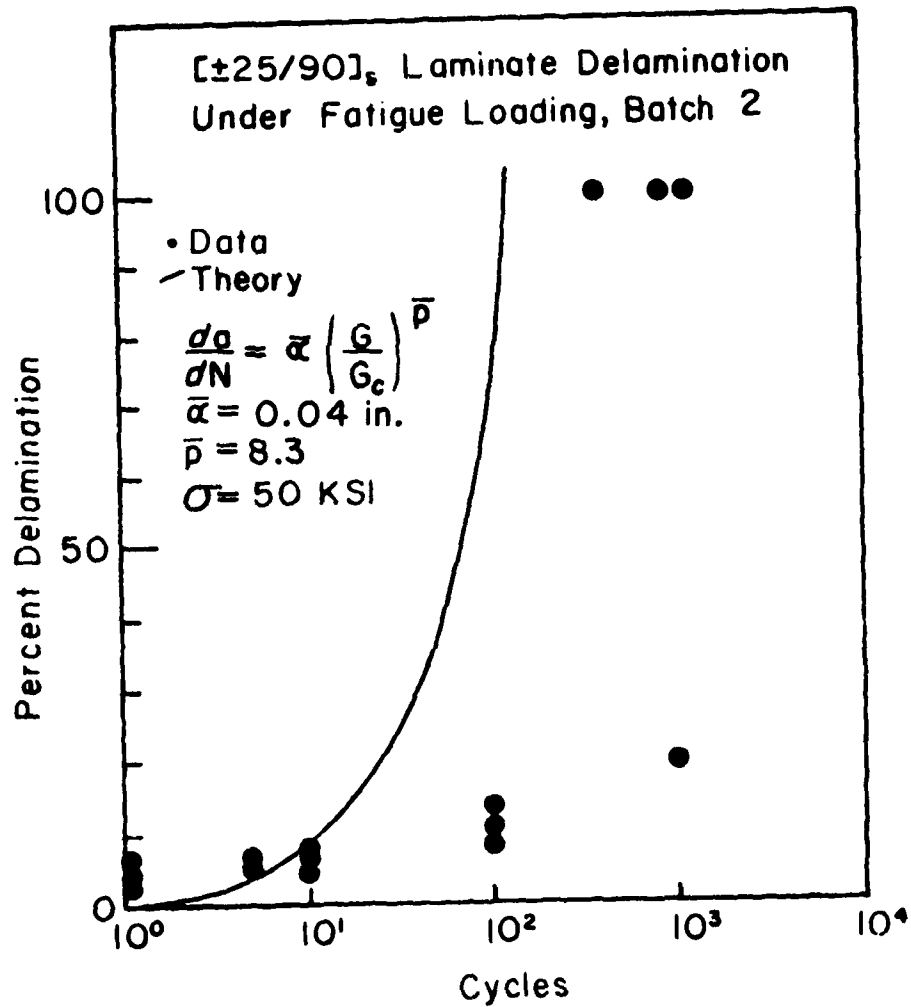


Figure F-5 Percent Delamination vs. Fatigue Cycles for
[±25/90]_s Laminates, $\sigma = 50 \text{ KSI}$.

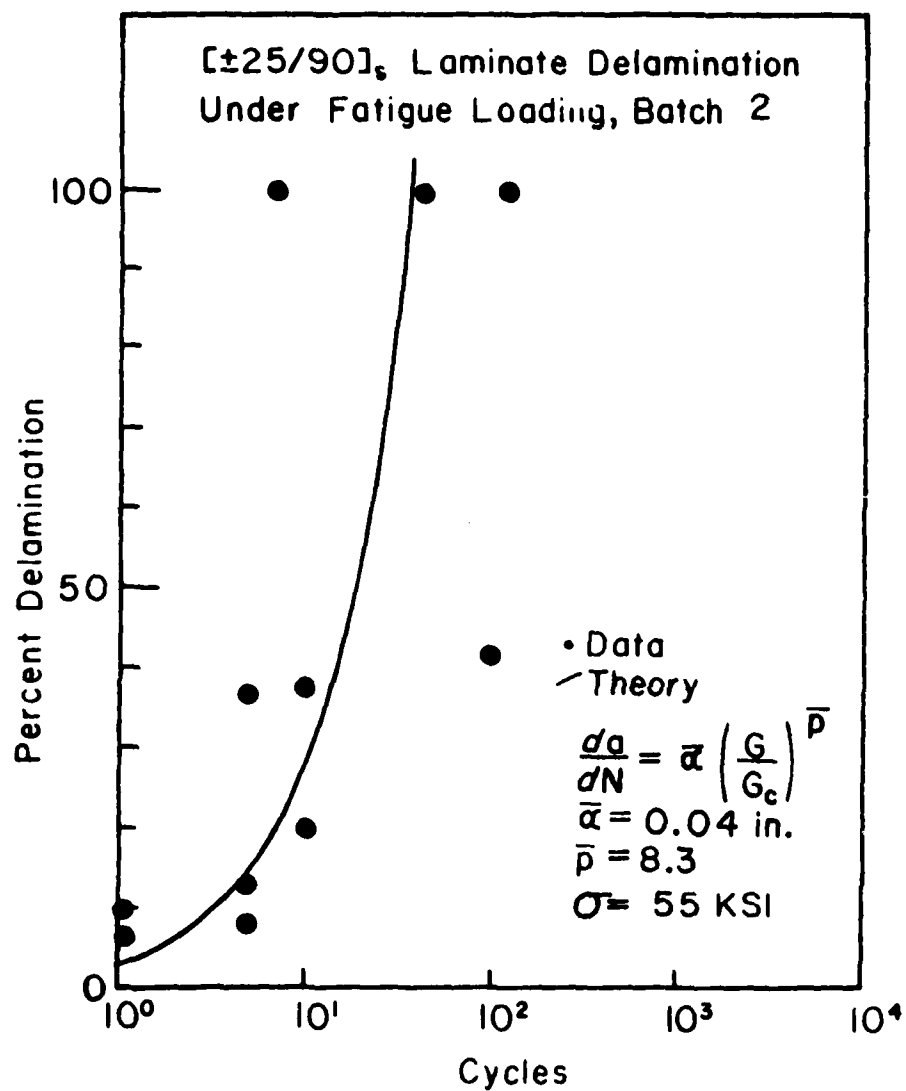


Figure F-6 Percent Delamination vs. Fatigue Cycles for
[±25/90]_s Laminates, $\sigma = 55 \text{ KSI}$.

APPENDIX G. FREE EDGE DELAMINATION - CUMULATIVE DAMAGE

G1. Phase-I Data.

Some of the free edge delamination data under variable amplitude fatigue loading obtained in Phase-I was used in the discussions in Section 2.8. For completeness, all test results and their simulated counterparts are graphically displayed in Figures G-1 to G-5.

Note that in each of the figures, the test results and the simulated results are displayed in the $\sigma - N$ space, which is spanned by a set of "constant damage lines." The constant damage lines were generated by the crack growth equation (F-1) along with the parameters in (F-2). Test results (delamination in % of specimen half-width) in each of these figures are indicated by the number (in %) in parentheses.

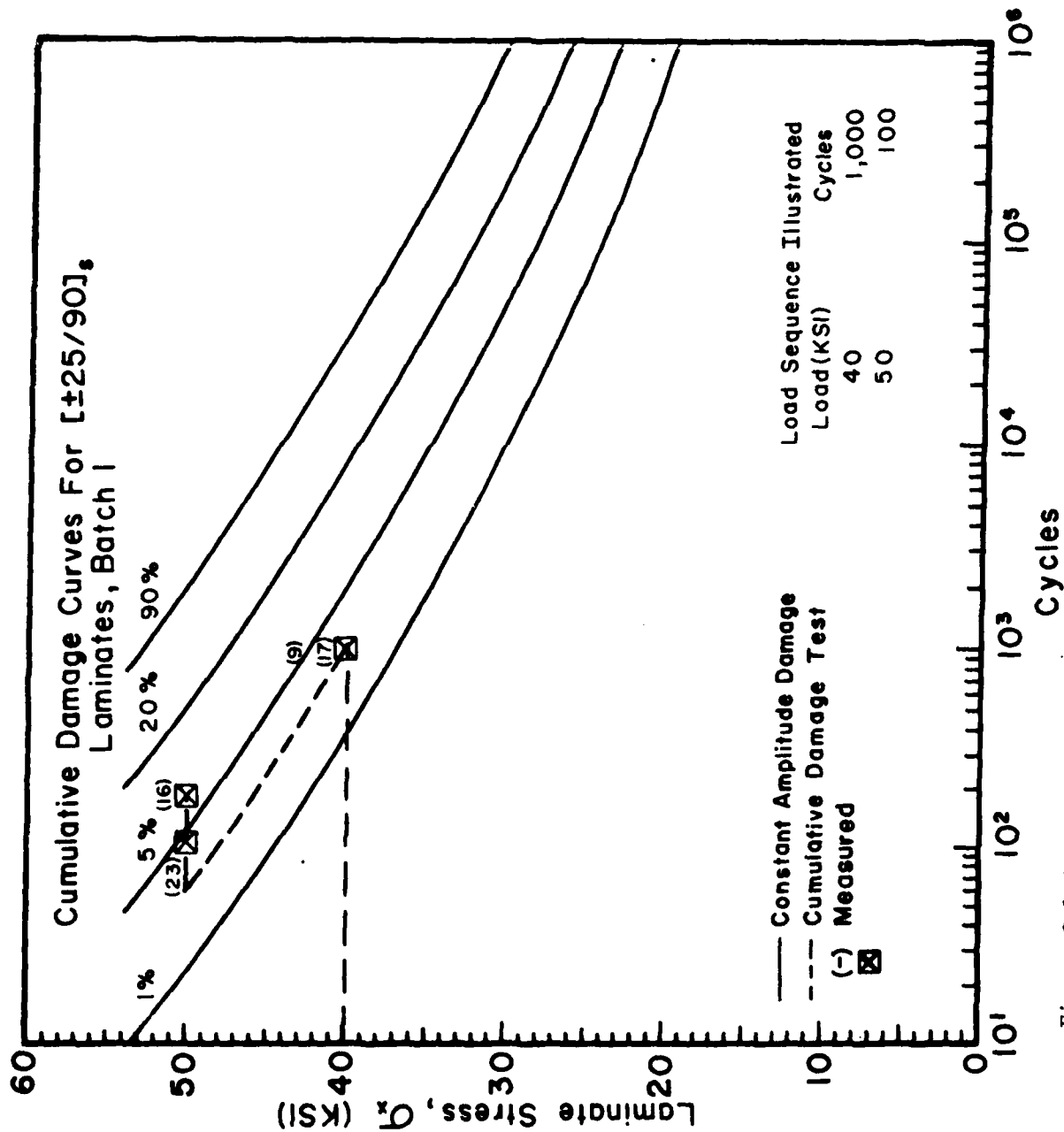


Figure G-1 Cumulative Damage Tests for $[\pm 25/90]_s$ Laminates.

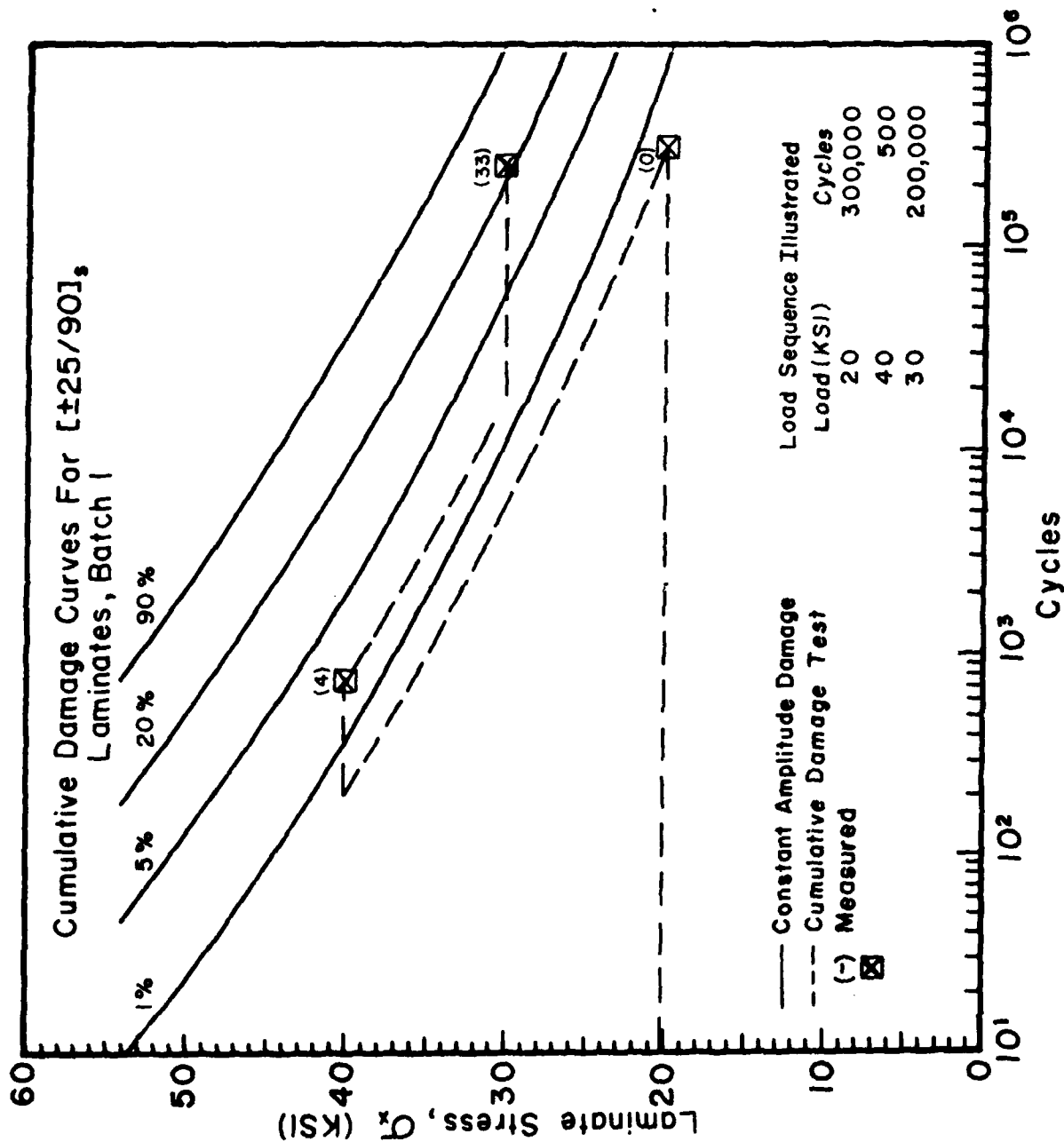


Figure G-2 Cumulative Damage Tests for $[\pm 25/90]_s$ Laminates.

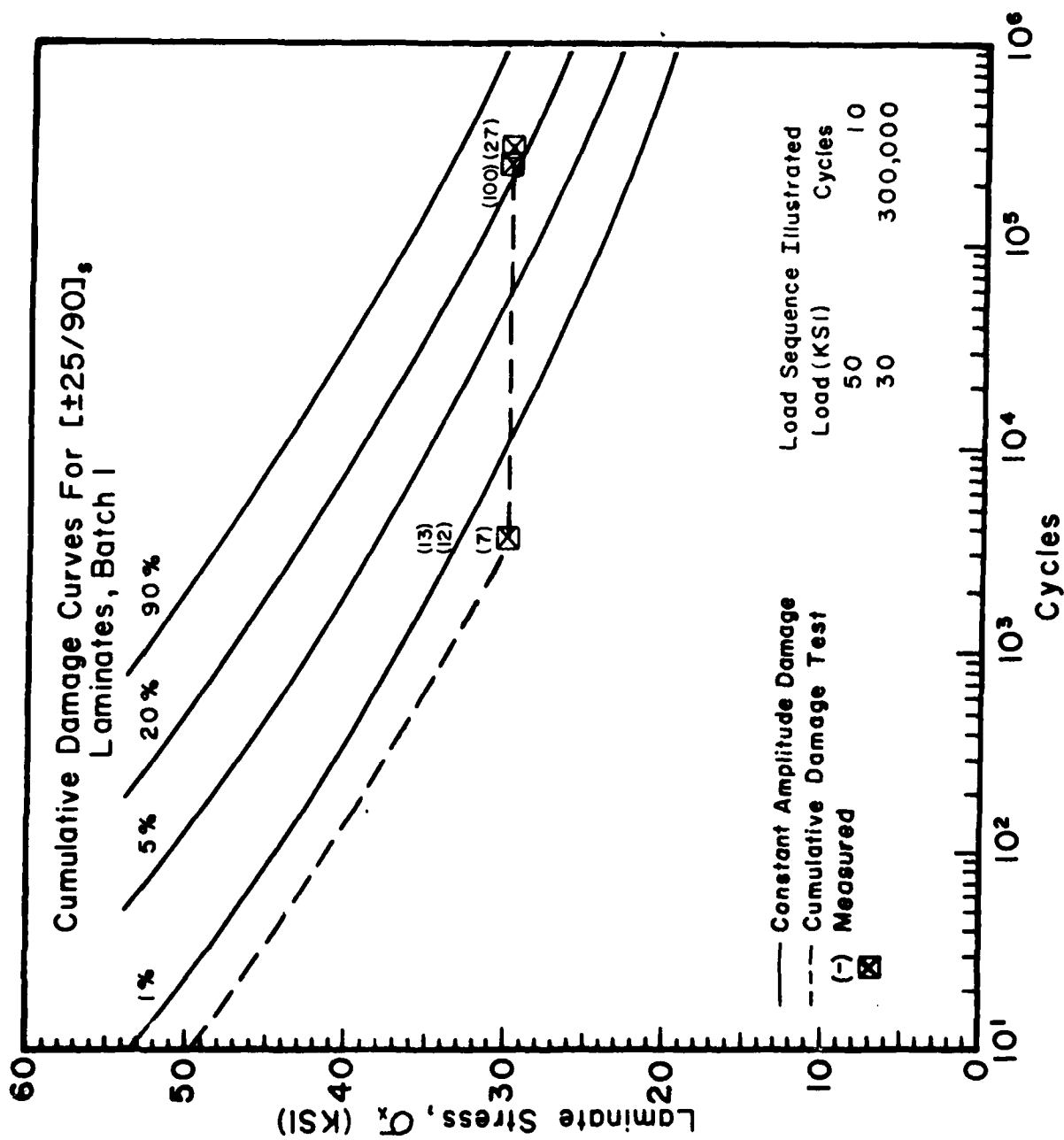


Figure G-3 Cumulative Damage Tests for $[\pm 25/90]_s$ Laminates.

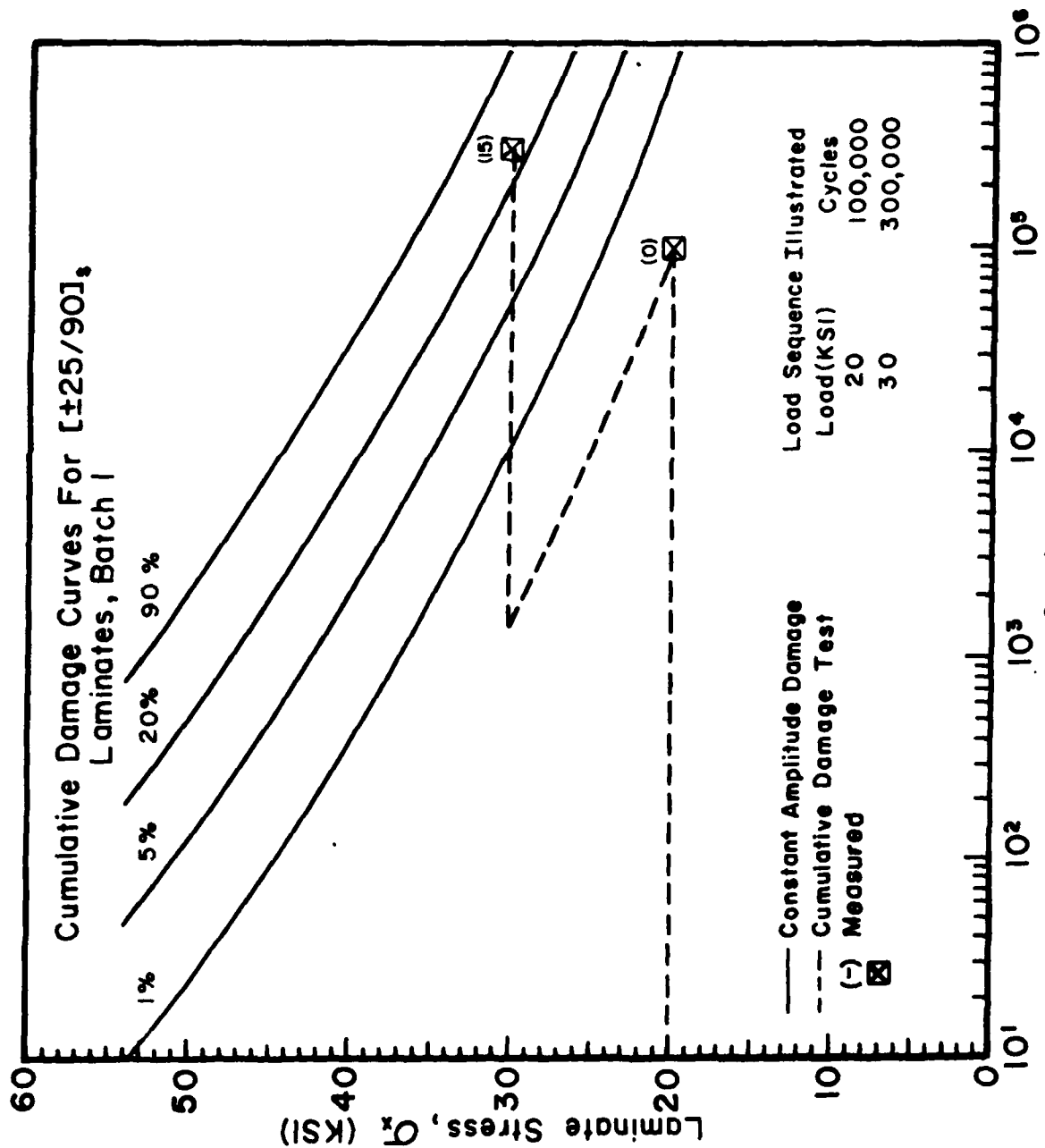


Figure G-4 Cumulative Damage Tests for $[\pm 25/90]_s$ Laminates.

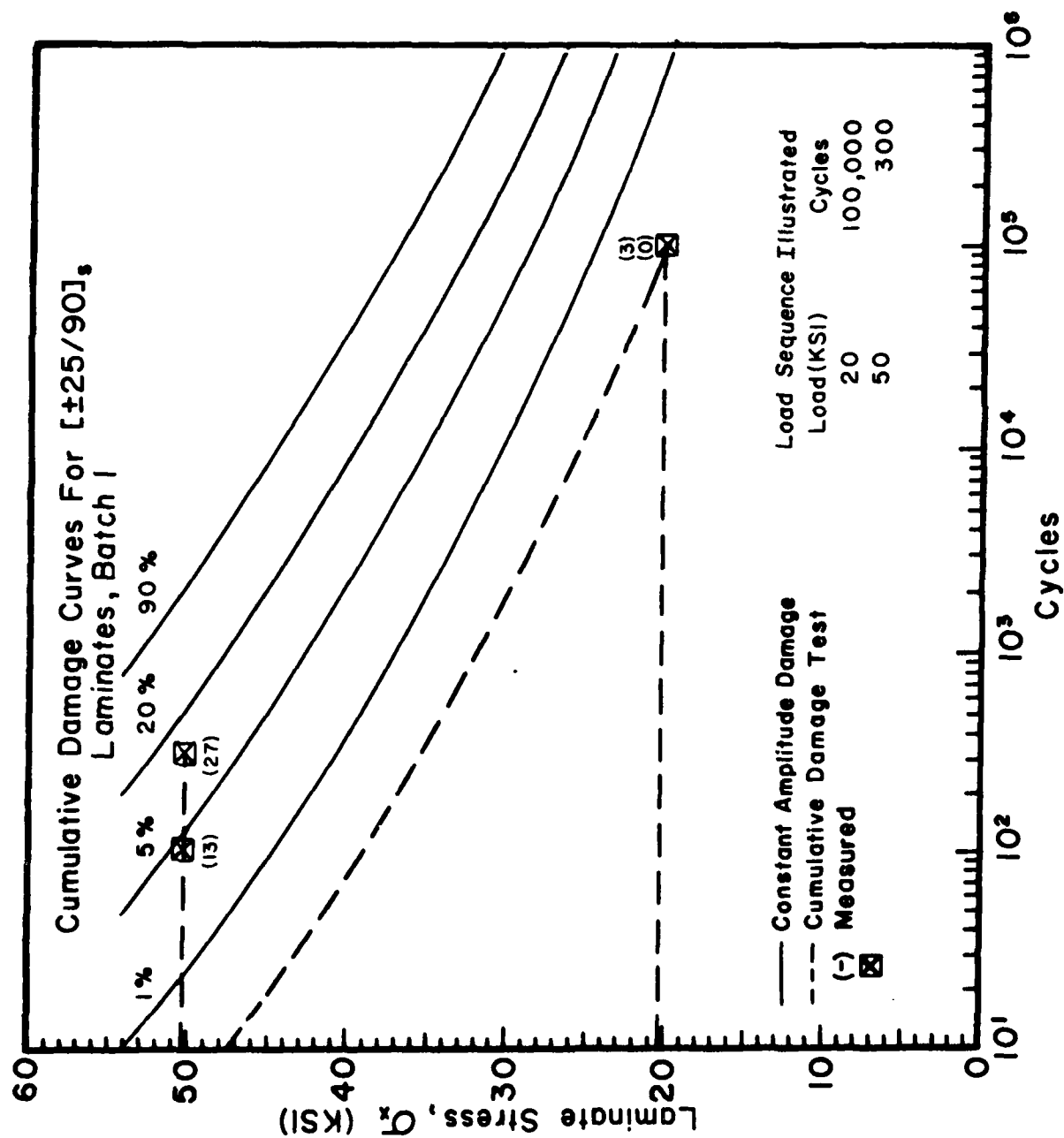


Figure G-5 Cumulative Damage Test for $[\pm 25/90]_s$ Laminates.

G2. Phase-II Data.

Similar comparative results obtained in Phase-II are shown in Figures G-6 through G-10. Here, again, are five study cases for the cumulative damage under variable amplitude fatigue loadings.

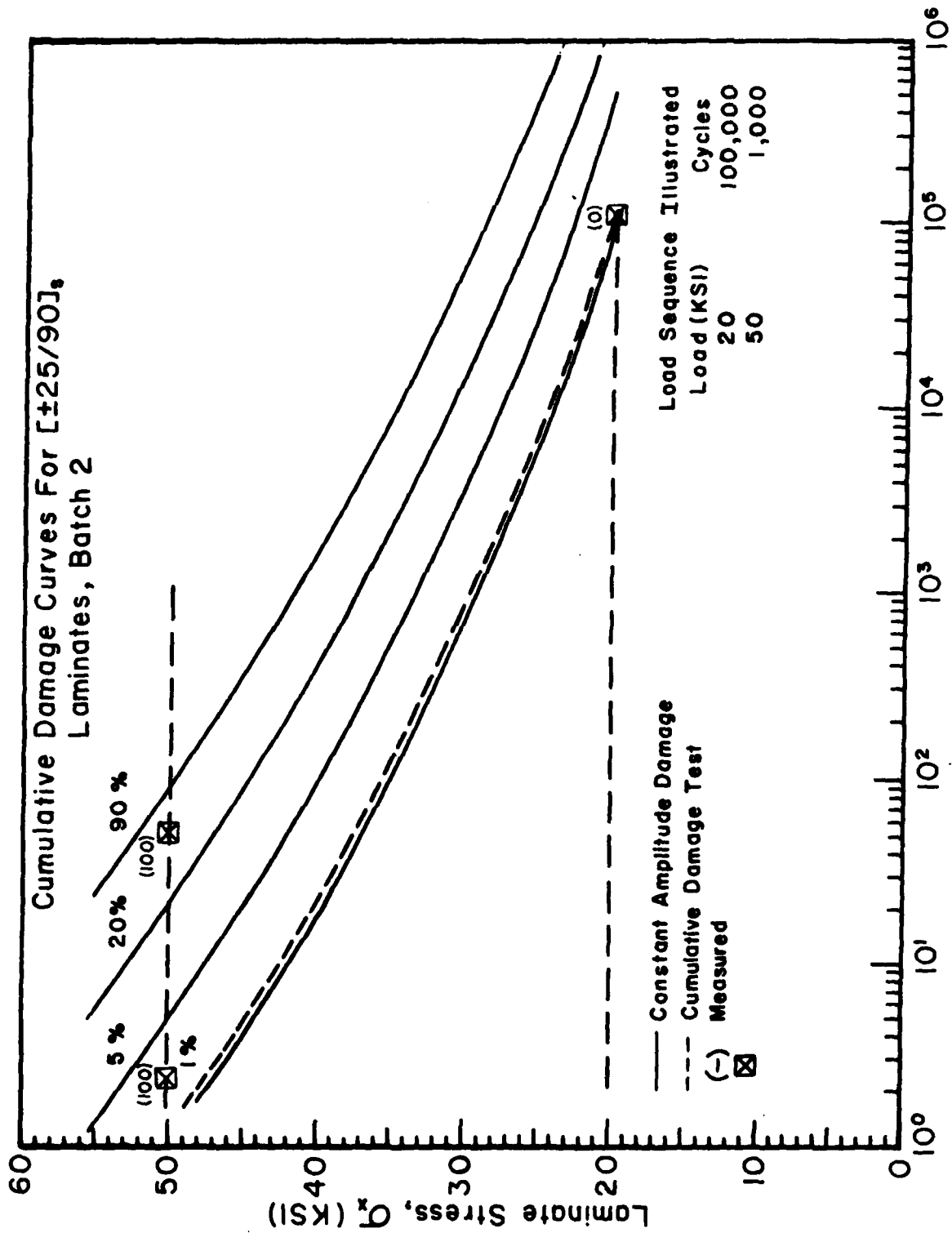


Figure G-6 Cumulative Damage Tests for $[\pm 25/90]_s$ Laminates.

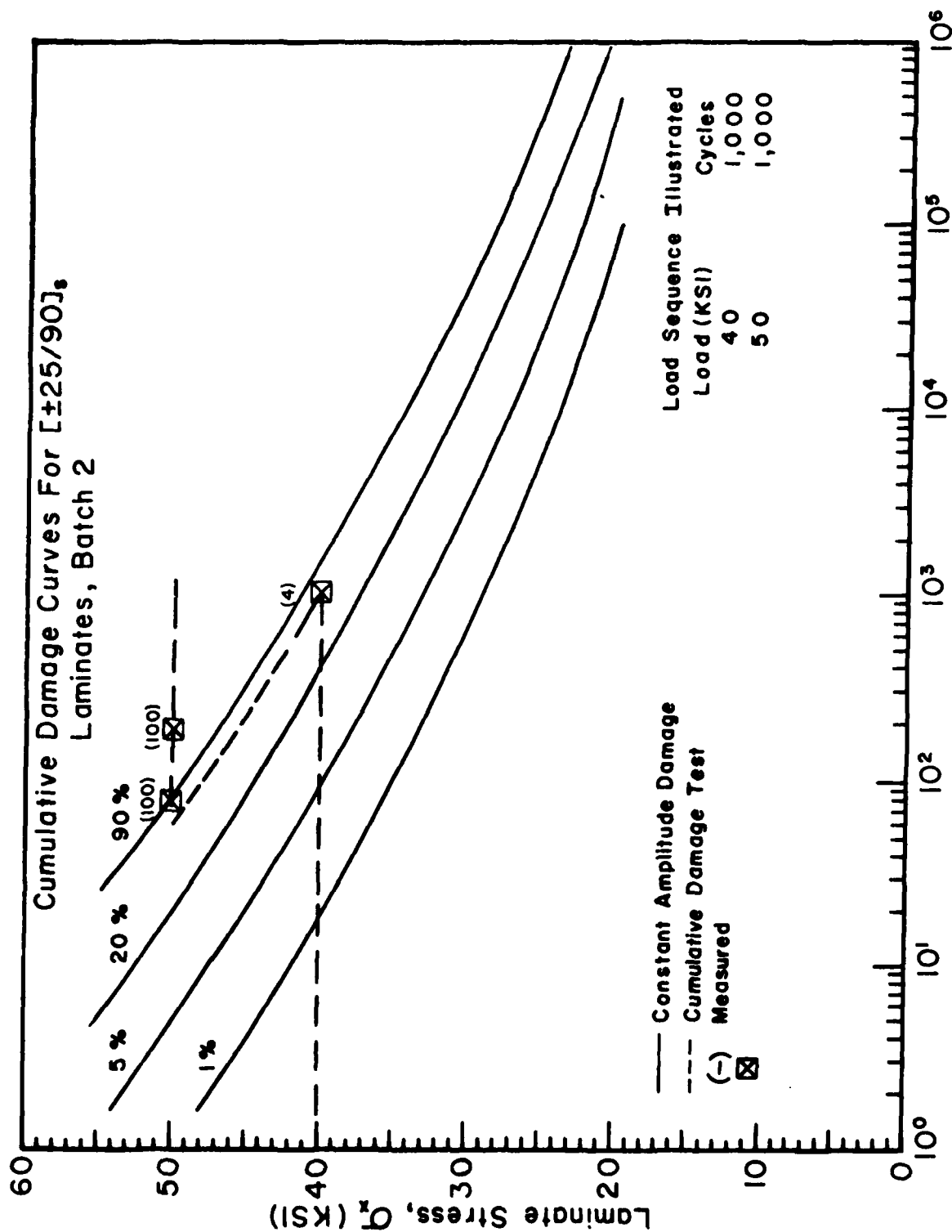


Figure G-7 Cumulative Damage Tests for $[\pm 25/90]_s$ Laminates.

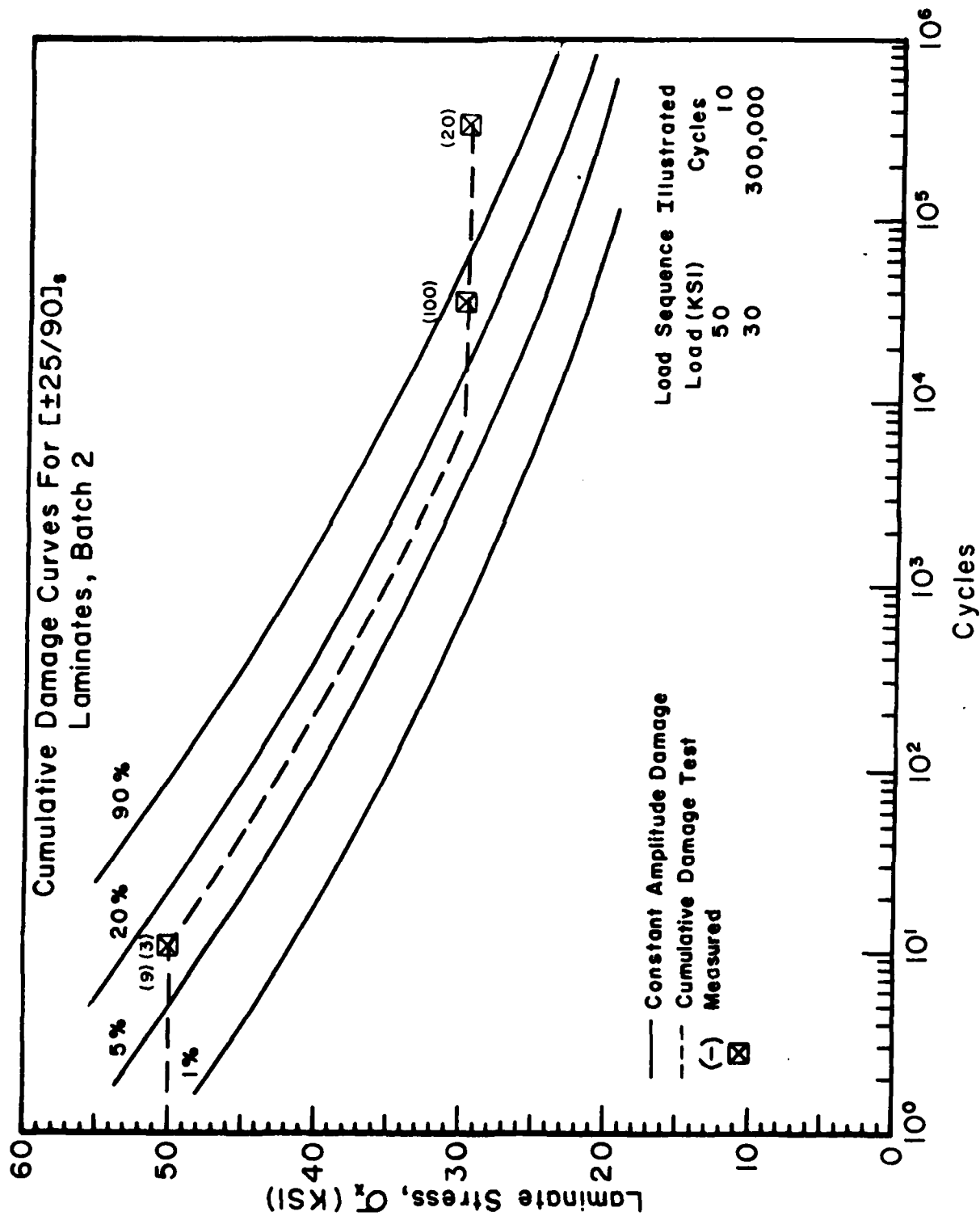


Figure G-8 Cumulative Damage Tests for $[\pm 25/90]_s$ Laminates.

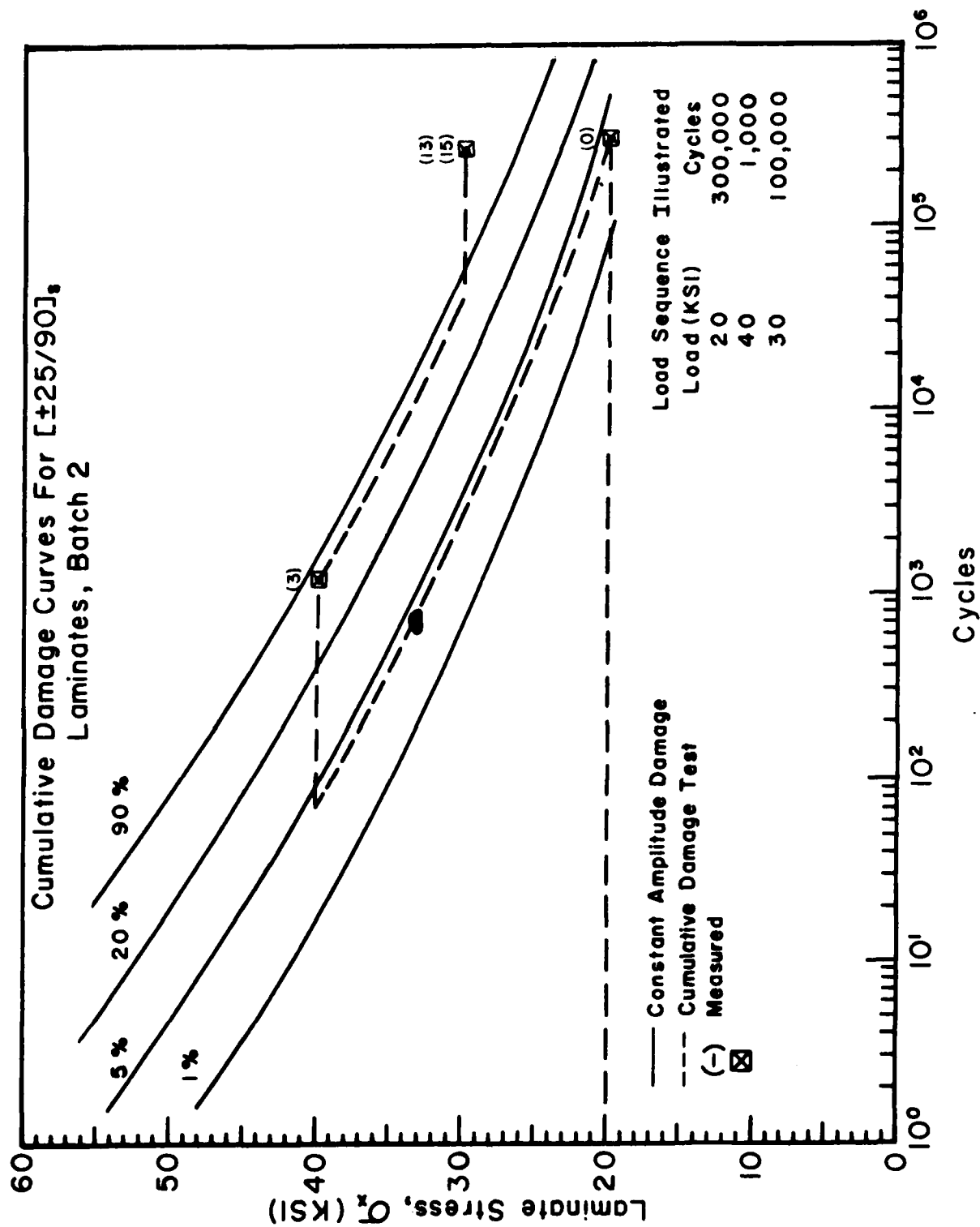


Figure G-9 Cumulative Damage Tests for $[\pm 25/90]_s$ Laminates.

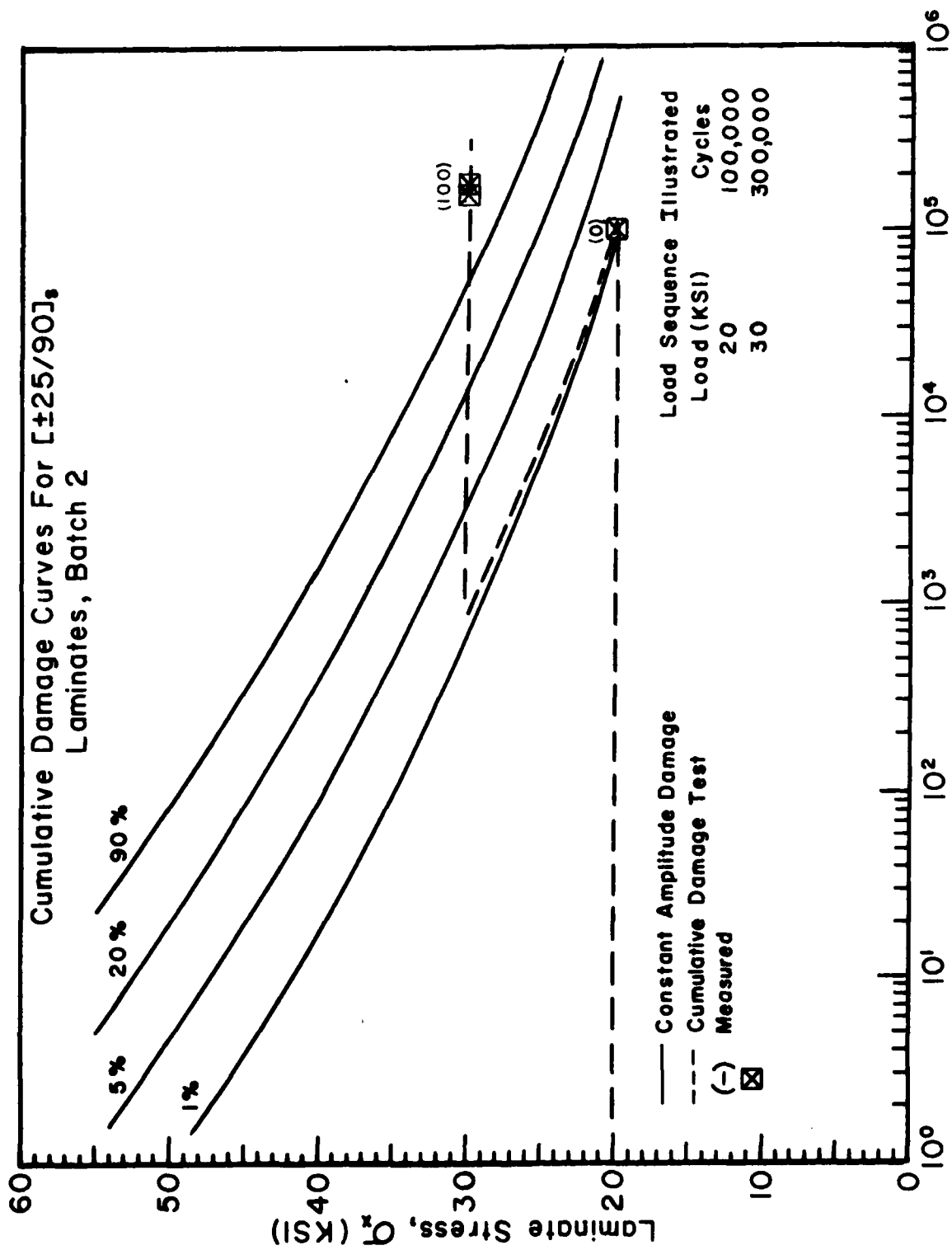


Figure G-10 Cumulative Damage Tests for $[\pm 25/90]_s$ Laminates.

APPENDIX H. BASIC MATERIAL CHARACTERIZATION

H1. Material Property Characterization in Phase-II.

A new batch of material (AS-3501-06) was used in the experiment during Phase-II. Material properties of the new batch were determined and compared with those obtained during Phase-I.

Some of the important material properties for the U.D. and other laminates are shown in Tables H-1, H-2, and H-3. Generally a $\pm 10\%$ difference is noted. But, this difference is considered to be within the experimental scatter. So, basically, the new batch of material is considered similar to the old batch of material.

Figure H-1 illustrates the tensile strength property scatter of $[0_8]$ laminate between the old and new batches of materials. In this case, the new batch of material exhibited a great scatter in the tensile strength property.

A comparison of the transverse crack growth curves (number of cracks versus applied tensile load) of $[0_2/90_2]_s$ between the old and new batches is shown in Figure H-2; a similar comparison for $[0_2/90_3]_s$ is shown in Figure H-3. The present batch showed a stronger resistance to transverse cracking. This is due possibly to the slightly stiffer E_L property of the 0° -ply, see Table H-1.

The free edge induced delamination growth curves in $[\pm 25/90_n]_s$, $n = 1, 2, 3$ are shown, respectively, in Figures H-4, H-5, and H-6. Again, the difference between the new and the old batches can be noted. Generally, the new batch of specimens developed edge delamination at a lower load and the growth of it also showed a faster rate. The reason for the difference is not immediately clear, however.

TABLE I. MATERIAL PROPERTIES OF U. D. SYSTEM

Properties	Previous Batch (1)	New Batch (2)
E_L (comp.) MPa (ksi)	132.2×10^3 (19.19×10^3)	--
E_L (Ten.) MPa (ksi)	139×10^3 (20.17×10^3)	157.7 (23.10×10^3)
E_T (Ten.) MPa (ksi)	11.1×10^3 (1.6×10^3)	--
ν_{LT}	0.269	0.319
σ_u , L MPa (ksi)	1826 (265)	1845 (268)
σ_u , T MPa (ksi)	60 (8.7)	--
V_f , %	66.45%	66.7%
Sp. Gr.	1.55	1.58
G_{LT}	4825 (700)	--

TABLE II. LAMINATE PROPERTIES UNDER TENSION

<u>Laminate</u>	<u>E_x MPa (ksi)</u>	<u>ν_{xy}</u>	<u>σ_u MPa (ksi)</u>	<u>Sp. Gr.</u>
$[\underline{+45}]_2$	19.1×10^3 (2780)	0.83	157.7 (22.87)	1.64
$[0_2/90_2]_s$ old	72.1×10^3 (10460)	0.0704	859 (124.6)	1.67
new	75.1×10^3 (10900)	0.074	882 (128.0)	--
$[0_2/90_3]_s$ old	63.6×10^3 (9220)	0.045	782 (113.5)	1.59
new	62.9×10^3 (9110)	0.060	738 (107.1)	--
$[\underline{+25/90}]_s$ old	63.8×10^3 (9250)	0.29	406.8 (59.0)	1.56
new	57.2×10^3 (8300)	0.27	371.0 (53.8)	--
$[\underline{+25/90}_2]_s$ old	46.1×10^3 (6700)	0.162	315.4 (45.75)	1.57
new	49.9×10^3 (7250)	0.181	350 (50.7)	--
$[\underline{+25/90}_3]_s$ old	42.0×10^3 (6100)	0.101	274.9 (39.9)	1.58
new	42.1×10^3 (6120)	0.14	284.5 (41.4)	--

TABLE III. ONSET LOADS FOR DAMAGE

<u>Laminate</u>	<u>Transverse Cracking</u>		<u>Edge Delamination</u>	
	MPa (ksi)		MPa (ksi)	
[0 ₂ /90 ₂] _s	old	330.7 (48.0)	--	
	new	345.0 (50.0)	--	
[0 ₂ /90 ₃] _s	old	262.0 (38.0)	--	
	new	275.5 (40.0)	--	
[+25/90] _s	old	314.0 (47.0)	314.0 (47)	
	new	282.4 (41.0)	327.0 (47.5)	
[-25/90 ₂] _s	old	186.0 (28.0)	265.5 (40)	
	new	172.3 (25.0)	282.4 (41)	
[-25/90 ₃] _s	old	158.5 (23.0)	255.0 (37)	
	new	137.8 (20.0)	241.2 (35)	

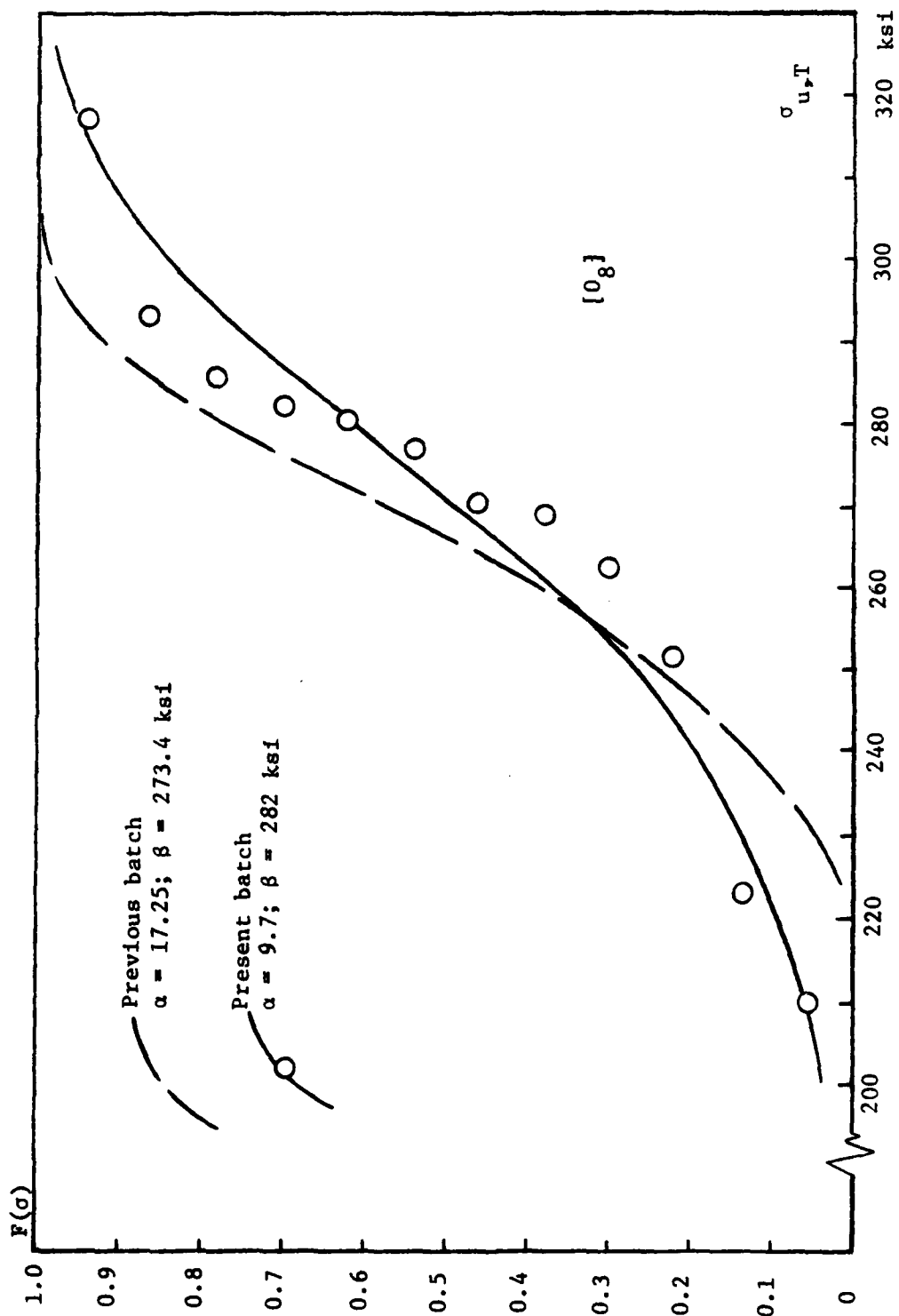


Figure H-1 Comparison of the Tensile Strength Distributions of the New and the Old Batches of Materials.

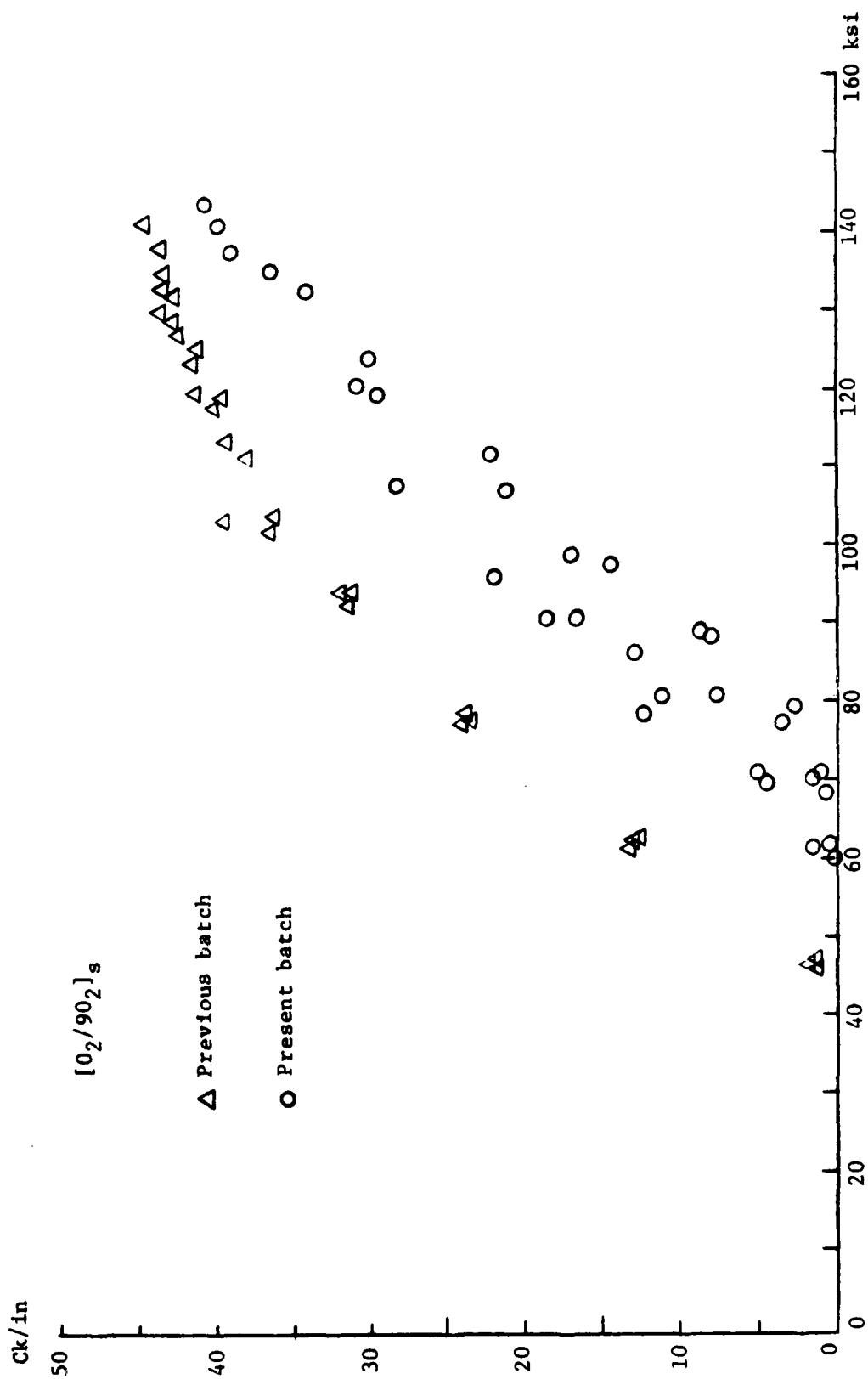


Figure H-2 A Comparison of the Transverse Crack Growth Curves Between the New and the Old Batches of Materials. $[O_2/90_2]_s$

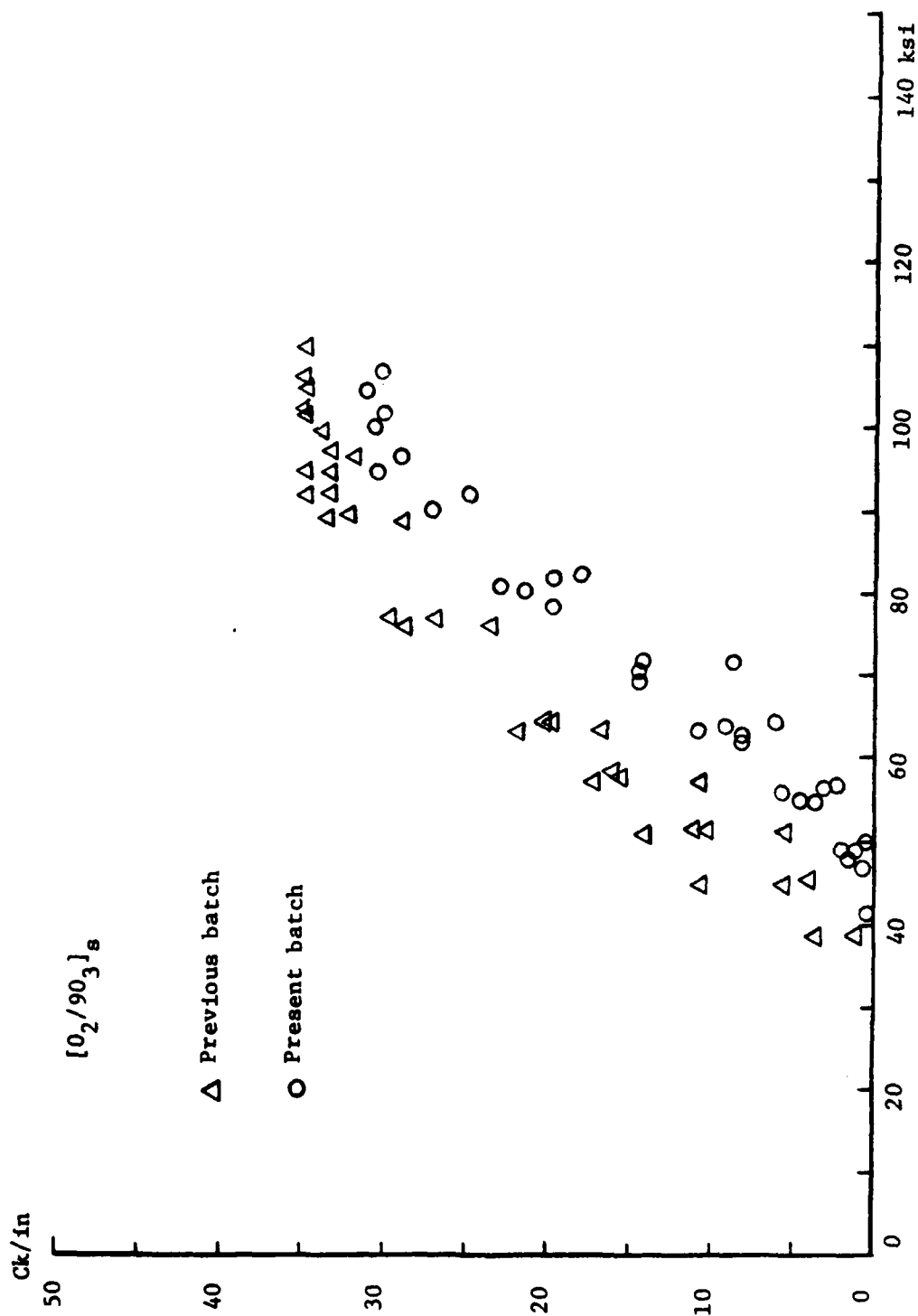


Figure H-3 A Comparison of the Transverse Crack Growth Curves Between the New and the Old Batches of Materials. $[O_2/90_3]_s$

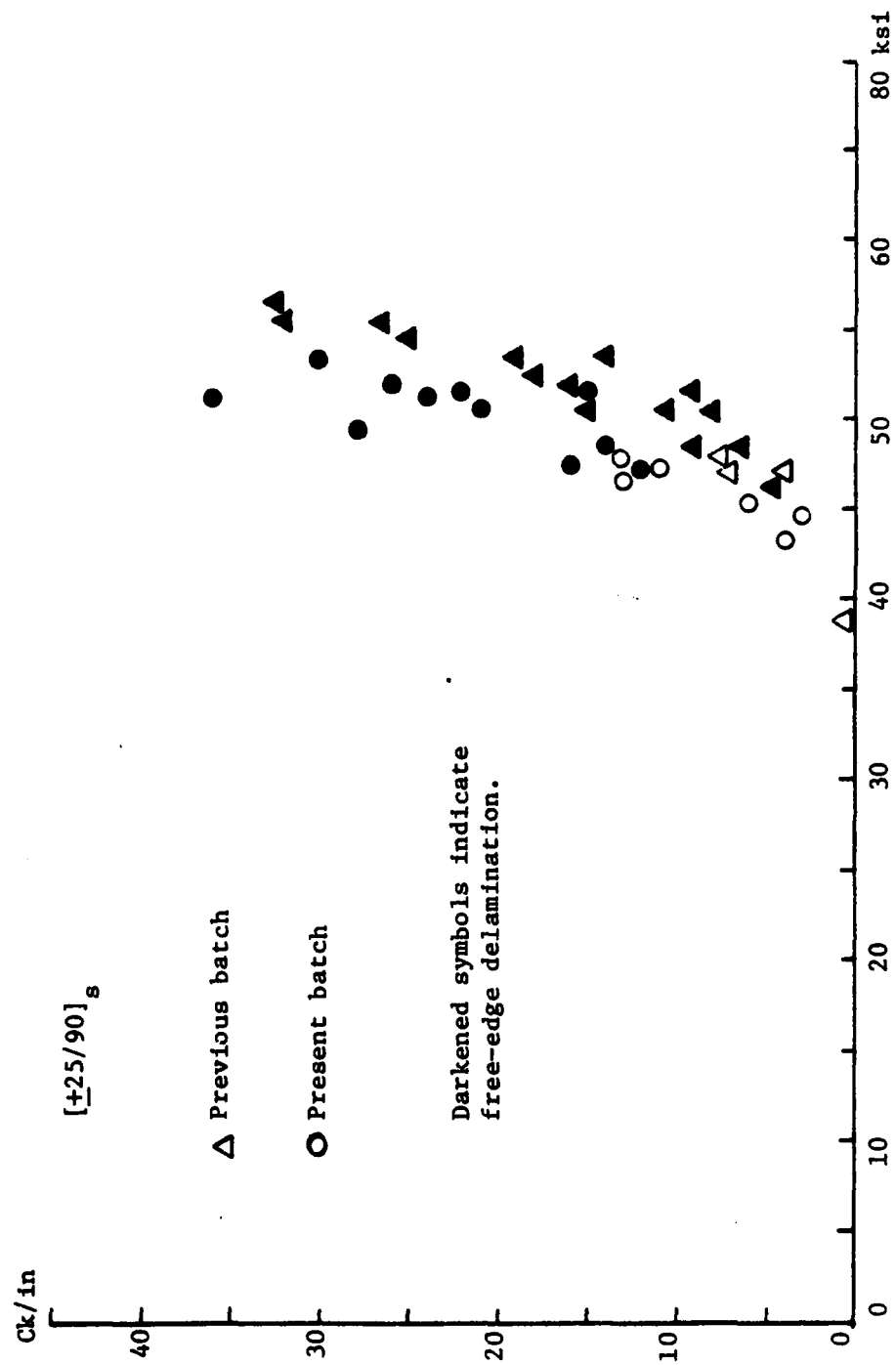


Figure H-4 A Comparison of the Free Edge Delamination Growth Curves Between the New and the Old Batches of Materials. $[+25/90]_s$

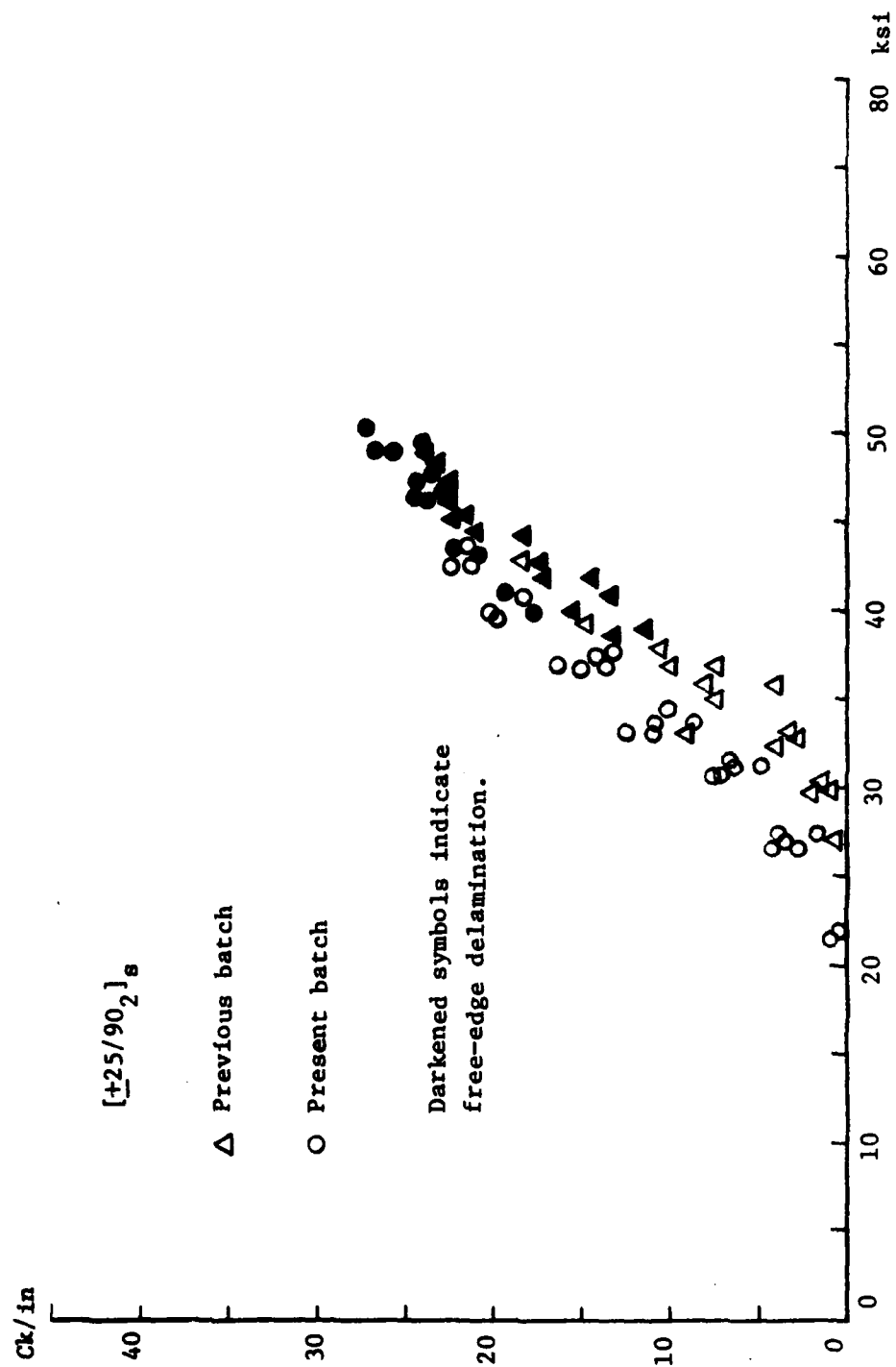


Figure H-5 A Comparison of the Free Edge Delamination Growth Curves Between the New and the Old Batches of Materials. $[+25/90_2]_s$

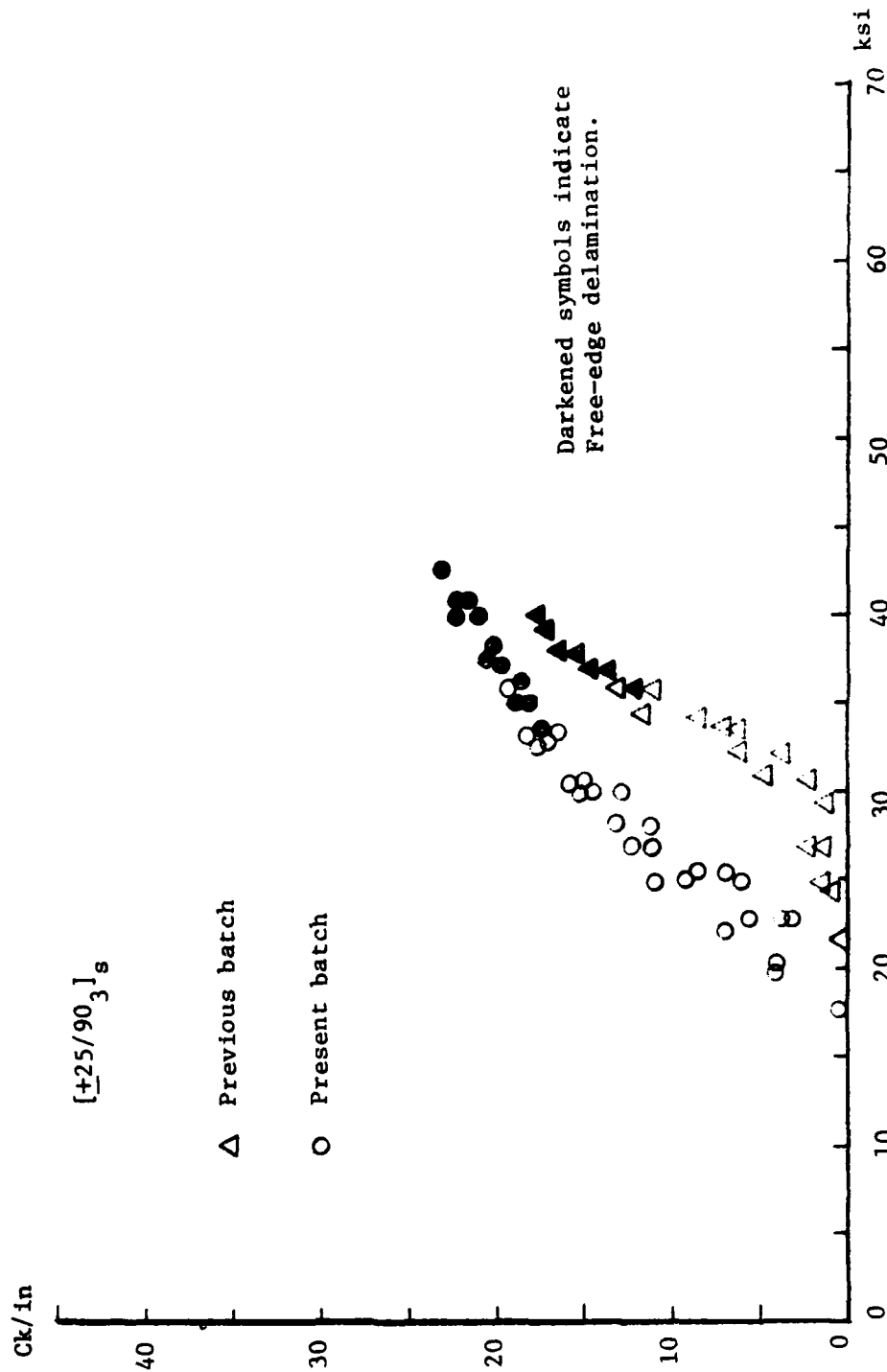


Figure H-6 A Comparison of the Free Edge Delamination Growth Curves Between the New and the Old Batches of Materials. $[+25/90]_3$ s

END

FILMED

10-84

DTIC